

Dust in the average galaxy: attenuation, emission, and opacity from 0 < Z < 7

Downloaded from: https://research.chalmers.se, 2026-11-23 06:59 UTC

Citation for the original published paper (version of record):
Casey, C., Akins, H., Battisti, A. et al (2026). Dust in the average galaxy: attenuation, emission, and opacity from 0 < Z < 7. Open Journal of Astrophysics, 9. http://dx.doi.org/10.33232/001c.167549

N.B. When citing this work, cite the original published paper.

research.chalmers.se offers the possibility of retrieving research publications produced at Chalmers University of Technology. It covers all kind of research output: articles, dissertations, conference papers, reports etc. since 2004. research.chalmers.se is administrated and maintained by Chalmers Library

(article starts on next page)

Version August 18, 2026
Preprint typeset using LaTeX style openjournal v. 09/06/15

arXiv:2606.17270v2 [astro-ph.GA] 17 Aug 2026

DUST IN THE AVERAGE GALAXY: ATTENUATION, EMISSION, AND OPACITY FROM $0 < Z < 7$

Caitlin M. Casey [1,2], Hollis B. Akins [3,*], Andrew J. Battisti [4,5], Jed McKinney [3,†], Ezequiel Treister [6], Jorge A. Zavala [7], Hiddo Algera [8], Manuel Aravena [9,10], Yingjie Cheng [11], Nicole E. Drakos [12], Andreas L. Faisst [13], Maximilien Franco [14], Seiji Fujimoto [15], Ghassem Gozaliasl [16,17], Ali Hadi [18], Santosh Harish [19], Michaela Hirschmann [20,21], Olivier Ilbert [22], Kohei Inayoshi [23], Jeyhan S. Kartaltepe [24], Anton M. Koekemoer [19], Claudia del P. Lagos [4,2], Ronaldo Laishram [25], Erini Lambrides [26,‡], Daizhong Liu [27], Arianna S. Long [11], Georgios E. Magdis [2,28,29], Sinclaire M. Manning [7], Crystal L. Martin [1], Felix Martinez III [24], Richard Massey [30], Jacqueline E. McCleary [31], Henry Joy McCracken [32], Lauro Moscardini [33,34,35], Desika Narayanan [36,2], Louise Paquereau [37], Jason Rhodes [38], Brant E. Robertson [39], Rasha M. Samir [40], Claudia Scarlata [41], Marko Shuntov [2,29,42], Laura Sommovigo [43], Aswin P. Vijayan [44], Wuji Wang [13], Can Xu [45,46,47], and Dhruv Zimmerman [36]

Version August 18, 2026

Abstract

We present constraints on the dust emission and attenuation properties of galaxies across $0<z<7$ using JWST imaging from the COSMOS-Web Survey combined with deep far-infrared (FIR) and (sub)millimeter data from *Spitzer*, *Herschel*, SCUBA-2, NIKA2 and ALMA. We analyze over 500,000 galaxies to independently constrain attenuation as inferred in the rest-frame ultraviolet (UV) and optical as well as dust emission from stacked FIR spectral energy distributions (SEDs), enabling a direct comparison between the two. We find UV/optical attenuation systematically underpredicts IR luminosity by a factor of $\sim$3$\times$ at $0.5 < z < 7$ and up to an order of magnitude for $M_\star > 10^{10.5}$ M$_\odot$. We derive empirical relationships for the effective attenuation (A_{UV} and A_V), dust temperature, fraction of star formation that is unobscured, and dust-to-stellar mass ratio as functions of redshift and stellar mass. On galaxy-integrated scales, we separate the first order effect of star/dust geometry from dust grain properties by combining constraints on the IR SED, the UV SED, and the dust mass surface density. Importantly, we measure over an order of magnitude decrease in κ_{UV}/κ_{FIR}— the ratio of dust mass absorption coefficients in the UV at 1600Å and FIR at 500μm — from $z \sim 0$ to $z \sim 7$. A depressed κ_{UV}/κ_{FIR} ratio is consistent with a deficit of small dust grains, possibly attributable to the intense radiation fields of high-z star formation; indeed, we find a redshift-invariant inverse relationship between κ_{UV}/κ_{FIR} and Σ_{SFR}. Assuming the varying dust opacity is dominated by changes to small grains and not large grains, we infer a modest evolution in the dust-to-stellar mass ratio $\propto (1+z)^{1.36}$ with secondary stellar mass dependence, $\propto M_\star^{-0.3}$. Most evolution in the dust-to-stellar ratio is at $z < 1$, the product of mild downward evolution in the dust-to-gas ratio combined with steep evolution in the gas-to-stellar ratio. The significant evolution and dynamic range of κ_{UV}/κ_{FIR} and prevailing disconnect between the UV/optical and FIR regimes emphasize that direct dust constraints are irreplaceable for the majority of star-forming galaxies at $z < 7$, not just the most extreme star-formers.

Subject headings: Galaxies, Attenuation, Dust

1. INTRODUCTION

Dust makes up a negligible fraction of the cosmic mass budget ($\lesssim 1\%$), and yet it has a profound impact on the perception of starlight via attenuation (Salim and Narayanan 2020; Schneider and Maiolino 2024). While dust efficiently absorbs ultraviolet and optical photons and converts them to thermal energy re-radiated at much longer wavelengths, our ability to fully characterize interstellar dust beyond our immediate neighborhood has been severely limited by observational hurdles and degeneracies. Dust extinction measurements are limited to individual stellar sightlines in the Milky Way relative to localized measurements of the hydrogen column density (Reina and Tarenghi 1973; Gorenstein 1975; Predehl and Schmitt 1995; Güver and Özel 2009). Dust attenuation curves have been constrained for nearby galaxies and increasingly larger samples out to $z \sim 3$ (Reddy *et al.* 2015; Shivaei *et al.* 2020; Battisti *et al.* 2022), but the inference relies on assumptions – empirical effective laws (Calzetti *et al.* 2000), specific star/dust geometries, or fixed grain populations – that have not been independently tested. Direct comparison between attenuation derived from the UV/optical and absorption derived from the FIR remains rare. Dust in emission has been seen predominantly in the rarest of bright submillimeter galaxies (e.g. Smail *et al.* 1997, see reviews by Blain, Smail, Ivison, Kneib, and Frayer 2002 and Casey, Narayanan, and Cooray 2014a), with relatively little understanding as to how exceptional that dust emission is relative to more 'normal' galaxies at high redshift.

The framework through which we study dust in the distant universe is thus anchored to nearby universe calibrations, with a limited range of attenuation curves, dust mass absorption coefficients, and assumptions about star/dust geometries. We implicitly assume that these calibrations apply at greater redshifts. If these assumptions are systemically inaccurate, then much of what we infer regarding dust at high redshift may not hold —

dust masses may be off by up to an order of magnitude, and even stellar masses could be under/over-estimated based on the application of an inappropriate attenuation law (e.g. McKinney *et al.* 2025). Furthermore, dust is built from metals and complex molecules, thus its total mass is also inherently linked to the metallicity of the interstellar medium (ISM) and star formation histories in galaxies (Draine and Li 2007; Rémy-Ruyer *et al.* 2014; De Vis *et al.* 2019). Both metallicity and star formation histories are believed to be quite different for the 'average' galaxy at $z = 2 - 8$ than at $z = 0$ (Maiolino *et al.* 2008; Mannucci *et al.* 2010; Zahid *et al.* 2014; Jain *et al.* 2026): more metal poor and potentially burstier. Observations of dust at these epochs may reveal interesting details about the integrated enrichment and star formation history. Further it may also reveal its future potential for star formation as a key catalyst for gas cooling in molecular clouds.

Studying and calibrating the impact of dust is intrinsically difficult beyond the local universe, given that extraordinary sensitivity is required to understand the 'normal' galaxy population. In this paper we place empirical constraints on galaxies' dust emission and absorption, and the direct relationship between the two, out to $z \sim 7$ using the marriage of improved constraints from the James Webb Space Telescope, JWST, and the Atacama Large Millimeter and submillimeter Array, ALMA, combined with other FIR datasets, together in the Cosmic Evolution Survey (COSMOS) field (Scoville *et al.* 2007). By pushing near-infrared imaging more than 10× deeper than previous imaging at high spatial resolution over large areas, JWST has revolutionized the precision at which we characterize galaxies' photometric and spectroscopic redshifts as well as the intrinsic shape of galaxies' rest-frame optical SEDs (Shuntov *et al.* 2025). This in turn also dramatically improves constraints on their star formation histories (Arango-Toro *et al.* 2025) and stellar masses measurements. JWST fundamentally pushes this characterization of the rest-frame UV/optical for $\sim 3\times$ more galaxies per unit area on the sky, and for galaxies much fainter (1-2 magnitudes) than previously possible. ALMA, along with other (sub)mm facilities, adds constraints on galaxies' dust emission. The wealth of ALMA data in JWST-imaged areas has ballooned in recent years, such that many galaxies less luminous than traditional dusty star-forming galaxies are now routinely accessible. Furthermore, large areas in the COSMOS field now have deep ALMA continuum maps, enabling truly sensitive stacking experiments propelled in sensitivity by the density of JWST-detected galaxies on the sky.

This paper is organized as follows. § 2 provides a framework for understanding the goals of this work; it discusses the physical relationship between attenuation and emission, and discusses key unknowns. § 3 presents the JWST, ALMA, and other submillimeter data used in this work, focused in and around the COSMOS-Web JWST Survey (Casey *et al.* 2023). § 4 presents the methodology by which we constrain the UV/optical and, independently, the dust SEDs for galaxies measured as a function of stellar mass and redshift through a FIR stacking analysis. § 5 presents a number of key measurements of implied physical characteristics, their evolution, and redshift dependence; this includes properties derived from the UV/optical portion of the SED, properties derived from the stacked dust SEDs in the FIR, and properties that present physical measurements through a combination of the two. § 6 connects the unique constraints presented in the previous section; we focus in particular on applying the framework of § 2 to separate out the impact of star/dust geometry from dust grain properties and comment on the underlying drivers of the evolution in the dust-to-stellar ratio. § 7 concludes. Throughout, we presume a Kroupa initial mass function (Kroupa 2001) and a Planck cosmology (Planck Collaboration *et al.* 2020). All appearances of log imply $\log_{10}$ and ln implies a natural logarithm.

2. FRAMEWORK & APPROACH

It is beneficial to revisit fundamental definitions linking galaxies' dust attenuation to their emission and mass to clarify our aims in this work. The relationship between optical depth τ, the dust mass absorption coefficient κ_λ, path length ds, and dust density ρ, is $d\tau_\lambda = -\kappa_\lambda \rho ds$. From that, it follows that the magnitudes of attenuation A_λ and dust mass surface density, $\Sigma_{\rm dust}$, relate via:

$$A_{\lambda,\rm screen} = \frac{2.5}{\ln(10)} \kappa_\lambda \Sigma_{\rm dust}. \quad (1)$$

This presumes a simple foreground screen of dust in front of a light source (i.e. starlight).

The dust mass absorption coefficient κ_λ (Weingartner and Draine 2001; Draine 2003) encodes the complex absorption properties of different dust grains, and the grain type and size distribution, as a function of wavelength. It may also be broken into two components corresponding to the intrinsic *absorptive* properties of the dust ($\kappa_{\lambda,abs}$, which goes directly into reradiated thermal emission) and a scattered light component ($\kappa_{\lambda,scat}$, accounting for photons of wavelength λ that are not destroyed, but rather scattered), such that the total $\kappa_\lambda = \kappa_{\lambda,abs} + \kappa_{\lambda,scat}$. Milky Way dust has significant scattering for UV/optical photons such that $\kappa_{\lambda,scat}/\kappa_\lambda \approx 0.3 - 0.6$ (Cardelli *et al.* 1989). The scattering vs. absorption distinction is crucial in the consideration of narrow sightlines over which extinction is being measured (e.g. in the Milky Way); in the case of integrated light from entire galaxies, κ_λ is taken entirely as an absorption factor due to all scattered light being accounted for within the galaxy aperture, as discussed in Calzetti *et al.* (2000).

Generalizing to a mixed star/dust geometry then can be written as:

$$A_\lambda = \frac{2.5}{\ln(10)} \mathcal{G}_\lambda \kappa_\lambda \Sigma_{\rm dust} \quad (2)$$

where the additional term, $\mathcal{G}_\lambda$, we introduce as a wavelength-dependent factor that encodes the star/dust geometry. It may be defined as the ratio of the effective optical depth ($\tau_\lambda^{\rm eff}$, or optical depth of "apparent extinction", Charlot and Fall 2000) to the physical optical depth, or similarly the ratio of observed A_λ (measured using standard techniques in the rest-frame UV/optical) to directly inferred $A_{\lambda,\rm direct}$ (inferred by measures of dust mass surface density, $\Sigma_{\rm dust}$). By its nature, $\mathcal{G}_\lambda$ is bounded such that $0 < \mathcal{G}_\lambda \leq 1$ (the following works all explore the crucial role of geometry, though they do not explicitly use the convention we have outlined with

$\mathcal{G}_\lambda$; Disney *et al.* 1989; Byun *et al.* 1994; Witt and Gordon 1996, 2000; Charlot and Fall 2000; Chevallard *et al.* 2013; Narayanan *et al.* 2018; Trayford *et al.* 2020; Ferrara *et al.* 2022; Qin *et al.* 2024; Sommovigo *et al.* 2026). $\mathcal{G}_\lambda = 1$ corresponds to a uniform foreground slab, and $\mathcal{G}_\lambda \approx 1/2$ for a uniform, optically thin ($\tau \ll 1$) slab with stars mixed uniformly throughout. A case where stars are completely decoupled from dust would correspond to $\mathcal{G}_\lambda \approx 0$ (i.e. a *background* dust screen), but the reality of mixed star/dust geometries is that some emergent starlight usually escapes near the surface, and $\mathcal{G}_\lambda$ should not get very close to 0. The impact of $\mathcal{G}_\lambda$ is to *lessen* A_λ for a given dust mass surface density, and while $\mathcal{G}_\lambda$ can be worked out analytically for some simple toy models (dust screen, dust slab, exponential disks at given inclination, etc.), it will generally not be a function that is easy to directly measure or derive. For example, it is understood that geometry also has a strong wavelength dependence, such that a clumpy ISM with narrow escape channels for starlight results in a *grayer* attenuation curve (Natta and Panagia 1984; Calzetti *et al.* 1994; Witt and Gordon 2000; Salim and Narayanan 2020) or bluer rest-frame UV slope (Goldader *et al.* 2002; Howell *et al.* 2010; Casey *et al.* 2014b; Narayanan *et al.* 2018) for fixed dust mass. A clear illustration is given by Granato *et al.* (2000), who find that radiative transfer through the age-dependent, two-phase geometry of a model starburst produces an emergent attenuation curve closely resembling the empirical Calzetti *et al.* (2000) law, despite adopting a grain mixture tuned to reproduce the Milky Way extinction curve. In the language of Eq. 2, this is a case where the wavelength dependence of $\mathcal{G}_\lambda$ dominates over that of κ_λ in setting the shape of the observed attenuation curve.

What is known about κ_λ from observational constraints? The dust mass absorption coefficient has been empirically measured in the Milky Way via the relation:

$$\frac{A_\lambda}{\Sigma_{\rm dust}} = \frac{A_\lambda/N_H}{(M_{\rm dust}/M_H)m_H}\mathcal{G}_\lambda = \frac{2.5}{\ln(10)}\mathcal{G}_\lambda\kappa_\lambda \quad (3)$$

where A_λ/N_H is the attenuation per unit hydrogen column density measured for individual stellar sightlines in the Milky Way to be $\mathrm{A_V/N}_H \approx 5.3\times10^{-22}\,\mathrm{mag\,cm^2\,/H}$ (Bohlin *et al.* 1978; Diplas and Savage 1994; Güver and Özel 2009) in the V-band, where a dust-screen is implicitly assumed ($\mathcal{G}_V = 1$). $\mathrm{M_{dust}}/M_H$ is the dust to hydrogen gas ratio which has some metallicity dependence (Draine and Li 2007; Rémy-Ruyer *et al.* 2014); for the Milky Way, solar metallicity, and a uniform dust screen ($\mathcal{G}_V = 1$), this gives $\kappa_V \approx 3.2-3.3\times10^4\,\mathrm{cm^2\,g^{-1}}$. This is fairly well constrained to $\lesssim$10% under these conditions. For a general metallicity-dependent dust-to-gas ratio, and no metallicity-dependent geometry, one would expect κ_λ (in the optical where A_V/N_H is measured) to scale with metallicity following, e.g., Eq 9 of Draine *et al.* (2014).

At longer wavelengths, the total dust mass of a galaxy scales linearly with the rest-frame flux density in the optically thin portion of the spectrum (Hildebrand 1983):

$$M_{\rm dust} = \frac{S_\nu^{\rm rest} D_{\rm L}^2}{\kappa_\nu B_\nu(T_{\rm dust})}. \quad (4)$$

Here $S_\nu^{\rm rest}$ is the rest-frame flux density of a given dust reservoir emitting longward of $\geq$250 μm (i.e. on the Rayleigh-Jeans tail of dust blackbody emission), D_L is the luminosity distance, κ_ν is the dust mass absorption coefficient at the frequency where the flux density is inferred (i.e. in the FIR), $T_{\rm dust}$ is the mass-weighted average dust temperature in the reservoir, and $B_\nu(T_{\rm dust})$ is the Planck function evaluated at temperature $T_{\rm dust}$. The re-radiated spectrum per dust grain is given by[1] $\kappa_\nu B_\nu(T_{\rm dust})$ and the total dust luminosity set by $4\pi D_L^2 S_\nu^{\rm rest}$; another factor of 4π arises from the conversion of B_ν from specific intensity to a grain-normalized luminosity, and they cancel out.

The optically thin portion of the dust spectrum typically occurs at rest-frame wavelengths longward of $\lambda \gtrsim 250\,\mu$m. For this work, we will use rest-frame 500μm emission to anchor dust mass calculations. Here we adopt a dust mass absorption coefficient at 500 μm, $\kappa_{\rm FIR}^{\rm fix} = 2\,\mathrm{cm^2\,g^{-1}}$ following Clark *et al.* (2019), and we note that $\kappa_{\rm FIR} \propto \lambda^{-\beta}$ where $\beta = 2$ throughout the FIR/mm regime. Throughout this paper we will refer to $\kappa_{\rm FIR}$ as specifically evaluated at 500μm, with the Clark *et al.* (2019) value denoted $\kappa_{\rm FIR}^{\rm fix}$. Importantly, we emphasize that dust mass coefficients in the FIR are highly uncertain because the FIR lacks direct empirical constraints unlike the UV/optical where attenuation along stellar sightlines can be directly constrained. A suite of foundational grain models (Mathis *et al.* 1977) calculate $\kappa_{\lambda,abs}$ from the UV through the submm (Draine and Lee 1984), and highlight the impact of dust grain morphology — fluffy aggregates vs. bare compact grains — on κ_λ (Ossenkopf and Henning 1994; Henning and Stognienko 1996). These models were updated to include polycyclic aromatic hydrocarbons (PAHs) in Weingartner and Draine (2001); Li and Draine (2001) and Draine (2003) with a complementary analysis on grain shape in Siebenmorgen *et al.* (2014). Given the lack of direct, empirical constraints on $\kappa_{\rm FIR}$, we conservatively caution that dust masses cannot be known better than within a factor of $\sim$2$\times$ following the 2$\times$ modeling uncertainty on $\kappa_{\rm FIR}$. The dust mass also has a dependence on flux density and presumed dust temperature $\mathrm{T_{dust}}$ via the Planck Function, and there is also a concern about applying single-temperature models to recover the total dust mass, which is discussed in detail in Sommovigo and Algera (2025). However, despite the dependence on dust temperature and flux density precision, the uncertainty of both ($\sim$20%) are dwarfed by the uncertainty of $\kappa_{\rm FIR}$.

Dust mass can then be translated to dust mass surface density with knowledge of the dust emitting size effective radius, $R_{\rm e}$. In practice, resolved dust sizes are not available for large samples of galaxies to high redshift, but for those that exist, FIR sizes and morphologies draw parallel to trends observed in optical light: higher redshift galaxies are smaller and FIR emission broadly appears consistent with Sérsic profiles with $n = 1$ (Hodge and da Cunha 2020). In this work, we will generalize to use galaxies' measured sizes from JWST NIRCam imaging (rest-frame optical to near-infrared) as a good proxy of their dust sizes for the purpose of calculating dust mass surface densities. We will assert in this work that

[1] In practice, the Planck function is computed in $\mathrm{erg\,s^{-1}\,cm^{-2}\,Hz^{-1}\,str^{-1}}$ and the use of ν in Equation 4 reflects the use of Janskys in the FIR as typical convention.

$R_e^{\rm dust} \approx R_e^{\rm stars}/\sqrt{2}$. This presumption is one of convenience and necessitated by the limitation of current datasets; it could be lifted in the future with improved constraints on that relationship. The factor of $\sqrt{2}$ accommodates the fact that dust reservoirs are often slightly more compact than their stellar reservoirs and centrally peaked (Conselice 2014; Mosenkov *et al.* 2019); while this prefactor is not precisely constrained, the important component of this is that $R_e^{\rm dust}$ does not evolve in a wildly different manner than $R_e^{\rm stars}$, which is not just consistent with recent observations but also theoretical expectation (e.g. Popping *et al.* 2022). It then follows that dust mass surface density is then given by:

$$\Sigma_{\rm dust} = \frac{M_{\rm dust}}{\pi R_e^2} = \frac{S_{500}^{\rm rest} D_L^2}{\pi \kappa_{\rm FIR} B_{500}(T_{\rm dust}) R_e^2} \quad (5)$$

The dominant uncertainty on $\Sigma_{\rm dust}$ still comes from the uncertainty on $\kappa_{\rm FIR}$ based on the critical size assumption made here (where future observations could change the error budget).

Joining Equations 2 and 5 for attenuation at wavelength λ in the UV/optical regime gives:

$$A_\lambda = \frac{2.5}{\pi \ln(10)} \frac{S_{500}^{\rm rest} D_L^2}{B_{500}(T_{\rm dust}) R_e^2} \frac{\kappa_\lambda}{\kappa_{\rm FIR}} \mathcal{G}_\lambda \quad (6)$$

Here the observables from the FIR are $S_{500}^{\rm rest}$, from an SED fit to observed-frame photometric constraints, R_e from high-resolution imaging, and A_λ from a detailed SED fit to the UV/optical SED. The dominant uncertainty in this equation comes from the product of $(\kappa_\lambda/\kappa_{\rm FIR})\mathcal{G}_\lambda$ which we will set empirical limits on in this work in the UV (λ=1600Å). A simplified form of Eq. 6, applied in the limit of a fixed geometry, was used by Casey *et al.* (2024) to estimate dust masses in little red dots from their compact sizes and inferred attenuation; here we retain $\mathcal{G}_\lambda$ and $\kappa_\lambda/\kappa_{\rm FIR}$ as quantities to be constrained rather than assumed.

Following from Eq. 6, it will be handy later in this work to define the term

$$C_\lambda \equiv \frac{2.5}{\ln(10)} \kappa_{\rm FIR}^{\rm fix} \left(\frac{\kappa_\lambda}{\kappa_{\rm FIR}}\right) \mathcal{G}_\lambda \left[10^5\, M_\odot\, {\rm kpc}^{-2}\right] = A_\lambda \left[\frac{10^5\, M_\odot\, {\rm kpc}^{-2}}{\Sigma_{\rm dust}}\right] \quad (7)$$

which represents the ratio of effective attenuation to dust mass surface density. Here, $\kappa_{\rm FIR}^{\rm fix} = 4.2 \times 10^{-10}\,{\rm kpc}^2\,{\rm M}_\odot{}^{-1}$, our fiducial adopted value of the dust mass absorption coefficient at rest-frame 500μm in units of kpc^2 M$_\odot{}^{-1}$. This renders C_λ a unitless ratio of attenuation to dust mass surface density. In the V-band, Aniano *et al.* (2012) infer $C_V = 0.67$, and Draine *et al.* (2014) find $C_V = 0.74$, both based on Milky Way and dust model calibrations assuming a foreground screen.

If the FIR SED of a galaxy can be observed, then the integrated IR luminosity is known ($L_{\rm IR}$, typically integrated from rest-frame 8–1000 μm, but dominated by emission right around $\sim$100 μm rest-frame), in addition to constraints on dust mass $M_{\rm dust}$ from the Rayleigh-Jeans tail. While $M_{\rm dust}$ depends on $\kappa_{\rm FIR}$ which traces dust grain properties, *the IR luminosity is free of any such dependence.* Through energy balance, the IR tells us, objectively, how much light has ultimately been absorbed in the rest-frame UV/optical and reprocessed by dust grains. $L_{\rm IR}$ is simply equal to the difference between the intrinsic UV (and optical) luminosity and the observed $L_{\rm UV}$. A wealth of literature exists on ${\rm IRX} \equiv L_{\rm IR}/L_{\rm UV}$ where $L_{\rm IR}$ and $L_{\rm UV}$ are both *observed* quantities (e.g. Meurer *et al.* 1999) and its relationship to both $A_{\rm UV}$ (Buat *et al.* 2005; Hao *et al.* 2011; Cortese *et al.* 2008) and rest-frame UV slope (Calzetti *et al.* 1994; Reddy *et al.* 2006; Gil de Paz *et al.* 2007; Takeuchi *et al.* 2012). We can thus draw a direct line between IRX, this ratio of energy output in the IR and UV, and the attenuation that *should* be seen in the optical if a simple dust screen is assumed:

$$A_{\rm UV,direct} = 2.5 \log\left[1 + \frac{\rm IRX}{B'}\right] = 2.5 \log\left[1 + \left(\frac{C'_{\rm TIR}}{C'_{\rm FUV}}\right) \frac{1 - f_{\rm unobs}}{B'\, f_{\rm unobs}}\right] \quad (8)$$

The coefficient B' is the ratio of two bolometric correction factors, BC(1600Å)/BC(FIR), as discussed in Meurer *et al.* (1999) and McLure *et al.* (2018). B' is approximately equal to one, dominated by the bolometric correction in the UV (where 1600Å luminosity does not reflect the total UV light that is absorbed by dust); later in § 6.1 we discuss B' further and describe how it can be directly inferred for a given UV/optical SED. The second term in Eq. 8 follows from the first, where $f_{\rm unobs}$ is the ratio of the star-formation rate (SFR) that is unobscured relative to the total, i.e. $f_{\rm unobs} \equiv {\rm SFR_{UV}}/({\rm SFR_{UV}}+{\rm SFR_{IR}})$, which is another convenient conceptual way of framing IRX. The coefficient, $C'_{\rm TIR}/C'_{\rm FUV}$, then represents the ratio of SFR-to-luminosity scalings[2] between the total infrared (TIR), and far ultraviolet, FUV, in Kennicutt and Evans (2012): $C'_{\rm TIR}/C'_{\rm FUV} \approx 1.15$.

We can then draw direct comparison between $A_{\rm UV,direct}$, the attenuation that *should* be present if all of the dust were concentrated in a screen, and $A_{\rm UV}$, the effective or 'observed' attenuation in the UV. The latter may be derived through detailed UV/optical SED fitting when sufficient constraints are at hand to also constrain the star formation history (there is always some degeneracy between stellar age and attenuation causing redder SEDs in the UV/optical; see review on stellar population synthesis by Conroy 2013). The difference between $A_{\rm UV,direct}$ and $A_{\rm UV}$ is attributable to geometry alone, such that:

$$\mathcal{G}_{\rm UV} = \frac{A_{\rm UV}}{A_{\rm UV,direct}} \quad (9)$$

This also follows from dividing Eq. 2 by Eq. 1 in the UV (we will use 1600Å to denote UV in this work). So while the geometry itself is complex, we can use the rest-frame UV to directly parameterize $\mathcal{G}_{\rm UV}$ in a global, integrated sense. Then we may combine Eq. 6 with Eq. 8 and Eq. 9 and place constraints on the galaxy-integrated ratio of dust mass absorption coefficients, $\kappa_{\rm UV}/\kappa_{\rm FIR}$ directly:

$$\left(\frac{\kappa_{\rm UV}}{\kappa_{\rm FIR}}\right) = \pi \ln(10) \log\left[1 + \frac{IRX}{B'}\right] \frac{B_{500}(T_{\rm dust}) R_e^2}{S_{500}^{\rm rest} D_L^2} \quad (10)$$

[2] C is used in Kennicutt and Evans (2012) to denote the coefficient between luminosity and SFR, but here we use C' to be clear this is a different quantity than is denoted in Eq. 7

Measurement of this ratio can provide some first steps towards a greater understanding of the dust grain properties in the early Universe through a relatively straightforward set of observations. The observables[3] here are L_{IR}, L_{UV}, S_{500}^{rest}, T_{dust} and R_e. We also note that the ratio of L_{IR} and S_{500}^{rest} form a proxy for T_{dust}, leaving the number of true independent, observational constraints needed to four. We note that, theoretically, κ_{UV}/κ_{FIR} is a microphysical characteristic of dust grain properties, but here we are calculating a quantity linked in meaning, but integrated on macroscopic scales, which inherently folds in second-order effects of ISM geometry, which are complex and not directly measured. While this ratio may still be uncertain within a factor of two or more (again, from uncertainty on κ_{FIR}), we can infer if it *evolves*, which can inform future models of dust grain physics in the early Universe where no direct constraints on κ_λ exist.

Our work aims to make such measurements, and simultaneously present observations on the evolution and stellar-mass dependence of related quantities: the magnitudes of attenuation in the UV and optical, the effective attenuation law slope, L_{IR}, M_{dust} and T_{dust}, the fraction of unobscured star formation relative to total (f_{unobs}), and the dust-to-stellar mass ratio. This paper focuses on a stacking analysis, while a future work will focus on the specific characteristics of galaxies that have direct detections in the IR.

3. DATA

We use data from the COSMOS-Web Survey (PIs: Kartaltepe & Casey; Casey *et al.* 2023). The unique combination of depth and area covered by JWST and ALMA datasets in recent years is particularly notable in the COSMOS field, making it the only dataset uniquely capable of this type of measurement: stacking many thousands of galaxies across uniquely diverse (sub)mm datasets.

3.1. *JWST Data*

The JWST data in COSMOS, which forms the backbone of the dataset used in this paper, is described in the imaging reduction papers presenting NIRCam data (a contiguous 0.54 deg^2 in four filters; Franco *et al.* 2025) and MIRI data (0.2 deg^2 taken in parallel; Harish *et al.* 2025) and the COSMOS-Web "COSMOS2025" catalog description paper (Shuntov *et al.* 2025). To briefly summarize these data, NIRCam imaging in COSMOS-Web includes four filters (F115W, F150W, F277W, and F444W) with 5σ point source depth (in 0.″3 diameter apertures) roughly 27.5-28.2 AB. MIRI includes one filter (F770W) to a 5σ point source depth of 25.5-26 AB. The COSMOS2025 catalog was assembled using a NIRCam-only combined χ^2_+ detection image, hot+cold detection with Source Extraction and Photometry (SEP; Barbary *et al.* 2016), 2D morphological Sérsic model construction using SourceExtractor++ (SE++) on NIRCam, and fixed model photometric extraction on 37 photometric bands spanning ultraviolet through mid-infrared. The catalog contains 784,016 sources spanning the 0.54 deg^2 of NIRCam coverage. Photometric redshifts are fit using LePhare (Arnouts *et al.* 2002; Ilbert *et al.* 2006) and a broad range of templates spanning a wide range of attenuations, emission line strengths, and complex star formation histories (see Shuntov *et al.* 2025 for details on modifications made to LePhare for COSMOS-Web and Arango-Toro *et al.* 2025, for more detail on CIGALE-derived physical properties of sources in COSMOS2025 and the consistency of those properties with LePhare).

Of the 0.54 deg^2 area, 16% of the area (0.086 deg^2) is contained within ground-based star masks; in other words, the ground-based photometry in these regions is severely limited by spatial confusion with bright foreground stars that are less problematic in space-based imaging. Space-based photometric redshifts, including only *HST* and *JWST* photometry, are generated for all objects in the catalog and these are used in place of the full ground+space redshifts inside of these star masked regions (see Shuntov *et al.* 2025 for discussion of the broad consistency between ground+space and space-only photometric redshifts).

3.2. *(Sub)Millimeter Data*

COSMOS has a wealth of (sub)millimeter ([sub]mm) data from which we can derive accurate dust emission constraints. The most notable datasets of competitive depth and unique wavelength coverage include *Spitzer*/MIPS, *Herschel*/PACS+SPIRE, SCUBA-2, NIKA2, and ALMA coverage. *Spitzer* MIPS 24μm imaging (Sanders *et al.* 2007) covers the full field to 1σ=16 μJy depth. *Herschel* PACS 100μm and 160μm imaging (Lutz *et al.* 2011) also cover the full field to 2.37 mJy and 4.75 mJy 1σ depth, respectively. Similarly, *Herschel*/SPIRE imaging, at 250μm, 350μm, and 500μm (Oliver *et al.* 2012) is confusion-limited to a 1σ rms of 5.8 mJy, 6.3 mJy and 6.8 mJy respectively. SCUBA-2 imaging in the field is described by Simpson *et al.* (2019), which has 1σ depth ranging from 0.6–1.4 mJy at 870μm (while the effective wavelength of the filter is 870μm, the filter is often referred to as 850μm). NIKA2 data in the field covers an area of $\sim$0.3 deg^2 (Carvajal-Bohorquez *et al.* 2026; Béthermin *et al.* 2026) mostly overlapping the COSMOS-Web area; maps at 1.3 mm and 2 mm have 1σ depths of 0.32 mJy and 0.091 mJy, respectively, with corresponding spatial resolutions of 11″ and 17″.

Finally, ALMA data, though not exhaustive or uniform, covers a large number of sources at different frequencies and depths. The two roughly uniform blank-field survey datasets used in this work are the Ex-MORA survey (Long *et al.* 2026, a continuation of the Mapping Obscuration to Reionization with ALMA, MORA, survey described in Casey *et al.* 2021 and Zavala *et al.* 2021), a 2 mm deep field (1σ $\approx$90 μJy at $\sim$2.1 mm) covering 0.16 deg^2, and the CHAMPS survey (Faisst et al., in prep, Martinez et al., in prep Zavala *et al.* 2026), a 1.2 mm mosaic (1σ $\approx$0.14 mJy) covering the 0.2 deg^2 of JWST MIRI imaging in the field from COSMOS-Web and PRIMER (Donnan *et al.* 2024).

Beyond these blank-field efforts, we make use of the A3COSMOS[4] survey (Liu *et al.* 2019; Adscheid *et al.* 2024) to formulate a complete list of individual dust detections in the field, combining data from the SCUBA-Dive project (McKinney *et al.* 2024) on the brightest submm galaxies in the field, to CHAMPS, and Ex-

[3] The framework we discuss takes for granted that redshift, z, is reasonably well constrained.

[4] See https://sites.google.com/view/a3cosmos

MORA detections. The A3COSMOS dataset (in particular the 2025-03-12 data release) contributes most of the direct detection sources: 725 out of a total of 1024 across the field. In the stacking analysis that follows we keep track of these individual detections and their influence on the results but save analysis of their characteristics to a future work.

4. METHODS

Here we present the derivation of physical parameters closely associated with dust emission and absorption. To do this, we treat dust emission and dust absorption independently. The former is measured in the submm and the latter is measured from the rest-frame UV/optical portion of the SED. This is complementary to, though different than, common efforts that use energy balance techniques to fit both portions of the spectrum simultaneously. Energy balance approaches directly translate absorbed rest-frame UV/optical light to re-radiated FIR/millimeter emission (da Cunha *et al.* 2008, 2015; Burgarella *et al.* 2005; Noll *et al.* 2009; Boquien *et al.* 2019). Such energy balance techniques, though insightful, rely on some key assumptions we aim to break down empirically in this work: fixed (or relatively inflexible) attenuation laws, fixed dust mass absorption and emissivity assumptions, as well as fundamental presumptions made regarding star/dust geometry. A distinct class of models instead solves the radiative transfer explicitly through a specified, often age-dependent star/dust geometry, such that the emergent attenuation law is a prediction rather than an input (e.g. GRASIL; Silva *et al.* 1998; Granato *et al.* 2000). These avoid the assumption of a fixed attenuation curve, but require the geometry itself to be specified a priori – which is the quantity we aim to constrain empirically here. By not enforcing energy balance, we are able to compare the inferred attenuation to the output L_{IR} and assess, under what conditions, the UV/optical SED accurately recovers re-radiated dust emission.

In what follows we first describe the selection and pruning of galaxies in the COSMOS-Web catalog for stacking in FIR/(sub)mm datasets in § 4.1. Note that we explicitly aim to exclude quiescent systems from our stacks for ease of physical interpretation; at high masses and low redshifts, a significant population of quiescent galaxies are known to have markedly different dust characteristics than mass-matched galaxies with higher star-formation rates, with quiescent galaxies showing both suppressed dust emission and absorption (e.g. Paspaliaris *et al.* 2023; Chang *et al.* 2026). So it is in the interest of not mixing physically distinct populations – quenched systems and star forming systems – that we restrict to those thought to have dust warmed by the interstellar radiation field generated from star formation.

We then describe the IR SED fitting procedure to the stacked SEDs in § 4.2. Finally, we bootstrap the COSMOS2025 catalog to re-derive flexible attenuation law characteristics using priors based on the COSMOS2025 photometric redshifts (§ 4.3).

4.1. *Stacking*

Of 784,016 sources in the COSMOS-Web catalog, only 1024 (0.1%) currently have direct detections in the FIR/(sub)mm. Those individual galaxies are a focus of a separate work. We use submm stacking to characterize the dust properties of a broader dynamic range of 'normal' galaxies here. Submillimeter stacking is not a new enterprise (for example, Dole *et al.* 2006; Pascale *et al.* 2009; Penner *et al.* 2011; Viero *et al.* 2013; Béthermin *et al.* 2015a; Coppin *et al.* 2015; Tacconi *et al.* 2018; Inami *et al.* 2020; Magnelli *et al.* 2020; Euclid Collaboration *et al.* 2026). However, the limits of stacking results (in redshift, IR-luminosity, and mass) are dependent both on the size of the sample being stacked, and the precision with which its characteristics (like redshift, mass) are known, and the depth and wavelength of the (sub)mm data used in the stacking. JWST has taken us into a new realm of stackable samples: the on-sky density of galaxies has increased significantly, both at higher redshifts and for lower mass galaxies. JWST data has also significantly improved galaxies' photometric redshifts, improving the purity of stackable samples (Shuntov *et al.* 2025). Similarly, ALMA has now built up significant (sub)mm datasets to competitive depths such that stacking of yet-unreached mass regimes is now possible. ALMA also has more long wavelength data (>1 mm) than single-dish facilities that have covered wide areas (like Herschel, SCUBA-2); the long wavelengths, as well as ALMA-like depths at those wavelengths, are crucial for measuring reliable dust masses out to high redshifts (because they still probe the regime where the dust SED is safely optically thin, longward of rest-frame $\gtrsim$250 μm).

The FIR/(sub)millimeter data we stack in this analysis includes: *Spitzer* MIPS-24μm (Sanders *et al.* 2007), *Herschel*/PACS 100μm and 160μm maps (Lutz *et al.* 2011), *Herschel*/SPIRE 250μm, 350μm, and 500μm maps (Oliver *et al.* 2012), SCUBA-2 850μm (Simpson *et al.* 2019), NIKA2 1.3mm and 2mm (Carvajal-Bohorquez *et al.* 2026; Béthermin *et al.* 2026), CHAMPS 1.2mm (Martinez et al., Faisst et al., in prep), and ExMORA 2mm (Long *et al.* 2026).

We stack these datasets by stellar mass and photometric redshift as presented in the COSMOS2025 catalog (Shuntov *et al.* 2025). We first apply some basic filtering of the COSMOS2025 catalog to remove sources of potential low quality. Of the 784,016 sources in the catalog, we select those with:

1. `mag_model_f277w` $\leq$ 28.2 &
2. `warn_flag` = 0 &
3. (log(`chi_star`/`chi2_best`) > 1 `OR` log(`radius_sersic`×3600) > -2.3) &
4. (`flag_star_hsc` = 0 `OR` |`zpdf_med`-`zpdf_med_space`|/(1+`zpdf_med`) $\leq$ 0.15) &
5. |`zpdf_u68`-`zpdf_l68`|/(1+`zpdf_med`) $\leq$ 3

The first criterion selects sources brighter than the nominal 5σ point source detection limit in the deepest COSMOS-Web band; the second criterion selects non-flagged sources (see Shuntov *et al.* 2025, for flagging details, mostly related to artifacts). The third criterion serves to exclude Milky Way stars from analysis: unresolved point sources where the $\chi^2_{\rm stars} < 10\chi^2_{\rm galaxy}$. This is a bit more conservative than the stellar flag included in the COSMOS-Web catalog public release to prevent marginal or unclear sources from entering the stackable galaxy population. The fourth criterion requires a source

lie outside the Hyper Suprime-Cam (HSC) star mask region (where ground-based data is potentially faulty due to bright star contamination) or, if within the HSC star mask region, that there is close agreement between the redshift solutions found with and without exclusion of the ground-based photometric constraints. The last criterion down-selects to sources without significant bimodality in their redshift PDFs. This filtering of the catalog produces a set of 595,351 "stackable" sources (accounting for 79.6% of the COSMOS2025 catalog).

We make two final cuts to the set of stackable sources. The first cut removes sources with suspiciously high stellar mass estimates for their photometric redshift. To do this we calculate a mass threshold above which sources should be regarded with suspicion for formation within ΛCDM. We determine this redshift-dependent mass threshold using the Sheth and Tormen (1999) halo mass function and calculate the most massive object expected in a given redshift bin (of width $dz = 0.5$) in the $0.54\,\mathrm{deg}^2$ area of the survey, assuming that source has converted 30% of its baryons to stars (following the same logic as in Boylan-Kolchin 2023). The threshold of a 30% conversion exceeds typical expectation for the efficiency of star formation of, at most, $\sim 10\%$ (e.g. Evans *et al.* 2009; Bigiel *et al.* 2010; Thompson *et al.* 2005; Ostriker and Shetty 2011). Objects with masses higher than this redshift-dependent maximum mass limit are excluded from the stacks. There are 142 such sources above the limit, likely because their photometric redshifts are overestimated; alternatively their stellar masses may be overestimated due to significant non-stellar contributions to their SEDs. Whatever the origin, we make the conservative choice of cutting them out of the stacking process.

One final, important cut is made to remove quiescent galaxies. Galaxies at low redshifts and high stellar masses follow a bimodal division where the dust characteristics of star-forming massive galaxies are quite a bit different than for quiescent massive galaxies (Paspaliaris *et al.* 2023). We expect dust emission in the former and not the latter (Toni *et al.* 2026). We cut out quiescent systems using a SFR cut with respect to the galaxy main sequence, or SFR-$M_\star$ relation. For a given `zpdf_med` and `mass_med` (i.e. $z_{\rm phot}$ and $M_\star$), we calculate the expected main sequence SFR "$\mathrm{SFR_{MS}}$" using the Speagle *et al.* (2014) parameterization and excludes sources that are more than a dex lower than the main sequence. In other words, retained sources have $\mathrm{SFR} > \mathrm{SFR_{MS}}/10$; this includes all sources down to an order of magnitude below the main sequence. We explicitly test that the adoption of the Speagle *et al.* (2014) main sequence in this instance does not bias our results unintentionally; we alternatively test the Popesso *et al.* (2023) main sequence formulation and find our stack samples to differ by $\leq$1%. This reduces the total stackable star-forming galaxy sample to 501,656 sources (64.0% of COSMOS2025). The distribution of sources in the redshift, mass plane is shown in Figure 1, along with the mass and redshift bins used in this work ($\Delta z = 0.5$ and $\Delta \log(M_\star/M_\odot) = 0.25$).

We note that all stackable sources are covered by MIPS, PACS, SPIRE and SCUBA-2 maps. There are 351,222 of those within the NIKA2 1.3 mm map footprint, and 348,503 in the NIKA2 2 mm map footprint. Similarly there are 209,320 sources covered in the CHAMPS map and 149,685 in the Ex-MORA map. These numbers are reflective of the area within COSMOS-Web covered by each survey.

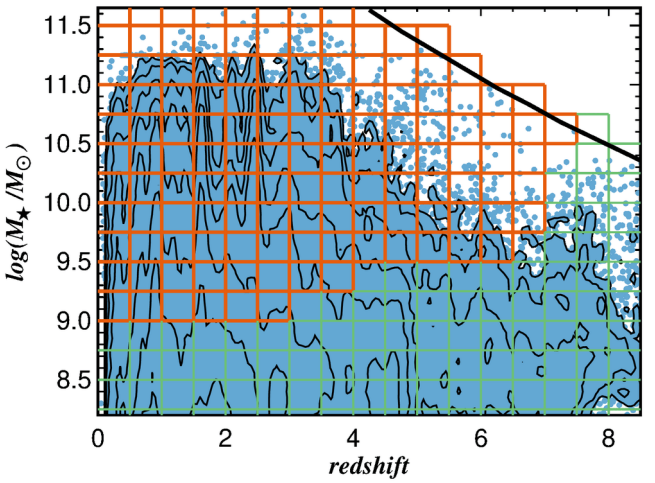

FIG. 1.— The distribution of the stackable 501,656 sources from the COSMOS field used in this work. Contours indicate concentrations of sources exceeding >5 per unit $\Delta z = 0.05$ and $\Delta \log(M) = 0.05$ (contours mark densities of 5, 10, 20, 50, 100, ... sources per same binning). The bins used for stacking are shown with green and orange gridlines, every $\Delta z = 0.5$ in redshift and $\Delta \log(M_\star/M_\odot) = 0.25$. Bins with converged dust SEDs (constraints for both dust emission and attenuation) are outlined in orange while bins with binned attenuation characteristics only (no derived dust emission) are shown in green. The thick black line marks the maximum allowable stellar mass we include in the stacking analysis: this redshift-dependent mass limit is determined by calculating the maximum halo mass found per survey volume and assuming that halo has a stellar baryon fraction of 30%.

Note that we do not explicitly *exclude* any additional special category of source from this list of stackable sources. Both X-ray active galactic nuclei (AGN) and submillimeter luminous galaxies are included as a result. We have relatively few concerns about 'contamination' of IR flux by the former. Luminous X-ray AGN do correlate somewhat with IR luminous galaxies (Iwasawa *et al.* 2011), however the wavelengths of light we are stacking predominantly correspond to cold ISM dust. Constraints in the mid-infrared, where an AGN might boost the luminosity substantially, are very weak relative to the longer-wavelength, cold dust constraints. The primary concern regarding AGN is their impact on a galaxy's SED-modeled stellar mass (Ciesla *et al.* 2015; Florez *et al.* 2020; Buchner *et al.* 2024), such that stellar masses may be overestimated with inclusion of buried AGN luminosity in the UV/optical SED fitting. This is likely a persistent issue, indeed, and the fix for it would involve a very careful analysis of AGN content of the galaxies being stacked, which is beyond the scope of this work. We do note the number of direct-detection X-ray AGN in the COSMOS2025 catalog is 1039, which is statistically insignificant compared to the number of stacked sources (1039/501,656≈0.2%) and preferentially only exist for the most massive subset of systems (above 10^{10} $M_\odot$) at $z < 3.5$.

The incidence of AGN activity has been measured by stellar mass and redshift for mass-selected samples spanning our parameter space, using independent methodologies – forward-modeling the X-ray luminosity function through the stellar mass function (Georgakakis *et al.* 2017), stacking X-ray data for NIR-selected galaxies

(Aird *et al.* 2018), and semiparametric inference across many different surveys (Yang *et al.* 2018; Zou *et al.* 2024) – and is consistently found to vary smoothly and monotonically, with the specific accretion rate distribution shifting steadily up with increasing redshift and stellar mass. This suggests that whatever systematic offset is imparted to stellar masses by AGN contamination is likely to vary smoothly across the redshift and mass range studied here, like it is in the cosmically-averaged black hole accretion rate density and star-formation rate density (Delvecchio *et al.* 2014; Madau and Dickinson 2014). We expect the effect of AGN to be most significant in our most massive, highest-redshift bins where AGN duty cycles are relatively higher; this may manifest most importantly in the elevated dust temperatures seen at high mass and high-z.

The inclusion of IR luminous galaxies (e.g. DSFGs broadly defined) is a potential contaminant some readers may worry about as it is possible their IR flux densities are significantly elevated above the norm. To check the impact of the IR luminous population, we have run two versions of our stacks: one with the 1024 direct detections explicitly removed and one including them. We find our stacking results, with and without DSFGs, consistent within errors and attribute this to the relative on-sky rarity of IR luminous galaxies compared to the size of the samples used in the stacking (1024/501,656≈0.2%). The bins that are most substantially affected (where $\gtrsim 50\%$ of the stackable sample is removed) are at $\log(M_\star/M_\odot) > 11$, though the resulting flux densities are consistent within (large) errors. For the sake of simplicity in our measurements, and in the interest of avoiding cherry-picking the stacked sample, we proceed in our analysis without excluding IR luminous galaxies.

Our stacked flux densities are measured via a weighted inverse-variance median based on the rms of the (sub)mm datasets (not the quality of the redshift or stellar mass estimates). Because we are not accounting for redshift uncertainties, we will point out that there will be some level of 'bin-smearing' in bins where the photometric redshift quality is a bit worse. This happens at the low-mass and high-z end of our stacks where $\sigma_z/(1+z)$ is of order the bin size; the vast majority of bins have somewhat precise photometric redshift uncertainties, $\sigma_z/(1+z) \approx 0.03$, out to $z \sim 7$. A full description of the stacking procedure, including a comparative analysis of correcting flux densities for clustering bias, is detailed in the Appendix. We note that confusion noise, due to low spatial resolution maps from *Herschel* or SCUBA-2, is greatly mitigated when combining data during a stack as the maps are set to have zero background, a key advantage that lets us push the depth of these maps with sufficient statistics. We provide stacked cutouts as well as a full tabulation of the measured flux densities (Table 2) and derived SED characteristics (Table 3, derivation thereof described below) from the stacked samples above stellar masses 10^9 $M_\odot$ from $0 < z < 7.5$ in the Appendix[5].

4.2. *Fitting IR Dust SEDs*

[5] Both tables are available online in fits format at https://github.com/caitlinmcasey/duststacks .

Our IR SED fitting follows the methodology of MCIRSED described in Drew and Casey (2022), built on earlier SED methodology described in Casey (2012), which joins a single modified blackbody to a mid-infrared power law and fits SEDs to photometry in a Bayesian framework. In this framework, non-detections are handled in the same fashion as detections with flux density measurements and uncertainties folded into the fit, where non-detections are statistically consistent with zero flux density at a given wavelength. The model is quite flexible and requires some choices. The free parameters of the dust SED are the following, from best-constrained to least-constrained:

1. the integrated IR luminosity L_{IR} (which determines the normalization of the fit and is canonically integrated between 8–1000μm),
2. the luminosity-weighted cold dust temperature T_{dust},
3. the emissivity spectral index β (which determines the slope of the Rayleigh-Jeans tail of dominant dust blackbody emission),
4. the mid-infrared spectral slope α_{MIR} (which determines the relative proportion of warm dust to the dominant cold dust in the SED), and
5. an assumption regarding the opacity of the dust (i.e. at what wavelength the SED transitions from optically thin to thick, $\lambda_0 \equiv \lambda_{\tau=1}$).

In only rare cases — DSFGs with a wealth of IR photometric constraints as well as spatially resolved IR maps — can all of these parameters be directly constrained. In practice, most galaxies have a tremendous dearth of information in this wavelength regime, so some assumptions must be applied. That is the case for the stacked SEDs.

After extensive testing and evaluation of the resulting SEDs, we decide to uniformly fix the last parameter described above: the wavelength at which opacity shifts from thick to thin (λ_0). We use $\tau = 1$ at $\lambda_0 = 100\,\mu$m, which is consistent with existing constraints in the literature (Draine 2006; Conley *et al.* 2011; Greve *et al.* 2012; Simpson *et al.* 2017). We note that the choice of λ_0 impacts the mapping of the rest-frame peak wavelength, λ_{peak}, to the dust temperature, T_{dust} (see Figure 20 of Casey, Narayanan, and Cooray 2014a), but it does not significantly change the shape of the best-fit SED. For example, a similar optically thin SED fit would produce the same peak wavelength λ_{peak} and same L_{IR}, but a correspondingly lower dust temperature. Note that the observables really are λ_{peak} and L_{IR}, and our inference of temperature is model dependent. The adopted opacity model, similarly, does not impact dust mass, because the mass is inferred from the optically thin portion of the dust SED, longward of rest-frame $\gtrsim 250\,\mu$m.

Our constraints on the mid-infrared, governing α_{IR}, come from *Spitzer* 24μm and *Herschel* PACS. Over a large range of low-redshift SEDs both *Spitzer* and PACS measurements have high signal-to-noise ratio (SNR), so we allow α_{IR} to vary as long as there are two or more photometric constraints $> 3\sigma$ significant short-ward of rest-frame 200 μm. When those constraints are not present, we adopt $\alpha_{IR} = 4.5$ translating to a moderately steep

drop off of the Wien's side of the dust blackbody. We note this is somewhat steeper than the empirically measured $\alpha_{\rm IR} \approx 2 - 2.5$ for local (U)LIRGs (U *et al.* 2012; Casey 2012), but consistent with many other high-z DSFGs (Kirkpatrick *et al.* 2012; Casey *et al.* 2014a) and our own measurements in bins where it is explicitly measured: $\langle \alpha_{\rm IR} \rangle = 4.61^{+0.35}_{-0.22}$.

Our constraints on the Rayleigh-Jeans tail are quite good below $z \sim 4$ allowing for a direct fit of the emissivity spectral index, β. If there are more than two photometric constraints $> 3\sigma$ significant at rest-frame wavelengths longward of 300 μm, we allow a free fit for β. We otherwise fix the value to $\beta = 2$ (Hildebrand 1983; Dunne and Eales 2001; da Cunha *et al.* 2008). This fixed value is consistent with the bins where β was directly fit, $\langle \beta \rangle = 1.98^{+0.24}_{-0.18}$, as well as other recent literature constraints (Casey *et al.* 2021; Cooper *et al.* 2022; Long *et al.* 2026). While one might be concerned about a comparison of fits with free $\alpha_{\rm IR}$ and β to those with fixed values, we note that the dynamic range of both parameters impact the measured $L_{\rm IR}$ by less than 20%.

Photometry is given an additional 10% flux calibration uncertainty and individual stack measurements are capped at a maximum SNR of 10 in order to minimize the statistical power of individual high SNR photometric measurements (e.g. 24μm). $L_{\rm IR}$ and $T_{\rm dust}$ are left as free parameters for all fits. Dust mass is not a parameter fit for explicitly, but inferred directly within the SED fitting and calculated using Eq. 4 for each set of SED parameters. All SED fitting is corrected for cosmic microwave background (CMB) heating following the prescriptions provided in da Cunha *et al.* (2013). A gallery of resulting SED fits over all stacked bins is shown in Figure 2.

4.3. *Derivation of Attenuation Characteristics*

The primary purpose of the COSMOS2025 catalog is to measure photometric redshifts and, second, to measure basic physical characteristics like rest-frame UV magnitude and stellar mass. Photometric redshift fitting requires a delicate balance of increased free parameters dictating the galaxy template SEDs against obtaining a realistically constrained redshift. The COSMOS2025 approach, more thoroughly described in Shuntov *et al.* (2025), uses more free parameters than the simplest photometric redshift techniques like EAZY (Brammer *et al.* 2008). This is done to provide the most realistic estimates on photometric redshift uncertainties; with too few free parameters, the uncertainty is often underestimated, and with too many it will be overestimated.

A crucial piece of photometric redshift fitting is applying an attenuation law to galaxy templates. So as not to introduce too many free parameters into the fits, COSMOS2025 adopts three possible rigid attenuation laws – the Calzetti *et al.* (2000) starburst attenuation law, the Arnouts *et al.* (2013) attenuation law and the Salim *et al.* (2018) attenuation law – with a range of $E(B-V)$ spanning 0–1.2 in bins of 0.1 magnitudes. This roughly translates to magnitudes of attenuation $0 < A_{\rm V} < 5$, with a majority of sources (∼99%) fit to $A_{\rm V} < 2.5$. Most sources (51%) are fit to the Calzetti *et al.* (2000) attenuation law, while the remainder are evenly split between the Arnouts *et al.* (2013) and Salim *et al.* (2018) laws. This range of choices – quantized choices of $E(B-V)$ and attenuation law – is well suited for the broad application of fitting photometric redshifts. However, in this work we are digging deeper into the attenuation characteristics of galaxies as measured from the UV/optical and to do that, we need some more flexible, direct fits to the primary parameters governing attenuation.

To constrain sources' attenuation characteristics, we fit detailed SEDs to all COSMOS-Web galaxies' fiducial model-based photometry using BAGPIPES (Carnall *et al.* 2018). We use the BPASS stellar model grids (Eldridge and Stanway 2009). A Gaussian prior is placed on redshift centered on the median redshift from LEPHARE (`zpdf_med`) with standard deviation set to the maximum value of the upper or lower 68th percentiles with hard limits at $\pm 3\sigma$ (or $0 < z < 20$, whichever is more restrictive). A non-parametric star formation history with a continuity prior is used (a t-distribution with degrees of freedom ν=2 and scale = 0.3); twelve bins are used at $z < 4$, nine bins are used at $4 < z < 8$, and seven bins are used at $z > 8$. The four most recent bins have fixed age intervals of 0-10, 10-30, 30-100 and 100-300 Myrs, and the remainder are spaced uniformly in log(time) from >300 Myr to $z = 20$. A uniform prior on metallicity is placed between 0–2.5× solar, and nebular emission is fit with uniform prior between $-4 < \log U < -1$.

A flexible attenuation law is modeled with a Salim *et al.* (2018) parameterization originally presented in Noll *et al.* (2009), with uniform prior on $A_{\rm V}$ between $0 < A_{\rm V} < 6$, uniform prior on δ, the power-law deviation from a Calzetti dust law, between $-0.5 < \delta < 0.1$ (where $\delta = -0.4$ corresponds roughly to the Small Magellanic Cloud, SMC, attenuation curve), and a uniform prior on the 2175Å bump strength between $0 < B < 3$. To reproduce the attenuation curve for a given δ and B, the Calzetti attenuation law, $k'_{\rm Cal}(\lambda)$, (specifically equation 4 of Calzetti *et al.* 2000) is manipulated via equations 3, 4 and 9 in Salim *et al.* (2018).

We save the posterior median and 68th-percentile confidence intervals on redshift, stellar mass, $A_{\rm V}$, $A_{\rm UV}$, δ (deviation from Calzetti dust law), B (bump strength), $M_{\rm UV}$, and β (rest-frame UV slope). $A_{\rm UV}$ and $M_{\rm UV}$ are evaluated at rest-frame 1600Å. We note that, given this is a photometrically constrained sample with some redshift uncertainty, attenuation characteristics are uncertain on a source-by-source basis: δ is only well constrained for sources with well-sampled rest-frame UV and optical, while bump strength, B is not well constrained in a majority of cases; however we still keep it as a free parameter in an effort to realistically inflate the uncertainties on other attenuation-related quantities.

We verify that BAGPIPES output is consistent with LEPHARE-derived characteristics, as shown in Figure 3. The posterior on derived BAGPIPES redshift differs by $\sigma_{\Delta z/(1+z)} = 0.04$, of order the uncertainty on the photometric redshift, without any systematic offset. The derived BAGPIPES stellar masses are 0.06 dex lower than those from LEPHARE, slightly less than the average uncertainty on the LEPHARE stellar mass, of 0.07 dex. Further, we also drew comparison to the stellar masses derived in Arango-Toro *et al.* (2025) using CIGALE and find similar consistency. While the LEPHARE attenuation fits are quantized, they too are broadly consistent with the attenuation fit in BAGPIPES with a slight skew towards higher magnitudes of attenuation with BAGPIPES.

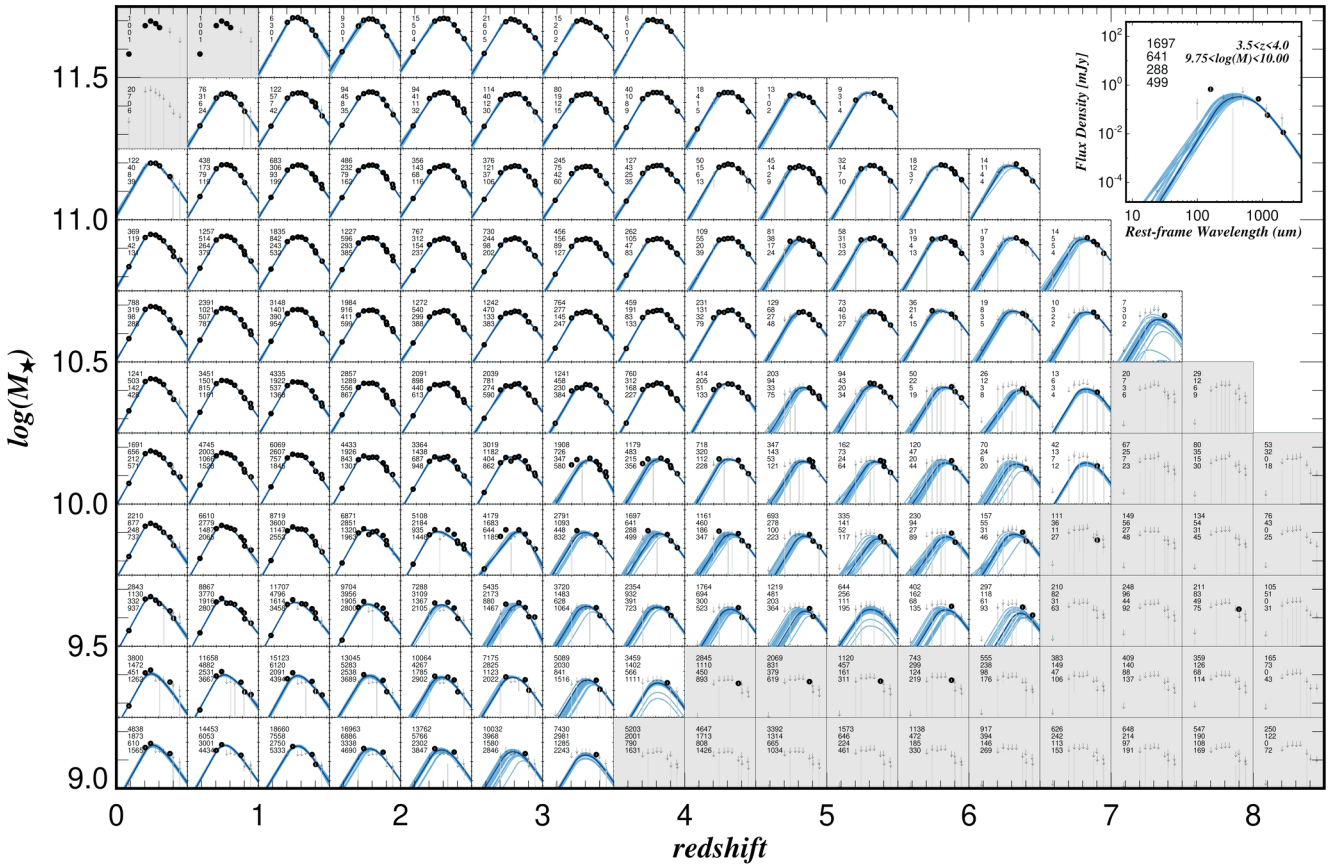

FIG. 2.— The best-fit dust SEDs to stacked (sub)millimeter photometry for stellar mass and redshift selected samples. Each panel shows a schematic of the dust SED (blue, with light blue SEDs sampling the uncertainty) superimposed on the stacked photometry (black with gray error bars). Upper limits ($< 3\sigma$) are shown as downward facing arrows at their 3σ upper limits (error bars are still shown in light gray). Panels with gray backgrounds have photometric constraints of too poor quality to fit a converged dust SED (fewer than two points above 3σ significance). The numbers in the upper left of each panel indicate the number of sources stacked across (1) Spitzer, Herschel and SCUBA-2, (2) NIKA2, (3) CHAMPS, and (4) Ex-MORA (the latter three cover smaller areas than the full field). Inset to the top right is one example panel in finer detail to show the wavelength and flux density axis, which is fixed for every subpanel.

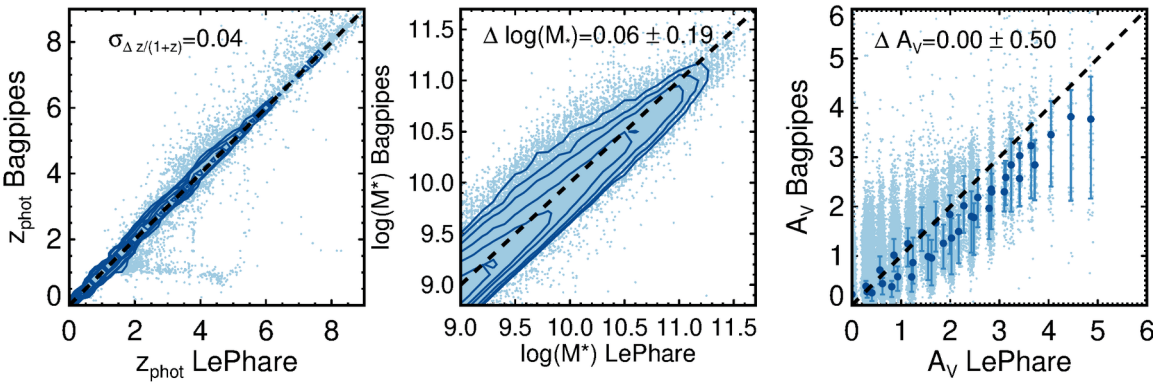

FIG. 3.— A comparison of derived properties from LEPHARE (Shuntov *et al.* 2025) and our BAGPIPES-derived quantities based on the same model-based photometry. At left, LEPHARE photometric redshifts and their uncertainties were used as input to BAGPIPES; the resulting agreement is tight with $\sigma_{\Delta z/(1+z)} = 0.04$. Middle, the stellar masses agree within uncertainties. At right, the derived A_V from BAGPIPES agrees with the (quantized) values of A_V inferred from more rigid LEPHARE SED fits; for visual clarity, we have perturbed LEPHARE A_V values about their fixed values to show the breadth of the underlying population.

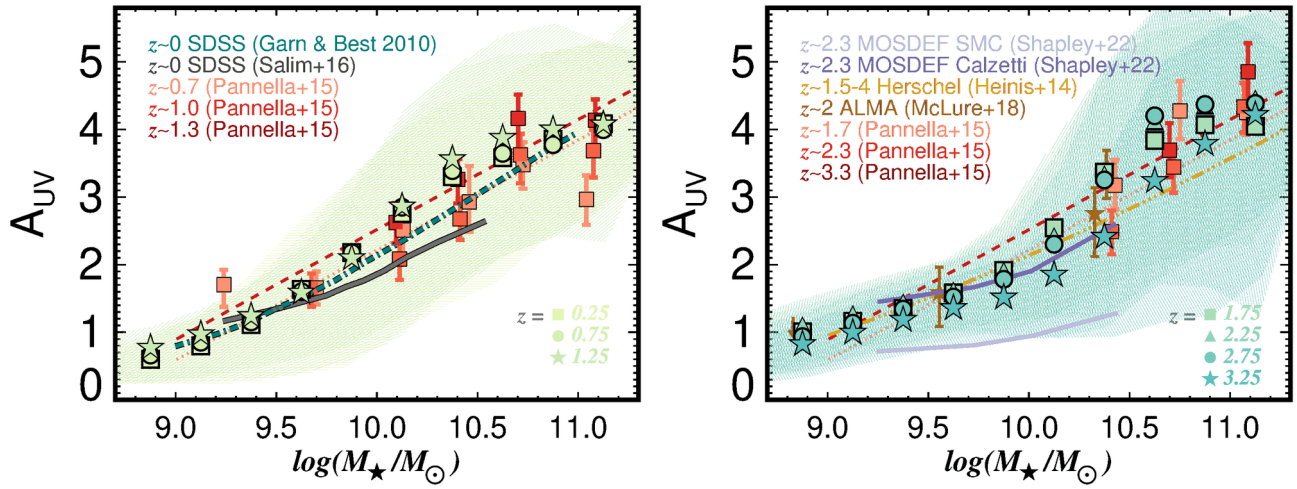

FIG. 4.— A comparison of our binned A_{UV}-$M_\star$ relation (shades of green/cyan) compared to literature compilations spanning $0 < z < 1.5$ (left) and $1.5 < z < 3.5$ (right). Our points represent the median A_{UV} per mass and redshift bin with shaded regions showing the inner 68% confidence interval on the spread of measured A_{UV} in the corresponding bin; the errors on the median are of order the size of each data point. At $z \sim 0$ we compare to Garn and Best (2010) and Salim *et al.* (2016); while aligned at low masses, we find higher A_{UV} around $10^{10.5}\,M_\star$ (albeit we are only presenting binned A_{UV} for the star-forming subset and not the quiescent systems). Our comparisons with *Herschel* measurements at $z \approx 0.7 - 4$ (Heinis *et al.* 2014; Pannella *et al.* 2015) and ALMA $z \sim 2$ (McLure *et al.* 2018) are largely consistent within uncertainties. When comparing to MOSDEF measurements anchored to the Balmer decrement (Shapley *et al.* 2022), here translated to A_{UV}, our attenuations are consistent assuming a Calzetti attenuation curve (and less consistent for the steeper SMC attenuation curve); we discuss trends in the best-fit attenuation curves more in § 5.2.

5. RESULTS

Here we summarize a number of comparisons between physically derived galaxy properties. In § 5.1 and § 5.2 we first analyze the results of attenuation characteristics, derived from UV/optical SEDs alone, *independent* from dust SEDs. We look at the attenuation - stellar mass relation and the implied evolution of inferred attenuation characteristics. Next we analyze galaxies' FIR SED characteristics, measured *independently* from UV/optical SEDs. In § 5.3 we show the evolution of L_{IR} and M_{dust}, and in § 5.4 we show the evolution of dust temperatures. § 5.5 summarizes the measured mid-infrared slope and emissivity spectral index from the dust SED. Finally, we measure quantities that draw both on the results of UV/optical SED fitting and FIR SED fitting; in § 5.6 we analyze the fraction of star formation that is unobscured as a function of stellar mass and redshift, and in § 5.7 we present the mass and redshift dependence of galaxies' dust-to-stellar (DTS) ratios. Throughout this paper we use a uniform color scheme to show different mass bins evolving with redshift (drawn from the magma color palette) and redshift bins as a function of stellar mass (viridis color palette).

5.1. *Attenuation - Mass Relation*

The relationship between stellar mass and globally-averaged attenuation has been established in the literature (Devour and Bell 2016; Bogdanoska and Burgarella 2020; Qin *et al.* 2024). The relation exists between stellar mass and A_{UV} as well as A_V, where the difference is driven by the underlying nature of the attenuation curve (A_{UV}≈2.5A_V for a Calzetti attenuation curve). We first anchor our measurements to other literature measurements of A_{UV}-$M_\star$ and proceed to interpret trends we measure across the full range of mass and redshift accessible in our analysis. We emphasize that we are discussing the effective or observed attenuation here, derived from constraints in the UV/optical only.

Figure 4 presents a comparison of our derived $A_{UV} - M_\star$ relation against literature measurements from $9 < \log(M_\star/M_\odot) < 11$ and $0 < z < 3$. Plotted are the median values of A_{UV} and 68% spread on A_{UV} values in each bin. At intermediate redshifts ($z \sim 1-3$), literature measurements are broadly consistent with our findings within uncertainties; these literature measurements draw specifically on *Herschel* (Heinis *et al.* 2014; Pannella *et al.* 2015) and ALMA-observed (McLure *et al.* 2018) samples of galaxies, and sources with direct Balmer decrement measurements (Shapley *et al.* 2022). The primary discrepancy is at the lowest redshifts ($z \lesssim 1$) where we infer systematically higher median attenuation, $A_{UV} \approx 3.5-4$ for galaxies with stellar mass $\sim 10^{10.5}$ $M_\odot$ compared to local measurements of $A_{UV} \approx 2.5-3$ in the same mass range (Garn and Best 2010; Salim *et al.* 2016). While the median attenuations differ, we note that all literature measures fall well within the inner 68% confidence interval of sample measurements. Note that constraints on A_{UV} in the lowest redshift bin, $z = 0.25$, in our work will be somewhat more uncertain than both the literature constraints at similar redshifts or our work at higher redshifts because we have not explicitly included GALEX photometric constraints in the COSMOS2025 catalog. Our measurements of A_{UV}-$M_\star$ suggest little evolution across this mass and redshift range, and broad consistency with the literature, especially at $1 < z < 3$.

Given the relatively good agreement, we present the extended attenuation - stellar mass relationships in fixed redshift bins out to $z \sim 8$ in Figure 5.

While there was little evidence for evolution in A_{UV}-$M_\star$ out to $z < 3$ (Shapley *et al.* 2022), the data in Figure 5 suggest some slight downward evolution in A_{UV} at fixed stellar mass with increasing redshift out to $z \sim 6$. The same trend is seen in A_V at fixed stellar mass as a function of increasing redshift. The lower A_{UV} and A_V is most striking in the mass range $9.5 < \log(M_\star/M_\odot) < 10.5$ from $0 < z < 6$. Higher stellar mass bins show little evolutionary trend, suggesting that non-quenched massive galaxies tend to be quite obscured regardless of redshift.

Both A_V-$M_\star$ and A_{UV}-$M_\star$ resemble logistic growth functions with a monotonic decline in A_{UV} and A_V at fixed stellar mass with redshift (out to $z \sim 6$). Thus we fit our binned data to a simplified model describing the average A_V expected at a given stellar mass and redshift:

$$A_V(M, z) = I(M) + S(M)\,(1+z),$$
$$I(M) = \frac{A_{\max}}{1 + \exp[-k\,(M - M_0)]}, \qquad (11)$$
$$S(M) = -\exp(b_0 + b_1\,M)\,.$$

where $M \equiv \log(M_\star/M_\odot)$. We similarly fit this same model to $A_{UV}(M, z)$ and report the derived parameters for both relations in our appendix, Table 1. We also plot the fitted relation split into individual redshift panels in the appendix.

At redshifts higher than $z \sim 6$, we see an interesting inflection in the data, such that A_{UV} and A_V at fixed stellar mass increase with redshift, where the minimum attenuation is around $z \approx 6$. The sample scatter on binned A_{UV} and A_V are significant, but the increase from $z \sim 6$ to $z \sim 8$ is seen in every mass bin between $10^9 - 10^{10.5}$ $M_\odot$. The reason for this reversal is unclear. $z \sim 6$ is the end of reionization, before which the intergalactic medium (IGM) is more optically thick; though our model fitting with Bagpipes lacks a direct implementation of the IGM damping wing (Miralda-Escudé and Rees 1998) or significant nebular 2-photon continuum contributions (Katz *et al.* 2024), both of which could artificially redden the spectra of galaxies without dust. Another possibility is that galaxies' ISM at earlier times may undergo some type of transition around $z \sim 6$, related to their compact sizes, star/dust geometry, and/or sources of early dust. We will leave a further investigation of this phenomenon – whether physical or an artifact of our SED modeling – to a future work.

5.2. *Evolution in the Attenuation Curve*

Salim and Narayanan (2020) provide an overview of recent (pre-JWST) results pertaining to the derivation of the attenuation curve, both for low redshift and high redshift samples. To briefly summarize the consensus view, the literature clearly demonstrates that galaxies' attenuation curves are diverse; there is significant evidence that some star-forming galaxies in the local volume have attenuation curves similar to (if not steeper than) the SMC (Conroy *et al.* 2010; Leja *et al.* 2017; Salim *et al.*

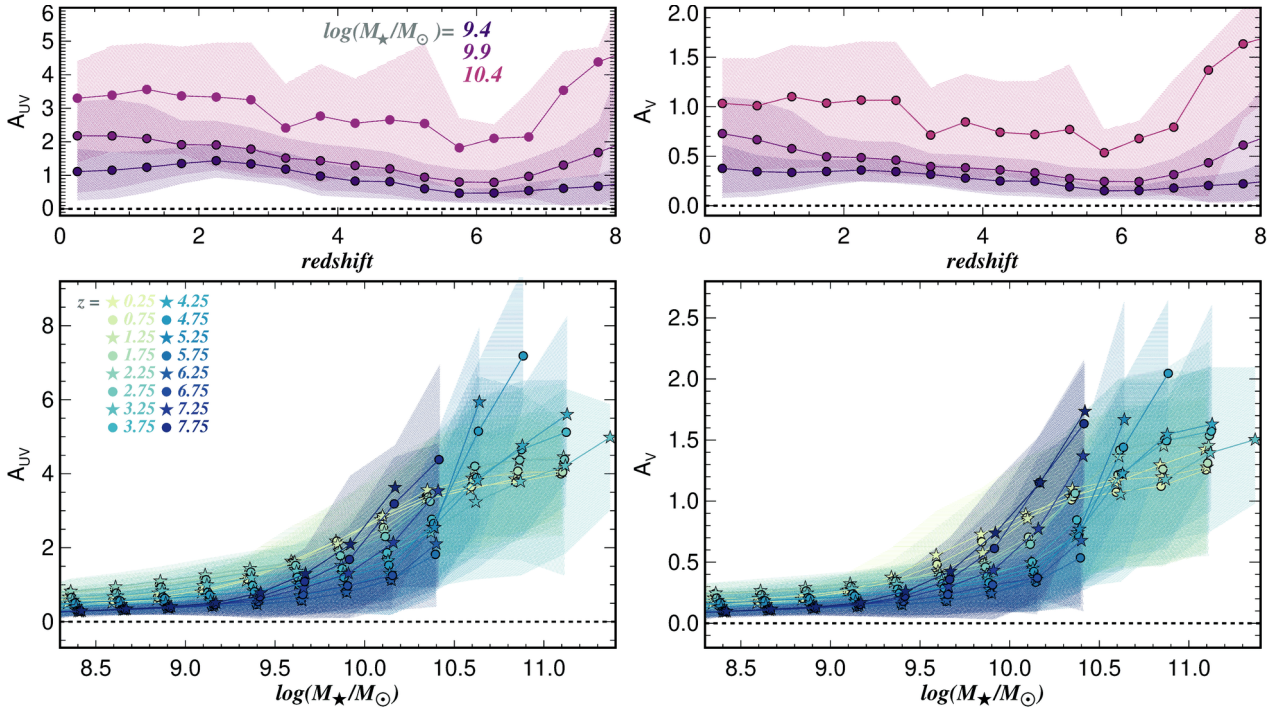

FIG. 5.— Our mass- and redshift-binned A_{UV}-$M_\star$ relation (left) and A_V-$M_\star$relation (right) from $0 < z < 8$. Note bins shown on Figure 4 at $z < 3.5$ are the same as shown here. The shaded regions are the 68% confidence interval for each binned interval. Only bins containing more than 50 sources are shown. We see mild evolution in the A_{UV}-$M_\star$ (A_V-$M_\star$) relation with redshift, made more clear on the top-left and top-right panels at three fixed mass bins covered across the full range of our data. Across all masses, we generally see a decrease in the average A_{UV} (A_V) with redshift to $z \sim 6$; at higher redshifts, there is then an increase. This inflection point coincides with the end of reionization but requires further investigation as to its origins. Two figures in the appendix (Fig. 22 & 23), show the breakdown of this relation against our fitted relation (Eq. 11) in more detail.

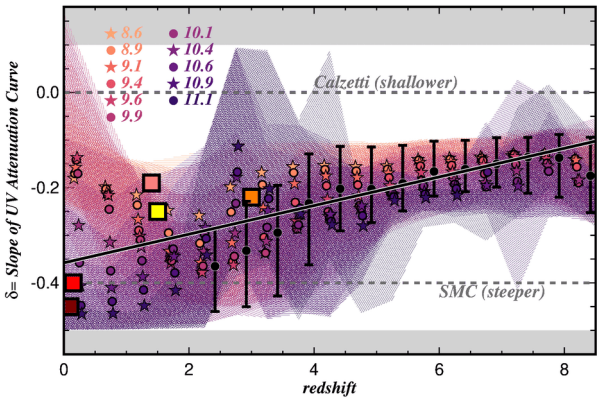

FIG. 6.— The redshift evolution of δ, the parameter describing the rest-frame UV slope of the attenuation curve. δ describes the deviation from a Calzetti attenuation curve, where δ=0 recovers Calzetti, and a negative δ produces a steeper attenuation curve. Gray regions denote the bounds of modeled δ allowed in our fits, ranging from $-0.5 < \delta < 0.1$. The SMC attenuation curve roughly follows δ=-0.4, which is consistent with the average attenuation curve recovered by Salim *et al.* (2018, red square) and Conroy *et al.* (2010, dark red square). Higher-z literature measurements come from Buat *et al.* (2012) (yellow square), Kriek and Conroy (2013, pink square) and Reddy *et al.* (2016, orange square). We show the evolution of δ binned by stellar mass ($\Delta \log M = 0.25$ bins) with colored points and stars, and the average δ across all masses as open black circles between $2 < z < 8$ (shaded regions show the inner 68% confidence interval of all measured δ per mass bin). The best-fit relationship (black line) is presented in the text in Eq 12.

2018) and significantly steeper than the Calzetti attenuation law (Calzetti *et al.* 2000, see also Battisti *et al.* 2016), though it is perhaps stellar mass and metallicity dependent in the local volume. Similarly, work beyond $z > 0.5$ from the pre-JWST era suggests steeper-than-Calzetti attenuation laws may be common, but not quite as steep as work on local star-forming galaxies.

Figure 6 highlights our primary finding, that δ, the deviation of the attenuation law slope from Calzetti, averaged over mass-matched bins shows redshift dependence from $z = 2$ to $z = 8$, with especially pronounced evolution seen over $2 < z < 4$. We do not find that δ has a significant stellar mass dependence though slight mass variance is seen in Figure 6 at fixed redshift, but we caution that lower mass sources are fainter and their attenuation curve slopes are less well constrained (cf. Vijayan *et al.* 2024). Specifically we find that the average attenuation law steepens with decreasing redshift such that:

$$\langle \delta(z) \rangle = (-0.36 \pm 0.07) + (0.030 \pm 0.014) z \qquad (12)$$

This is explicitly fit to all sources above stellar masses 10^9 $M_\odot$ and $2 < z < 8$ where δ is best constrained. Our results, though of marginal significance (the redshift evolution is $\sim 2.1\sigma$ significant) are consistent with the prior measurements of the attenuation law slope from both $z < 0.5$ (Conroy *et al.* 2010; Salim *et al.* 2018) and $z \sim 1 - 3$ samples (Buat *et al.* 2012; Kriek and Conroy 2013; Reddy *et al.* 2016), though our data show significant scatter at $z < 2$. We attribute the scatter at low-z to a limitation of our data: specifically, the GALEX data was not included in the COSMOS2025 catalog, and thus

measurement of our low-z attenuation curves are done from extrapolation from the u-band blueward. At $z > 2$ our photometric data cover the entirety of the rest-frame UV, and correspondingly, the distribution in measured slopes narrows.

We note that our results here are complementary though less constrained than spectroscopic analyses (Markov *et al.* 2025a,b; Shivaei *et al.* 2025). We also note that constraints from Balmer decrements (Calzetti *et al.* 2000; Reddy *et al.* 2015; Battisti *et al.* 2022) can differ from SED-fitting methods and favor a steepening of attenuation law with increasing redshift.

5.3. $L_{\rm IR}$ *and* $M_{\rm dust}$

Pivoting in focus to the FIR SEDs, we present the derived IR luminosities and dust masses of our stacked SEDs in Figure 7 split into stellar mass bins to highlight their redshift evolution. We observe a few general trends in the SEDs: at $z < 1$, IR luminosities are exceedingly low, with median $L_{IR} \lesssim 10^{10}$ $L_\odot$ even for galaxies around masses $\sim 10^{11.5}$ $M_\odot$. IR luminosities are a factor of $\sim$100$\times$ brighter around $z \sim 2$, the peak of the cosmic star formation rate density, across all mass bins for which we have measured SEDs. This sharp evolution in galaxies' IR luminosities is well documented in the literature going back to some of the first measurements of the IR luminosity function from *Spitzer* and *Herschel* and implications for the star-formation rate density (e.g. Le Floc'h *et al.* 2005; Caputi *et al.* 2007; Casey *et al.* 2012; Gruppioni *et al.* 2013). Two phenomena conspire to produce the great abundance of IR-luminous galaxies at $z \sim 2$: the evolution of the galaxy SFR-$M_\star$ relation such that galaxies' SFRs at $z \sim 2$ are much higher likely driven by increased gas surface densities at $z \sim 2$, and in parallel, the observed star formation is dominated by dust-reradiated emission and not direct UV light at high stellar masses, above $M_\star > 10^{9.5}$ $M_\odot$, which we will discuss more in § 5.6.

At $z > 2$, extending out to $z \sim 7$ (the limit of our stacked SEDs), IR luminosities at fixed stellar masses appear flat to 0th order. However, a more detailed look sees some higher order variation. At low stellar masses $< 10^{9.5}$ $M_\odot$, IR luminosities at $z > 4$ are markedly lower than they are at $z \sim 2$ where they peak (though not as low as at $z \sim 0$). Galaxies of intermediate masses, $9.5 \lesssim \log(M_\star/M_\odot) \lesssim 10.5$, do appear to have non-evolving IR luminosities. Galaxies in the highest mass bins, $> 10^{10.5}$ $M_\odot$, appear to have *higher* IR luminosities at $z \sim 4-6$ than at $z \sim 2$. Note that, if galaxies' IR luminosities were to track exactly with their SFRs as given by the evolution of SFR-$M_\star$ (using the parameterization of Speagle *et al.* 2014), they would rise by 0.3 dex from $z \sim 2$ to $z \sim 4$ and then rise another 0.3 dex out to $z \sim 8$, following the dashed lines on the left panel of Figure 7.

Dust masses tell a slightly different narrative. The caveat of the dust mass here is that the dominant source of uncertainty is $\kappa_{\rm FIR}$, and here we apply a fixed value and assert no redshift evolution, a topic we return to in the discussion. With fixed $\kappa_{\rm FIR}$ in mind, galaxies at $z \sim 0$ have less dust than at $z \sim 2$. The drop in the recent universe is less severe than galaxies' IR luminosities, about a factor of 5-10$\times$. Beyond $z > 2$, the highest stellar mass systems have a non-evolving average dust mass. At intermediate masses, dust masses at $z \sim 5-6$ are slightly larger than at $z \sim 2$ (by 3-5$\times$) and lower beyond $z > 6$, though $z > 6$ constraints are limited to two mass bins and increasingly uncertain SEDs. At lower stellar masses there may be a significant inflection, such that galaxies with $< 10^{9.5}$ $M_\odot$ may have lower dust masses at earlier epochs than they do at $z \sim 2$.

We will return to a discussion of these trends in $L_{\rm IR}$ and $M_{\rm dust}$ in the context of potential predictive power from UV/optical-derived characteristics in the discussion, in particular § 6.1.

5.4. *Evolution of Dust Temperature*

Galaxies' dust temperatures have been shown in a number of works to evolve with redshift (Béthermin *et al.* 2015b; Schreiber *et al.* 2018; Bouwens *et al.* 2020; Viero *et al.* 2022; Drew and Casey 2022; Jones and Stanway 2023). Most commonly this evolution is traced with galaxies directly detected in the IR, for the obvious reason that those are the sources for which it can be measured, though recent stacking results also show increasing SED dust temperatures to $z \sim 3$ (Euclid Collaboration *et al.* 2026). In all works, the actual observable is the rest-frame peak wavelength of the dust SED, $\lambda_{\rm peak}$, but as discussed in § 4.2, the mapping to a dust temperature is opacity-model dependent, so works that assume different IR SED methodology do not have directly comparable dust temperatures. In this work we explicitly constrain $\lambda_{\rm peak}$ and convert that to a representative dust temperature using:

$$\log(T_{\rm dust}/K) \approx 3.756 - 1.048 \log(\lambda_{\rm peak}/\mu m) \qquad (13)$$

which falls out directly based on the presumption of an optically thick SED short-ward of $\lambda_0 \sim 100\,\mu$m as described in § 4.2; this equation is also explicitly described in Burnham *et al.* (2021). We report dust temperatures from elsewhere in the literature at face value as they are reported in those works. Overall, existing studies have concluded that galaxies' dust SEDs increase in temperature with increasing redshift.

Figure 8 shows the evolution in measured dust temperatures of our stacks, binned by stellar mass out to $z \sim 7$. We note a few key trends: from $0 < z < 2$, dust temperatures for all mass bins evolve similarly, with the hottest SEDs at higher-z, ranging between 50–70 K (25–40 K) at $z \sim 2$ for the adopted opacity model (for optically thin SEDs). In other words, at a given redshift $z \lesssim 2$, $T_{\rm dust}$ appears to have *no* stellar mass dependence. At higher redshifts, the lower mass bins $< 10^{10}$ $M_\odot$ have constant temperatures out to $z \sim 6$, hovering around 50 K (30 K for optically thin), while galaxies of higher stellar masses continue to evolve upward, reaching average temperatures of $\sim$90 K (50 K, optically thin) at $z \sim 5$ above $> 10^{10.5}$ $M_\odot$.

Three curves from the literature are overplotted on Figure 8. Drew and Casey (2022) is a comprehensive analysis of galaxies' dust temperatures at $z < 2$ that deduces a fundamental relationship between $L_{\rm IR}$ and $T_{\rm dust}$, such that more luminous galaxies are hotter. They explore the possible redshift evolution of $T_{\rm dust}$ due to galaxies' increasing IR luminosities at higher redshifts, and that relation is shown in Figure 8; its evolution marks the change in SFR of a main sequence galaxy, which sees

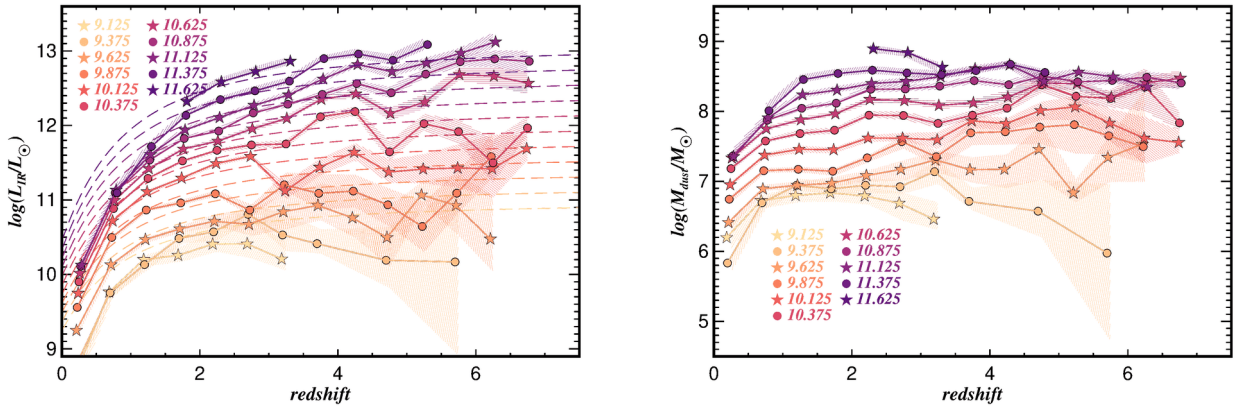

FIG. 7.— The redshift evolution of L_{IR} (left) and M_{dust} (right) in fixed stellar mass bins. Dashed lines at left denote the total IR luminosity that would be expected if 100% of star-formation were obscured, and the SFR is taken from the main-sequence of star formation, or the $M_\star$-SFR relation (Speagle *et al.* 2014). Between $0 < z < 2$, we see a 100× increase in the average L_{IR} and 5-10× increase in M_{dust} per mass bin above 10^{10} $M_\odot$. Beyond $z \sim 2$, evolution is more subtle; at high $M_\star$, there is a factor of 10× higher L_{IR} at $z \sim 6$ than at $z \sim 2$, while masses below $10^{10.5}$ $M_\odot$ see no evolution or a dropoff in L_{IR}. Dust masses in the highest mass galaxies show no evolution, while there is mild evidence suggesting a threefold increase in dust masses for intermediate masses.

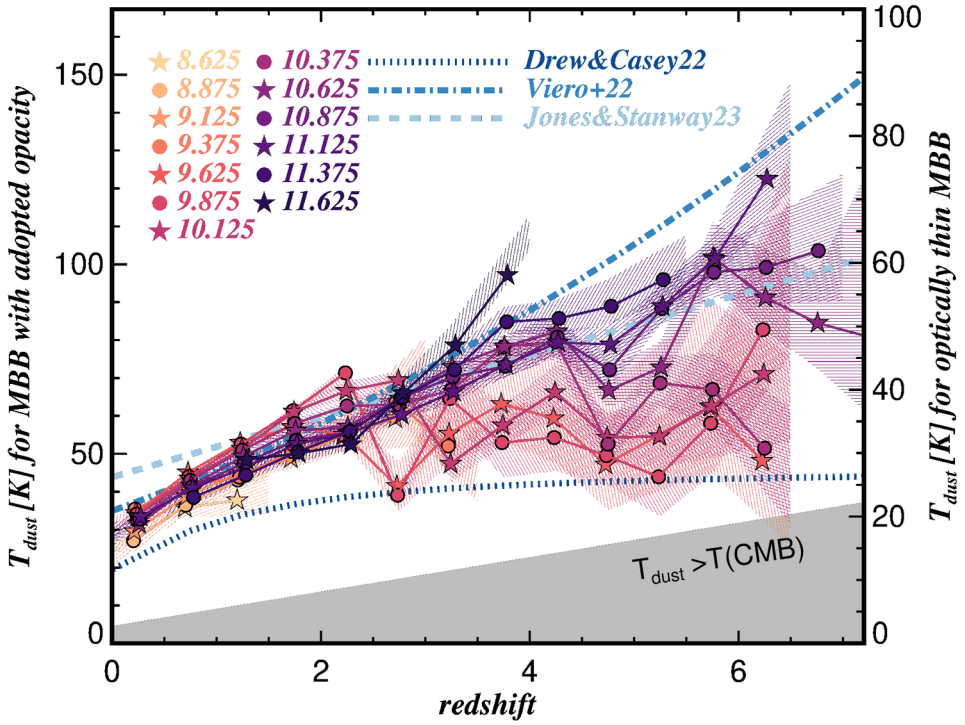

FIG. 8.— The redshift evolution of dust temperature derived for stacked SEDs in fixed stellar mass bins ranging $8.6 < \log(M_\star/M_\odot) < 11.6$. The floor on dust temperature is set by the temperature of the CMB which evolves as $T_{CMB} = 2.73(1+z)$ (gray filled region). Three literature relations are overplotted. From Drew and Casey (2022) we show the expectation of the evolution of T_{dust} at fixed stellar mass given the evolution in the SFR-$M_\star$ relation, where SFR scales to L_{IR}, and T_{dust} has a direct relationship with L_{IR}; the Drew and Casey work was calibrated against $0 < z < 2$ samples. Viero *et al.* (2022) uses *Herschel* data to infer T_{dust} for stacked samples of galaxies drawn from COSMOS2020 and find a steep $T_{dust}(z)$ dependence. Last we show the empirical relation presented in Jones and Stanway (2023) which uses a meta-analysis to address the $T_{dust}(z)$ dependence observed in various literature datasets. Our data are shown from low-mass bins (yellow) through high-mass bins (dark blue) superimposed. Below masses $\log(M_\star) \sim 10.4$, we see relatively little evolution in T_{dust} beyond $z \sim 2$ while higher mass bins show a marked increase in T_{dust} from $z \sim 2$ to $z \sim 6$. Figure 24 in the Appendix show this evolution in more detail against the derived relation given in Eq. 14.

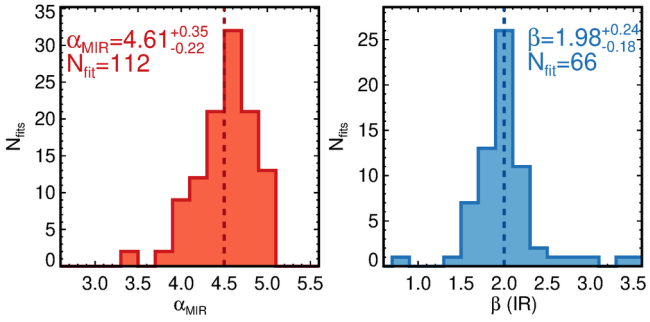

FIG. 9.— The distribution in the mid-infrared slope, $\alpha_{\rm MIR}$, and emissivity spectral index, β, for redshift-stellar mass bins where sufficient photometric constraints allow for direct fitting. The vertical lines mark the adopted values for stacked SED bins where direct fits of $\alpha_{\rm MIR}$ and β are not possible.

the most evolution from $0 < z < 2$ and evolves shallowly at $z > 2$. We also overplot the relation derived in Viero *et al.* (2022) which drew from stacked IR SEDs out to $z \sim 10$ using COSMOS2020; Viero *et al.* fit a polynomial to their $T_{\rm dust}(z)$ data finding a steep evolution. Many of their higher mass, higher redshift bins are somewhat overpopulated; in other words, the COSMOS2020 catalog, at face value, has many galaxies at high stellar masses and high redshifts ($z > 7$), some masses unphysically large. These bins in the Viero *et al.* analysis may skew towards unusually hot temperatures either from contamination from low-z sources (where redshift and $T_{\rm dust}$ have a degeneracy, such that low-z 'cold' SEDs could be mistaken as high-z 'hot' SEDs) or galaxies with especially strong AGN boosting their stellar masses above a reasonable threshold (and an AGN can also serve to heat ISM dust).

The last literature relationship we show is the meta-analysis presented in Jones and Stanway (2023), that empirically draw a linear increase in dust temperatures from $0 < z < 8$, which is between the extremes set by Drew and Casey (2022) and Viero *et al.* (2022) works. The Jones and Stanway (2023) fits the evolution we see in $T_{\rm dust}(z)$ fairly well, especially for stellar masses $\sim 10^{11}$ $M_\odot$. While Jones and Stanway does not explicitly address the stellar mass range of their analysis, we can infer they are likely high mass systems from the existence of direct dust detections. We note that the $T_{\rm dust}(z)$ trends recovered here are properties of a stellar-mass selected sample. For luminosity-limited samples of 870μm-selected galaxies, Dudzevičiūtė *et al.* (2020) find no evolution in dust temperature at fixed $L_{\rm IR}$ across $z \approx 1.5-4$, indicating that much of the apparent temperature evolution has a complex relationship with the SFR-$M_\star$ relation and galaxies' size-mass relation, which we elaborate on in § 6.4.

We directly fit all of our $\lambda_{\rm peak}$ data to a relation of the form:

$$\lambda_{\rm peak}(z, M) = a + b(M - 10) + c\log(1 + z) \qquad (14)$$

where $M \equiv \log(M/M_\odot)$. We infer coefficients of $a = 2.213 \pm 0.012$, $b = -0.035 \pm 0.007$, and $c = -0.53 \pm 0.02$. This relation, as well as the $\log(\lambda_{\rm peak})$-$T_{\rm dust}$ relationship, is given in our appendix, Table 1. We discuss the physical driver of dust temperature and its relation to other measured quantities more in the discussion, in § 6.4.

5.5. *Mid-IR Slope and Emissivity Spectral Index*

Two parameters of the IR SEDs that are less well constrained than $L_{\rm IR}$ and $T_{\rm dust}$ are the mid-infrared power law slope, $\alpha_{\rm MIR}$, and the emissivity spectral index, β. $\alpha_{\rm MIR}$ reflects the slope of the dust emission on the Wien side of the dust blackbody and β reflects the emission on the Rayleigh-Jeans tail of the blackbody. Only when sufficient SED constraints are on-hand do we explicitly fit for one or both. Figure 9 show the distribution of both for stacked bins where the parameter is fit. Within the range of available data, we see no clear evolutionary or mass-dependent trend. The median of both distributions, $\alpha_{\rm MIR} = 4.61^{+0.35}_{-0.22}$ and $\beta = 1.98^{+0.24}_{-0.18}$, motivate the choice of the fixed values $\alpha_{\rm MIR} \equiv 4.5$ and $\beta \equiv 2$ for SEDs without sufficient SNR on either end of the blackbody peak.

5.6. $f_{\rm unobs}$- *Mass Relation*

The relationship between the unobscured fraction of star formation and stellar mass gives some intuitive sense as to the dominant sources of both UV and IR emission and is complementary to $A_{\rm UV}(M,z)$ discussed in § 5.1, though most closely a probe of the 'direct' attenuation as given in Eq 8. The unobscured fraction of star formation, $f_{\rm unobs}$, is equal to the star-formation rate probed in the UV over the total (i.e. $f_{\rm unobs} = SFR_{\rm UV}/(SFR_{\rm IR} + SFR_{\rm UV})$). Conversely, the obscured fraction, $f_{\rm obs} \equiv SFR_{\rm IR}/(SFR_{\rm IR} + SFR_{\rm UV})$, is $= 1 - f_{\rm unobs}$. For the remainder of this work, we focus on $f_{\rm unobs}$ rather than $f_{\rm obs}$ given the dynamic range of $f_{\rm unobs}$ seen in the data. Measurements of galaxies' star formation rates from SED fitting should theoretically be sensitive to $SFR_{\rm total}$, accounting for both unobscured and obscured components. However, they typically do this by extrapolating the measurement of dust from A_V with a fixed set of IR templates, and in some cases implements a full energy-balance technique to fit out to submillimeter wavelengths (da Cunha *et al.* 2015; Boquien *et al.* 2019). The COSMOS2025 catalog does not fit the IR portion of the SED for lack of constraints for the vast majority of sources which are not directly detected at long wavelengths. For the purposes of this paper where we are intentionally decoupling the two, our BAGPIPES fitting from § 4.3 also does not fit the IR.

To calculate $f_{\rm unobs}$ for our mass and z bins we need both $SFR_{\rm UV}$ and $SFR_{\rm IR}$. First we remeasure rest-frame UV magnitudes for all individual sources from BAGPIPES; this $M_{\rm UV}$ is very close to the $M_{\rm NUV}$ circulated in the COSMOS2025 catalog, but evaluated at 1600Å rather than in the NUV filter. That $M_{\rm UV}$ is then converted to $L_{\rm UV}$ using the Kennicutt and Evans (2012) FUV scaling. $SFR_{\rm IR}$ is calculated from $L_{\rm IR}$ using the Kennicutt and Evans TIR scaling. For each bin, we keep track of the full distribution in $M_{\rm UV}$ and the posterior distribution on $L_{\rm IR}$ for the same bin to derive realistic, representative uncertainties on $f_{\rm unobs}$ at a given stellar mass and redshift.

Figure 10 shows the breakdown between IR and UV components of the star-forming main sequence (or SFR-$M_\star$ relation) relative to the total SFR calculated over the same mass and redshift bins using COSMOS2025. We note that the coaddition of UV and IR components of the SFR agrees very well with the Speagle *et al.* (2014) meta-

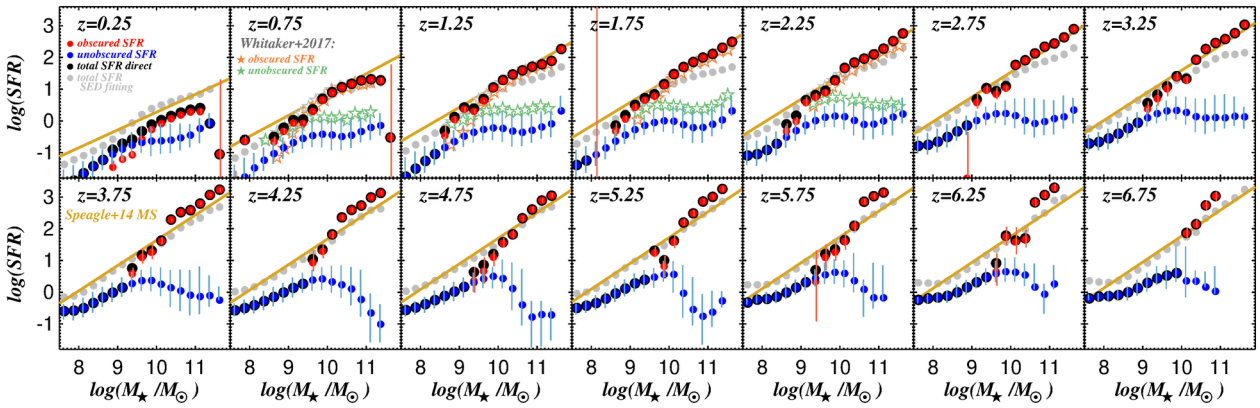

FIG. 10.— The star-formation rate, stellar mass relation (SFR-M$_\star$) shown in $dz = 0.5$ bins broken down into the UV (blue) and IR (red) components. The coaddition of the UV and IR together are shown as black points, while the average SFR taken directly from the COSMOS2025 catalog LePhare SED fits are shown as gray points. In the four panels $0.5 < z < 2.5$ we overplot the measurements of Whitaker *et al.* (2017) which used galaxies from the 3D-HST survey as well as 24μm-extrapolated IR constraints on SFR. There is a significant discrepancy (as much as an order of magnitude) in total SFR reported in the COSMOS2025 catalog for massive galaxies ($> 10^{10}$ M$_\odot$) between $0 < z < 2.5$ and those derived via direct coaddition of UV and IR components.

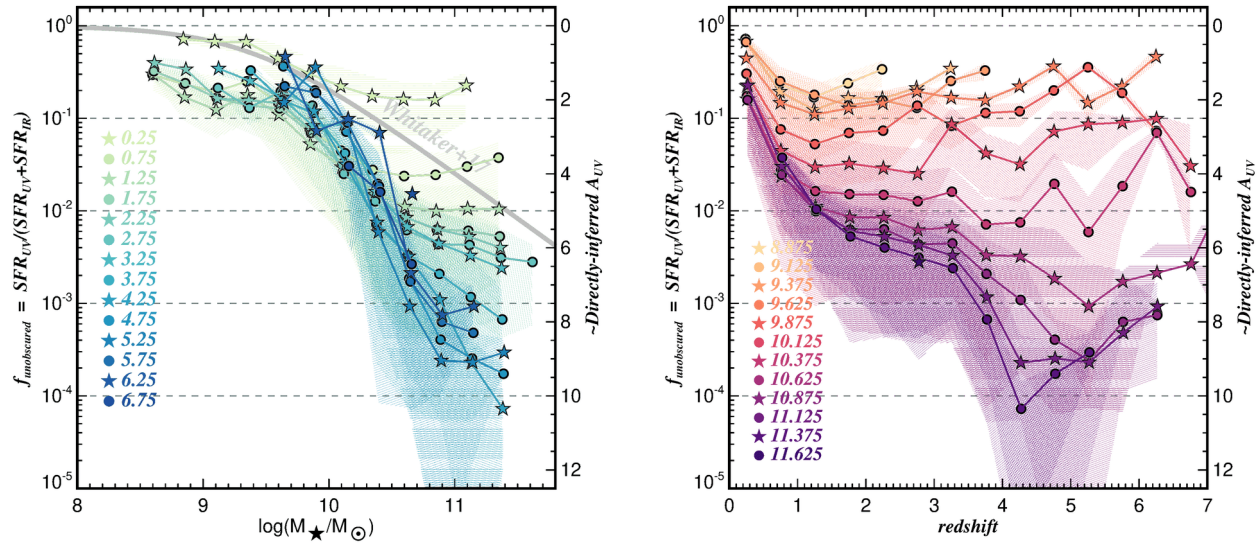

FIG. 11.— The stellar mass and redshift dependence of f$_{\rm unobs}$. Broadly consistent with prior findings at $z < 3$ from Whitaker *et al.* (2017), we find a very strong stellar mass dependence in f$_{\rm unobs}$, such that >90% of star formation is obscured above a stellar mass of 10^{10} M$_\odot$ at all redshifts beyond $z \sim 0.5$. The diminishingly low fraction of unobscured star formation that is seen at high masses is even smaller at $z \sim 4-6$ than it is at $z \sim 2$. Masses below $\sim 10^{10}$ M$_\odot$ show relatively little evolution in f$_{\rm unobs}$ between $2 < z < 6$, with slight indication of *higher* f$_{\rm unobs}$ at $z > 4$ compared to $z \sim 2$. Overall, we find that more star formation is obscured relative to Whitaker *et al.* (2017) at fixed stellar mass and we attribute the difference to improved constraints on the IR SED in this work. Figure 25 and 26 show a more detailed breakdown of this figure in redshift and stellar mass against the empirical fit described in Eq 15 as well as simulations expectations from Zimmerman *et al.* (2024).

analysis of the main sequence parameterization from $0 < z < 6$ (shown as gold lines on Fig. 10) as well as the prior measurements out to $z \sim 2.5$ in Whitaker *et al.* (2017).

Figure 11 shows the derived f$_{\rm unobs}$-M$_\star$ relation in redshift bins spanning $0 < z < 7$ as well as the redshift evolution of f$_{\rm unobs}$ in fixed mass bins. We overplot the relation as measured by Whitaker *et al.* (2017) in gray, who found no evidence for an evolution from $0.5 < z < 3$; their analysis used data from the 3D-HST survey (Whitaker *et al.* 2014; Skelton *et al.* 2014) as well as 24μm-extrapolated IR star-formation rates. Our stacked SEDs suggest a lower f$_{\rm unobs}$ at fixed stellar mass than found by Whitaker *et al.* (2017), though we largely attribute the offset to the different treatment of the IR SED, primarily our direct fits vs. a 24μm-extrapolation, as well as a discrepancy in UV SFR tracer, NUV (≈2300Å) vs. FUV (≈ 1600Å). We can reproduce the Whitaker *et al.* (2017) relation if we use a similar approach as described therein.

The main takeaway from Figure 11 is that all galaxies seem heavily obscured, even at relatively low stellar masses at all redshifts, with exception of the lowest redshift bin $z < 0.5$ (we exclude the $z = 0.25$ bin as an outlier). There is a steep mass dependence to f$_{\rm unobs}$ at all redshifts, with some subtle redshift evolution on f$_{\rm unobs}$ for values < 1% at M$_\star$> $10^{10.5}$ M$_\odot$.

We fit these data to a generalized logistic growth function such that:

$$\log(f_{\rm unobs}) = \mathcal{F}_0 - \log\Big[1 + 10^{\,\alpha(z)\,(M - M_t(z))}\Big] \quad (15)$$

again where $M \equiv \log(M_\star/M_\odot)$. We first fit this function to each redshift bin and note some broad evolutionary trends, such that $\mathcal{F}_0$ is constant and α and M_t can be described as smooth functions of z within measurement error:

$$\alpha(z) = \alpha_0 + \alpha_1\,\log(1+z) \quad (16)$$

$$M_t(z) = M_{t,0} + M_{t,1}\,\log(1+z) \quad (17)$$

Given the smooth evolution observed across a broad range of redshifts, we fit the five parameters ($\mathcal{F}_0$, α_0, α_1, $M_{t,0}$, $M_{t,1}$) to the measured $f_{\rm unobs}(M,z)$ data from $0.5 < z < 7$ and present the derived values in our appendix, Table 1.

The first notable observation is that $\mathcal{F}_0$ tells us that even at low stellar masses, only $\sim$38$\pm$5% of the star-formation is probed directly by the rest-frame UV on average. The second notable effect is that the stellar mass at which the obscured component overwhelms the unobscured component is between $9 < \log(M_\star/M_\odot) < 10$, closer to 10^9 $M_\odot$ at $z \sim 2$ and evolving to higher masses with increasing redshift. The third observation is that the drop off with mass is *steep* and steepens with increasing redshift, with $\alpha \sim 1$ at $z \sim 1$ steepening to $\alpha \sim 3$ at higher redshifts. We note that Whitaker *et al.* (2017) observed no evidence for redshift evolution of $f_{\rm obs}$-$M_\star$. Without the extended redshift lever arm available in this work, our results over the same redshift range $0.5 < z < 2.5$ would not be well-enough constrained to claim redshift evolution either. This is similar to the observed trends in $f_{\rm obs}$-$M_\star$ seen in the SIMBA cosmological hydrodynamic simulations, where redshift evolution is seen over $0 < z < 6$ but is subtle at $z < 3$ (Zimmerman *et al.* 2024); the Zimmerman *et al.* (2024) results, translated to $f_{\rm unobs}$ from $f_{\rm obs}$, are shown in the full panel version of the $f_{\rm unobs}$-$M_\star$ relation in the Appendix. We will return to a detailed comparison of $f_{\rm unobs}$ and $A_{\rm UV}$ measures further in the discussion.

5.7. *Dust to Stellar Mass Ratio*

Dust is the byproduct of star formation, thus it follows that the total dust mass of star-forming galaxies should be fundamentally linked to their stellar masses. This relation may be further complicated by growth of dust in the ISM or, alternatively, dust destruction by supernovae and feedback, the rates of which depend on a complex mix of physical conditions: density, temperature, clumpiness, metallicity, and strength/hardness of the radiation field (Galliano *et al.* 2018). The dust-to-gas ratio (DTG) is more often studied, as well as the gas-to-stellar ratio (GTS), due to gas's direct link to the star formation process, and dust's key role in cooling gas and thus catalyzing star formation. However, the lion's share of gas measurements at high-z, in practice, actually measure dust and presume a DTG rather than provide an independent anchor by which to assess the relative relationship (Scoville *et al.* 2016); this is because dust continuum observations are much more time efficient than CO observations.

Measurements of the dust-to-stellar ratio (DTS) is less broadly discussed in the literature but has advantages in that the two quantities – dust and stars – are measured from vastly different parts of a galaxy's spectrum. Most literature samples with measurements of the DTS ratio are either local samples, or limited high-z samples. For example, directly detected IR-luminous sources, like local ULIRGs (e.g. da Cunha *et al.* 2010), and *Herschel*-selected galaxies presented in the HATLAS survey (Dunne *et al.* 2011) or PEP and HerMES surveys (Santini *et al.* 2014). Beyond this, a volume-limited sample of local galaxies with IR constraints exists from the *Herschel* Reference Survey (HRS) and is presented in Cortese *et al.* (2012) and Andreani *et al.* (2018) and from DustPedia presented in Galliano *et al.* (2021).

We compare the inferred dust-to-stellar ratios of our stacked dust SEDs to literature measurements at $z < 2.5$ in Figure 12 and the full constraints of our data out to $z \sim 7$ are shown in Figure 13. In the literature comparison, we note that both Dunne *et al.* (2011) and Santini *et al.* (2014) observe a steep rise in the DTS from $z = 0$ to $z \sim 0.5$. Though our stacks are only sampled in $\Delta z = 0.5$ bins, we note the same rise from $z = 0.25$ to $z = 0.75$. Like Santini *et al.* (2014), we see this rapid evolution in the DTS at low redshift level out towards higher redshifts ($z \sim 2$), and both datasets exhibit a lower DTS at higher stellar masses. The trend of a lower DTS at higher masses is also seen in the nearby HRS sample (Cortese *et al.* 2012; Andreani *et al.* 2018, note the DustPedia sample occupies very similar space). Galaxies explicitly selected to be dust-luminous (ULIRGs and DSFGs; da Cunha *et al.* 2010, 2015) have higher dust-to-stellar ratios than our stacks suggest is typical for galaxies of their same stellar mass. We note that we broadly observe the same trends in the DTS ratio with redshift and mass, but the normalization of the DTS is often offset. For example, the $z = 0$ HRS sample seems to show a consistent DTS-$M_\star$ relation as we measure at $1 < z < 2$, at much higher DTS than our redshift-matched sample. Similarly the *Herschel* samples have consistently higher DTS than we measure over the same mass and redshift ranges. We attribute the differences to the methodology of deriving the dust mass itself (dust mass absorption coefficient assumed, which carries significant uncertainty, and to a lesser extent dust temperature).

Looking in more detail at Figure 13, we draw a few conclusions over a wide dynamic range of mass and redshift. The DTS ratio falls by nearly an order of magnitude between $z \sim 3$ and $z \sim 0$, most of that evolution at $z < 0.5$. Also all mass bins show no significant (or very shallow) evolution toward higher redshifts ($3 < z < 7$). It is notable that no significant drop in the DTS is seen even beyond $z > 6$ where we have sufficient sensitivity to draw measurements from our stacks. Then where constraints on lower-mass $M_\star < 10^{9.5}$ $M_\odot$ galaxies exist ($z < 3$), their DTS ratios are markedly higher than at higher stellar masses. The mass and redshift dependence seen in Figure 13 is well described via a power law, such that

$$\log(M_{\rm dust}/M_\star)(z, M) = A + \eta_0(M - 10) + \eta_1\log(1+z) \quad (18)$$

again where $M \equiv \log(M_\star/M_\odot)$. We fit the parameters of the function as $A = -3.237 \pm 0.036$, $\eta_0 = -0.296 \pm$

0.023 and $\eta_1 = 1.364 \pm 0.066$. These parameters are also summarized in Table 1. We will expand on how these constraints on the DTS inform our understanding of the changing evolution of galaxies' dust content, and relationship to gas and stars, further in the discussion, § 6.5.

5.8. $z < 0.5$ *measurements as an outlier*

The lowest redshift bin is a persistent outlier in this analysis. Why? We have noted higher average A_V (and A_{UV}) than literature measurements and low L_{IR} and M_{dust}, as well as higher f_{unobs}. The low L_{IR} and M_{dust} are in agreement with prior literature (e.g. Le Floc'h *et al.* 2005; Santini *et al.* 2014). However, the slightly higher average attenuation, particularly around 10^{10} $M_\odot$, is discrepant with the literature. To form a clear understanding of potential systematics in our dataset, we dug deeper into the cause of this low-redshift discrepancy. The relevant population are largely Milky Way analogs at $z \lesssim 0.5$: spirals with some lenticulars and early type galaxies.

The Salim *et al.* (2016), henceforth S16, derivation of the local A_{UV}-$M_\star$ relation is anchored on the GALEX-SDSS-WISE legacy dataset, drawn from SDSS spectroscopically confirmed $z < 0.3$ galaxies in the local volume. Strauss *et al.* (2002) describes this sample, selected to be brighter than $r < 17.8$; they note that the color distribution of the population is rather narrow about $|g - r| \approx 0.5$, which is consistent with photometry from COSMOS2025 in the HSC g and r filters for the matched population. Forty-six of the GALEX-SDSS-WISE sources sit in the COSMOS-Web field so we use that sample to directly compare derived A_V, A_{UV}, and $M_\star$. The predicted masses are 0.21±0.38 dex lower for BAGPIPES-derived SEDs than found in S16. Despite this, there is a persistent discrepancy between predicted attenuations: A_V=0.20±0.09 (S16) vs our A_V=1.36±0.53 and A_{UV}=1.63±0.58 (S16) vs our A_{UV}=5.07±2.52.

One might suspect that differences in photometry or SED fitting techniques cause the discrepancy in inferred dust attenuation with the literature. SED fitting in S16 is performed with CIGALE with a similar suite of flexible (though parametric) star formation histories as used here for BAGPIPES. The photometry for the overlapping sample is broadly consistent, whether modeled or based on Kron apertures (Kron 1980), though one key difference is extreme ends of wavelength coverage for either set of photometry. Our fits include much longer rest-frame wavelengths (i.e. F444W and F770W) and omit the rest-frame UV (from GALEX). These two differences are significant – in the case of S16 it results in fits with lower SFR and older stellar populations than we have fit. This leads our models to have a higher A_V and SFR (and thus predicted L_{IR}) than may hold.

Last, we emphasize our initial down-selection to our 'stackable' sample, where we excluded quiescent galaxies. S16 does not exclude quiescent systems, and so the fact that they find lower A_V at fixed stellar mass correlate, in part, with real differences in either sample. For these reasons we have excluded the lowest redshift bin from a number of our fitted relations and we issue caution in particular on the interpretation of UV/optical-inferred properties of the lowest redshift stacks in this work, leaving a more careful approach to the low-z subsample to a future work.

6. DISCUSSION

The measurements in this paper — thanks in particular to the remarkable sensitivity of both JWST and ALMA — present a new view on the average dust absorption and emission characteristics of galaxies over the majority of cosmic time for typical galaxies, down to stellar masses of $\sim 10^9$ $M_\odot$ and out to $z \sim 7-8$. Such progress is enabled by the rich density of galaxies detected by JWST imaging, and the increased precision with which we can characterize their redshifts, masses, sizes, and star formation characteristics. It is also enabled by the decades' long accumulation of exquisitely deep FIR/(sub)mm imaging in fields like COSMOS; taken in aggregate, from *Spitzer*, *Herschel*, SCUBA-2 and ALMA, average galaxies' dust SEDs can finally be well understood to much lower masses and higher redshifts than previously accessible.

This discussion focuses on the relationship between quantities presented in § 5, the physical interpretation of those quantities and relationship to ongoing discussions elsewhere in the literature. Specifically we touch on the UV/optical's ability to capture dust attenuation and emission (§ 6.1), the relationship between A_V and Σ_{dust} (§ 6.2), a discussion of a possible grain size distribution evolution (§ 6.3), dust temperature evolution (§ 6.4), and inference from the dust-to-stellar ratio of galaxies (§ 6.5).

6.1. *Can rest-frame UV/optical SEDs accurately measure attenuation, or infer L_{IR}?*

A wealth of literature on DSFGs has made clear that the rest-frame optical imaging or spectra for the most dust-rich galaxies has zero constraining power on our understanding of the *actual* attenuation present, because the ISM in such galaxies is optically thick through the near-IR. Swinbank *et al.* (2004) and Chapman *et al.* (2005) demonstrate that far-infrared star formation rates measured in the submm are factors of 10-120× higher than predicted from the UV/optical. In other words, the most extreme star-forming galaxies simply look like typical Lyman-break galaxies in the UV/optical (Adelberger and Steidel 2000); they may not even be particularly red (Smail *et al.* 2004; McKinney *et al.* 2024). So, while DSFGs are "catastrophic failures" of the predictive power of the UV/optical, what about the full range of stellar masses and redshifts probed in this work?

To answer this question, we can compare the UV/optical-inferred attenuation, as measured with BAGPIPES, with the *direct* attenuation inferred from f_{unobs} or IRX. Revisiting our framework from § 2, Equation 8 describes such a $A_{UV,direct}$, which is representative of the A_{UV} you would expect to see if all of the dust in the galaxy presented as a foreground dust screen (which is often taken as the presumed geometry in the interpretation of A_{UV}). We note that Eq. 8 does have a coefficient not yet described, B', which is the ratio of bolometric corrections between the UV and the FIR. Conceptually, it translates our non-bolometric proxies (L_{UV} measured at rest-frame 1600Å and L_{IR} integrated between 8–1000 μm) for absorbed light (UV/optical) and emitted light (FIR) to their bolometric ideals: the integrated

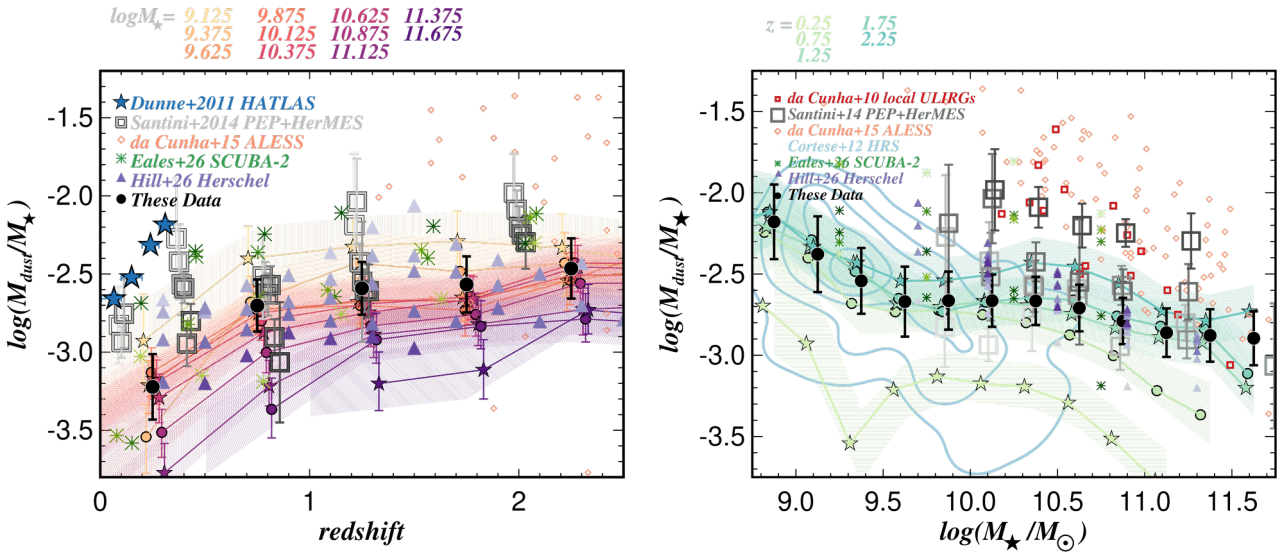

FIG. 12.— A literature comparison of the dust-to-stellar ratio, DTS, with our data. The redshift evolution is shown at left and stellar mass dependence at right. HATLAS-detected galaxies show strong evolution in the DTS from $z = 0$ to $z \sim 0.5$ (blue stars; Dunne *et al.* 2011). Work from the PEP+HerMES surveys is shown in gray boxes (Santini *et al.* 2014); lighter gray boxes correspond to lower stellar mass bins. We also show individually detected dusty star-forming galaxies from ALESS (da Cunha *et al.* 2015) in light red diamonds. Recent SCUBA-2 stacking from Eales *et al.* (2026) and *Euclid-Herschel* stacking from Hill et al. (Euclid Collaboration *et al.* 2026) is shown in green asterisks and purple triangles, respectively. Though significant scatter in literature DTS measurements exist, our data agree with the steep redshift evolution seen at $z < 0.5$ by Dunne *et al.* (2011), and shallower increase out to $z \sim 2$ found by Santini *et al.* (2014). At right, we see a net decrease in the DTS at high stellar masses. The Cortese *et al.* (2012) compilation of dust masses from the Herschel Reference Survey (see also Andreani *et al.* 2018) are shown in contours broadly aligns with our measurement of the DTS-M$_\star$ relation at $1 < z < 2$ rather than at $z = 0$, though this is likely due to different adopted conventions for deriving dust mass. In comparison we note that both local ULIRGs (da Cunha *et al.* 2010) and high-z DSFGs (da Cunha *et al.* 2015) are a bit more dust-rich, likely by construction given their selection as dust-luminous sources.

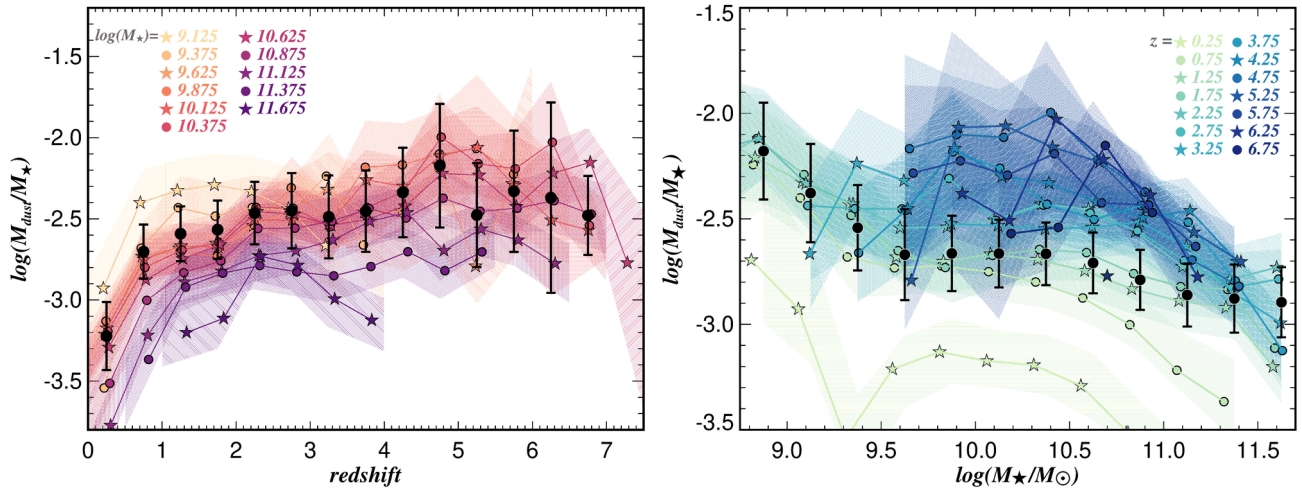

FIG. 13.— The redshift (left) and stellar mass (right) dependence of the dust-to-stellar ratio, DTS, measured via stacking. The redshift evolution of the DTS is predominantly flat over all individual mass bins (light green to purple color) as well as averaged over all masses (black points). The most significant variance is seen in the lowest redshift bin, $z < 0.5$. In contrast, the stellar mass dependence of the DTS is strong and persists to high redshifts. We fit a redshift, and mass-dependent functional form to the DTS as given in Eq. 18. Figures 28 and 27 in the appendix show the relation broken down relative to the Eq. 18 fit.

light lost due to attenuation from the UV through the near-IR and the total light emitted over all wavelengths in the dust's modified blackbody emission. The value[6] of B' has been discussed as a constant 1.19±0.20 (Meurer *et al.* 1999), 1.71±0.05 (McLure *et al.* 2018), 1.75 (Cullen *et al.* 2017), or BC(1600Å)=1.66±0.15 (Meurer *et al.* 1999; Seibert *et al.* 2005; Overzier *et al.* 2011). Hao *et al.* (2011) fit a value of 0.46±0.12 for $1/B'$, which would imply $B' \approx 2.17$. While prior works have largely treated B' as a scalar, B' can be derived precisely for a given modeled SED. For example, BC(1600Å) has a predictable dependence on the shape of the intrinsic UV spectrum (like the observed rest-frame UV slope $\beta_{\rm UV}$), the total attenuation (like A_V), properties of the attenuation law (δ and B); similarly BC(FIR) should have some dependence on the FIR SED shape (primarily driven by $T_{\rm dust}$).

[6] Meurer *et al.* (1999) and McLure *et al.* (2018) refer to this as a bolometric correction ratio simply as B, but here we name it B' to avoid confusion with the modeled bump strength, B. It is defined such that $B' \equiv BC(1600\text{Å})/BC(\text{FIR})$.

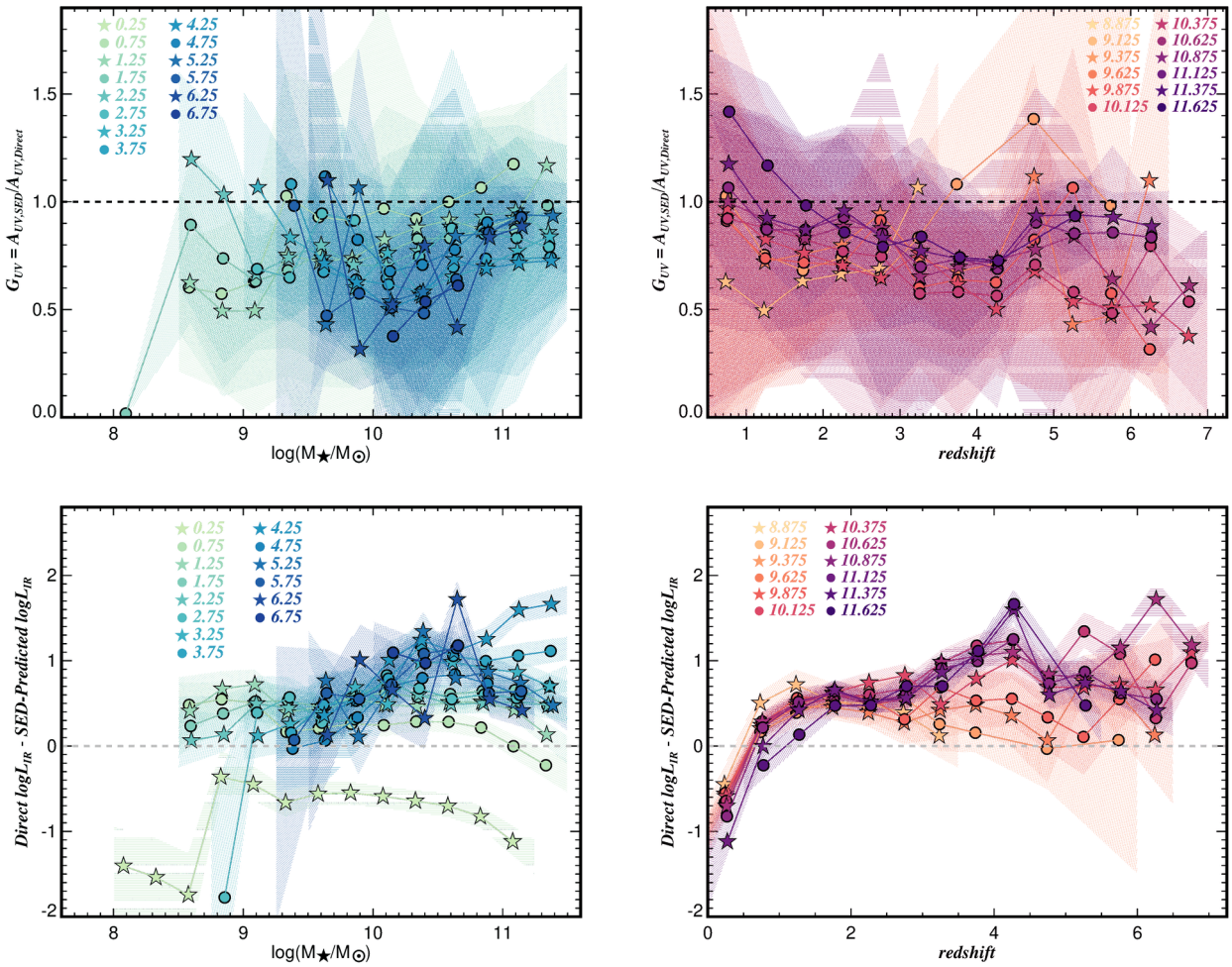

FIG. 14.— At top, we show $\mathcal{G}_{\rm UV}$, the star/dust geometry prefactor that relates the magnitudes of attenuation using SED-based techniques, $A_{\rm UV}$, anchored to rest-frame UV/optical constraints, to $A_{\rm UV,direct}$, a *directly*-inferred $A_{\rm UV}$ measured from IRX as given in Eq. 8. $\mathcal{G}_{\rm UV} = 1$ corresponds to a foreground dust screen and $\mathcal{G}_{\rm UV} < 1$ corresponds to mixed star/dust geometry that serves to *lessen* the perceived attenuation for a given known dust column density. At bottom, we show the same quantity a different way: the difference in $L_{\rm IR}$ measured directly with $L_{\rm IR}$ as inferred from $A_{\rm UV}$ in the UV/optical assuming energy balance. Here we see that the underprediction of $A_{\rm UV}$ leads to the $\sim$0.5 dex $\approx 3\times$ underestimation of $L_{\rm IR}$, with more substantial variation at high masses and high redshift.

We used a wide array of BAGPIPES-generated SEDs and FIR SEDs to derive the following approximation for B' on A_V, $\beta_{\rm UV}$, and δ, noting that bump strength B and $T_{\rm dust}$ (assuming $T_{\rm dust} \lesssim 100$ K) have <1% impact. We find this approximation is able to infer B' to within $\sim$5-10% accuracy based on our model SEDs:

$$B'(A_V, \beta_{\rm UV}, \delta) = 10^{c_0 + c_1 A_V + c_2 \beta_{\rm UV} + c_3 \delta} \quad (19)$$

where $c_0 = 0.2665 \pm 0.0006$, $c_1 = -0.0451 \pm 0.0003$, $c_2 = -0.02087 \pm 0.00016$, and $c_3 = 0.9774 \pm 0.0014$. The scatter about this relation (owing to other critical details driving the SED like the star-formation history and ionization parameter) is of order $\sigma_{B'} \approx 0.08$. Galaxies with low attenuation and blue $\beta_{\rm UV}$ have higher $B' \approx 1.5$ than those with more attenuation or redder UV slopes ($B' \approx 1$). The dependence on δ is such that shallower attenuation results in higher B'. For the BAGPIPES SEDs fit directly to the COSMOS-Web sample, the median $\langle B' \rangle = 1.16 \pm 0.32$. For each mass and redshift bin of our stack, we calculate a median value of B' to use in the comparison of $A_{\rm UV}$ to $A_{\rm UV,direct}$.

Figure 14 shows the ratio of SED-inferred $A_{\rm UV}$ and the directly inferred $A_{\rm UV,direct}$ as a function of stellar mass and redshift. As a reminder, this ratio is a direct proxy for the impact of star/dust geometry, $\mathcal{G}_{\rm UV}$, as noted in Equation 9. The figure also shows a direct comparison between the measured $L_{\rm IR}$ luminosity and a SED-*predicted* $L_{\rm IR}$, based on inverting Eq. 8 to solve for $L_{\rm IR}$ (via IRX) and using the SED-derived $A_{\rm UV}$ instead of $A_{\rm UV,direct}$; in other words, this would be the observed $L_{\rm IR}$ if the presumption of a foreground dust screen were correct.

We note a few key observations from these comparisons, first the $A_{\rm UV}$ comparison. Recalling that $\mathcal{G}_{\rm UV}$ should be bounded by $0 < \mathcal{G} \leq 1$, we note that our data are broadly consistent with that limit. One notable exception again is the $z = 0.25$ bin, which overall sits off the plot around $\mathcal{G}_{\rm UV} \approx 2 - 3$. Values of $\mathcal{G}_{\rm UV} > 1$ are technically unphysical; but this can arise if $A_{\rm UV}$ from SED fitting *overpredicts* the dust content. This may be the case for the $z = 0.25$ bin as discussed in § 5.8. Above $z > 0.5$, we note that all measurements of $\mathcal{G}_{\rm UV}$ are statis-

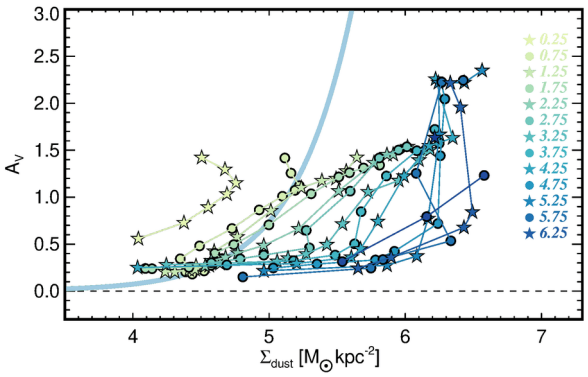

FIG. 15.— The relationship between A_V and Σ_{dust} as a function of redshift, with color indicating different redshift bins. The thick light blue line corresponds to a foreground screen of dust calibrated to the properties of Milky Way dust, with C_V=0.74, where C_V is defined in Eq. 7. With increasing redshift, a clear trend is seen where fixed A_V corresponds to a higher and higher dust mass surface density Σ_{dust}.

tically consistent with values ≤ 1. Lower values of $\mathcal{G}_{UV}$ correspond to a larger mismatch between SED-measured A_{UV} and directly inferred $A_{UV,direct}$, implying that the ISM is more optically thick and/or clumpy. While the scatter on $\mathcal{G}_{UV}$ is large, because the range of A_{UV} in each bin is somewhat broad, we note the general trend that it increases slightly with stellar mass (approaching the 'screen' approximation) but decreases with increasing redshift, perhaps signaling that at fixed stellar mass, the ISM is more optically thick to UV photons at higher redshifts. This is not entirely surprising when we also consider how higher redshift galaxies are more compact at fixed stellar mass (Yang *et al.* 2025).

Looking at the L_{IR} comparisons in Figure 14, which is an alternative way of digesting the same information, we note that overall, L_{IR} from UV/optical SEDs underpredicts the true IR luminosity. From $0.5 < z < 3$ across all mass bins, this seems to be by roughly a factor of $\sim$0.5 dex $\approx 3\times$. For intermediate masses $\sim 10^{10}$ $M_\odot$ this factor of 3 underprediction holds out to $z \sim 6-7$, while for the highest mass bins the underprediction grows to $\sim$1 dex or a factor of $10\times$.

Are these results surprising? If the reader reminds themselves that the results of Figure 14 are not for DSFGs, but rather representative of the average galaxy at these masses and redshifts, the answer is likely yes. It has often been thought that there is a great chasm between the attenuation properties of 'normal' galaxies and DSFGs (Swinbank *et al.* 2004), with the latter an extreme caricature of the former. It has long been thought that rare, extreme phenomena, like gas rich mergers (Hopkins *et al.* 2010), drive these extreme characteristics (star formation rates, dust production, disturbed star/dust geometries) making them so different from galaxies' normal mode.

What our data suggest is that this chasm does not exist. Rather, DSFGs are simply the tip of the iceberg, or the light-post that was always there giving us early hints that the dust in all galaxies' ISM is transformative across a wide mass and redshift range. These results reinforce the idea that galaxies simply are moderately to significantly optically thick through the rest-frame UV, and that, as a result, UV diagnostics – not just continuum but corresponding line diagnostics – can only tell a partial story of galaxies' ISM, permeating one optical depth path length into a much more complex ecosystem that can be revealed through its dust emission. Indeed, other recent results from JWST reinforce this result, that optically luminous galaxies also have optically thick dust (Cheng *et al.* 2025). Furthermore, radiative transfer models applied to cosmological simulations have long emphasized these global trends, that UV can underestimate the total SFR across a wide range of masses (Sommovigo *et al.* 2020; Liang *et al.* 2021; Parente *et al.* 2024).

A related consequence of these comparisons is in the practical application of energy balance SED fitting. Energy balance itself *should* hold, but in the case where the UV portion of the SED is optically thick, there is no guarantee that the attenuation measured in the UV should match the emission seen in the FIR.

6.2. *The A_V - Σ_{dust} relation*

While direct comparisons of L_{IR} and A_{UV} tell us about dust geometry, the A_V-Σ_{dust} relation tells us about both dust geometry and the inherent properties of the dust. This is because of the reliance on the dust mass absorption coefficient, κ, in calculating dust mass from flux density on the Rayleigh-Jeans tail. Beyond our earlier calculation of M_{dust} for our stacked SEDs, we take some steps to convert to Σ_{dust}. Rather than applying any scaling relations on galaxies' sizes, we directly compute median and inner 68% confidence intervals on sizes for the stacked galaxy samples in each bin, and propagate the uncertainties on both M_{dust} and R_e via Monte Carlo sampling to generate a realistic distribution of Σ_{dust} per mass and redshift bin. Figure 15 shows where the stacks fall in A_V vs. Σ_{dust} directly in redshift bins. Higher stellar masses at all redshifts are at higher A_V, following from § 5.1 and Fig. 5. It is striking how the stacks evolve sharply with redshift toward higher dust mass surface densities. This is especially interesting considering our earlier discussion of the decreasing measured attenuation (A_V) with increasing redshift; in other words, at higher redshifts, A_V decreases (mildly) while Σ_{dust} increases by over an order of magnitude.

While the evolution in Figure 15 is striking, we can be a bit more precise in our calculations if we instead show the mass dependence and evolution of C_{UV} and C_V, measured via Eq 7. Because the IR SEDs are stacked, we cannot undo the 'averaging' that is inherent to the stack, i.e. we have a single measurement of M_{dust} per mass and redshift bin. However, we have complete information on A_{UV} (A_V) and R_e for each source contributing to that stack. Thus, to compute the most precise bin-averaged C_{UV} (C_V), we compute the median and inner 68th quartile on $A_{UV}R_e^2$, such that $\Sigma_{dust} = (A_{UV}R_e^2)\,\pi/M_{dust}$.

Figure 16 shows the mass dependence and evolution of C_V and C_{UV} with redshift. Higher C_V (or C_{UV}) corresponds to higher A_V (A_{UV}) per unit dust mass surface density. As a reminder, C_V groups the effect of both geometry ($\mathcal{G}_V$) and dust physics (κ_V/κ_{FIR}) into one factor and reveals how it evolves. This figure shows us a strong redshift dependence in C_{UV} and C_V, where both are over an order of magnitude lower at $z \sim 6$ compared to $z \sim 1$. The stellar mass variance shows interesting second order

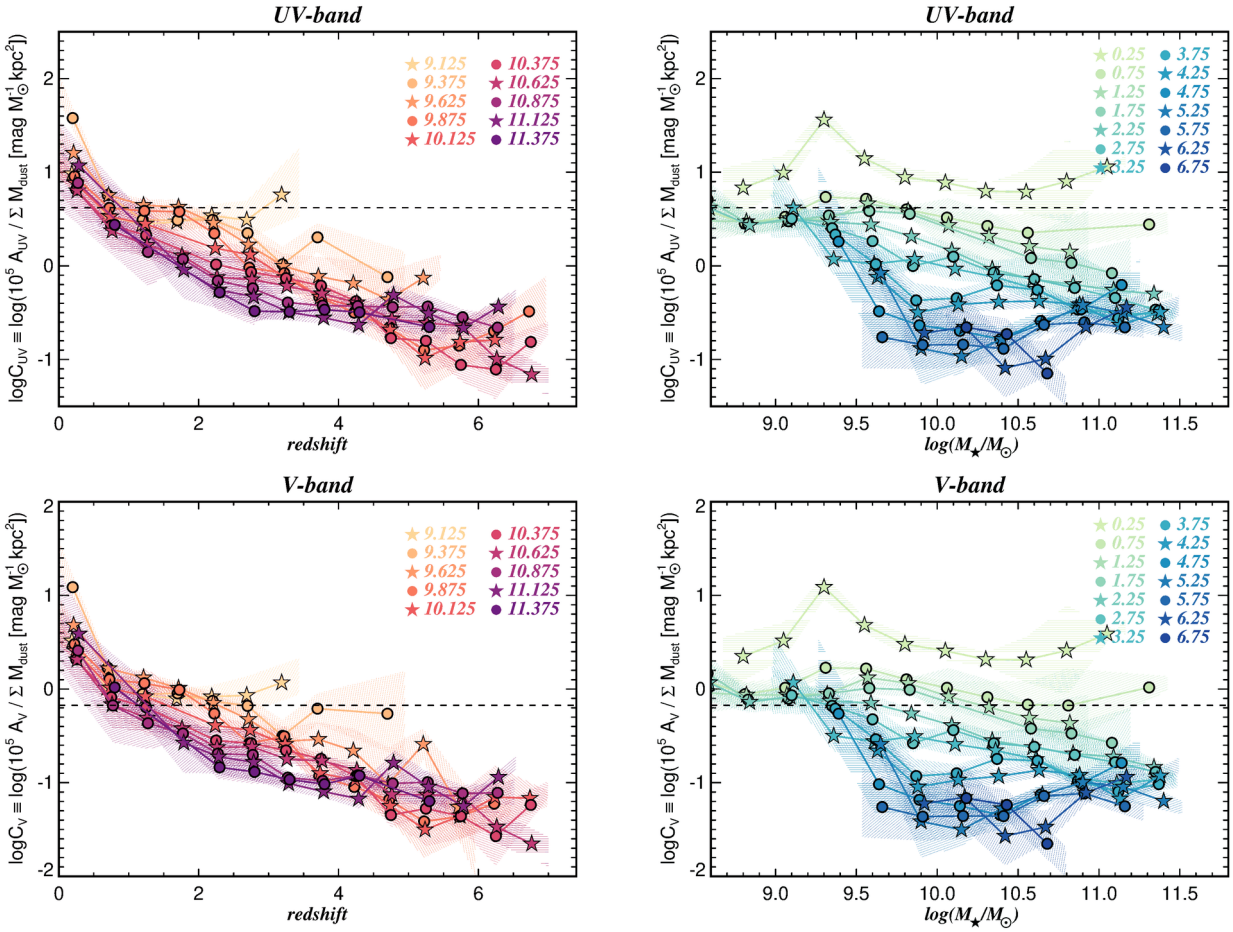

FIG. 16.— The redshift and stellar mass dependence of C_{UV} (top) and C_V (bottom); C_λ is the ratio relating A_λ to Σ_{dust}, i.e. it captures the evolution seen Figure 15 in one coefficient, defined through Eq. 7. C_λ captures the unknowns of both star/dust geometry and dust opacity. The values applicable to the Milky Way are marked in a dashed horizontal line at C_{UV}=4.18 and C_V=0.67. Both C_{UV} and C_V show a strong redshift dependence that is nearly identical, mirroring the similarities in Figure 5. To a lesser extent, C_{UV} and C_V also show a stellar mass dependence, whereby higher stellar masses have lower C_λ from $0 < z < 4$; above $z > 4$, there may be an inversion such that higher masses may have higher C_λ. The fact that C_{UV} and C_V show very similar behavior means that the evolution is not driven by the evolution in attenuation curve slope (as shown in Figure 6).

effects: at the highest stellar masses the redshift evolution is more subtle than at lower masses where the change in C_V (or C_{UV}) is more extreme. What drives the striking redshift evolution in particular, given that dust masses M_{dust} is relatively constant with redshift, and A_V (A_{UV}) only drops by a factor of $\sim$2$\times$ towards high redshifts? It comes from the evolution in galaxy sizes, where, because dust masses (and the DTS ratio) seem relatively constant but higher redshift galaxies are smaller, the dust mass surface density of those high-z systems are substantially higher.

How do we interpret this drop in C_V (or C_{UV}) at high-z? Is this related to the graying of the attenuation curves at higher-z seen in Figure 6? Both the attenuation curve and C_V (C_{UV}) carry the uncertainty of star/dust geometry as well as grain size distribution and dust grain properties. How much of it is geometry versus the fundamental characteristics of the dust grains themselves? We begin to disentangle the two in the next subsection.

6.3. *An evolving grain size distribution?*

The wealth of our stacks capture enough detail in the IR SEDs relative to the rest-frame UV and optical to inform a direct calibration of the relative opacity of dust grains, from the UV to the FIR, as they evolve to high redshifts. This relative opacity is captured in our dataset by the ratio of dust mass absorption coefficients in the UV to the FIR, κ_{UV}/κ_{FIR}; this quantity traces the integrated effects of the grain size distribution (relative mass ratio of small to large grains), the dust composition, and the morphology of dust grains. As a reminder, it is not a true measure of dust microphysics, given that it is a galaxy-integrated quantity. Equation 10 sets the measurement of κ_{UV}/κ_{FIR} that we use, set by a measurement of the relative luminosities emitted in the UV and IR, as well as shape of the IR SED and galaxy size. The nominal value of the ratio for Milky Way dust is $\approx 10^5$ (Draine and Li 2007).

Figure 17 shows the ratio's stellar mass dependence and evolution. The ratio clearly falls by over *an order of magnitude* from $0 < z < 7$ across all stellar masses. High stellar mass galaxies have low κ_{UV}/κ_{FIR} at all redshifts beyond $z > 2$. From $1 < z < 4$ there is substantial stellar mass dependence. What physical phenomena explain this complex evolution in κ_{UV}/κ_{FIR}?

The Draine (2003) grain model indicates that κ_{UV}

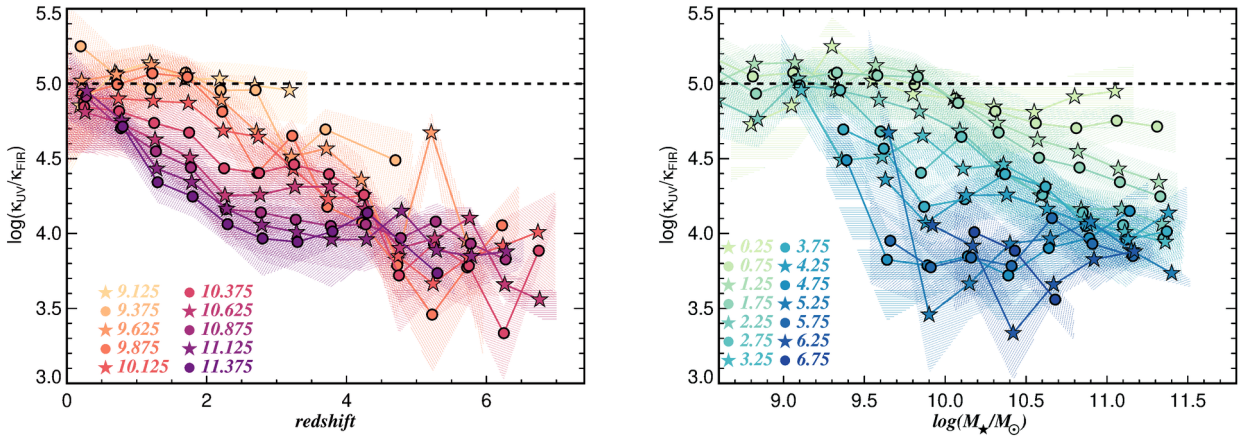

FIG. 17.— Measurements of the variation in $\kappa_{\rm UV}/\kappa_{\rm FIR}$ (see Eq. 10) in redshift and stellar mass. $\kappa_{\rm UV}/\kappa_{\rm FIR}$ is a galaxy-integrated indicator of dust grain properties in the ISM – the grain size distribution, composition, and the morphology of dust grains. *First-order effects of star/dust geometry do not impact the measurement of* $\kappa_{\rm UV}/\kappa_{\rm FIR}$. The nominal Milky Way value of $\kappa_{\rm UV}/\kappa_{\rm FIR}= 10^5$ originates from (Li and Draine 2001) models. There is a precipitous fall in $\kappa_{\rm UV}/\kappa_{\rm FIR}$ with increasing redshift, over an order of magnitude from $z = 0$ to $z \sim 4-5$. From $0 < z < 4$ there is substantial mass dependence as well, with lower $\kappa_{\rm UV}/\kappa_{\rm FIR} \approx 10^4$ in massive galaxies compared to lower mass galaxies. Beyond $z > 4$, all mass bins (with data) have low $\kappa_{\rm UV}/\kappa_{\rm FIR}$. $\kappa_{\rm UV}$ is most sensitive to the small grain distribution, thus lower $\kappa_{\rm UV}/\kappa_{\rm FIR}$ at high-redshift indicates a fundamental depletion of small grains, potentially caused by intense radiation fields at early cosmic times; at later times, those small grains are only destroyed in the still intense radiation fields of high-mass star-forming galaxies with less destruction in lower mass galaxies, and at low redshifts the radiation fields are significantly less intense across all mass ranges.

is dominated by the small grain population, including PAHs and very small carbonaceous and silicate grains. On the other hand, $\kappa_{\rm FIR}$ depends on the total grain cross-section dominated by the larger grain population. The factor of 10 drop in $\kappa_{\rm UV}/\kappa_{\rm FIR}$ from $0 < z \lesssim 4$ signals a significant depletion of the small grain population at high redshifts relative to larger grains. This may be expected for a number of reasons. First, small grains tend to be destroyed in intense radiation fields (Engelbracht *et al.* 2005; Calzetti *et al.* 2007); galaxies are more compact and have higher SFRs at high redshifts, driven by their higher gas fractions (Tacconi *et al.* 2018). Intense radiation fields leads to sputtering, Coulomb destruction, and photo-destruction of PAHs and other very small grains (Draine and Li 2007; Rémy-Ruyer *et al.* 2014). Second, high redshift galaxies' ISMs are generally more metal-poor at fixed mass (Maiolino and Mannucci 2019); at lower metallicities, the dominant dust production channels shift (Galliano *et al.* 2018). AGB stars – while efficient producers of small carbonaceous grains – have not had time to contribute significantly to the ISM at $z > 4$ (Schneider and Maiolino 2024) in galaxies that are metal poor and did not have significant star formation at early times. Instead, dust production may be dominated by core-collapse supernovae and ISM grain growth, which is thought to preferentially produce larger grains (Asano *et al.* 2013a,b; Zhukovska *et al.* 2016). There is additional complexity introduced by the concept of shattering and coagulation. Grain-grain collisions (shattering) in turbulent media can replenish the small grain population (Hirashita and Omukai 2009; Jones *et al.* 2017), but at sufficient densities, dust coagulation may counterbalance shattering by turning smaller grains into larger grains, shifting the balance of $\kappa_{\rm UV}/\kappa_{\rm FIR}$. Last, aside from intense star formation, AGN can also produce the radiation fields that lead to the destruction of small grains (Laor and Draine 1993; Maiolino *et al.* 2001a,b) further complicating the physical drivers of an evolving $\kappa_{\rm UV}/\kappa_{\rm FIR}$.

Because we see a distinctly different behavior in the evolution of $\kappa_{\rm UV}/\kappa_{\rm FIR}$ in different mass bins, and because an underlying physical hypothesis as to the driver of its evolution is the intensity of the stellar radiation field, we plot $\kappa_{\rm UV}/\kappa_{\rm FIR}$ against $\Sigma_{\rm SFR}$, the star-formation rate surface density, in Figure 18. What we see is clear: that the more intense radiation fields that are thought to accompany high SFR surface densities have a much lower $\kappa_{\rm UV}/\kappa_{\rm FIR}$, consistent with a depletion of small dust grains. We fit the relationship between $\Sigma_{\rm SFR}$ and $\kappa_{\rm UV}/\kappa_{\rm FIR}$ as:

$$\log\left(\frac{\kappa_{\rm UV}}{\kappa_{\rm FIR}}\right) = (10.79 \pm 0.50) - (2.58 \pm 0.11)\log(\Sigma_{\rm SFR}) \quad (20)$$

where the fit has an overall scatter of 0.69 dex. This fit is summarized in our appendix, Table 1.

Complementary work on cosmological simulations (e.g. Aoyama *et al.* 2017; Hou *et al.* 2019) suggests a similar trend, that a deficit of small grains at high-z produces flatter (grayer) intrinsic extinction curves (Narayanan *et al.* 2026). And while, in this work, we cannot disentangle the relative impact of grain size distribution and geometry on the attenuation curve, we do note that the suggested depletion of small grains at high-z would result in both a grayer attenuation curve (higher δ at higher-z) and decrease in $\kappa_{\rm UV}/\kappa_{\rm FIR}$. Similarly, $\Sigma_{\rm SFR}$ is found to drive significant variation in line-of-sight attenuation (Sommovigo and Algera 2025).

Indeed, the evolution in $\kappa_{\rm UV}/\kappa_{\rm FIR}$, and the evolution in C_λ (the scaling between A_λ and $\Sigma_{\rm dust}$) and δ (slope of the attenuation law) are all intertwined. Both C_λ and δ are dependent on *both* star/dust geometry and inherent dust properties, while $\kappa_{\rm UV}/\kappa_{\rm FIR}$ only informs the latter. Empirically, we have measured steep evolution in $\kappa_{\rm UV}/\kappa_{\rm FIR}$ and C_λ (both changing by over an order of magnitude across $0 < z < 7$), while the evolution in δ is more subtle. The fact that $C_{\rm UV}$ and $C_{\rm V}$ evolve in very

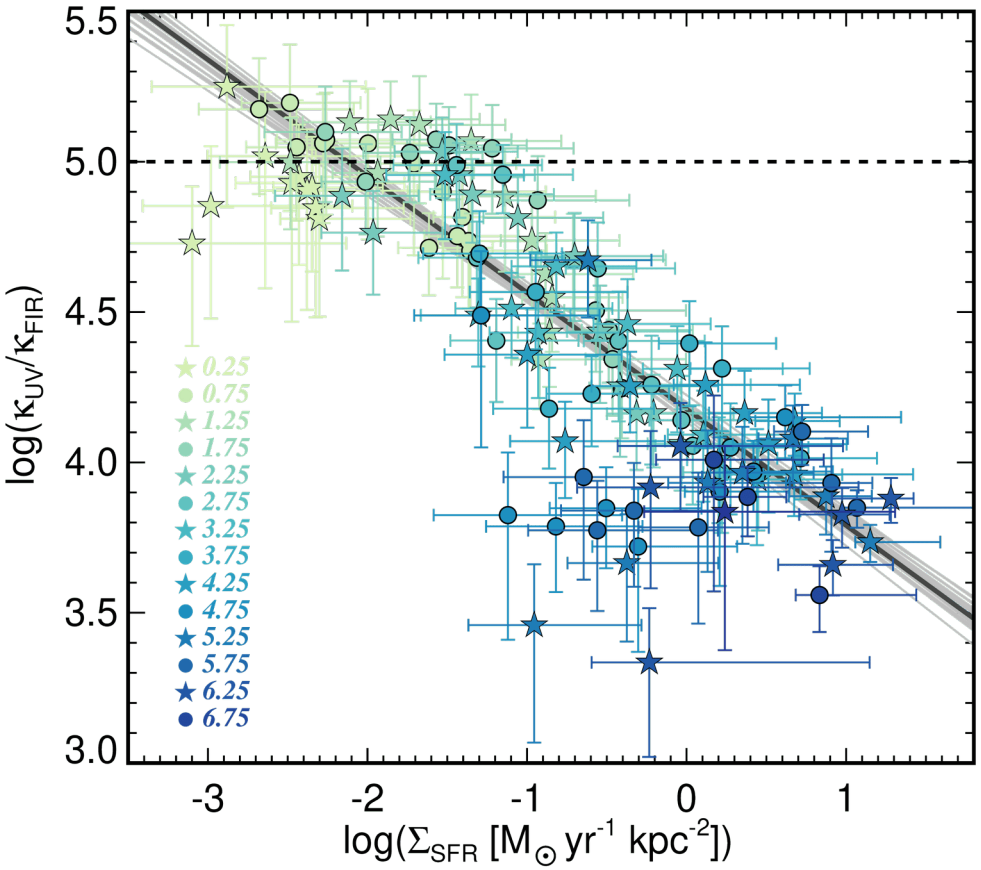

FIG. 18.— The relationship between SFR surface density and $\kappa_{\rm UV}/\kappa_{\rm FIR}$ for all redshift and stellar mass bins shown on Figure 17. The horizontal line marks the $\kappa_{\rm UV}/\kappa_{\rm FIR}$ of the Milky Way. Here we find evidence that the underlying physical driver of variation in $\kappa_{\rm UV}/\kappa_{\rm FIR}$ may be the SFR surface density. In the most intense radiation fields where $\Sigma_{\rm SFR}$ is high, our results are consistent with a depletion of small grains relative to the large dust grain population. The black line indicates the best-fit relation as given in Eq. 20 with gray lines representing 25 random draws from the fit's posterior distribution; scatter about the relation is 0.69 dex.

similar ways to one another relates closely to the subtle evolution of δ (a steeper evolution in δ would mean that $C_{\rm UV}$ and $C_{\rm V}$ evolve very differently from one another). It is difficult to take the interpretation of the magnitude of evolution of these measurements – i.e. steep evolution in $C_{\rm UV}$ and $\kappa_{\rm UV}/\kappa_{\rm FIR}$ relative to δ – further without making some significant assumptions (on the relative ratio of geometries between UV and V, and between the unanchored evolution of $\kappa_{\rm UV}/\kappa_{\rm V}$). Another cautionary note is that we fundamentally restricted the dynamic range of δ to $-0.5 < \delta < 0.1$ to avoid overfitting the UV/optical portion of galaxies' SEDs. Future work with large spectroscopic samples may be able to disentangle the relationship between δ and fundamental dust properties, as well as geometry, further with more precise constraints on hand.

6.4. *What drives dust temperature?*

The physical drivers of a galaxies' average dust temperature have been extensively discussed in the literature (e.g. Chapman *et al.* 2003; Symeonidis *et al.* 2013; Magnelli *et al.* 2014; Simpson *et al.* 2017) with many works, especially those focusing on nearby galaxies where SEDs are often more extensively studied (Lehnert and Heckman 1996; Chanial *et al.* 2007; Lutz *et al.* 2016; Díaz-Santos *et al.* 2010) drawing the conclusion that star formation surface density, or IR luminosity surface density, $\Sigma_{\rm IR}$, correlates most tightly with $T_{\rm dust}$. This conclusion is also drawn in Burnham *et al.* (2021) for high-z galaxies studied with high-resolution ALMA imaging and from radiative transfer simulations (Parente *et al.* 2025). The framework from Burnham *et al.* is useful for parameterizing a predictive behavior of $T_{\rm dust}$ as a function of both redshift and stellar mass. While Drew and Casey (2022) recognized that galaxies' dust temperatures at fixed stellar masses would evolve primarily between $0 < z < 2$ from the evolution of the SFR-$M_\star$ relation alone, it did not account for the potential increase in temperature due to galaxies' smaller sizes and thus increase in $\Sigma_{\rm IR}$. To accurately model the evolution of $\Sigma_{\rm IR}$ and its impact on $T_{\rm dust}$, the size evolution of galaxies forms a critical piece. Following the work of Yang *et al.* (2025) using the COSMOS-Web data, we fit a global average relation to the size-mass evolution of galaxies' half light radii in the stacked sample we use in the analysis:

$$R_{\rm e}(M_\star, z) = C M_\star^{\alpha} (1+z)^{-\beta}. \quad (21)$$

We measure $C = 0.0178^{+0.0018}_{-0.0011}$, $\alpha = 0.287 \pm 0.004$, and $\beta = 1.23 \pm 0.02$. We note that Yang *et al.* measure $\alpha = 0.20$ and $\beta = 1.21$ which roughly agrees with our fit

to the 'stackable' sample here.

From a galaxy's stellar mass and redshift, one can estimate the star formation rate using the Speagle *et al.* (2014) parameterization. Burnham *et al.* (2021) presents, in their Eq. 7, a tight empirical relationship between $\lambda_{\rm peak}$ ($\propto {\rm T_{dust}}^{-1}$) and $\Sigma_{\rm IR}$. The translation of that relation using SFR and $R_{\rm e}$ directly is:

$$\log(\lambda_{\rm peak}) = \frac{1}{(3.80 \pm 0.16)} \Big[(28.61 \pm 0.33) - \log({\rm SFR}) + \log\left(\pi R_{\rm e}^2\right) \Big] \quad (22)$$

With SFR in $\rm M_\odot\,yr^{-1}$ and $R_{\rm e}$ in kpc. The translation between $\log(\lambda_{\rm peak})$ and $\rm T_{dust}$ for the type of SED fitting used in this work is given in Eq 13.

We refer to Equation 22, or the expected relationship between SFR surface density and $\lambda_{\rm peak}$, as the "Stefan-Boltzmann" expectation. This is because the backbone of this inference comes from an application of the Stefan-Boltzmann law to galaxy scales (see the Burnham *et al.* 2021 discussion § 5.1 and measurement in 5.2.1). To summarize, Stefan-Boltzmann informs the relationship between the emergent luminosity and temperature from an optically thick body; galaxies are likely optically thick in some regimes but certainly not others. In the rest-frame millimeter, we explicitly presume they are optically thin (allowing the calibration of the dust masses and dust mass surface densities), but the dominant IR emission is at significantly shorter wavelengths, at rest-frame $\approx$100 μm. Despite complex geometry, by making a simplified assumption (that galaxies are optically thick disks rather than spheroids), Equation 22 emerges. Does it hold with our data?

Figure 19 compares measurements to this Stefan-Boltzmann expectation at fixed stellar mass intervals. All mass bins show increasing temperatures over the $0 < z < 2$ mass range, consistent with the dominant evolution in the SFRs of galaxies on the main sequence between those epochs. At higher redshifts, we note that the high mass bins ($> 10^{10.5}$ $\rm M_\odot$) show remarkably good agreement with the Stefan-Boltzmann model; those bins predict the steepest evolution in dust temperature due to their relatively compact sizes and high SFRs. The intermediate mass bins ($\approx 10^{9.5-10.5}$ $\rm M_\odot$) are slightly discrepant from the model, with some indication of flatter temperature evolution than expected beyond $z > 2$. That may indicate that the ISM is less optically thick near the $\approx 100\,\mu$m peak. The lowest mass bins do not have sufficient constraints at high redshifts to draw conclusions.

We note that Dudzevičiūtė *et al.* (2021) compare dust-mass matched samples at $z = 1-2$ and $z = 3-4$ and find dust continuum sizes roughly half as large at higher redshifts, which is consistent with increased star formation surface densities and higher dust temperatures.

6.5. *Dust-to-Stellar Ratio in the context of evolving metallicity and gas fractions*

In Figure 13 we have measured the evolution and mass dependence of the dust-to-stellar ratio finding a $\propto (1+z)^{1.36}$ evolution and $\propto M_\star^{-0.3}$ stellar mass dependence. How does this measured DTS evolution stack up against other literature measurements?

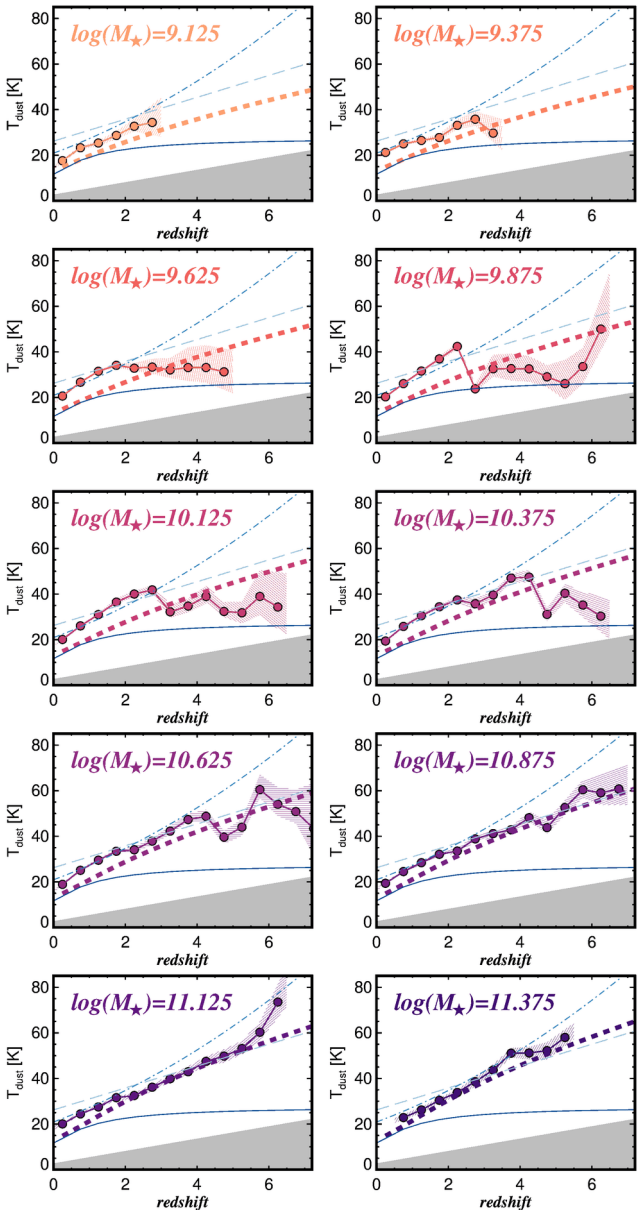

FIG. 19.— The evolution of dust temperature, broken into different stellar mass bins, compared against expectation for an optically thick-through-100μm disk with SFR and size determined by evolution in the SFR-$\rm M_\star$ and the size-mass relationships (dashed lines matched in color to the data). The expected temperature given an SFR and size is given by Equation 22. The model fits the data well at high stellar masses ($\rm M_\star > 10^{10.5}$ $\rm M_\odot$), suggesting the optically thick assumption may be an appropriate approximation in that mass regime across all redshifts. At more modest masses, temperatures are flat beyond $z > 2$, perhaps indicating that the model is less appropriate in that mass regime. The three blue lines are the same literature comparisons shown in Figure 8.

Theoretical predictions for the DTS are largely inferred through semi-analytic models that employ scaling relations determined using hydrodynamic simulations on smaller cosmological volumes, with radiative transfer applied. Our work here does not perform detailed comparisons with simulations predictions (given the scope required for such a comparison), though we do note the general trends expected for the DTS in a suite of semi-analytic models including the Santa Cruz model (Popping *et al.* 2017), SHARK (Lagos *et al.* 2019, 2024),

L-Galaxies (Vijayan *et al.* 2019), and Gaea (Osman *et al.* 2025). The mean model expectations are shown in Figure 20 relative to the averaged binned relations in our work. Popping *et al.* (2017) generally observe a DTS that falls with cosmic time, in line with our observations, though their stellar mass dependence is substantially flatter than what our data suggest. SHARK (Lagos *et al.* 2018, 2019, 2024) shows similar trends as the Santa Cruz model, though with generally better agreement with our measurements over the mass and redshift ranges where there is constraining power. The L-Galaxies model (Vijayan *et al.* 2019) predicts a trend in the opposite direction, such that higher redshift galaxies have lower DTS ratios, discrepant with our data, though the stellar mass dependence in L-Galaxies, like SHARK, reflects what we see: higher mass galaxies have lower DTS ratios. Dusty-Gaea (Osman *et al.* 2025) show lower DTS ratios at higher redshifts and higher DTS ratios with increased mass. From existing models, it seems clear there is little convergence on the behavior of the DTS with stellar mass and redshift.

Observational measurements of the DTS at high-z are somewhat limited, though Béthermin *et al.* (2015a), Magnelli *et al.* (2020), Donevski *et al.* (2020), and recently Jolly *et al.* (2025) and Eales *et al.* (2026) offer direct measurements for high-redshift samples. The Béthermin *et al.* is analogous to our measurements here, in that they stack massive galaxies in the Ilbert *et al.* (2013) iteration of the COSMOS catalog and fit full dust SEDs (a notably shallower catalog than used herein, though the best available at the time). Their analysis is limited to $z < 4$. While they did not have the resolution to infer a stellar mass dependence of the DTS, they do see some redshift evolution $\propto (1+z)^{0.4-0.7}$, shallower than seen in our dataset. This could be driven by the limitation of their analysis to the most massive stellar reservoirs.

The Magnelli *et al.* work does stack galaxies by stellar mass and redshift in ASPECS 1.2 mm maps, and infers dust mass with adopted $\kappa_{\rm FIR}$, as we do in this work (though we stack multiple FIR datasets). They anchor the DTS measurement in an integrated sense by comparing the dust mass density to the stellar mass function (Mortlock *et al.* 2015) and constrain it to $z \sim 3$ as having a steeper redshift dependence than we find here, $\propto (1+z)^{2.6}$ and shallow stellar mass dependence, $\propto M_\star^{0.1}$. Broadly speaking, our results are consistent in order of magnitude: most of the change in the DTS is in its redshift evolution, with a more minor variation dependent on the underlying galaxy mass.

The Donevski *et al.* work presents the DTS for galaxies directly detected in the IR; they find a much shallower redshift evolution in this sample $\propto (1+z)^{0.5}$ with a stellar mass dependence $\propto M_\star^{-(0.2-0.6)}$. While our stacking results indicate steeper redshift evolution of the DTS, we are consistent with Donevski *et al.* in its finding of a weak, but negative, stellar mass dependence.

Jolly *et al.* (2025) stacks 1.2 mm continuum data from the ALMA Lensing Cluster Survey and find mild evidence for lower dust-to-stellar mass ratios at higher redshifts than at $z \sim 1$; their assumptions regarding $\kappa_{\rm FIR}^{\rm fix}$ are different than our work by a factor of two and high-z samples are limited by small sample sizes; the work does see lower DTS ratios in higher mass galaxies.

Euclid Collaboration *et al.* (2026) stack *Euclid*-detected main-sequence galaxies on both *Herschel* and SCUBA-2 imaging, fitting modified blackbodies in a similar fashion as our analysis, stepping out to $z = 3$. They find higher DTS ratios at higher redshifts, with a flattening past $z > 1$ with lower DTS ratios at higher stellar masses, which mirrors our data directly as shown in Figure 12.

Finally, recent work in Eales *et al.* (2026) presents a similar stacking analysis as our work, using the COSMOS2025 catalog to stack the SCUBA-2 imaging and infer dust mass evolution with stellar mass and Hubble Sequence. Even stacking on a single band and varying their assumptions with respect to dust temperatures, Eales *et al.* (2026) find an evolution of the DTS that is consistent with what we find: increasing DTS at higher redshift and lower stellar masses.

These literature sources set the stage for contextualizing the (lack of) precision with which the DTS is understood. It is helpful to pedagogically break the DTS into its components:

$$\frac{M_{\rm dust}}{M_\star} = \left[\frac{M_{\rm dust}}{M_{\rm gas}}\right]\left[\frac{M_{\rm gas}}{M_\star}\right] = \left[\frac{M_{\rm dust}}{M_{\rm gas}}\right]\mu_{\rm gas}$$
$$\mathrm{DTS} = \mathrm{DTG}(\mathrm{Z}(\mathrm{M}_\star, \mathrm{z})) \times \mathrm{GTS} \quad (23)$$

In other words, the DTS ratio can be expressed as the product of the dust-to-gas (DTG) ratio and the gas-to-stellar (GTS) ratio, or $\mu_{\rm gas}$. Does our earlier fit to the DTS ratio agree with literature measurements of the DTG ratio and $\mu_{\rm gas}$?

Our understanding of the dust-to-gas and its metallicity dependence is anchored to works like Rémy-Ruyer *et al.* (2014) and Galliano *et al.* (2021). The DTG ratio is substantially lower at lower metallicity. Further, the relationship between galaxies' metallicities and their stellar masses is extensively studied (Maiolino *et al.* 2008; Mannucci *et al.* 2010; Zahid *et al.* 2013, 2014; Maiolino and Mannucci 2019; Curti *et al.* 2020; Sanders *et al.* 2021, 2023; Jain *et al.* 2026). While some work argue for a fundamental metallicity relationship, where Z is exclusively determined from $\mathrm{M}_\star$ and SFR alone, we instead adopt an evolving mass-metallicity relationship (MZR) in the form of Eq. 2 of Curti *et al.* (2020) with redshift evolution described by Eq. 4 of Jain *et al.* (2026).

Combining the MZR with the GTS ratio in Rémy-Ruyer *et al.* (2014), then gives us a concrete prediction of the evolution in the DTG ratio with redshift and stellar mass. We show the implied DTG evolution, renormalized to the measured DTS ratio, in Figure 21 and parameterize it as a 2nd order polynomial of the form

$$\log(\mathrm{DTG}) = A + b\,\Delta M + c\,\Delta M^2 + d\,\ell_z + e\,\Delta M\,\ell_z + f\,\ell_z^2 \quad (24)$$

Where $\Delta M \equiv \log(M_\star/10^{10}\,M_\odot)$ and $\ell_z \equiv \log(1+z)$. We fit the coefficients such that $(A, b, c, d, e, f) = (-2.191, +0.143, -0.056, -0.178, +0.135, -0.069)$. The DTG ratio increases for higher stellar masses (due to their higher metallicities) but decreases at high redshift (due to their higher star formation rates and overall lower metallicities).

Given the expectation for the evolution of the DTG ratio in Eq. 24, and the earlier fit to the DTS ratio in Eq. 18, we explicitly predict that the gas-to-stellar ratio

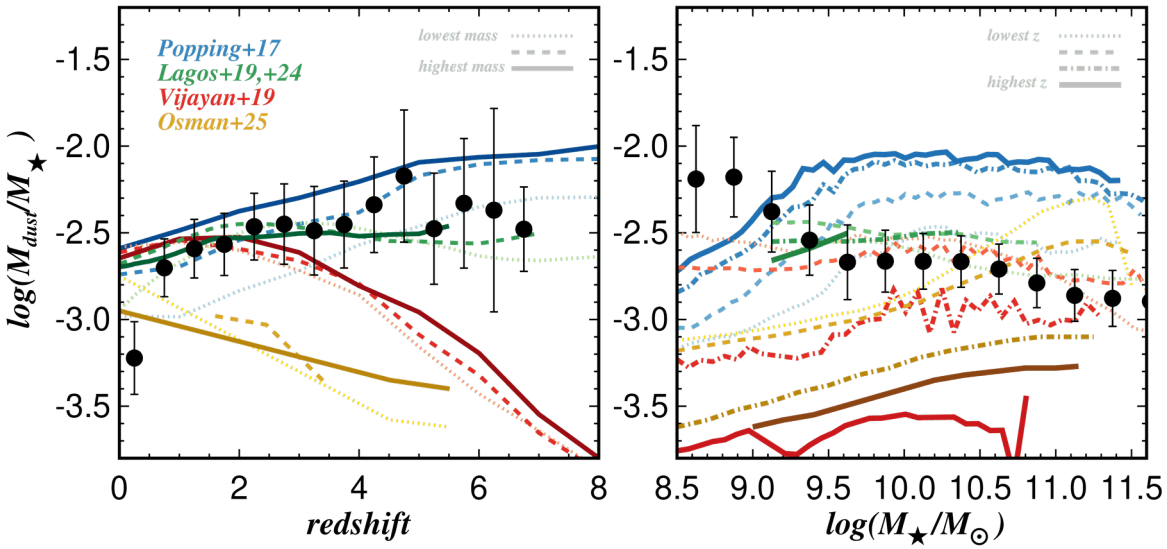

FIG. 20.— A comparison of the averaged binned dependence of the DTS from our data (black points, taken from Figure 13) against expectations from semi-analytic models with dust prescriptions. Blue lines show expectation from the Santa Cruz model Popping *et al.* (2017); mass bins taken at $10^{9.125}$ $M_\odot$, $10^{9.675}$ $M_\odot$, and $10^{10.125}$ $M_\odot$ and redshift bins at $z = 1$, $z = 3$, $z = 5$, and $z = 7$. Green lines are from SHARK (Lagos *et al.* 2019, 2024) with the same mass and redshift bins. Red lines are from L-GALAXIES (Vijayan *et al.* 2019); mass bins are 10^9 $M_\odot$, $10^{9.5}$ $M_\odot$, and 10^{10} $M_\odot$and the same redshift bins. Yellow/golden lines are from DUSTY-GAEA (Osman *et al.* 2025), with the same mass bins as L-GALAXIES but shown at $z = 1.6$, $z = 2.45$, $z = 3.48$ and $z = 5.51$. On the left panel, darker colors and progressively more solid lines correspond to higher stellar mass bins. On the right panel, darker colors and progressively more solid lines correspond to higher redshift bins.

would evolve as $\mu_{\rm gas} \propto M_\star^{-0.49}(1+z)^{1.57}$. In other words, this would imply that higher gas-to-stellar ratios exist at higher redshifts but that at fixed redshift, higher mass systems have lower relative gas-to-stellar ratios. This implied GTS evolution is also shown in Figure 21; again, it represents the difference in evolution between the measured DTS and the implied DTG given our understanding of metallicity evolution and dependence of DTG on metallicity.

We can then compare this directly to measurements of $\mu_{\rm gas}$ from Tacconi *et al.* (2018) and Liu *et al.* (2019) and reflect on discrepancies. Both Tacconi *et al.* and Liu *et al.* find a steeper redshift dependence and shallower mass dependence than is implied in our data, such that $\mu_{\rm gas} \propto (1+z)^{2.5} M_\star^{-0.36}$ and $\mu_{\rm gas} \propto (1+z)^{2.9} M_\star^{-0.69}$, respectively. What causes this discrepancy? There may be wiggle room in this comparison that alleviates sufficient tension, or it may hint at some breakdown of assumptions.

A major assumption on our part in the measurement of the DTS is that $\kappa_{\rm FIR}$ *does not evolve*; all dust masses in this work use a fixed value. That would place all of the evolution we observe in $\kappa_{\rm UV}/\kappa_{\rm FIR}$ on the evolution of $\kappa_{\rm UV}$ and the lack of small grains, with little to no change in the large grain population to which $\kappa_{\rm FIR}$ is most sensitive. If, instead, there is some redshift evolution in $\kappa_{\rm FIR}$ due to different characteristics of the large grain population, that would change the redshift evolution of the DTS measured in Eq. 18. Importantly, simulations suggest that the dust-to-stellar ratio is also directly related to the dust size distribution and thus $\kappa_{\rm FIR}$: SN-produced dust would preferentially form larger grains dictating lower DTS ratios (Schneider and Maiolino 2024). An evolving $\kappa_{\rm FIR}$ would not only impact the measured DTS, but indeed it would also percolate to an evolution in DTG,

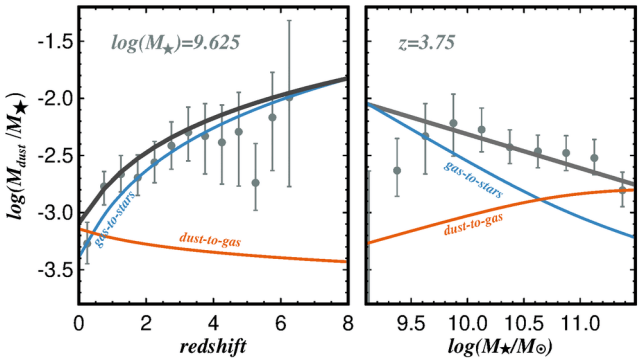

FIG. 21.— An illustration of the estimated relative contributions to the evolution of the dust-to-stellar (DTS) mass ratio. Here we show a single mass bin and its evolution in redshift ($\log(M_\star) = 9.625$, left) and a single redshift bin and the stellar mass dependence of the DTS ratio ($z = 3.75$, right). By anchoring to literature measurements of the mass metallicity relation (Zahid *et al.* 2014; Jain *et al.* 2026) and the metallicity dependence of the dust-to-gas ratio (Rémy-Ruyer *et al.* 2014), we infer the evolutionary shape and mass dependence of the dust-to-gas (DTG) ratio (orange curves). It deviates substantially from the evolution seen in the DTS ratio (gray curves, Eq 18). The difference can be accounted for by the steep evolution (and mass dependence) of the gas-to-stellar ratio (GTS; blue curves). While Tacconi *et al.* (2018) and Liu *et al.* (2019) measure an even steeper evolution in the GTS ($\propto (1+z)^{2.5}$ and $\propto (1+z)^{2.9}$ vs. our inferred $\propto (1+z)^{1.6}$), there is sufficient uncertainty in the possible evolution of $\kappa_{\rm FIR}$ to make up the difference.

because the DTG-Z relationship derived in Rémy-Ruyer *et al.* (2014) would have an additional redshift dependence with a variable $\kappa_{\rm FIR}$. Furthermore, a changing $\kappa_{\rm FIR}$ would *also* change the GTS ratio; this is not because gas or stars are directly linked to $\kappa_{\rm FIR}$, but because many of the gas measurements used to anchor measurements of GTS rely on dust masses and a presumed DTG

ratio!

Beyond this concern regarding the evolution of $\kappa_{\rm FIR}$ is the additional dependence of dust mass on dust temperature where, for example, Tacconi *et al.* (2018) presume a mass-weighted dust temperature of 25 K; if that differs substantially at higher redshifts where dust temperatures may be higher, then dust masses could be lower than currently inferred, drawing down the GTS ratio.

The complex relationship between $\kappa_{\rm FIR}$ and the evolution of DTS, as well as DTG and GTS is beyond the scope of what our data can constrain directly, but with more detailed sets of observations to calibrate these relationships at high-z, we may learn quite a bit about the relative role that dust and gas play in shaping our interpretation of the growth of galaxies alongside their well-studied stellar components.

7. CONCLUSIONS

In this work we have presented a detailed comparison of galaxies' attenuation characteristics – inferred from the rest-frame UV/optical – to their average dust emission characteristics – inferred from the rest-frame FIR. We take >500,000 galaxies from the latest JWST catalog in the COSMOS field and pair that catalog with some of the deepest, wide-field submm extragalactic maps to reach sensitivities down to stellar masses $\sim 10^9$ M$_\odot$ and redshifts $z \sim 7$ in a stacking analysis. Our main conclusions are as follows:

1. **Attenuation inferred from the UV/optical is a strong function of mass and falls slightly at increased redshift (§ 5.1, Eq. 11, Figs. 4, 5).** Specifically the UV attenuation to stellar mass relation ($A_{\rm UV}$-$M_\star$) shows mild redshift evolution out to $z \sim 6$ with decreasing $A_{\rm UV}$ (and $A_{\rm V}$) towards high-z, followed by a reversal and upturn beyond $z \sim 6$ whose origin is uncertain.

2. **Attenuation curves are grayer at higher redshifts (§ 5.2, Eq. 12, Fig. 6).** The slope of the attenuation curve, as inferred from UV/optical tracers, evolves with redshift, steepening monotonically toward lower redshift with the slope evolving as $\langle\delta(z)\rangle = -0.36 + 0.03z$, transitioning from near-Calzetti at high-z to SMC-like slopes locally. This points to a deficit of small grains in the early Universe.

3. **Dust temperatures rise steeply with redshift, tracking expectations from a toy Stefan-Boltzmann model at $> 10^{10}$ M$_\odot$ (§ 5.4, 6.4, Eq 13, 22 Fig. 8, 19).** We postulate this is driven by the evolution of star formation surface densities. Lower mass galaxies show less evolution in dust temperature beyond $z > 2$ than high mass galaxies, possibly hinting that FIR SEDs for lower-mass systems are less optically thick around their peak at rest-frame 100 μm.

4. **Star formation is overwhelmingly obscured ($> 90\%$) for galaxies above $z > 0.5$ and stellar masses $> 10^{10}$ M$_\odot$ (§ 5.6, Eq. 15 Fig. 11).** Higher mass galaxies are *more* obscured at increasing redshifts, with unobscured SFR fractions $\lesssim$1% at $> 10^{10.5}$ M$_\odot$. Galaxies with stellar masses $\sim 10^{9.5}$ M$_\odot$ are ∼10% unobscured at all redshifts $z > 1$.

5. **UV/optical SED fitting systematically underestimates attenuation and obscured star formation by a factor of $\sim 3\times$ at $z > 0.5$ (§ 6.1, Fig. 14)** for all mass bins, and by up to an order of magnitude for the most massive galaxies at high redshifts. Put another way, energy balance fits driven by OIR constraints will underestimate the dust SED, and nearly all galaxies are effectively optically thick to rest-frame UV light, meaning UV diagnostics alone give a fundamentally incomplete picture of star formation and the ISM.

6. **The relationship between dust mass surface density and UV/optical attenuation evolves by over an order of magnitude between $0 < z < 7$ (§ 6.2, Figs. 15, 16).** The $A_{\rm UV}$-$\Sigma_{\rm dust}$ ($A_{\rm V}$-$\Sigma_{\rm dust}$) relation is parameterized via the evolution of $C_{\rm UV}$ ($C_{\rm V}$), a coefficient relating the two. The strong evolution seen in $C_{\rm UV}$ and $C_{\rm V}$ is attributable to both an evolving star/dust geometry and dust grain size distribution and composition. By combining constraints that relate $A_{\rm UV}$ to $L_{\rm IR}$ (independent of dust properties) and $\Sigma_{\rm dust}$-$A_{\rm UV}$, we loosely constrain the evolution in dust geometry, $\mathcal{G}_{\rm UV}$. We find that the impact of geometry is weakly evolving though largely inconsistent with a foreground dust screen across all masses and redshifts $z > 0.5$.

7. **Significant evolution in the grain size distribution is inferred via the measurement of $\kappa_{\rm UV}/\kappa_{\rm FIR}$ (§ 6.3, Eq 20 Figs. 17, 18).** $\kappa_{\rm UV}/\kappa_{\rm FIR}$ is measured independent of first-order geometric effects and is inferred to fall by over an order of magnitude from $z \sim 0$ to $z \sim 7$. This is consistent with preferential destruction of small grains by intense radiation fields at early cosmic times and appears to be primarily driven by a redshift-invariant inverse relationship to SFR surface density.

8. **The dust-to-stellar mass ratio (DTS) evolves as $\sim (1+z)^{1.36}$ with slight mass dependence $\sim M_\star^{-0.3}$, with the most rapid evolution seen between $z \sim 0$ and $z \sim 0.5$ (§ 5.7, 6.5, Eq. 23, Figs. 12, 13, 21).** The evolution in the dust-to-stellar ratio is dominated by the steep redshift dependence of the gas-to-stellar mass ratio which counterbalances the shallow (and negative) evolution in the dust-to-gas ratio. The mass dependence originates from the higher gas fractions of lower mass galaxies.

We have found that the standard framework for inferring dust properties from the rest-frame UV/optical – attenuation curves, a presumed foreground dust screen geometry, and fixed opacity – is insufficient across most masses and redshifts. The combination of JWST photometry and deep ALMA/(sub)mm stacking reveals that the ISM of typical star-forming galaxies is moderately to significantly opaque through the rest-frame UV across a wide range of masses and redshifts, not just the extreme, dusty star-forming galaxy population as previ-

ously thought. This holds even with high quality constraints from JWST. As a result, FIR measurements remain irreplaceable for accurate star formation rate budgets across cosmic time: UV/optical SEDs are not simply noisy proxies for the total SFR, but systematically biased ones whose systematics worsen in precisely the mass and redshift regimes where the most star formation is occurring.

The measurement of an evolving $\kappa_{\rm UV}/\kappa_{\rm FIR}$, constrained independent of first-order star/dust geometry effects, suggests a significant shift in typical ISM dust grain properties in the early Universe relative to now. This may serve as direct observational evidence that small grains are being preferentially destroyed in the intense radiation fields of early star-forming galaxies, but we caution that we are constraining the galaxy-integrated ratio, $\kappa_{\rm UV}/\kappa_{\rm FIR}$, not the UV and FIR evolution of κ independently, and certainly not on microscopic scales; it is possible that, aside from small grain depletion, the evolution of large grains and dust composition could impact this ratio significantly. The implications of such an evolution, whatever the cause, are significant. It implies that interpretation and calibration of both dust attenuation inferences and dust mass measurements may be moving targets. Any high-z work relying on fixed dust prescriptions calibrated in the local universe should proceed with caution.

We thank the anonymous referee for helpful comments that improved the manuscript. CMC thanks the University of California Santa Barbara's Division of Mathematical, Life and Physical Sciences for support of this work, as well as the National Science Foundation for support through grants AST-2009577 and AST-2307006 and to NASA through grant JWST-GO-01727 awarded by the Space Telescope Science Institute, which is operated by the Association of Universities for Research in Astronomy, Inc., under NASA contract NAS 5-26555. HBA acknowledges support from the Harrington Graduate Fellowship at UT Austin as well as the National Science Foundation Graduate Research Fellowship. ET acknowledges support from the ANID CATA-BASAL program FB210003, and FONDECYT Regular 1241005 and 1250821. This project has received funding from the European Union's Horizon 2020 research and innovation program under the Marie Skłodowska-Curie grant agreement No. 101148925. MA is supported by FONDECYT grant number 1252054, and gratefully acknowledges support from ANID Basal Project FB210003, ANID MILENIO NCN2024_112 and ANID + Vinculación Internacional + FOVI250261. The NIKA2 N2CLS is based on observations carried out under project 192-16 with the IRAM 30m telescope, and follow-up projects W16EE, E16AI, W21CV, W23CX, W23CJ, and S24CF with NOEMA. Much of this work was conducted on land traditionally occupied by the Chumash people in what is now known as the Santa Barbara area of California. We pay our respects to the Chumash elders, past, present, and future, who call this place-—the land that the university sits upon—-their home.

APPENDIX

BEST-FIT RELATIONS DERIVED IN THIS WORK

Here we provide a summary of the fitted relations in this work and show those fitted relations explicitly binned by stellar mass and redshift. These include attenuation as a function of redshift and mass, both in the UV, $A_{\rm UV}(z,M)$, as well as optical, $A_{\rm V}(z,M)$; the fraction of star formation that is unobscured, $f_{\rm unobs}(z,M)$; the dust-to-stellar mass ratio, DTS(z,M); the rest-frame peak wavelength of the dust SED, $\log(\lambda_{\rm peak})(z,M)$ ($\lambda_{\rm peak}$ is inversely proportional to temperature); and the relationship between $\kappa_{\rm UV}/\kappa_{\rm FIR}$ and $\Sigma_{\rm SFR}$. Table 1 presents a summary of the derived relationships and their best-fit parameters.

Figure 22 and Figure 23 show the stellar mass dependence in redshift bins, and redshift evolution in stellar mass bins, respectively for $A_{\rm UV}$. A similar behavior is seen in the evolution of $A_{\rm V}$. Figure 24 show the redshift evolution of dust temperature via the measured quantity, $\log(\lambda_{\rm peak})$, in different stellar mass bins. Figure 25 and Figure 26 show the behavior of $f_{\rm unobs}$ with redshift and stellar mass. Figure 27 and Figure 28 show the evolution of the dust-to-stellar mass ratio as well as its stellar mass dependence; note that the DTS calculations presume that there is no redshift evolution or mass dependence of $\kappa_{\rm FIR}$ as discussed in the main text.

STACKING PROCEDURE DETAILS

There are several possible approaches that have been used to stack IR/submm data in the literature. We specifically explore direct mean and median stacking (Schreiber *et al.* 2015), and a clustering-based approach to modeling the stacking signal (Kurczynski and Gawiser 2010; Viero *et al.* 2013, 2022; Béthermin *et al.* 2015b, 2017). The stacking methodology will change the results of the stacking in regimes where maps are dominated by confusion noise: large beamsizes and high source densities. In practice this is most significant in the *Herschel*/SPIRE bands, as detailed in many of the references above.

To fully test stacking techniques and their sensitivity to confusion noise and clustering we generate two sets of mock submillimeter images. The first set of maps use random positions to populate maps and are thus unclustered, while the second set of maps is built on the framework of a cosmological light cone and thus contains clustering.

The unclustered model maps are built on the framework presented in Casey *et al.* (2018) to generate the infrared luminosity function; the exact IRLF parameters are specified in Zavala *et al.* (2021) which also uses the same framework. Stellar masses are assigned to sources of a given IR luminosity working backward from the SFR-$M_\star$ relation (adopting the Speagle *et al.* 2014, model) following similar methodology to Long *et al.* (2023); scatter is added as inferred from the width of the SFR-$M_\star$ relation.

The clustered model builds on the Simulated Infrared Dusty Extragalactic Sky (SIDES) framework (Béthermin *et al.*

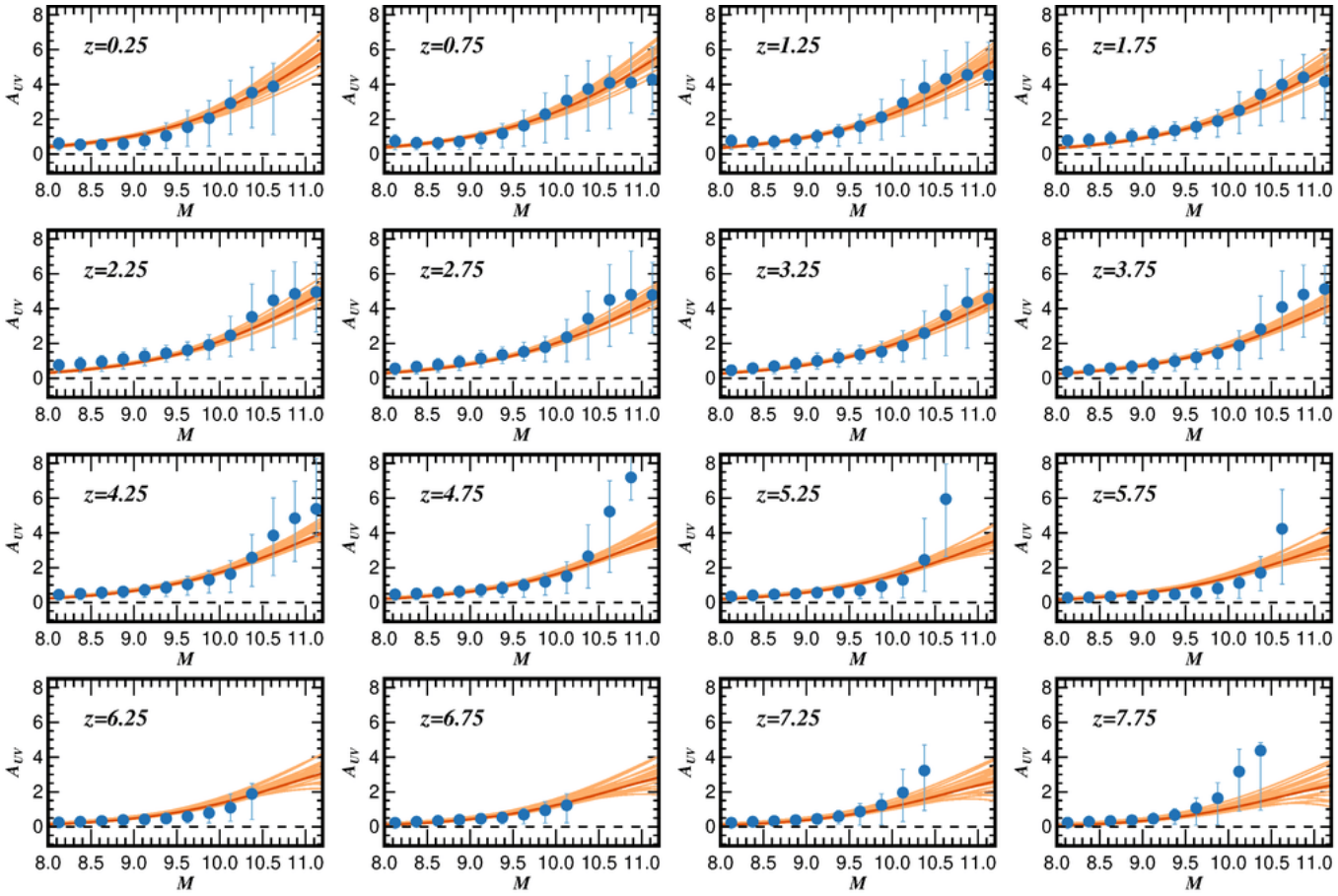

FIG. 22.— Redshift evolution of the A_{UV}-$M_\star$ relation as measured in our dataset (blue points with 68% confidence intervals on the sample distribution). Orange curves show the best-fit derived relation for $A_{UV}(z,M)$ (Eq. 11) fit jointly to all data points shown.

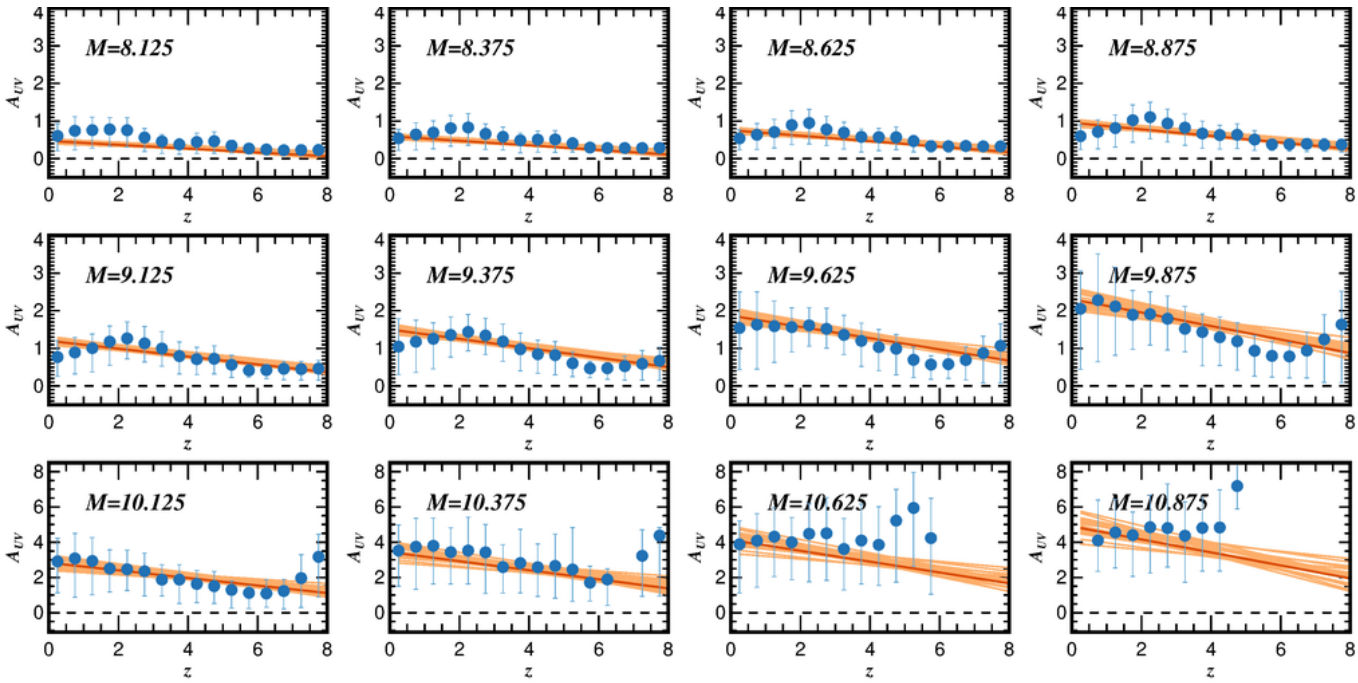

FIG. 23.— Stellar mass bins showing the redshift evolution of A_{UV} (blue points). Orange curves show best-fit model as given in Eq 11.

TABLE 1
SUMMARY OF EMPIRICAL RELATIONS DERIVED IN THIS WORK.

Relationship	Description & Parameters
Eq. 11: Attenuation	
$A_\lambda(z,M) = I(M) + S(M)(1+z)$ $I(M) = \frac{A_{\rm max}}{1+\exp(-k(M-M_0))}$ $S(M) = -\exp(b_0 + b_1 M)$	Applies to both $A_{\rm UV}(z,M)$ and $A_{\rm V}(z,M)$. The best-fit parameters for $A_{\rm UV}$: $A_{\rm max,UV} = 16.33^{+3.87}_{-3.00}$, $k = 0.970^{+0.073}_{-0.074}$, $M_0 = 11.652^{+0.191}_{-0.189}$, $b_0 = -8.84^{+1.31}_{-1.37}$, and $b_1 = 0.722^{+0.141}_{-0.143}$. The best-fit parameters for $A_{\rm V}$: $A_{\rm max,V} = 4.37^{+1.32}_{-0.96}$, $k = 0.932^{+0.085}_{-0.089}$, $M_0 = 11.675^{+0.201}_{-0.196}$, $b_0 = -9.94^{+1.47}_{-1.57}$, and $b_1 = 0.693^{+0.166}_{-0.163}$.
Eq. 12: Attenuation Slope	
$\langle\delta(z)\rangle = a + bz$	Best-fit parameters are: $a = -0.36 \pm 0.07$, and $b = 0.030 \pm 0.014$.
Eq. 14: Dust Temperature (Rest-Frame Peak Wavelength of Dust SED)	
$\log(\lambda_{\rm peak}/\mu{\rm m}) = a + b\,(M-10) + c\,\log(1+z)$	Best-fit parameters are: $a = 2.213 \pm 0.012$, $b = -0.035^{+0.007}_{-0.006}$, and $c = -0.531 \pm 0.022$.
Rest-Frame Peak Wavelength to Dust Temperature Conversion	
Optically-thin dust: $\log(T_{\rm dust}/K) = 3.462 - \log(\lambda_{\rm peak}/\mu{\rm m})$ **Generic Opacity (this work):** $\log(T_{\rm dust}/K) = 3.756 - 1.048\log(\lambda_{\rm peak}/\mu{\rm m})$	When a dust SED is measured, the observable quantity is $\log(\lambda_{\rm peak})$, the rest-frame peak wavelength. $\lambda_{\rm peak} \propto T_{\rm dust}^{-1}$ via Wien's Displacement Law. However, the exact mapping of modeled dust temperature to $\log(\lambda_{\rm peak})$ depends on the opacity of the dust throughout the IR. Caution should be used in comparing dust temperatures from different works that use different opacity assumptions; it is safest to use $\log(\lambda_{\rm peak})$ and understand how $T_{\rm dust}$ relates to the observable.
Eq. 15: Fraction of Star Formation that is Unobscured	
$\log(f_{\rm unobs})(z,M) = \mathcal{F}_0 - \log\left[1 + 10^{\,\alpha(z)(M-M_t(z))}\right]$ $\alpha(z) = \alpha_0 + \alpha_1\log(1+z)$ $M_t(z) = M_{t,0} + M_{t,1}\log(1+z)$	Best-fit parameters are: $\mathcal{F}_0 = -0.420^{+0.050}_{-0.047}$, $\alpha_0 = -0.206^{+0.128}_{-0.146}$, $\alpha_1 = 3.118^{+0.380}_{-0.288}$, $M_{t,0} = 8.198^{+0.159}_{-0.161}$, and $M_{t,1} = 2.197^{+0.154}_{-0.157}$.
Eq. 18: Dust-to-Stellar Mass Ratio	
$\log(M_{\rm dust}/M_\star)(z,M) = A + \eta_0\,(M-10) + \eta_1\,\log(1+z)$	Best-fit parameters are: $A = -3.237 \pm 0.036$, $\eta_0 = -0.296 \pm 0.023$, and $\eta_1 = 1.364 \pm 0.066$.
Eq. 20: Ratio of Dust Mass Absorption Coefficients UV-to-FIR	
$\log(\kappa_{\rm UV}/\kappa_{\rm FIR})(\Sigma_{\rm SFR}) = c_0 + c_1\,\log\Sigma_{\rm SFR}$	While this ratio shows clear redshift evolution and mass dependence, it shows a more direct relation to the inferred star formation surface density, $\Sigma_{\rm SFR}$. Best-fit parameters are: $c_0 = 10.79 \pm 0.50$, and $c_1 = -2.58 \pm 0.11$.

NOTE. — $M \equiv \log(M_\star/M_\odot)$ throughout. Parameter uncertainties represent 68% credible intervals from MCMC sampling.

2017) and uses the same $2\,{\rm deg}^2$ light cone produced from the Bolshoi-Planck cosmological simulation (Klypin *et al.* 2016; Rodríguez-Puebla *et al.* 2016). Béthermin *et al.* (2017) populated dark-matter halos using abundance matching (Vale and Ostriker 2004) and assigned various physical (luminous) properties to galaxies in the halos using the 2SFM model (Sargent *et al.* 2012; Béthermin *et al.* 2012, 2013). While the SIDES model itself has associated submillimeter maps, we note that SIDES has adopted a different IR SED convention than we have in this work. In order to directly test the impact of clustering alone, and not clustering *plus* the differences in IR SEDs, we use a uniform procedure for assigning flux densities to simulated sources. Thus we use the stellar masses and positions from the light cone, but reassign flux densities. We do note that the clustered model (473,500 sources) has about 50% more sources as the unclustered model (318,900 sources).

The IR emission associated with sources in the unclustered maps is generated using a tweak of the prescription given in Casey *et al.*; mainly, we introduce some redshift evolution of dust temperature towards higher redshifts following the Jones and Stanway (2023) meta-analysis with a characteristic scatter about the mean temperature of ∼20% (in line with observations of large samples at $z < 2$, Drew and Casey 2022). We note that this model is roughly in agreement with our final findings of the evolution of dust temperature with redshift in § 5.4. Monochromatic flux densities are then inferred from SEDs and injected into maps at each wavelength, then convolved with the observed beam as noted in Table 1 of Casey *et al.* (2018). Instrumental noise is added to match the observed dataset. In the *Herschel*/SPIRE bands, there is a strong positive skew to the flux distribution in the map from confusion noise; we then subtract the median value of the map to reset the pixel distribution about zero. This has minimal impact for highly significant emission and allows stacking to proceed with the expected results: a null result for stacking on blank sky. We note that SPIRE maps, by default, have the *mean* set to zero (not the median) so we shift the map to the median using offsets of 1.262 mJy, 1.202 mJy and 0.946 mJy at 250μm, 350μm, and 500μm, respectively.

We first present the results of random position stacks on the real maps, simulated unclustered maps, and simulated clustered maps in Figure 29. Within each mass and redshift bin we have stacked the same number of sources that exist in the real data, but scrambled their positions in the map such that they should probe blank portions of sky. Thus, the

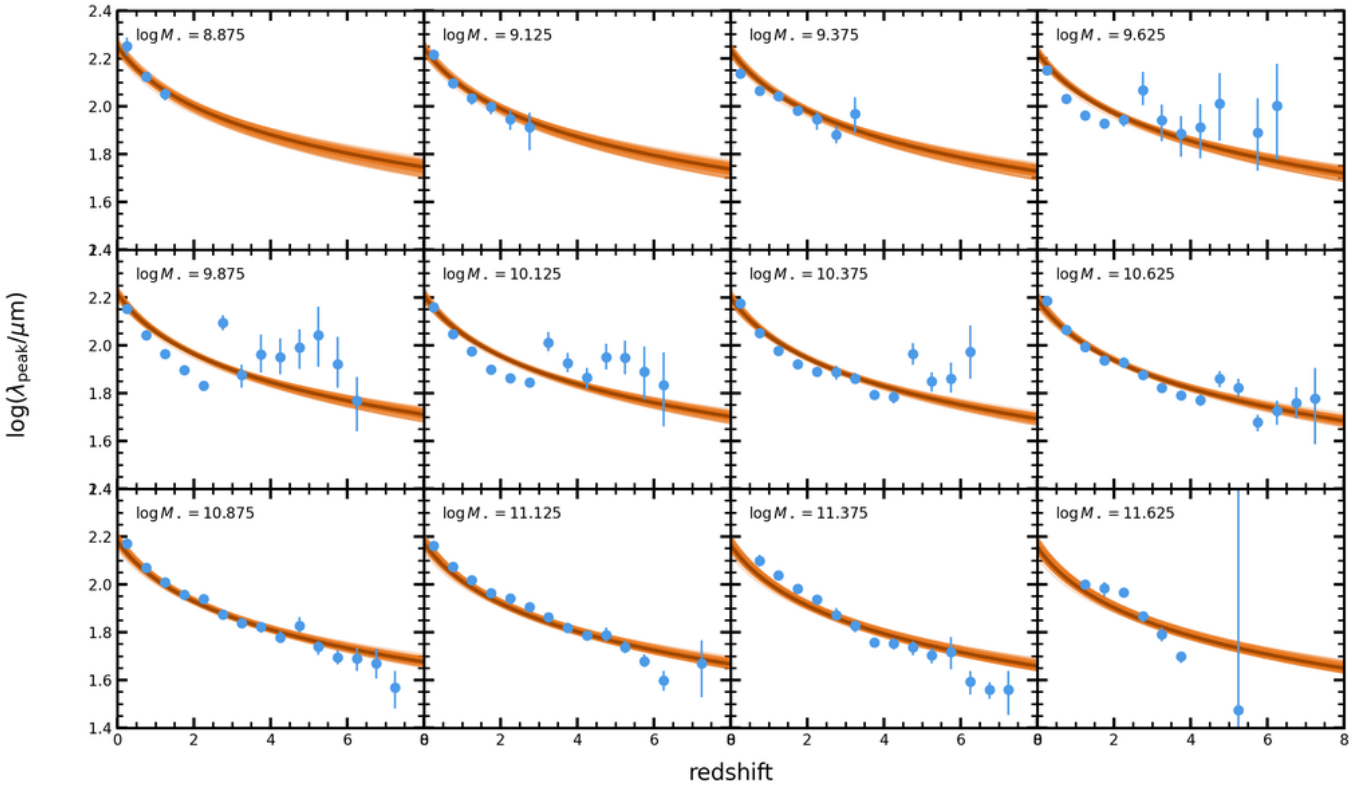

FIG. 24.— The evolution in dust temperature, as given by $\log(\lambda_{\rm peak})$, in stellar mass bins. Blue points show our data while orange shows the best-fit model from Eq. 14.

random stacks give us the intrinsic map background. As should be the case for random positions, there is no significant deviation from zero across all redshift and stellar mass bins at any wavelength. We note that SPIRE bands, due to their significant source confusion, do show slight deviations in the positive direction, even after median subtraction, though these deviations are well within the measurement uncertainty inferred through 100 different realization of stacking measurements over the same map.

We then proceed to analyze the input and output of median stacking measurements on the simulated maps to understand the impact of both confusion noise and clustering. We first investigate the ratio of measured output flux density to input flux density across all redshifts and stellar masses. Figure 30 shows the results. Within uncertainties, we see broad agreement with a flux ratio of unity, especially where the significance of real stacked detections is high ($>3\sigma$, solid lines). However, there are some regimes of greater concern. In the unclustered simulation, some of the lower mass bins in SPIRE 350μm or 500μm show significantly elevated output flux density ($\sim$2-4$\times$ input) from $0 < z < 2$. This is more significant in the clustered simulation, but extends to PACS 160μm and all of the SPIRE bands, with SPIRE 500μm the most severe, with 4$\times$ elevated flux density at $\sim 10^{9.3}$ M$_\odot$ and even higher, reaching $\sim$10$\times$ at $10^{8.5}$ M$_\odot$. We note that uncertainties on this ratio are quite large in the higher redshift bins: in this regime source numbers dwindle. We note that, despite large implied ratios of stacked flux to true input flux in this regime, *none* of the reported flux densities in the corresponding mass, redshift, wavelength bins are deemed statistically significant. In other words, only flux density limits are used to constrain the SED in this regime.

The deviation towards higher stacked flux densities than input is a result of how confusion-limited the maps are in the given mass regime – when stacking low mass galaxies with a very high source density and low expected flux density, the contribution of flux from other (brighter) sources within the beamsize becomes significant. If we are to recover true flux densities in this regime, we should divide the measured stacked flux by the measured ratio implied in Figure 30, in particular using the results from the clustered simulation. Indeed, the difference between non-clustered and clustered simulations should be caused by the relative clustering of low mass galaxies around higher mass galaxies which does not exist in the unclustered maps. This is the approach that Béthermin *et al.* (2015a) take; we overplot their measured clustering bias for galaxies (in their samples for galaxies with $M_\star > 3\times10^{10}$ M$_\odot$) as a solid black line on the bottom row of Figure 30; our clustered map results agree for the matched mass bins with the Béthermin *et al.* estimate of clustering bias. We infer a much larger clustering correction for lower mass galaxies, below the mass threshold fit in previous stacking analyses. However, an important note is that we infer much larger uncertainties on the ratio of output to input flux density than previous work suggests. In other words, we find the same clustering bias but at far less statistical significance. We attribute the difference in the significance of the clustering signal to be due to the differences between our SED model and that of SIDES: with greater dynamic range of SED shapes (ie. input dust temperatures thus input flux density distributions in a given mass and redshift bin), there is naturally far larger

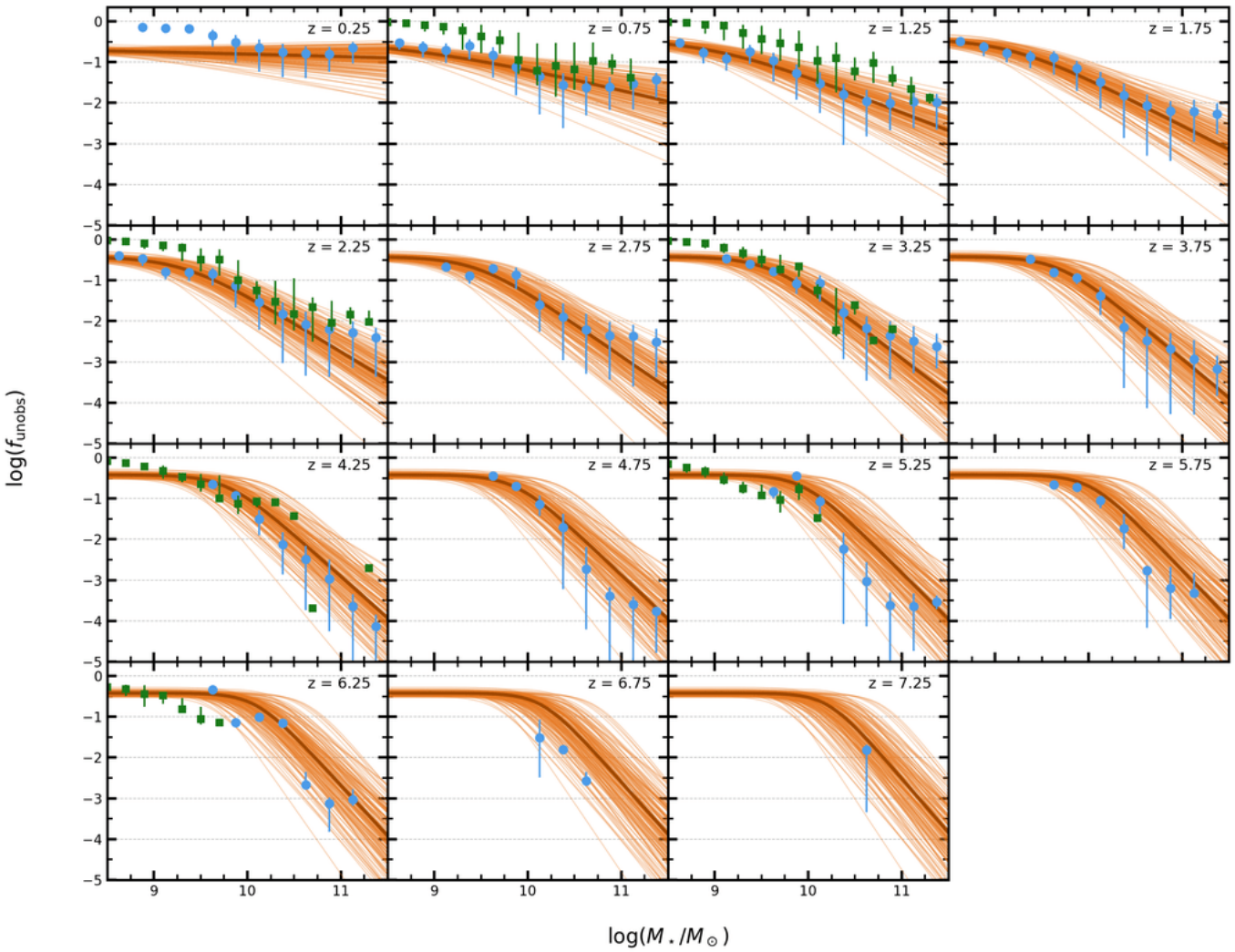

FIG. 25.— The fraction of star formation that is unobscured as a function of $M_\star$ in different redshift bins. Blue show our data and orange show the model fit jointly across all z, M bins simultaneously. Green points are drawn from hydrodynamic simulations in Zimmerman *et al.* (2024), showing clear redshift evolution that is more pronounced in higher redshift bins than lower redshift bins, and in agreement with the broad trend we observe in this dataset.

scatter in the resulting output stack measurement and associated uncertainty, as well as greater range in the input flux density. While it is a less tidy outcome, we feel this may better reflect the true range of SEDs present in the real universe.

Given the low significance of implied clustering bias inferred from our analysis, it is not entirely clear if the correction of clustering bias should be applied to our measured flux densities or not. To test the relative impact, we did a direct comparison of clustering-corrected flux densities to non-corrected flux densities, the impact on the best-fit SEDs and the scientific conclusions in this work overall. As per Figure 30, the most clustering-impacted regime is at low mass ($M_\star < 10^{9.5}$ $M_\odot$); beyond $z > 2$, the maximum SNR in this mass regime is $\approx 3\sigma$ across all PACS and SPIRE bands, but the stacks are primarily dominated by non-detections. We found that, given the inherently low SNR of the stacks and the uncertainty of the clustering correction factor, the clustering-corrected flux densities are statistically consistent with the original flux density measurements and have no resulting impact on the derived SED properties. One might think that the additional uncertainty introduced by the correction factor would change at least the uncertainty on the derived dust temperature, for example; however, the uncertainties on luminosity and dust temperature remain about the same with and without the correction because the clustering correction downweights the flux density while inflating the uncertainty, so the $\sim 2\sigma$ upper limits on non-detections is largely unchanged. Because we find that the clustering effect is, in the end, not impacting our conclusions and simultaneously is dependent on model assumptions for SEDs and HOD modeling, we decline to implement it in our flux density measurements to provide a more straightforward reporting of our direct measurements.

A full table of our measured flux density constraints in every redshift and mass bin shown in Figure 2 is given in Table 2. Note we only report flux densities for bins where dust SED fits have been measured: those with at least two $>3\sigma$ significant detections or one $>5\sigma$ detection. For illustrative purposes, we also show stacked cutouts in all mass and redshift bins at each wavelength in the following: Figure 31 (24μm), Figure 32 (100μm), Figure 33 (160μm),

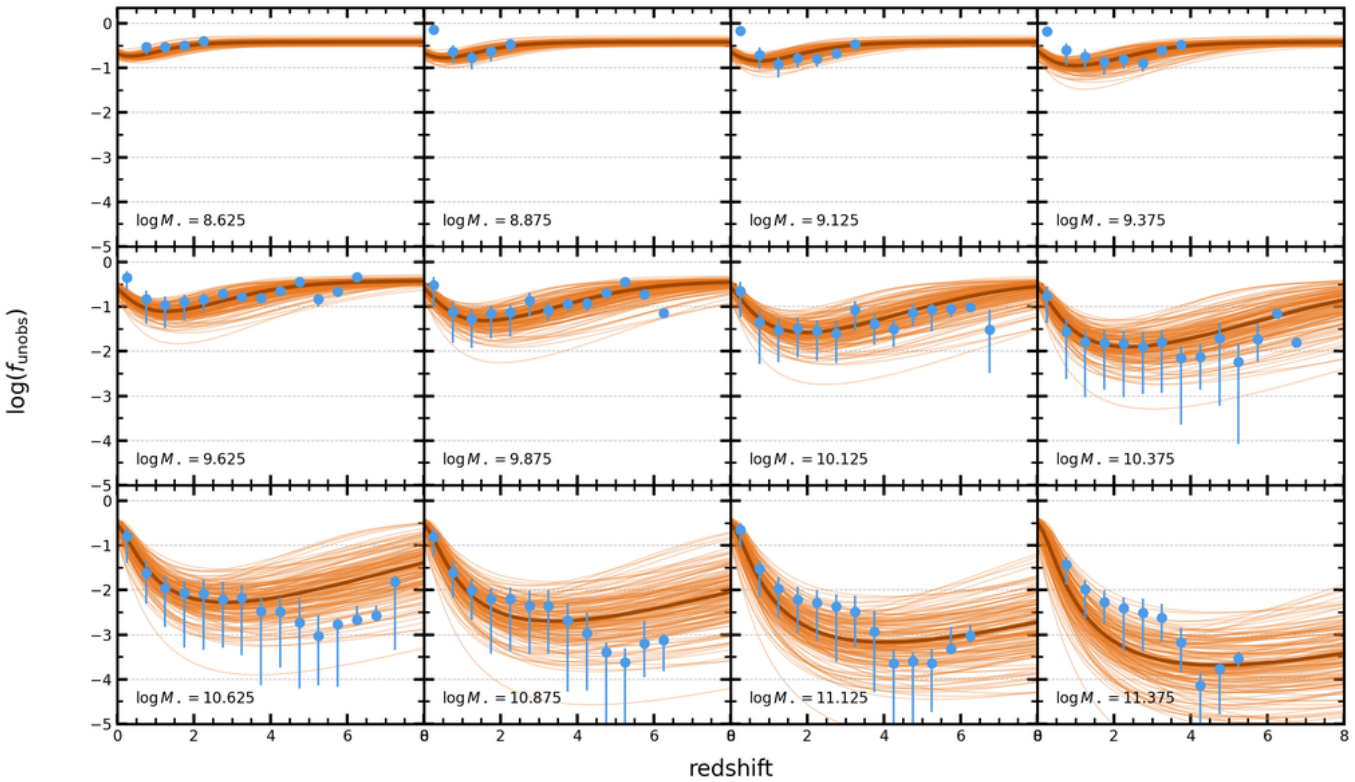

FIG. 26.— The fraction of star formation that is unobscured as a function of redshift. Blue show our data and orange show the best-fit model; one notes that the general trend is, at fixed stellar mass, that f_{unobs} drops precipitously from $0 < z < 2$ but then rises modestly at higher redshifts.

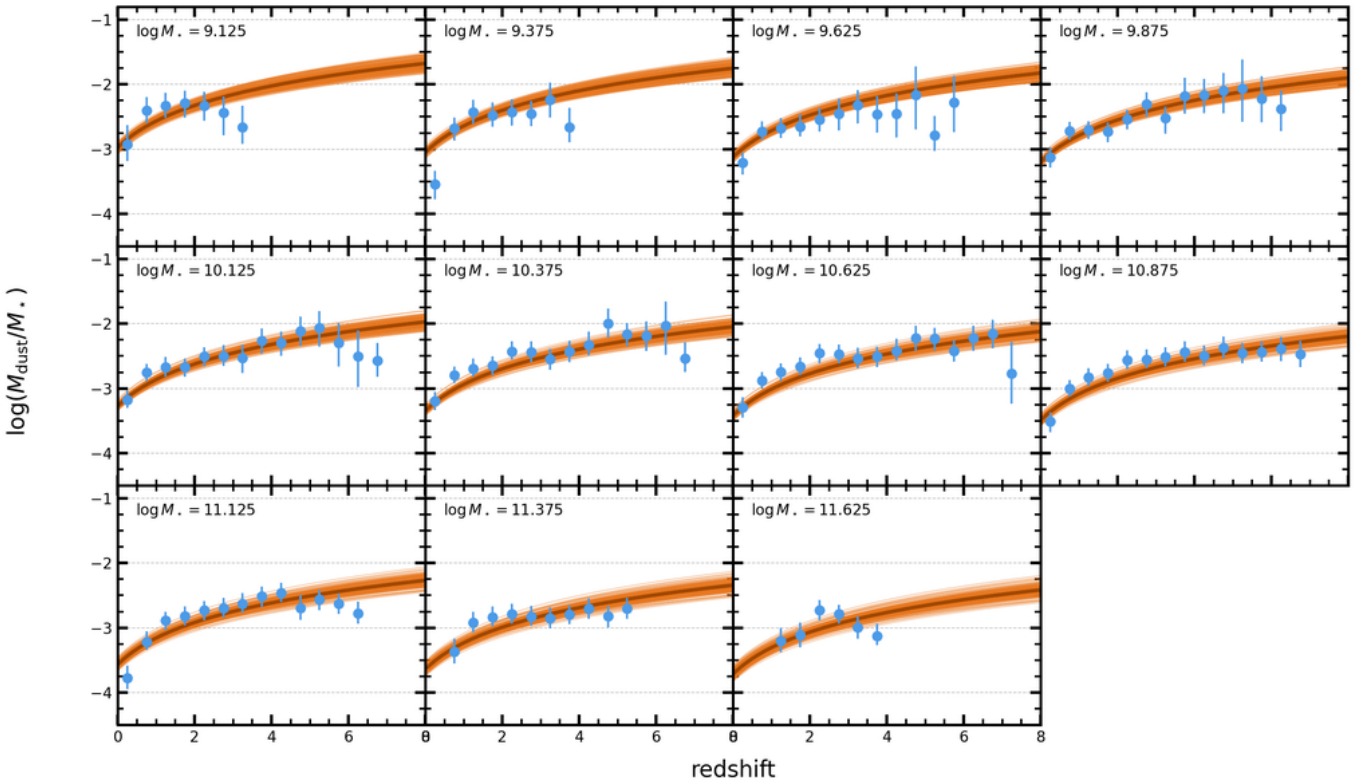

FIG. 27.— The evolution of the dust-to-stellar mass ratio assuming a fixed κ_{FIR}. Blue points show our data while orange shows the best-fit model from Eq. 18.

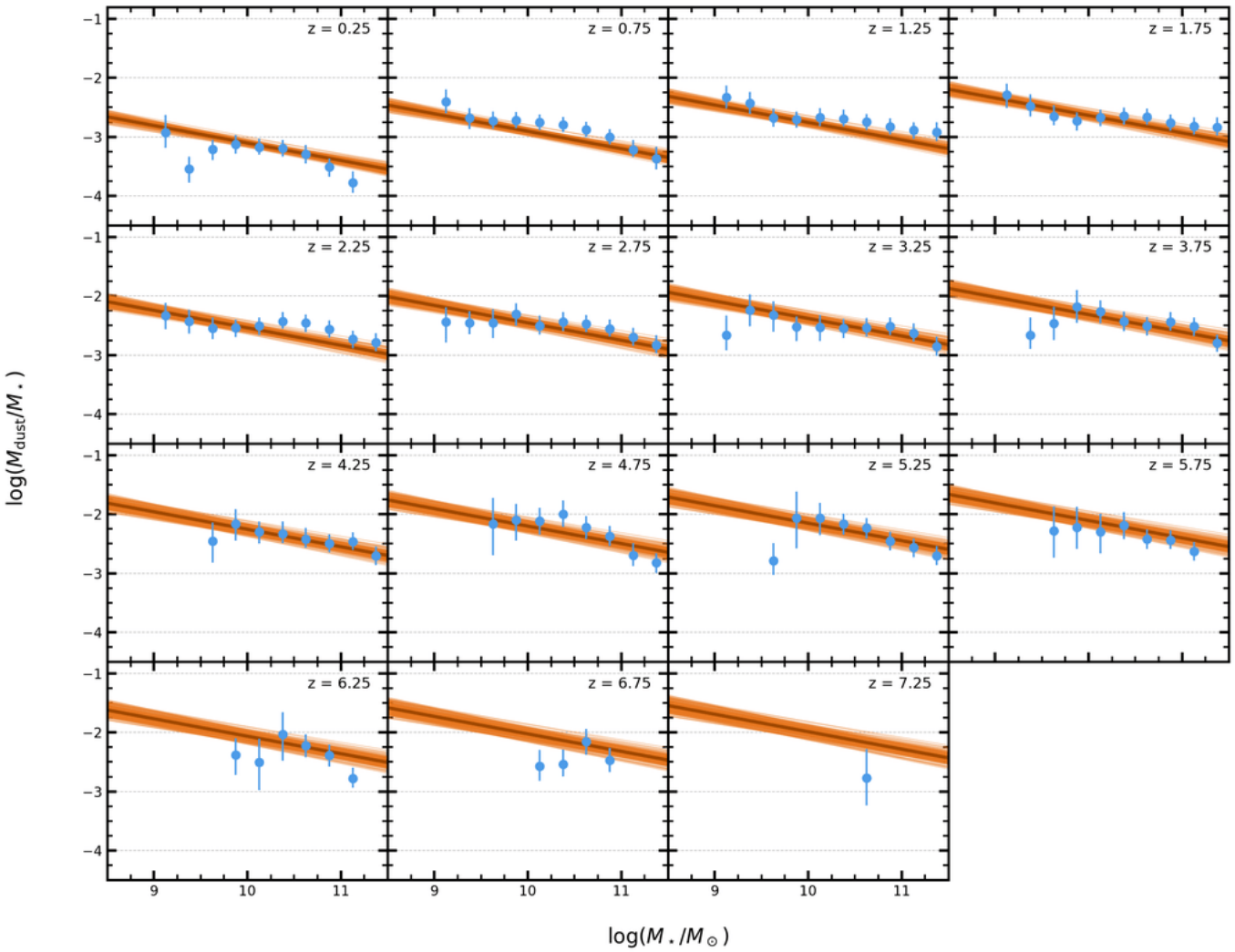

FIG. 28.— The stellar mass dependence of the dust-to-stellar mass ratio assuming a fixed $\kappa_{\rm FIR}$.

Figure 34 (250μm), Figure 35 (350μm), Figure 36 (500μm), Figure 37 (850μm), Figures 38 and 39 (1200μm from CHAMPS and 1300μm NIKA2, respectively), and Figures 40 and 41 (2100μm from Ex-MORA and 2000μm from NIKA2, respectively). Stacked 2D images are generated by shifting imaging on sub-pixel scales to center sources before median stacking. Bins with SED fits are outlined in thick black.

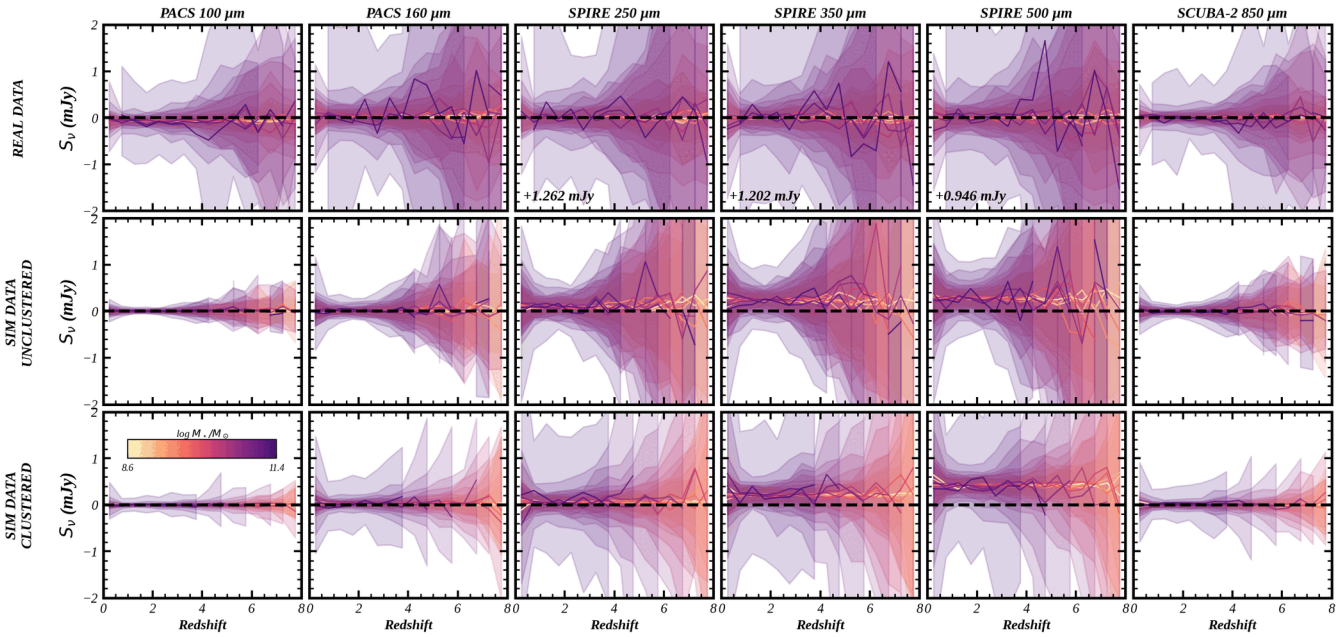

FIG. 29.— The measured stacked flux density in the real maps, simulated unclustered, and simulated clustered maps when sampling the same number of sources in the real data with scrambled, random positions. Median stacking on a median-subtracted map results in median flux density measurements of zero across all flux densities, redshifts and mass bins. What is important to gather from this plot is that the random stacking on simulated maps is analogous to the random stacking on real maps.

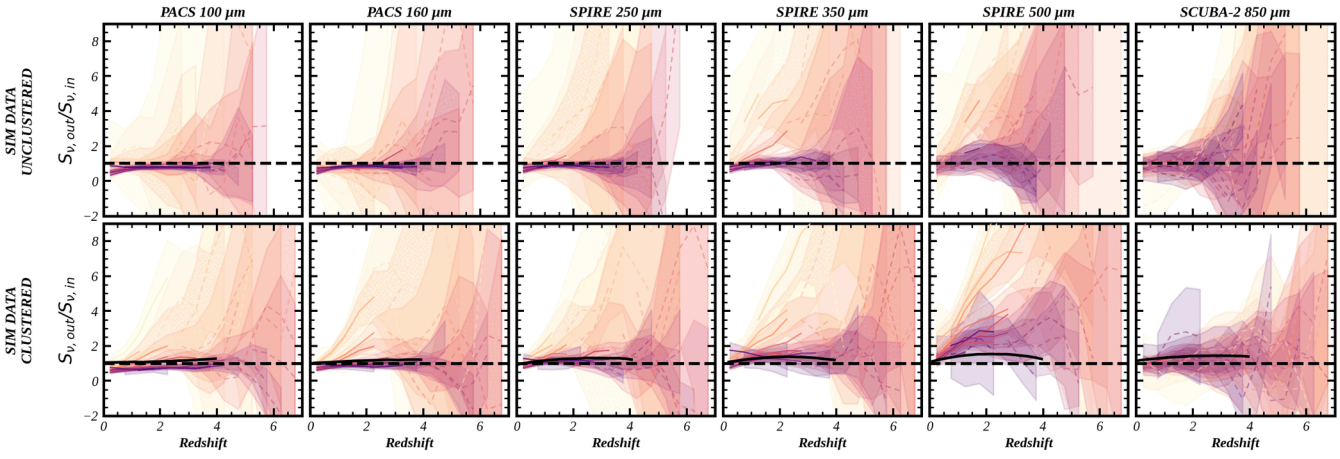

FIG. 30.— A comparison of output stacked flux density in redshift and mass bins relative to input flux density (median of the population in the same bin) across the unclustered (top row) and clustered (bottom row) simulations. Solid lines denote a regime (redshift and stellar masses) where the significance of the stacked result in the real maps is $>3\sigma$ and dashed lines indicate stacked flux densities $<3\sigma$. Within measurement uncertainties for $>3\sigma$ significant measurements, ratios are broadly consistent with unity, with some exception for the SPIRE bands at low mass (unclustered maps) or SPIRE and PACS 160μm maps in the clustered analysis. The solid black lines show the estimates of clustering bias from Béthermin *et al.* (2015b) for galaxies above stellar masses $> 3 \times 10^{10}$ $M_\odot$.

TABLE 2
MASTER STACKED FLUX DENSITIES.

z	$\log M_*$ ($M_\odot$)	N_F	N_1	N_2	N_{N1}	N_{N2}	S_{24} (mJy)	S_{100} (mJy)	S_{160} (mJy)	S_{250} (mJy)	S_{350} (mJy)	S_{500} (mJy)	S_{850} (mJy)	$S^{\rm CHAMPS}_{1.2\,mm}$ (mJy)	$S^{\rm NIKA2}_{1.3\,mm}$ (mJy)	$S^{\rm NIKA2}_{2.0\,mm}$ (mJy)	$S^{\rm ExMORA}_{2.1\,mm}$ (mJy)
0.25	9.125	4838	1873	1565	615	610	(0.039 ± 0.032)	0.282 ± 0.057	0.76 ± 0.12	(-0.55 ± 0.10)	(-0.38 ± 0.11)	(-0.293 ± 0.089)	0.066 ± 0.013	(0.0025 ± 0.0031)	(0.020 ± 0.021)	(0.0009 ± 0.0079)	(-0.0028 ± 0.0018)
0.25	9.375	3800	1472	1262	454	451	0.239 ± 0.046	0.672 ± 0.071	1.31 ± 0.14	(-0.11 ± 0.10)	(-0.05 ± 0.13)	(-0.11 ± 0.11)	0.074 ± 0.014	(0.0036 ± 0.0034)	(0.036 ± 0.021)	(0.001 ± 0.011)	(0.0016 ± 0.0019)
0.25	9.625	2843	1130	937	337	332	0.673 ± 0.072	1.28 ± 0.11	2.31 ± 0.18	0.98 ± 0.15	0.43 ± 0.14	(0.04 ± 0.12)	0.076 ± 0.016	0.0126 ± 0.0039	(0.041 ± 0.034)	(0.019 ± 0.011)	(0.0053 ± 0.0023)
0.25	9.875	2210	877	737	249	248	1.38 ± 0.16	1.99 ± 0.19	3.93 ± 0.29	2.40 ± 0.17	1.28 ± 0.17	0.45 ± 0.14	0.144 ± 0.019	0.0194 ± 0.0045	(0.042 ± 0.031)	(0.0156 ± 0.0089)	(0.0074 ± 0.0025)
0.25	10.125	1691	656	571	211	212	2.28 ± 0.24	2.83 ± 0.30	5.40 ± 0.36	3.85 ± 0.23	2.26 ± 0.17	0.98 ± 0.18	0.204 ± 0.021	0.0295 ± 0.0052	(0.154 ± 0.053)	(0.022 ± 0.010)	0.0106 ± 0.0029
0.25	10.375	1241	503	428	143	142	3.20 ± 0.28	3.63 ± 0.40	7.13 ± 0.54	6.10 ± 0.32	3.76 ± 0.24	1.76 ± 0.19	0.257 ± 0.025	0.0494 ± 0.0059	(0.083 ± 0.037)	(0.026 ± 0.017)	(0.0097 ± 0.0033)
0.25	10.625	788	319	288	99	98	4.23 ± 0.39	4.66 ± 0.62	9.41 ± 0.74	8.43 ± 0.46	5.57 ± 0.35	2.39 ± 0.30	0.390 ± 0.031	0.0543 ± 0.0074	(0.141 ± 0.060)	(0.040 ± 0.016)	0.0184 ± 0.0040
0.25	10.875	369	119	131	43	42	5.22 ± 0.94	5.62 ± 0.83	12.1 ± 1.1	10.23 ± 0.68	5.68 ± 0.51	2.55 ± 0.41	0.487 ± 0.046	0.060 ± 0.012	0.208 ± 0.065	(0.032 ± 0.028)	0.0249 ± 0.0061
0.25	11.125	122	40	39	8	8	(5.9 ± 3.1)	(6.6 ± 2.4)	12.5 ± 3.5	12.1 ± 2.0	6.5 ± 1.0	(1.84 ± 0.78)	0.494 ± 0.078	(0.052 ± 0.021)	(0.02 ± 0.32)	(0.063 ± 0.064)	(0.005 ± 0.011)
0.25	11.375	20	7	6	0	0	(4.8 ± 8.1)	(5 ± 13)	(11 ± 16)	(10.6 ± 7.4)	(5.5 ± 3.9)	(1.7 ± 1.9)	(0.60 ± 0.20)	(0.076 ± 0.049)	...	...	(0.006 ± 0.029)
0.75	9.125	14453	6053	4434	3015	3001	(-0.053 ± 0.013)	0.142 ± 0.024	0.557 ± 0.050	(-0.621 ± 0.056)	(-0.408 ± 0.070)	(-0.205 ± 0.055)	0.0448 ± 0.0074	(0.0040 ± 0.0017)	(0.011 ± 0.011)	(0.0026 ± 0.0033)	(0.0021 ± 0.0010)
0.75	9.375	11658	4882	3667	2550	2531	0.092 ± 0.016	0.318 ± 0.031	0.917 ± 0.060	(-0.216 ± 0.062)	(-0.043 ± 0.074)	(-0.008 ± 0.054)	0.0711 ± 0.0082	0.0071 ± 0.0019	(0.0028 ± 0.0094)	(0.0044 ± 0.0036)	0.0037 ± 0.0011
0.75	9.625	8867	3770	2807	1925	1916	0.391 ± 0.022	0.648 ± 0.044	1.521 ± 0.077	0.470 ± 0.076	0.492 ± 0.078	0.356 ± 0.081	0.0983 ± 0.0094	0.0112 ± 0.0022	0.047 ± 0.015	(0.0069 ± 0.0041)	0.0039 ± 0.0013
0.75	9.875	6610	2779	2065	1493	1487	0.875 ± 0.033	1.107 ± 0.062	2.381 ± 0.094	1.623 ± 0.090	1.20 ± 0.10	0.813 ± 0.095	0.152 ± 0.011	0.0172 ± 0.0025	0.060 ± 0.013	(0.0107 ± 0.0044)	0.0066 ± 0.0015
0.75	10.125	4745	2003	1528	1073	1066	1.521 ± 0.057	1.659 ± 0.093	3.55 ± 0.11	2.87 ± 0.12	2.06 ± 0.12	0.99 ± 0.11	0.232 ± 0.013	0.0337 ± 0.0029	0.064 ± 0.015	(0.0105 ± 0.0046)	0.0105 ± 0.0018
0.75	10.375	3451	1501	1161	825	815	2.320 ± 0.078	2.18 ± 0.10	4.70 ± 0.18	4.26 ± 0.15	3.05 ± 0.14	1.48 ± 0.12	0.294 ± 0.015	0.0612 ± 0.0034	0.077 ± 0.021	0.0189 ± 0.0048	0.0072 ± 0.0020
0.75	10.625	2391	1021	787	506	507	2.923 ± 0.097	2.51 ± 0.19	5.83 ± 0.23	5.96 ± 0.20	4.59 ± 0.15	2.07 ± 0.15	0.404 ± 0.018	0.0792 ± 0.0041	0.114 ± 0.024	0.0262 ± 0.0060	0.0117 ± 0.0025
0.75	10.875	1257	514	379	264	264	3.61 ± 0.17	3.08 ± 0.23	7.17 ± 0.40	7.89 ± 0.35	5.91 ± 0.25	2.87 ± 0.21	0.584 ± 0.025	0.0944 ± 0.0058	0.209 ± 0.024	(0.031 ± 0.013)	0.0199 ± 0.0036
0.75	11.125	438	173	119	79	79	4.15 ± 0.32	3.25 ± 0.36	8.13 ± 0.71	8.77 ± 0.54	6.89 ± 0.40	3.15 ± 0.43	0.633 ± 0.042	0.1161 ± 0.0099	(0.158 ± 0.071)	(0.027 ± 0.014)	(0.0112 ± 0.0065)
0.75	11.375	76	31	24	6	6	3.80 ± 0.81	2.96 ± 0.88	7.5 ± 1.9	9.5 ± 1.8	7.4 ± 1.3	3.7 ± 1.2	0.650 ± 0.098	0.122 ± 0.024	(0.07 ± 0.17)	(0.03 ± 0.11)	(0.014 ± 0.014)
1.25	9.125	18660	7558	5333	2780	2750	(-0.1024 ± 0.0090)	(0.065 ± 0.023)	0.364 ± 0.045	(-0.628 ± 0.046)	(-0.469 ± 0.049)	(-0.228 ± 0.065)	0.0531 ± 0.0066	0.0049 ± 0.0015	(0.0208 ± 0.0097)	(0.0025 ± 0.0030)	(0.00275 ± 0.00094)
1.25	9.375	15123	6120	4394	2113	2091	(0.008 ± 0.011)	0.165 ± 0.024	0.683 ± 0.047	(-0.292 ± 0.051)	(-0.159 ± 0.064)	(-0.040 ± 0.071)	0.0870 ± 0.0073	0.0081 ± 0.0017	(0.017 ± 0.014)	(-0.0039 ± 0.0035)	0.0033 ± 0.0010
1.25	9.625	11707	4796	3458	1623	1614	0.210 ± 0.013	0.356 ± 0.030	1.085 ± 0.058	(0.160 ± 0.066)	0.420 ± 0.074	0.368 ± 0.061	0.1272 ± 0.0083	0.0126 ± 0.0019	0.047 ± 0.015	(0.0067 ± 0.0047)	(0.0026 ± 0.0012)
1.25	9.875	8719	3600	2553	1154	1147	0.530 ± 0.019	0.657 ± 0.033	1.653 ± 0.068	0.991 ± 0.079	0.989 ± 0.082	0.796 ± 0.088	0.1704 ± 0.0096	0.0219 ± 0.0022	0.051 ± 0.016	(0.0095 ± 0.0058)	0.0041 ± 0.0014
1.25	10.125	6069	2607	1845	765	757	0.991 ± 0.033	1.006 ± 0.043	2.428 ± 0.092	1.97 ± 0.10	1.856 ± 0.098	1.155 ± 0.094	0.260 ± 0.011	0.0410 ± 0.0026	(0.054 ± 0.021)	0.0188 ± 0.0060	0.0075 ± 0.0016
1.25	10.375	4335	1922	1368	538	537	1.644 ± 0.041	1.360 ± 0.069	3.31 ± 0.11	3.13 ± 0.12	2.82 ± 0.13	1.62 ± 0.10	0.383 ± 0.013	0.0716 ± 0.0030	0.089 ± 0.022	0.0206 ± 0.0064	0.0100 ± 0.0019
1.25	10.625	3148	1401	954	398	390	2.219 ± 0.063	1.719 ± 0.078	4.26 ± 0.15	4.54 ± 0.16	4.24 ± 0.13	2.41 ± 0.14	0.522 ± 0.016	0.1064 ± 0.0035	0.199 ± 0.027	(0.023 ± 0.011)	0.0148 ± 0.0022
1.25	10.875	1835	842	532	249	243	2.895 ± 0.077	2.08 ± 0.11	5.06 ± 0.24	6.44 ± 0.20	6.08 ± 0.23	3.65 ± 0.17	0.740 ± 0.021	0.1445 ± 0.0046	0.232 ± 0.040	(0.027 ± 0.012)	0.0195 ± 0.0030
1.25	11.125	683	306	199	92	93	3.38 ± 0.15	2.32 ± 0.19	5.84 ± 0.43	7.91 ± 0.43	7.40 ± 0.43	4.67 ± 0.33	0.968 ± 0.034	0.2177 ± 0.0075	0.408 ± 0.050	0.075 ± 0.012	0.0288 ± 0.0050
1.25	11.375	122	57	42	7	7	3.52 ± 0.41	2.90 ± 0.58	8.2 ± 1.5	10.0 ± 1.5	10.2 ± 1.2	6.9 ± 1.1	1.350 ± 0.078	0.365 ± 0.017	0.88 ± 0.23	(0.14 ± 0.12)	0.041 ± 0.010
1.75	9.125	16963	6886	4690	3351	3338	(-0.1392 ± 0.0085)	(-0.016 ± 0.020)	0.227 ± 0.044	(-0.781 ± 0.048)	(-0.612 ± 0.058)	(-0.196 ± 0.056)	0.0920 ± 0.0069	(0.0046 ± 0.0016)	(0.019 ± 0.010)	(0.0011 ± 0.0026)	(0.0004 ± 0.0010)
1.75	9.375	13045	5283	3689	2554	2538	(-0.0559 ± 0.0098)	(0.051 ± 0.023)	0.435 ± 0.051	(-0.521 ± 0.059)	(-0.345 ± 0.067)	(0.028 ± 0.057)	0.1126 ± 0.0079	0.0074 ± 0.0018	(0.026 ± 0.010)	(0.0065 ± 0.0040)	(0.0018 ± 0.0011)
1.75	9.625	9704	3956	2800	1917	1905	0.068 ± 0.015	0.177 ± 0.029	0.718 ± 0.063	(-0.171 ± 0.068)	(0.028 ± 0.071)	0.298 ± 0.069	0.1438 ± 0.0091	0.0113 ± 0.0021	0.038 ± 0.012	(0.0076 ± 0.0038)	(0.0026 ± 0.0013)
1.75	9.875	6871	2851	1963	1328	1320	0.291 ± 0.021	0.393 ± 0.044	1.069 ± 0.072	0.267 ± 0.086	0.501 ± 0.093	0.600 ± 0.090	0.213 ± 0.011	0.0234 ± 0.0025	0.062 ± 0.015	(0.0142 ± 0.0047)	(0.0031 ± 0.0016)
1.75	10.125	4433	1926	1301	851	843	0.689 ± 0.027	0.660 ± 0.049	1.60 ± 0.11	1.04 ± 0.12	1.21 ± 0.12	1.166 ± 0.085	0.310 ± 0.013	0.0483 ± 0.0030	0.109 ± 0.018	0.0185 ± 0.0052	(0.0054 ± 0.0019)
1.75	10.375	2857	1289	867	558	556	1.250 ± 0.047	0.876 ± 0.065	2.37 ± 0.14	2.31 ± 0.14	2.51 ± 0.15	1.81 ± 0.13	0.457 ± 0.017	0.0783 ± 0.0037	0.135 ± 0.022	0.0294 ± 0.0071	0.0159 ± 0.0024
1.75	10.625	1984	916	599	416	411	1.893 ± 0.062	1.188 ± 0.075	3.20 ± 0.15	3.65 ± 0.20	4.00 ± 0.21	2.82 ± 0.20	0.648 ± 0.020	0.1267 ± 0.0043	0.219 ± 0.035	0.0449 ± 0.0083	0.0234 ± 0.0029
1.75	10.875	1227	596	385	293	293	2.561 ± 0.072	1.51 ± 0.11	4.14 ± 0.22	5.28 ± 0.21	5.46 ± 0.24	4.32 ± 0.24	0.887 ± 0.025	0.1876 ± 0.0054	0.319 ± 0.036	0.0624 ± 0.0096	0.0221 ± 0.0036
1.75	11.125	486	232	162	80	79	3.22 ± 0.14	2.08 ± 0.17	5.19 ± 0.37	7.30 ± 0.48	7.72 ± 0.55	6.06 ± 0.42	1.304 ± 0.040	0.2884 ± 0.0087	0.504 ± 0.074	0.078 ± 0.022	0.0351 ± 0.0055
1.75	11.375	94	45	35	8	8	4.49 ± 0.36	3.01 ± 0.48	8.5 ± 1.2	12.6 ± 1.4	12.4 ± 1.3	9.0 ± 1.1	2.174 ± 0.092	0.491 ± 0.019	(1.18 ± 0.47)	(0.154 ± 0.073)	0.056 ± 0.011
2.25	9.125	13762	5766	3847	2326	2302	(-0.1507 ± 0.0094)	(-0.033 ± 0.022)	0.218 ± 0.046	(-0.918 ± 0.063)	(-0.679 ± 0.060)	(-0.057 ± 0.062)	0.0952 ± 0.0076	(0.0041 ± 0.0017)	(0.029 ± 0.014)	(0.0065 ± 0.0037)	(0.0012 ± 0.0011)
2.25	9.375	10064	4267	2902	1806	1785	(-0.091 ± 0.011)	(-0.018 ± 0.029)	0.304 ± 0.065	(-0.666 ± 0.061)	(-0.409 ± 0.062)	0.243 ± 0.070	0.1215 ± 0.0089	0.0072 ± 0.0020	(0.039 ± 0.014)	(0.0035 ± 0.0039)	(0.0008 ± 0.0013)
2.25	9.625	7288	3109	2105	1372	1367	(0.013 ± 0.014)	(0.033 ± 0.036)	0.499 ± 0.064	(-0.384 ± 0.081)	(-0.115 ± 0.090)	0.582 ± 0.088	0.150 ± 0.010	0.0121 ± 0.0024	(0.041 ± 0.016)	(0.0120 ± 0.0046)	(0.0038 ± 0.0015)
2.25	9.875	5108	2184	1448	943	935	0.221 ± 0.018	0.255 ± 0.036	0.858 ± 0.094	(0.008 ± 0.090)	(0.27 ± 0.10)	0.84 ± 0.11	0.283 ± 0.012	0.0327 ± 0.0029	0.058 ± 0.016	0.0236 ± 0.0055	0.0084 ± 0.0018
2.25	10.125	3364	1438	948	692	687	0.569 ± 0.029	0.445 ± 0.046	1.30 ± 0.11	0.74 ± 0.14	1.11 ± 0.14	1.41 ± 0.13	0.485 ± 0.015	0.0727 ± 0.0035	0.111 ± 0.025	(0.0181 ± 0.0066)	0.0133 ± 0.0023
2.25	10.375	2091	898	613	445	440	0.984 ± 0.034	0.614 ± 0.058	1.70 ± 0.14	1.52 ± 0.17	2.09 ± 0.20	2.32 ± 0.19	0.698 ± 0.019	0.1260 ± 0.0045	0.259 ± 0.029	0.0469 ± 0.0067	0.0247 ± 0.0028
2.25	10.625	1272	540	388	301	299	1.480 ± 0.062	0.780 ± 0.079	2.00 ± 0.19	2.50 ± 0.24	3.51 ± 0.24	3.15 ± 0.24	0.989 ± 0.025	0.1946 ± 0.0058	0.300 ± 0.050	0.055 ± 0.011	0.0381 ± 0.0035
2.25	10.875	767	312	237	156	154	2.033 ± 0.089	1.02 ± 0.11	2.78 ± 0.25	3.76 ± 0.30	4.95 ± 0.34	3.88 ± 0.39	1.387 ± 0.032	0.2720 ± 0.0075	0.467 ± 0.064	0.087 ± 0.018	0.0471 ± 0.0045
2.25	11.125	356	143	116	68	68	2.61 ± 0.19	1.61 ± 0.19	3.98 ± 0.43	5.53 ± 0.56	7.42 ± 0.63	6.40 ± 0.59	2.043 ± 0.046	0.383 ± 0.011	(0.42 ± 0.14)	0.111 ± 0.032	0.0542 ± 0.0064
2.25	11.375	94	41	32	11	11	3.72 ± 0.52	2.68 ± 0.43	6.5 ± 1.1	10.1 ± 1.5	12.2 ± 1.3	9.8 ± 1.3	2.919 ± 0.090	0.577 ± 0.020	1.19 ± 0.36	0.211 ± 0.067	0.092 ± 0.012
2.75	9.375	7175	2825	2022	1130	1123	(-0.129 ± 0.021)	(-0.001 ± 0.033)	0.257 ± 0.063	(-0.715 ± 0.075)	(-0.572 ± 0.087)	(0.097 ± 0.089)	0.128 ± 0.011	0.0103 ± 0.0025	(0.009 ± 0.016)	(-0.0047 ± 0.0063)	(0.0010 ± 0.0015)
2.75	9.625	5435	2173	1467	890	880	(-0.054 ± 0.015)	(-0.008 ± 0.037)	0.379 ± 0.074	(-0.451 ± 0.090)	(-0.19 ± 0.10)	0.536 ± 0.098	0.168 ± 0.012	0.0190 ± 0.0028	(0.053 ± 0.018)	0.0172 ± 0.0053	(0.0033 ± 0.0018)
2.75	9.875	4179	1683	1185	651	644	0.071 ± 0.022	0.172 ± 0.046	0.842 ± 0.098	(-0.06 ± 0.10)	(0.19 ± 0.11)	0.82 ± 0.11	0.298 ± 0.014	0.0432 ± 0.0032	(0.061 ± 0.025)	(0.0125 ± 0.0075)	0.0084 ± 0.0020
2.75	10.125	3019	1182	862	410	404	0.258 ± 0.026	0.320 ± 0.044	1.13 ± 0.11	0.47 ± 0.13	1.10 ± 0.12	1.43 ± 0.15	0.499 ± 0.016	0.0780 ± 0.0039	0.121 ± 0.036	0.0266 ± 0.0083	0.0144 ± 0.0024
2.75	10.375	2039	781	590	277	274	0.537 ± 0.039	0.482 ± 0.059	1.29 ± 0.14	1.10 ± 0.15	1.92 ± 0.17	2.17 ± 0.18	0.734 ± 0.020	0.1441 ± 0.0048	0.180 ± 0.030	0.039 ± 0.012	0.0252 ± 0.0029
2.75	10.625	1242	470	383	133	133	0.956 ± 0.059	0.684 ± 0.083	1.83 ± 0.17	2.19 ± 0.22	3.02 ± 0.24	2.68 ± 0.25	1.052 ± 0.025	0.2337 ± 0.0062	0.236 ± 0.061	(0.039 ± 0.018)	0.0440 ± 0.0036
2.75	10.875	730	244	202	97	98	1.554 ± 0.099	0.90 ± 0.10	3.06 ± 0.26	3.74 ± 0.37	5.12 ± 0.33	3.84 ± 0.35	1.573 ± 0.034	0.3508 ± 0.0086	0.372 ± 0.097	0.075 ± 0.016	0.0647 ± 0.0049
2.75	11.125	376	121	106	37	37	2.11 ± 0.21	1.28 ± 0.20	3.87 ± 0.44	5.11 ± 0.50	6.69 ± 0.61	5.66 ± 0.57	2.115 ± 0.046	0.505 ± 0.012	(0.51 ± 0.19)	0.159 ± 0.043	0.0666 ± 0.0067
2.75	11.375	114	40	30	12	12	3.32 ± 0.46	2.17 ± 0.36	6.0 ± 1.0	6.7 ± 1.3	8.4 ± 1.2	8.0 ± 1.2	2.570 ± 0.083	0.720 ± 0.021	(0.47 ± 0.30)	(0.076 ± 0.070)	0.102 ± 0.012
3.25	9.375	5089	2030	1516	845	841	(-0.158 ± 0.028)	(-0.016 ± 0.041)	(0.030 ± 0.078)	(-0.858 ± 0.088)	(-0.85 ± 0.10)	(-0.26 ± 0.11)	0.115 ± 0.013	0.0132 ± 0.0029	(0.003 ± 0.019)	(0.0000 ± 0.0056)	(0.0034 ± 0.0018)
3.25	9.625	3720	1483	1064	638	628	(-0.135 ± 0.017)	(-0.024 ± 0.046)	(0.253 ± 0.098)	(-0.70 ± 0.11)	(-0.57 ± 0.12)	(0.03 ± 0.11)	0.164 ± 0.015	0.0242 ± 0.0034	(0.052 ± 0.027)	(0.0114 ± 0.0059)	(0.0033 ± 0.0021)
3.25	9.875	2791	1093	832	456	448	(-0.098 ± 0.024)	(0.035 ± 0.051)	0.681 ± 0.098	(-0.52 ± 0.12)	(-0.19 ± 0.14)	(0.38 ± 0.13)	0.259 ± 0.017	0.0408 ± 0.0040	(0.036 ± 0.027)	(0.0061 ± 0.0088)	(0.0058 ± 0.0024)
3.25	10.125	1908	726	580	352	347	(-0.007 ± 0.036)	0.192 ± 0.057	0.68 ± 0.12	(-0.08 ± 0.14)	(0.35 ± 0.16)	0.94 ± 0.17	0.423 ± 0.021	0.0602 ± 0.0049	0.177 ± 0.042	0.0349 ± 0.0097	0.0118 ± 0.0029
3.25	10.375	1241	458	384	230	230	0.161 ± 0.042	0.386 ± 0.080	0.81 ± 0.15	0.72 ± 0.19	1.76 ± 0.23	1.54 ± 0.23	0.633 ± 0.026	0.1221 ± 0.0061	(0.129 ± 0.056)	(0.018 ± 0.012)	0.0228 ± 0.0036
3.25	10.625	764	277	247	146	145	0.434 ± 0.064	0.59 ± 0.11	1.81 ± 0.25	2.13 ± 0.26	2.84 ± 0.30	2.38 ± 0.31	0.913 ± 0.033	0.2301 ± 0.0079	0.308 ± 0.053	0.055 ± 0.016	0.0458 ± 0.0045

TABLE 2 — *Continued*

z	$\log M_*$ ($M_\odot$)	N_F	N_1	N_2	N_{N1}	N_{N2}	S_{24} (mJy)	S_{100} (mJy)	S_{160} (mJy)	S_{250} (mJy)	S_{350} (mJy)	S_{500} (mJy)	S_{850} (mJy)	$S^{\rm CHAMPS}_{1.2\,mm}$ (mJy)	$S^{\rm NIKA2}_{1.3\,mm}$ (mJy)	$S^{\rm NIKA2}_{2.0\,mm}$ (mJy)	$S^{\rm ExMORA}_{2.1\,mm}$ (mJy)
3.25	10.875	456	156	127	89	89	0.85 ± 0.12	0.66 ± 0.13	2.99 ± 0.34	3.38 ± 0.40	4.38 ± 0.44	3.65 ± 0.39	1.510 ± 0.043	0.405 ± 0.010	0.547 ± 0.091	0.103 ± 0.022	0.0772 ± 0.0062
3.25	11.125	245	75	60	42	42	1.70 ± 0.19	0.99 ± 0.21	3.68 ± 0.53	4.71 ± 0.66	5.72 ± 0.69	5.31 ± 0.60	2.037 ± 0.058	0.634 ± 0.015	(0.76 ± 0.26)	(0.176 ± 0.060)	0.0960 ± 0.0088
3.25	11.375	80	19	15	12	12	3.33 ± 0.35	1.64 ± 0.40	5.7 ± 1.0	6.3 ± 1.4	8.2 ± 1.4	7.8 ± 1.4	2.23 ± 0.10	0.802 ± 0.029	0.83 ± 0.25	0.208 ± 0.044	0.101 ± 0.017
3.75	9.625	2354	932	723	393	391	(-0.153 ± 0.019)	(0.038 ± 0.050)	(0.18 ± 0.11)	(-0.90 ± 0.12)	(-0.60 ± 0.15)	(-0.34 ± 0.13)	0.137 ± 0.019	0.0245 ± 0.0043	(-0.005 ± 0.036)	(-0.0097 ± 0.0071)	(0.0038 ± 0.0026)
3.75	9.875	1697	641	499	290	288	(-0.127 ± 0.024)	(0.098 ± 0.062)	0.68 ± 0.14	(-0.60 ± 0.15)	(-0.04 ± 0.16)	(0.31 ± 0.18)	0.271 ± 0.022	0.0585 ± 0.0052	(0.074 ± 0.033)	(0.029 ± 0.013)	0.0114 ± 0.0031
3.75	10.125	1179	483	356	218	215	(-0.025 ± 0.033)	0.258 ± 0.068	0.80 ± 0.17	(0.07 ± 0.18)	(0.55 ± 0.22)	0.96 ± 0.22	0.503 ± 0.026	0.0981 ± 0.0060	0.161 ± 0.034	(0.022 ± 0.011)	0.0227 ± 0.0037
3.75	10.375	760	312	227	169	168	0.171 ± 0.054	0.54 ± 0.10	1.40 ± 0.23	1.55 ± 0.28	2.52 ± 0.32	2.17 ± 0.31	0.867 ± 0.033	0.1880 ± 0.0076	0.287 ± 0.029	0.058 ± 0.010	0.0397 ± 0.0046
3.75	10.625	459	191	133	83	83	0.392 ± 0.086	0.66 ± 0.14	2.41 ± 0.36	2.87 ± 0.43	3.68 ± 0.45	3.67 ± 0.39	1.298 ± 0.043	0.3341 ± 0.0094	0.407 ± 0.086	0.069 ± 0.019	0.0626 ± 0.0060
3.75	10.875	262	105	83	46	47	0.65 ± 0.14	(0.56 ± 0.19)	2.73 ± 0.39	3.38 ± 0.54	4.38 ± 0.59	3.94 ± 0.54	1.722 ± 0.055	0.545 ± 0.013	0.599 ± 0.091	0.129 ± 0.021	0.1024 ± 0.0075
3.75	11.125	127	43	35	25	25	1.39 ± 0.22	1.06 ± 0.29	3.91 ± 0.71	5.99 ± 0.85	7.08 ± 0.99	7.06 ± 0.80	2.497 ± 0.079	0.889 ± 0.020	(0.83 ± 0.28)	0.171 ± 0.042	0.157 ± 0.012
3.75	11.375	40	10	9	8	8	2.49 ± 0.46	2.49 ± 0.49	7.1 ± 1.3	11.0 ± 1.9	11.2 ± 2.0	10.3 ± 1.7	3.24 ± 0.15	1.189 ± 0.042	(1.38 ± 0.55)	(0.23 ± 0.10)	0.132 ± 0.023
4.25	9.625	1764	694	523	301	300	(-0.173 ± 0.022)	(-0.078 ± 0.067)	(0.10 ± 0.13)	(-0.92 ± 0.17)	(-0.69 ± 0.17)	(-0.26 ± 0.19)	0.163 ± 0.021	0.0160 ± 0.0051	(0.009 ± 0.033)	(0.001 ± 0.012)	(0.0068 ± 0.0030)
4.25	9.875	1161	460	347	188	186	(-0.138 ± 0.028)	(0.077 ± 0.076)	0.60 ± 0.17	(-0.75 ± 0.19)	(-0.10 ± 0.19)	(0.16 ± 0.23)	0.341 ± 0.026	0.0597 ± 0.0062	(0.057 ± 0.039)	(0.008 ± 0.013)	0.0167 ± 0.0037
4.25	10.125	718	320	228	114	112	(-0.022 ± 0.036)	(0.275 ± 0.098)	0.80 ± 0.24	(0.12 ± 0.26)	(0.85 ± 0.30)	(0.89 ± 0.30)	0.588 ± 0.033	0.1200 ± 0.0074	(0.108 ± 0.046)	(0.009 ± 0.016)	0.0229 ± 0.0046
4.25	10.375	414	205	133	51	51	(0.106 ± 0.073)	0.53 ± 0.13	1.50 ± 0.33	(1.12 ± 0.41)	2.08 ± 0.41	1.90 ± 0.38	0.921 ± 0.043	0.2515 ± 0.0094	(0.26 ± 0.11)	0.088 ± 0.029	0.0550 ± 0.0060
4.25	10.625	231	131	79	32	32	(0.31 ± 0.14)	0.62 ± 0.20	2.41 ± 0.54	2.33 ± 0.57	3.57 ± 0.64	3.86 ± 0.60	1.499 ± 0.057	0.402 ± 0.012	0.39 ± 0.12	0.092 ± 0.017	0.0788 ± 0.0077
4.25	10.875	109	55	39	20	20	(0.46 ± 0.19)	(0.45 ± 0.27)	3.13 ± 0.59	3.91 ± 0.75	4.53 ± 0.75	4.59 ± 0.83	1.973 ± 0.083	0.649 ± 0.018	(0.47 ± 0.28)	(0.100 ± 0.038)	0.107 ± 0.011
4.25	11.125	50	15	13	6	6	(0.85 ± 0.31)	(0.45 ± 0.42)	4.65 ± 0.93	7.3 ± 1.4	10.1 ± 1.5	8.5 ± 1.4	3.35 ± 0.13	1.258 ± 0.033	(1.50 ± 0.99)	(0.24 ± 0.23)	0.176 ± 0.019
4.25	11.375	18	4	5	1	1	1.79 ± 0.56	(1.06 ± 0.65)	7.0 ± 1.8	11.1 ± 2.8	11.2 ± 3.4	10.8 ± 3.3	3.99 ± 0.21	1.735 ± 0.062	...	...	0.113 ± 0.031
4.75	9.625	1219	481	364	206	203	(-0.192 ± 0.032)	(-0.080 ± 0.068)	(-0.00 ± 0.16)	(-0.88 ± 0.18)	(-0.76 ± 0.21)	(-0.31 ± 0.21)	0.133 ± 0.025	0.0203 ± 0.0059	(0.073 ± 0.044)	(0.033 ± 0.013)	(0.0081 ± 0.0036)
4.75	9.875	693	278	223	103	100	(-0.148 ± 0.048)	(-0.07 ± 0.10)	(0.40 ± 0.22)	(-0.81 ± 0.21)	(-0.42 ± 0.28)	(-0.32 ± 0.23)	0.273 ± 0.033	0.0555 ± 0.0077	(0.098 ± 0.043)	(0.006 ± 0.018)	0.0142 ± 0.0047
4.75	10.125	347	143	121	53	53	(-0.093 ± 0.046)	(-0.10 ± 0.14)	(0.04 ± 0.28)	(-0.67 ± 0.36)	(-0.05 ± 0.39)	(-0.03 ± 0.42)	0.650 ± 0.047	0.121 ± 0.011	0.40 ± 0.11	(0.042 ± 0.025)	(0.0174 ± 0.0064)
4.75	10.375	203	94	75	33	33	(-0.100 ± 0.053)	(-0.02 ± 0.18)	(-0.18 ± 0.32)	(-0.39 ± 0.40)	(0.85 ± 0.50)	(1.36 ± 0.49)	0.784 ± 0.060	0.242 ± 0.014	0.303 ± 0.099	0.112 ± 0.035	0.0602 ± 0.0080
4.75	10.625	129	68	48	27	27	(-0.051 ± 0.071)	(0.40 ± 0.22)	(0.94 ± 0.44)	(0.93 ± 0.47)	2.26 ± 0.65	2.66 ± 0.52	1.394 ± 0.075	0.399 ± 0.016	(0.57 ± 0.22)	0.110 ± 0.026	0.095 ± 0.010
4.75	10.875	81	38	24	17	17	(0.18 ± 0.15)	(0.03 ± 0.30)	2.33 ± 0.60	(1.40 ± 0.67)	4.49 ± 0.93	2.97 ± 0.86	2.346 ± 0.097	0.685 ± 0.022	1.22 ± 0.29	(0.159 ± 0.070)	0.104 ± 0.015
4.75	11.125	45	14	9	2	2	(0.35 ± 0.25)	(0.02 ± 0.41)	4.07 ± 0.98	4.3 ± 1.2	6.4 ± 1.2	4.5 ± 1.1	3.28 ± 0.14	1.022 ± 0.037	1.55 ± 0.44	0.299 ± 0.049	0.111 ± 0.023
4.75	11.375	13	1	2	0	0	(0.74 ± 0.35)	(1.45 ± 0.54)	5.5 ± 1.6	(4.5 ± 1.7)	8.0 ± 1.5	5.0 ± 1.5	3.42 ± 0.28	1.06 ± 0.13	...	...	(0.144 ± 0.048)
5.25	9.875	335	141	117	54	52	(-0.145 ± 0.075)	(0.06 ± 0.16)	(0.04 ± 0.29)	(-0.87 ± 0.33)	(-0.40 ± 0.38)	(-0.81 ± 0.37)	0.163 ± 0.047	0.047 ± 0.011	(0.045 ± 0.072)	(0.005 ± 0.025)	(0.0121 ± 0.0063)
5.25	10.125	162	73	64	24	24	(-0.203 ± 0.053)	(0.01 ± 0.21)	(-0.66 ± 0.39)	(-0.55 ± 0.51)	(0.02 ± 0.58)	(-0.25 ± 0.54)	0.559 ± 0.067	0.131 ± 0.015	0.42 ± 0.11	(-0.017 ± 0.056)	0.0307 ± 0.0085
5.25	10.375	94	43	34	21	20	(-0.145 ± 0.074)	(-0.10 ± 0.20)	(-0.59 ± 0.42)	(0.13 ± 0.59)	2.47 ± 0.61	2.20 ± 0.73	1.060 ± 0.091	0.284 ± 0.020	(0.34 ± 0.20)	(0.043 ± 0.031)	0.081 ± 0.012
5.25	10.625	73	40	27	16	16	(-0.000 ± 0.090)	(-0.47 ± 0.29)	(0.94 ± 0.63)	(1.18 ± 0.75)	2.79 ± 0.87	2.66 ± 0.79	1.753 ± 0.100	0.486 ± 0.021	0.80 ± 0.16	(0.089 ± 0.054)	0.107 ± 0.015
5.25	10.875	58	31	23	13	13	(0.30 ± 0.13)	(-0.10 ± 0.28)	3.16 ± 0.88	(2.9 ± 1.1)	4.3 ± 1.0	5.17 ± 0.97	2.70 ± 0.11	0.778 ± 0.024	(0.32 ± 0.27)	(0.128 ± 0.072)	0.131 ± 0.015
5.25	11.125	32	14	10	7	7	(0.41 ± 0.23)	(0.26 ± 0.38)	3.22 ± 0.97	(3.6 ± 1.3)	7.1 ± 1.3	6.8 ± 1.1	3.32 ± 0.15	1.090 ± 0.037	(1.11 ± 0.50)	(0.10 ± 0.14)	0.172 ± 0.020
5.25	11.375	9	3	4	1	1	(0.74 ± 0.46)	1.81 ± 0.52	(5.4 ± 2.0)	(5.6 ± 3.5)	(9.1 ± 4.5)	9.4 ± 2.4	5.36 ± 0.30	1.406 ± 0.080	...	...	0.313 ± 0.037
5.75	9.875	230	94	89	28	27	(-0.121 ± 0.058)	(-0.14 ± 0.18)	(0.16 ± 0.35)	(-0.54 ± 0.38)	(-0.01 ± 0.43)	(-0.21 ± 0.46)	0.375 ± 0.056	0.043 ± 0.013	(0.175 ± 0.085)	(0.003 ± 0.037)	(0.0182 ± 0.0074)
5.75	10.125	120	47	44	20	20	(-0.203 ± 0.076)	(0.17 ± 0.24)	(-0.20 ± 0.51)	(0.13 ± 0.59)	(0.15 ± 0.69)	(-0.14 ± 0.73)	0.522 ± 0.078	0.091 ± 0.019	(0.05 ± 0.16)	(0.007 ± 0.043)	(0.031 ± 0.010)
5.75	10.375	50	22	19	5	5	(-0.20 ± 0.12)	(0.11 ± 0.35)	(0.29 ± 0.61)	(-0.43 ± 0.76)	(0.32 ± 0.94)	(-0.09 ± 0.91)	1.05 ± 0.13	0.311 ± 0.028	(0.16 ± 0.92)	(-0.031 ± 0.017)	0.073 ± 0.016
5.75	10.625	36	21	15	4	4	(0.27 ± 0.19)	(-0.85 ± 0.39)	3.43 ± 0.92	(2.8 ± 1.1)	(3.2 ± 1.3)	(2.4 ± 1.3)	1.51 ± 0.15	0.667 ± 0.028	(0.5 ± 1.1)	(0.017 ± 0.098)	(0.054 ± 0.020)
5.75	10.875	31	19	13	4	4	(0.42 ± 0.22)	(-0.04 ± 0.37)	3.9 ± 1.1	(3.5 ± 1.4)	4.3 ± 1.4	6.0 ± 1.5	2.38 ± 0.15	0.916 ± 0.030	1.78 ± 0.16	(0.47 ± 0.19)	0.127 ± 0.019
5.75	11.125	18	12	7	3	3	(0.60 ± 0.34)	(0.94 ± 0.45)	(3.4 ± 1.3)	(3.5 ± 1.3)	8.2 ± 1.5	7.2 ± 1.3	3.28 ± 0.18	0.967 ± 0.037	1.54 ± 0.25	(-0.01 ± 0.13)	0.238 ± 0.024
6.25	9.625	297	118	93	63	61	(-0.147 ± 0.067)	(0.08 ± 0.14)	(0.28 ± 0.32)	(-0.54 ± 0.31)	(-0.31 ± 0.41)	(0.04 ± 0.39)	0.188 ± 0.052	(0.017 ± 0.012)	(0.140 ± 0.076)	(-0.002 ± 0.014)	0.0271 ± 0.0073
6.25	9.875	157	55	46	32	31	(-0.083 ± 0.083)	(0.05 ± 0.22)	(0.34 ± 0.45)	(0.65 ± 0.57)	(0.99 ± 0.58)	(0.91 ± 0.54)	0.459 ± 0.071	0.055 ± 0.017	(0.08 ± 0.17)	(0.041 ± 0.022)	(0.017 ± 0.011)
6.25	10.375	26	12	8	3	3	(-0.35 ± 0.24)	(-0.18 ± 0.59)	(0.47 ± 0.84)	(-1.9 ± 1.1)	(-1.6 ± 1.6)	(-0.1 ± 1.4)	0.63 ± 0.18	0.228 ± 0.040	(0.67 ± 0.95)	(0.046 ± 0.080)	(0.043 ± 0.025)
6.25	10.625	19	8	5	3	3	(-0.20 ± 0.27)	(-1.02 ± 0.41)	(2.6 ± 1.1)	(2.8 ± 1.2)	(3.2 ± 1.8)	(1.7 ± 1.1)	1.76 ± 0.22	1.016 ± 0.044	(1.7 ± 1.6)	(0.16 ± 0.26)	(0.019 ± 0.034)
6.25	10.875	17	9	3	3	3	(0.12 ± 0.63)	(0.42 ± 0.53)	(4.0 ± 3.0)	(3.1 ± 2.1)	(4.7 ± 1.7)	5.1 ± 1.2	2.31 ± 0.22	1.350 ± 0.041	(0.69 ± 0.58)	(0.23 ± 0.14)	(0.107 ± 0.037)
6.25	11.125	14	11	4	4	4	(1.06 ± 0.70)	(1.75 ± 0.96)	(4.3 ± 3.8)	(5.5 ± 4.1)	(8.8 ± 3.2)	10.3 ± 2.2	2.68 ± 0.23	0.977 ± 0.038	1.49 ± 0.39	(0.25 ± 0.16)	0.170 ± 0.033
6.75	10.625	10	3	2	2	2	(-0.23 ± 0.16)	(-1.02 ± 0.72)	(3.0 ± 1.2)	(-0.9 ± 2.0)	(5.0 ± 2.7)	(3.5 ± 1.4)	2.37 ± 0.27	0.789 ± 0.073	(0.69 ± 0.26)	(-0.09 ± 0.18)	(0.014 ± 0.068)
6.75	10.875	14	5	4	5	5	(0.34 ± 0.70)	(-0.39 ± 0.61)	(4.7 ± 3.3)	(0.1 ± 3.0)	(5.0 ± 2.3)	5.3 ± 1.5	2.18 ± 0.23	0.983 ± 0.063	(0.66 ± 0.57)	(0.04 ± 0.23)	0.127 ± 0.033

NOTE. — Median (sub)mm stacked flux densities (mJy) per redshift and stellar-mass bin in this work. Values in parentheses are $< 3\sigma$ detections. N_F: number of sources stacked maps that cover the entirety of COSMOS-Web; N_1: number of sources covered in CHAMPS (1.2 mm); N_2: ExMORA (2.1 mm); N_{N1}: NIKA2 (1.3 mm); N_{N2}: NIKA2 (2.0 mm). This table is available online in fits format at https://github.com/caitlinmcasey/duststacks.

TABLE 3
Derived SED Physical Properties.

z	$\log M_*$ ($M_\odot$)	$L_{\rm IR}$ ($L_\odot$)	$\lambda_{\rm peak}$ (μm)	$\alpha_{\rm MIR}$	$\beta_{\rm IR}$	$M_{\rm dust}$ ($M_\odot$)	SFR$_{\rm UV}$ ($M_\odot$ yr^{-1})	SFR$_{\rm IR}$ ($M_\odot$ yr^{-1})	$f_{\rm unobs}$	B'	$A_{\rm UV}$ (mag)	A_V (mag)
0.25	9.125	$(4.21^{+1.27}_{-0.76})\times10^{8}$	$164.2^{+8.6}_{-8.6}$	$4.90^{+0.10}_{-0.06}$	–	$(1.58^{+0.92}_{-0.48})\times10^{6}$	$0.13^{+0.13}_{-0.07}$	$0.062^{+0.015}_{-0.010}$	$(6.75^{+1.35}_{-1.08})\times10^{-1}$	$1.43^{+0.22}_{-0.24}$	$0.80^{+0.41}_{-0.55}$	$0.26^{+0.15}_{-0.18}$
0.25	9.375	$(5.80^{+1.12}_{-0.81})\times10^{8}$	$136.9^{+4.5}_{-4.2}$	$4.92^{+0.08}_{-0.05}$	–	$(6.80^{+1.90}_{-1.80})\times10^{5}$	$0.17^{+0.27}_{-0.09}$	$0.086^{+0.013}_{-0.012}$	$(6.69^{+1.67}_{-1.28})\times10^{-1}$	$1.47^{+0.29}_{-0.31}$	$1.11^{+0.67}_{-0.86}$	$0.38^{+0.24}_{-0.30}$
0.25	9.625	$(1.77^{+0.13}_{-0.11})\times10^{9}$	$141.1^{+1.4}_{-3.7}$	–	$1.97^{+0.10}_{-0.12}$	$(2.59^{+0.37}_{-0.44})\times10^{6}$	$0.21^{+0.49}_{-0.11}$	$0.26^{+0.02}_{-0.02}$	$(4.46^{+1.74}_{-2.48})\times10^{-1}$	$1.49^{+0.43}_{-0.28}$	$1.64^{+0.94}_{-1.27}$	$0.56^{+0.36}_{-0.44}$
0.25	9.875	$(3.61^{+0.27}_{-0.28})\times10^{9}$	$142.3^{+2.0}_{-3.7}$	$4.93^{+0.07}_{-0.04}$	$1.96^{+0.07}_{-0.11}$	$(5.55^{+0.80}_{-0.64})\times10^{6}$	$0.23^{+0.44}_{-0.16}$	$0.52^{+0.03}_{-0.02}$	$(3.08^{+1.47}_{-2.43})\times10^{-1}$	$1.45^{+0.56}_{-0.30}$	$2.2^{+1.0}_{-1.7}$	$0.73^{+0.37}_{-0.60}$
0.25	10.125	$(5.57^{+0.20}_{-0.45})\times10^{9}$	$144.1^{+2.5}_{-2.8}$	$4.90^{+0.10}_{-0.05}$	$2.01^{+0.07}_{-0.12}$	$(8.94^{+0.94}_{-0.53})\times10^{6}$	$0.24^{+0.56}_{-0.14}$	$0.81^{+0.06}_{-0.04}$	$(2.26^{+1.47}_{-1.66})\times10^{-1}$	$1.33^{+0.56}_{-0.45}$	$2.8^{+1.2}_{-1.8}$	$0.89^{+0.47}_{-0.58}$
0.25	10.375	$(7.96^{+0.47}_{-0.59})\times10^{9}$	$150.1^{+2.9}_{-4.2}$	$4.80^{+0.14}_{-0.10}$	$2.08^{+0.08}_{-0.08}$	$(1.52^{+0.16}_{-0.13})\times10^{7}$	$0.25^{+0.55}_{-0.15}$	$1.2^{+0.1}_{-0.1}$	$(1.72^{+0.97}_{-1.50})\times10^{-1}$	$1.20^{+0.43}_{-0.57}$	$3.3^{+1.1}_{-1.9}$	$1.03^{+0.46}_{-0.65}$
0.25	10.625	$(1.04^{+0.10}_{-0.07})\times10^{10}$	$154.0^{+4.3}_{-5.8}$	$4.73^{+0.18}_{-0.14}$	$2.20^{+0.08}_{-0.10}$	$(2.16^{+0.27}_{-0.28})\times10^{7}$	$0.29^{+0.53}_{-0.18}$	$1.5^{+0.1}_{-0.1}$	$(1.59^{+0.97}_{-1.18})\times10^{-1}$	$1.16^{+0.46}_{-0.53}$	$3.6^{+1.1}_{-1.8}$	$1.15^{+0.44}_{-0.69}$
0.25	10.875	$(1.29^{+0.08}_{-0.10})\times10^{10}$	$147.9^{+4.1}_{-4.5}$	$4.81^{+0.18}_{-0.07}$	$2.06^{+0.10}_{-0.09}$	$(2.30^{+0.27}_{-0.29})\times10^{7}$	$0.36^{+0.44}_{-0.21}$	$1.9^{+0.2}_{-0.1}$	$(1.59^{+0.70}_{-1.15})\times10^{-1}$	$1.21^{+0.39}_{-0.58}$	$3.9^{+1.3}_{-1.5}$	$1.30^{+0.54}_{-0.63}$
0.25	11.125	$(1.33^{+0.28}_{-0.18})\times10^{10}$	$145.2^{+6.7}_{-6.7}$	$4.70^{+0.29}_{-0.13}$	–	$(2.25^{+0.51}_{-0.39})\times10^{7}$	$0.58^{+0.64}_{-0.38}$	$2.0^{+0.4}_{-0.2}$	$(2.24^{+0.69}_{-1.71})\times10^{-1}$	$1.22^{+0.28}_{-0.64}$	$4.1^{+1.2}_{-1.3}$	$1.42^{+0.66}_{-0.35}$
0.75	9.125	$(5.80^{+0.50}_{-0.83})\times10^{9}$	$124.8^{+2.8}_{-5.1}$	$4.93^{+0.07}_{-0.04}$	–	$(5.30^{+1.45}_{-1.14})\times10^{6}$	$0.21^{+0.28}_{-0.11}$	$0.84^{+0.09}_{-0.09}$	$(1.97^{+0.83}_{-1.21})\times10^{-1}$	$1.25^{+0.24}_{-0.31}$	$0.85^{+0.39}_{-0.58}$	$0.26^{+0.11}_{-0.17}$
0.75	9.375	$(5.64^{+0.93}_{-0.44})\times10^{9}$	$116.3^{+2.4}_{-3.4}$	–	$1.57^{+0.18}_{-0.14}$	$(4.94^{+0.81}_{-0.93})\times10^{6}$	$0.28^{+0.43}_{-0.15}$	$0.83^{+0.08}_{-0.13}$	$(2.52^{+1.10}_{-1.41})\times10^{-1}$	$1.23^{+0.26}_{-0.41}$	$1.15^{+0.54}_{-0.85}$	$0.34^{+0.17}_{-0.25}$
0.75	9.625	$(1.35^{+0.08}_{-0.07})\times10^{10}$	$107.6^{+1.6}_{-1.4}$	–	$1.53^{+0.06}_{-0.06}$	$(7.81^{+1.23}_{-0.49})\times10^{6}$	$0.34^{+0.63}_{-0.19}$	$2.0^{+0.1}_{-0.1}$	$(1.48^{+0.94}_{-1.05})\times10^{-1}$	$1.23^{+0.32}_{-0.49}$	$1.60^{+0.81}_{-1.21}$	$0.48^{+0.31}_{-0.36}$
0.75	9.875	$(3.14^{+0.19}_{-0.17})\times10^{10}$	$110.3^{+1.5}_{-2.4}$	–	$1.96^{+0.08}_{-0.06}$	$(1.42^{+0.14}_{-0.09})\times10^{7}$	$0.38^{+0.87}_{-0.23}$	$4.6^{+0.3}_{-0.2}$	$(7.61^{+5.22}_{-6.83})\times10^{-2}$	$1.20^{+0.38}_{-0.54}$	$2.2^{+1.1}_{-1.6}$	$0.67^{+0.40}_{-0.52}$
0.75	10.125	$(5.23^{+0.18}_{-0.37})\times10^{10}$	$111.6^{+0.7}_{-2.6}$	$4.91^{+0.08}_{-0.06}$	$2.04^{+0.08}_{-0.06}$	$(2.37^{+0.18}_{-0.19})\times10^{7}$	$0.36^{+0.89}_{-0.24}$	$7.7^{+0.4}_{-0.3}$	$(4.50^{+3.53}_{-4.19})\times10^{-2}$	$1.09^{+0.40}_{-0.50}$	$2.8^{+1.2}_{-1.9}$	$0.86^{+0.50}_{-0.61}$
0.75	10.375	$(7.65^{+0.33}_{-0.27})\times10^{10}$	$112.8^{+1.9}_{-2.5}$	$4.83^{+0.13}_{-0.04}$	$1.98^{+0.09}_{-0.07}$	$(3.76^{+0.31}_{-0.20})\times10^{7}$	$0.32^{+0.95}_{-0.20}$	11^{+1}_{-1}	$(2.83^{+2.63}_{-2.55})\times10^{-2}$	$0.96^{+0.44}_{-0.43}$	$3.4^{+1.5}_{-1.7}$	$1.01^{+0.48}_{-0.65}$
0.75	10.625	$(9.81^{+0.53}_{-0.46})\times10^{10}$	$116.5^{+2.2}_{-2.7}$	$4.70^{+0.20}_{-0.08}$	$2.06^{+0.06}_{-0.09}$	$(5.62^{+0.44}_{-0.37})\times10^{7}$	$0.35^{+0.84}_{-0.21}$	$14^{+1.0}_{-1}$	$(2.39^{+1.86}_{-2.12})\times10^{-2}$	$0.89^{+0.46}_{-0.34}$	$3.6^{+1.5}_{-1.5}$	$1.07^{+0.48}_{-0.61}$
0.75	10.875	$(1.25^{+0.04}_{-0.06})\times10^{11}$	$117.5^{+2.4}_{-3.0}$	$4.70^{+0.12}_{-0.13}$	$2.05^{+0.10}_{-0.05}$	$(7.46^{+0.56}_{-0.50})\times10^{7}$	$0.46^{+0.85}_{-0.25}$	$18^{+1.4}_{-1}$	$(2.51^{+1.56}_{-2.12})\times10^{-2}$	$0.89^{+0.47}_{-0.33}$	$3.8^{+1.4}_{-1.4}$	$1.12^{+0.44}_{-0.65}$
0.75	11.125	$(1.35^{+0.09}_{-0.11})\times10^{11}$	$118.5^{+3.5}_{-2.8}$	$4.66^{+0.19}_{-0.10}$	$2.10^{+0.09}_{-0.09}$	$(8.08^{+1.29}_{-0.48})\times10^{7}$	$0.62^{+0.79}_{-0.37}$	$20^{+1.3}_{-1.2}$	$(3.03^{+1.74}_{-2.31})\times10^{-2}$	$0.96^{+0.43}_{-0.40}$	$4.0^{+1.3}_{-1.2}$	$1.26^{+0.40}_{-0.69}$
0.75	11.375	$(1.25^{+0.26}_{-0.15})\times10^{11}$	$125.8^{+7.3}_{-7.2}$	$4.50^{+0.33}_{-0.26}$	$2.21^{+0.19}_{-0.16}$	$(1.02^{+0.27}_{-0.18})\times10^{8}$	$0.72^{+1.1}_{-0.37}$	$19^{+2.9}_{-2.2}$	$(3.67^{+2.09}_{-2.31})\times10^{-2}$	$1.43^{+0.30}_{-0.69}$	$3.88^{+1.30}_{-0.55}$	$1.42^{+0.23}_{-0.39}$
1.25	9.125	$(1.58^{+0.31}_{-0.29})\times10^{10}$	$108.2^{+4.8}_{-6.7}$	–	$2.22^{+0.39}_{-0.32}$	$(6.29^{+1.54}_{-1.25})\times10^{6}$	$0.33^{+0.39}_{-0.18}$	$2.1^{+0.4}_{-0.3}$	$(1.35^{+0.49}_{-0.82})\times10^{-1}$	$1.07^{+0.19}_{-0.29}$	$0.97^{+0.38}_{-0.63}$	$0.271^{+0.100}_{-0.157}$
1.25	9.375	$(1.36^{+0.23}_{-0.19})\times10^{10}$	$110.6^{+4.2}_{-4.2}$	$4.94^{+0.06}_{-0.03}$	$1.83^{+0.18}_{-0.21}$	$(8.78^{+2.15}_{-1.44})\times10^{6}$	$0.44^{+0.63}_{-0.23}$	$1.9^{+0.3}_{-0.2}$	$(1.86^{+0.80}_{-1.10})\times10^{-1}$	$1.00^{+0.21}_{-0.28}$	$1.24^{+0.50}_{-0.76}$	$0.34^{+0.13}_{-0.19}$
1.25	9.625	$(2.95^{+0.22}_{-0.25})\times10^{10}$	$91.6^{+1.9}_{-0.9}$	$4.96^{+0.03}_{-0.05}$	$1.51^{+0.11}_{-0.12}$	$(8.80^{+1.21}_{-0.85})\times10^{6}$	$0.54^{+0.89}_{-0.29}$	$4.4^{+0.5}_{-0.2}$	$(1.08^{+0.64}_{-0.76})\times10^{-1}$	$0.97^{+0.25}_{-0.28}$	$1.59^{+0.68}_{-0.97}$	$0.42^{+0.20}_{-0.27}$
1.25	9.875	$(7.33^{+0.55}_{-0.28})\times10^{10}$	$92.3^{+2.2}_{-0.8}$	$4.92^{+0.07}_{-0.04}$	$2.01^{+0.06}_{-0.14}$	$(1.49^{+0.11}_{-0.14})\times10^{7}$	$0.60^{+1.1}_{-0.36}$	11^{+1}_{-0}	$(5.38^{+3.25}_{-4.76})\times10^{-2}$	$0.96^{+0.36}_{-0.31}$	$2.1^{+1.0}_{-1.3}$	$0.58^{+0.38}_{-0.39}$
1.25	10.125	$(1.29^{+0.09}_{-0.08})\times10^{11}$	$94.5^{+2.5}_{-1.4}$	$4.81^{+0.15}_{-0.07}$	$2.06^{+0.12}_{-0.11}$	$(2.87^{+0.35}_{-0.32})\times10^{7}$	$0.58^{+1.4}_{-0.36}$	$19^{+0}_{-1.4}$	$(2.90^{+2.45}_{-2.61})\times10^{-2}$	$0.95^{+0.43}_{-0.36}$	$2.9^{+1.4}_{-1.6}$	$0.86^{+0.51}_{-0.60}$
1.25	10.375	$(1.95^{+0.10}_{-0.11})\times10^{11}$	$95.1^{+1.7}_{-2.6}$	$4.74^{+0.15}_{-0.13}$	$1.98^{+0.08}_{-0.09}$	$(4.81^{+0.68}_{-0.31})\times10^{7}$	$0.48^{+1.2}_{-0.32}$	$29^{+1.7}_{-1.2}$	$(1.61^{+1.36}_{-1.51})\times10^{-2}$	$0.93^{+0.41}_{-0.39}$	$3.6^{+1.4}_{-1.9}$	$1.10^{+0.52}_{-0.72}$
1.25	10.625	$(2.63^{+0.13}_{-0.14})\times10^{11}$	$98.3^{+2.4}_{-1.9}$	$4.64^{+0.19}_{-0.12}$	$1.98^{+0.11}_{-0.07}$	$(7.57^{+0.65}_{-0.63})\times10^{7}$	$0.44^{+1.1}_{-0.28}$	$39^{+2.1}_{-2.5}$	$(1.11^{+0.91}_{-1.00})\times10^{-2}$	$0.91^{+0.41}_{-0.38}$	$3.9^{+1.5}_{-1.7}$	$1.17^{+0.58}_{-0.71}$
1.25	10.875	$(3.43^{+0.17}_{-0.22})\times10^{11}$	$102.0^{+3.0}_{-1.9}$	$4.52^{+0.15}_{-0.16}$	$2.11^{+0.12}_{-0.12}$	$(1.10^{+0.12}_{-0.08})\times10^{8}$	$0.51^{+1.1}_{-0.30}$	$51^{+2.2}_{-3.0}$	$(9.92^{+7.71}_{-8.78})\times10^{-3}$	$0.90^{+0.40}_{-0.38}$	$4.0^{+1.6}_{-1.6}$	$1.20^{+0.54}_{-0.73}$
1.25	11.125	$(4.08^{+0.18}_{-0.14})\times10^{11}$	$104.2^{+1.4}_{-3.2}$	$4.46^{+0.15}_{-0.12}$	$1.92^{+0.10}_{-0.13}$	$(1.72^{+0.13}_{-0.17})\times10^{8}$	$0.64^{+1.4}_{-0.37}$	$60^{+3.0}_{-4.0}$	$(1.06^{+0.79}_{-0.91})\times10^{-2}$	$0.98^{+0.45}_{-0.42}$	$4.1^{+1.2}_{-1.8}$	$1.28^{+0.58}_{-0.67}$
1.25	11.375	$(5.21^{+0.62}_{-0.51})\times10^{11}$	$109.3^{+4.8}_{-5.5}$	$4.46^{+0.18}_{-0.28}$	$1.93^{+0.11}_{-0.16}$	$(2.85^{+0.50}_{-0.31})\times10^{8}$	$0.81^{+1.3}_{-0.50}$	$75^{+8.2}_{-8.3}$	$(1.06^{+0.56}_{-0.94})\times10^{-2}$	$1.48^{+0.39}_{-0.77}$	$4.4^{+2.6}_{-1.0}$	$1.42^{+0.24}_{-1.10}$
1.75	9.125	$(1.81^{+0.60}_{-0.32})\times10^{10}$	$99.3^{+5.3}_{-6.6}$	–	–	$(6.83^{+1.60}_{-1.70})\times10^{6}$	$0.53^{+0.54}_{-0.27}$	$2.5^{+0.7}_{-0.5}$	$(1.74^{+0.49}_{-0.91})\times10^{-1}$	$0.90^{+0.14}_{-0.20}$	$1.16^{+0.43}_{-0.62}$	$0.30^{+0.11}_{-0.13}$
1.75	9.375	$(3.05^{+0.61}_{-0.45})\times10^{10}$	$95.8^{+4.3}_{-4.3}$	–	$2.21^{+0.35}_{-0.24}$	$(7.79^{+2.13}_{-1.17})\times10^{6}$	$0.72^{+0.83}_{-0.37}$	$3.4^{+0.7}_{-0.6}$	$(1.75^{+0.57}_{-0.96})\times10^{-1}$	$0.85^{+0.13}_{-0.17}$	$1.35^{+0.48}_{-0.60}$	$0.35^{+0.11}_{-0.14}$
1.75	9.625	$(4.09^{+0.50}_{-0.42})\times10^{10}$	$85.0^{+3.7}_{-2.0}$	$4.93^{+0.07}_{-0.06}$	$1.58^{+0.14}_{-0.15}$	$(9.42^{+2.14}_{-1.03})\times10^{6}$	$0.89^{+1.3}_{-0.44}$	$6.1^{+0.5}_{-0.7}$	$(1.27^{+0.69}_{-0.75})\times10^{-1}$	$0.83^{+0.14}_{-0.16}$	$1.58^{+0.53}_{-0.69}$	$0.40^{+0.12}_{-0.18}$
1.75	9.875	$(9.13^{+1.03}_{-0.54})\times10^{10}$	$78.9^{+2.4}_{-1.2}$	$4.89^{+0.10}_{-0.06}$	$1.66^{+0.15}_{-0.12}$	$(1.39^{+0.15}_{-0.20})\times10^{7}$	$1.0^{+1.6}_{-0.6}$	$14^{+1}_{-1.0}$	$(6.82^{+4.41}_{-4.74})\times10^{-2}$	$0.84^{+0.21}_{-0.19}$	$1.92^{+0.72}_{-0.91}$	$0.49^{+0.22}_{-0.26}$
1.75	10.125	$(1.97^{+0.11}_{-0.12})\times10^{11}$	$79.4^{+1.8}_{-2.4}$	$4.81^{+0.15}_{-0.09}$	$1.74^{+0.12}_{-0.14}$	$(2.83^{+0.22}_{-0.30})\times10^{7}$	$0.98^{+2.0}_{-0.58}$	$29^{+1.4}_{-1.9}$	$(3.25^{+2.31}_{-2.84})\times10^{-2}$	$0.87^{+0.36}_{-0.29}$	$2.5^{+1.2}_{-1.3}$	$0.71^{+0.47}_{-0.44}$
1.75	10.375	$(3.35^{+0.15}_{-0.22})\times10^{11}$	$83.6^{+3.3}_{-2.0}$	$4.56^{+0.13}_{-0.21}$	$1.95^{+0.19}_{-0.10}$	$(5.37^{+0.49}_{-0.56})\times10^{7}$	$0.76^{+2.3}_{-0.48}$	$48^{+2.7}_{-2.3}$	$(1.56^{+1.49}_{-1.42})\times10^{-2}$	$0.94^{+0.40}_{-0.40}$	$3.4^{+1.5}_{-1.7}$	$1.04^{+0.57}_{-0.65}$
1.75	10.625	$(4.84^{+0.24}_{-0.28})\times10^{11}$	$86.5^{+1.4}_{-3.2}$	$4.45^{+0.13}_{-0.14}$	$1.88^{+0.12}_{-0.11}$	$(9.22^{+0.96}_{-0.67})\times10^{7}$	$0.62^{+1.6}_{-0.41}$	$71^{+4.2}_{-3.5}$	$(8.65^{+7.60}_{-8.06})\times10^{-3}$	$0.99^{+0.39}_{-0.45}$	$3.8^{+1.6}_{-1.9}$	$1.22^{+0.55}_{-0.79}$
1.75	10.875	$(6.69^{+0.52}_{-0.21})\times10^{11}$	$90.5^{+2.4}_{-2.5}$	$4.34^{+0.12}_{-0.14}$	$2.10^{+0.08}_{-0.10}$	$(1.31^{+0.12}_{-0.11})\times10^{8}$	$0.62^{+1.4}_{-0.42}$	$98^{+4.0}_{-5.7}$	$(6.31^{+5.06}_{-5.88})\times10^{-3}$	$1.00^{+0.38}_{-0.48}$	$4.1^{+1.6}_{-1.9}$	$1.26^{+0.58}_{-0.78}$
1.75	11.125	$(8.70^{+0.43}_{-0.50})\times10^{11}$	$92.2^{+3.0}_{-2.4}$	$4.31^{+0.11}_{-0.15}$	$2.08^{+0.12}_{-0.07}$	$(2.01^{+0.26}_{-0.16})\times10^{8}$	$0.79^{+2.1}_{-0.46}$	$132^{+9.8}_{-6.4}$	$(5.94^{+5.26}_{-5.20})\times10^{-3}$	$1.02^{+0.35}_{-0.56}$	$4.0^{+1.6}_{-1.7}$	$1.31^{+0.51}_{-0.73}$
1.75	11.375	$(1.37^{+0.16}_{-0.08})\times10^{12}$	$95.9^{+4.1}_{-3.5}$	$4.27^{+0.22}_{-0.11}$	$2.21^{+0.10}_{-0.17}$	$(3.47^{+0.55}_{-0.33})\times10^{8}$	$1.1^{+2.6}_{-0.5}$	205^{+14}_{-19}	$(5.22^{+4.33}_{-4.00})\times10^{-3}$	$1.14^{+0.46}_{-0.68}$	$4.5^{+1.5}_{-1.4}$	$1.34^{+0.32}_{-0.84}$
2.25	9.125	$(2.56^{+1.39}_{-0.55})\times10^{10}$	$88.5^{+7.3}_{-8.7}$	–	–	$(6.20^{+1.91}_{-1.59})\times10^{6}$	$0.74^{+0.81}_{-0.36}$	$3.6^{+1.5}_{-0.8}$	$(1.71^{+0.59}_{-0.55})\times10^{-1}$	$0.85^{+0.11}_{-0.17}$	$1.26^{+0.44}_{-0.55}$	$0.32^{+0.10}_{-0.12}$
2.25	9.375	$(3.73^{+1.43}_{-0.86})\times10^{10}$	$88.3^{+6.1}_{-8.6}$	$4.61^{+0.37}_{-0.18}$	–	$(8.80^{+2.19}_{-1.98})\times10^{6}$	$1.0^{+1.1}_{-0.5}$	$5.6^{+1.3}_{-1.2}$	$(1.55^{+0.48}_{-0.74})\times10^{-1}$	$0.81^{+0.09}_{-0.13}$	$1.44^{+0.47}_{-0.50}$	$0.36^{+0.11}_{-0.11}$

TABLE 3 — *Continued*

z	$\log M_*$ ($M_\odot$)	$L_{\rm IR}$ ($L_\odot$)	$\lambda_{\rm peak}$ (μm)	$\alpha_{\rm MIR}$	$\beta_{\rm IR}$	$M_{\rm dust}$ ($M_\odot$)	SFR$_{\rm UV}$ ($M_\odot$ yr^{-1})	SFR$_{\rm IR}$ ($M_\odot$ yr^{-1})	$f_{\rm unobs}$	B'	$A_{\rm UV}$ (mag)	A_V (mag)
2.25	9.625	$(5.18^{+1.34}_{-0.74})\times10^{10}$	$88.1^{+4.4}_{-6.0}$	$4.83^{+0.17}_{-0.08}$	–	$(1.21^{+0.24}_{-0.22})\times10^{7}$	$1.3^{+1.6}_{-0.7}$	$7.4^{+1.7}_{-1.0}$	$(1.50^{+0.53}_{-0.87})\times10^{-1}$	$0.80^{+0.11}_{-0.13}$	$1.61^{+0.48}_{-0.59}$	$0.40^{+0.11}_{-0.15}$
2.25	9.875	$(1.21^{+0.14}_{-0.09})\times10^{11}$	$67.9^{+2.1}_{-2.0}$	$4.88^{+0.11}_{-0.07}$	$0.86^{+0.22}_{-0.10}$	$(2.16^{+0.23}_{-0.26})\times10^{7}$	$1.4^{+2.0}_{-0.8}$	$18^{+2.7}_{-1.0}$	$(7.23^{+3.82}_{-5.08})\times10^{-2}$	$0.80^{+0.20}_{-0.15}$	$1.91^{+0.72}_{-0.75}$	$0.49^{+0.17}_{-0.24}$
2.25	10.125	$(3.09^{+0.18}_{-0.20})\times10^{11}$	$72.8^{+2.6}_{-2.7}$	$4.63^{+0.16}_{-0.19}$	$1.55^{+0.14}_{-0.16}$	$(4.15^{+0.45}_{-0.49})\times10^{7}$	$1.4^{+2.7}_{-0.8}$	$45^{+3.1}_{-2.9}$	$(2.95^{+1.97}_{-2.60})\times10^{-2}$	$0.84^{+0.35}_{-0.25}$	$2.4^{+1.2}_{-1.2}$	$0.66^{+0.39}_{-0.41}$
2.25	10.375	$(4.64^{+0.23}_{-0.31})\times10^{11}$	$77.4^{+2.9}_{-1.7}$	$4.34^{+0.11}_{-0.18}$	$1.47^{+0.13}_{-0.11}$	$(8.81^{+1.26}_{-0.56})\times10^{7}$	$1.0^{+3.0}_{-0.7}$	$68^{+2.5}_{-4.9}$	$(1.51^{+1.44}_{-1.40})\times10^{-2}$	$0.92^{+0.42}_{-0.41}$	$3.3^{+1.6}_{-2.1}$	$1.07^{+0.59}_{-0.72}$
2.25	10.625	$(6.17^{+0.50}_{-0.19})\times10^{11}$	$84.8^{+4.3}_{-2.9}$	$4.04^{+0.12}_{-0.17}$	$1.72^{+0.16}_{-0.12}$	$(1.48^{+0.14}_{-0.19})\times10^{8}$	$0.78^{+2.7}_{-0.52}$	$92^{+4.3}_{-7.8}$	$(8.34^{+9.12}_{-7.72})\times10^{-3}$	$1.01^{+0.43}_{-0.51}$	$4.1^{+1.7}_{-2.4}$	$1.37^{+0.63}_{-0.88}$
2.25	10.875	$(8.42^{+0.77}_{-0.32})\times10^{11}$	$87.1^{+2.8}_{-4.2}$	$3.95^{+0.18}_{-0.11}$	$1.84^{+0.12}_{-0.14}$	$(2.07^{+0.25}_{-0.21})\times10^{8}$	$0.79^{+2.0}_{-0.52}$	$128^{+6.9}_{-7.0}$	$(6.17^{+5.29}_{-5.71})\times10^{-3}$	$1.04^{+0.42}_{-0.57}$	$4.4^{+1.9}_{-2.2}$	$1.45^{+0.61}_{-0.93}$
2.25	11.125	$(1.28^{+0.09}_{-0.10})\times10^{12}$	$87.2^{+2.5}_{-4.9}$	$4.07^{+0.21}_{-0.12}$	$2.11^{+0.13}_{-0.17}$	$(2.50^{+0.23}_{-0.34})\times10^{8}$	$1.00^{+2.5}_{-0.64}$	188^{+11}_{-13}	$(5.29^{+4.44}_{-4.82})\times10^{-3}$	$1.10^{+0.37}_{-0.64}$	$4.5^{+2.0}_{-1.8}$	$1.45^{+0.61}_{-0.90}$
2.25	11.375	$(2.23^{+0.16}_{-0.27})\times10^{12}$	$86.7^{+2.9}_{-4.3}$	$4.24^{+0.22}_{-0.18}$	$2.22^{+0.10}_{-0.18}$	$(3.86^{+0.60}_{-0.40})\times10^{8}$	$1.3^{+2.3}_{-1.0}$	328^{+30}_{-28}	$(4.02^{+2.47}_{-3.86})\times10^{-3}$	$1.18^{+0.76}_{-0.24}$	$4.78^{+0.63}_{-1.61}$	$1.54^{+0.58}_{-0.79}$
2.75	9.375	$(6.40^{+2.51}_{-1.22})\times10^{10}$	$76.1^{+6.7}_{-6.1}$	–	–	$(8.38^{+2.05}_{-1.69})\times10^{6}$	$1.4^{+1.4}_{-0.7}$	$8.1^{+3.4}_{-1.5}$	$(1.48^{+0.49}_{-0.46})\times10^{-1}$	$0.85^{+0.14}_{-0.16}$	$1.34^{+0.46}_{-0.51}$	$0.34^{+0.11}_{-0.12}$
2.75	9.625	$(4.71^{+2.98}_{-1.43})\times10^{10}$	$116.8^{+22.1}_{-16.0}$	$4.41^{+0.53}_{-0.28}$	$3.56^{+0.50}_{-0.66}$	$(1.48^{+0.51}_{-0.45})\times10^{7}$	$1.7^{+2.0}_{-0.8}$	$9.6^{+4.1}_{-2.2}$	$(1.49^{+0.41}_{-0.68})\times10^{-1}$	$0.82^{+0.13}_{-0.15}$	$1.52^{+0.57}_{-0.51}$	$0.38^{+0.12}_{-0.13}$
2.75	9.875	$(7.31^{+1.33}_{-1.35})\times10^{10}$	$124.0^{+9.3}_{-8.7}$	$3.42^{+0.21}_{-0.28}$	$3.35^{+0.36}_{-0.54}$	$(3.69^{+0.83}_{-0.74})\times10^{7}$	$1.7^{+2.7}_{-1.0}$	$10^{+1.9}_{-2.1}$	$(1.41^{+0.68}_{-0.88})\times10^{-1}$	$0.84^{+0.20}_{-0.19}$	$1.78^{+0.64}_{-0.84}$	$0.46^{+0.18}_{-0.22}$
2.75	10.125	$(3.85^{+0.34}_{-0.24})\times10^{11}$	$69.8^{+2.9}_{-2.3}$	$4.74^{+0.20}_{-0.13}$	$1.79^{+0.19}_{-0.15}$	$(4.14^{+0.79}_{-0.41})\times10^{7}$	$1.5^{+3.7}_{-0.9}$	$57^{+4.1}_{-3.3}$	$(2.50^{+2.03}_{-2.20})\times10^{-2}$	$0.90^{+0.33}_{-0.30}$	$2.3^{+1.1}_{-1.4}$	$0.65^{+0.42}_{-0.42}$
2.75	10.375	$(5.47^{+0.42}_{-0.56})\times10^{11}$	$77.0^{+5.1}_{-5.3}$	$4.20^{+0.23}_{-0.23}$	$1.82^{+0.29}_{-0.17}$	$(8.71^{+1.32}_{-1.15})\times10^{7}$	$1.0^{+4.2}_{-0.7}$	$78^{+5.8}_{-7.7}$	$(1.32^{+1.56}_{-1.19})\times10^{-2}$	$0.99^{+0.36}_{-0.53}$	$3.3^{+1.7}_{-2.2}$	$1.06^{+0.59}_{-0.77}$
2.75	10.625	$(9.03^{+0.58}_{-0.76})\times10^{11}$	$75.1^{+2.9}_{-3.4}$	$4.24^{+0.20}_{-0.14}$	$1.67^{+0.18}_{-0.12}$	$(1.42^{+0.19}_{-0.13})\times10^{8}$	$0.83^{+4.3}_{-0.53}$	$133^{+9.6}_{-6.3}$	$(6.23^{+9.12}_{-5.69})\times10^{-3}$	$1.11^{+0.49}_{-0.55}$	$4.2^{+1.9}_{-2.5}$	$1.42^{+0.59}_{-0.97}$
2.75	10.875	$(1.47^{+0.09}_{-0.09})\times10^{12}$	$74.9^{+3.6}_{-1.8}$	$4.23^{+0.12}_{-0.16}$	$1.81^{+0.11}_{-0.09}$	$(2.08^{+0.33}_{-0.15})\times10^{8}$	$0.95^{+3.8}_{-0.60}$	217^{+11}_{-13}	$(4.37^{+5.33}_{-3.95})\times10^{-3}$	$1.19^{+0.42}_{-0.71}$	$4.4^{+1.9}_{-2.7}$	$1.50^{+0.58}_{-1.02}$
2.75	11.125	$(1.86^{+0.12}_{-0.16})\times10^{12}$	$80.4^{+2.7}_{-3.7}$	$4.02^{+0.13}_{-0.13}$	$2.16^{+0.17}_{-0.11}$	$(2.68^{+0.37}_{-0.26})\times10^{8}$	$1.2^{+3.3}_{-0.8}$	276^{+17}_{-19}	$(4.27^{+3.94}_{-3.99})\times10^{-3}$	$1.31^{+0.37}_{-0.86}$	$4.4^{+1.0}_{-3.1}$	$1.54^{+0.77}_{-0.80}$
2.75	11.375	$(2.92^{+0.40}_{-0.24})\times10^{12}$	$74.6^{+4.9}_{-3.6}$	$4.21^{+0.21}_{-0.24}$	$1.96^{+0.18}_{-0.19}$	$(3.53^{+0.59}_{-0.36})\times10^{8}$	$1.3^{+5.0}_{-0.8}$	428^{+54}_{-43}	$(3.14^{+3.42}_{-2.68})\times10^{-3}$	$1.42^{+0.60}_{-0.39}$	$4.29^{+0.80}_{-1.49}$	$1.50^{+0.76}_{-0.47}$
3.25	9.375	$(3.39^{+3.11}_{-1.33})\times10^{10}$	$93.1^{+16.2}_{-15.5}$	–	–	$(1.37^{+0.62}_{-0.46})\times10^{7}$	$1.7^{+1.5}_{-0.9}$	$4.6^{+4.4}_{-1.8}$	$(2.72^{+0.00}_{-0.19})\times10^{-1}$	$0.94^{+0.18}_{-0.24}$	$1.19^{+0.49}_{-0.50}$	$0.32^{+0.11}_{-0.12}$
3.25	9.625	$(6.95^{+5.27}_{-2.91})\times10^{10}$	$87.6^{+13.8}_{-16.1}$	–	–	$(2.02^{+0.70}_{-0.70})\times10^{7}$	$2.1^{+2.3}_{-1.1}$	$9.4^{+5.5}_{-3.0}$	$(1.80^{+0.50}_{-0.42})\times10^{-1}$	$0.87^{+0.15}_{-0.18}$	$1.36^{+0.52}_{-0.53}$	$0.35^{+0.13}_{-0.12}$
3.25	9.875	$(1.60^{+0.74}_{-0.29})\times10^{11}$	$75.1^{+7.7}_{-8.5}$	–	–	$(2.24^{+0.41}_{-0.61})\times10^{7}$	$2.1^{+3.7}_{-1.0}$	$15^{+11}_{-4.2}$	$(1.25^{+0.35}_{-0.49})\times10^{-1}$	$0.86^{+0.17}_{-0.17}$	$1.52^{+0.61}_{-0.61}$	$0.40^{+0.13}_{-0.18}$
3.25	10.125	$(1.32^{+0.41}_{-0.31})\times10^{11}$	$102.4^{+11.5}_{-8.1}$	$4.38^{+0.44}_{-0.37}$	$2.92^{+0.39}_{-0.45}$	$(3.92^{+1.14}_{-1.04})\times10^{7}$	$1.8^{+4.0}_{-1.1}$	$22^{+6.8}_{-5.1}$	$(7.90^{+4.96}_{-4.99})\times10^{-2}$	$0.88^{+0.23}_{-0.23}$	$1.85^{+0.85}_{-0.93}$	$0.49^{+0.25}_{-0.26}$
3.25	10.375	$(5.65^{+0.75}_{-0.58})\times10^{11}$	$72.5^{+4.4}_{-2.8}$	$4.66^{+0.28}_{-0.17}$	–	$(6.71^{+0.99}_{-0.88})\times10^{7}$	$1.4^{+3.7}_{-0.9}$	$83^{+10}_{-8.6}$	$(1.62^{+1.36}_{-1.50})\times10^{-2}$	$0.91^{+0.30}_{-0.35}$	$2.4^{+1.3}_{-1.5}$	$0.71^{+0.48}_{-0.42}$
3.25	10.625	$(1.24^{+0.11}_{-0.10})\times10^{12}$	$66.4^{+3.1}_{-2.7}$	$4.71^{+0.23}_{-0.14}$	$1.80^{+0.15}_{-0.19}$	$(1.21^{+0.20}_{-0.12})\times10^{8}$	$1.2^{+3.8}_{-0.9}$	181^{+17}_{-15}	$(6.78^{+6.55}_{-6.36})\times10^{-3}$	$0.94^{+0.41}_{-0.46}$	$3.2^{+1.8}_{-2.1}$	$1.06^{+0.44}_{-0.72}$
3.25	10.875	$(1.93^{+0.13}_{-0.18})\times10^{12}$	$69.0^{+3.1}_{-2.8}$	$4.49^{+0.19}_{-0.17}$	$1.74^{+0.14}_{-0.19}$	$(2.29^{+0.27}_{-0.25})\times10^{8}$	$1.3^{+5.3}_{-0.8}$	286^{+24}_{-19}	$(4.43^{+5.46}_{-4.03})\times10^{-3}$	$0.99^{+0.48}_{-0.59}$	$3.8^{+1.7}_{-2.5}$	$1.18^{+0.81}_{-0.51}$
3.25	11.125	$(2.57^{+0.28}_{-0.18})\times10^{12}$	$73.0^{+3.1}_{-2.6}$	$4.08^{+0.21}_{-0.15}$	–	$(3.12^{+0.51}_{-0.29})\times10^{8}$	$1.3^{+5.7}_{-0.7}$	380^{+27}_{-34}	$(3.29^{+4.37}_{-2.72})\times10^{-3}$	$1.00^{+0.52}_{-0.58}$	$4.2^{+2.1}_{-2.4}$	$1.40^{+0.70}_{-0.64}$
3.25	11.375	$(3.94^{+0.44}_{-0.43})\times10^{12}$	$67.2^{+3.4}_{-4.0}$	$4.10^{+0.20}_{-0.20}$	$1.95^{+0.14}_{-0.25}$	$(3.34^{+0.50}_{-0.46})\times10^{8}$	$1.4^{+4.6}_{-0.7}$	589^{+67}_{-57}	$(2.37^{+2.37}_{-1.87})\times10^{-3}$	$0.97^{+0.57}_{-0.48}$	$4.98^{+0.89}_{-1.97}$	$1.50^{+0.59}_{-0.52}$
3.75	9.625	$(8.44^{+8.20}_{-3.09})\times10^{10}$	$76.7^{+14.4}_{-15.2}$	–	–	$(1.46^{+0.75}_{-0.51})\times10^{7}$	$2.3^{+2.7}_{-1.2}$	$9.0^{+8.5}_{-4.2}$	$(2.05^{+0.22}_{-0.18})\times10^{-1}$	$1.00^{+0.17}_{-0.30}$	$1.20^{+0.47}_{-0.69}$	$0.32^{+0.12}_{-0.16}$
3.75	9.875	$(1.23^{+1.00}_{-0.49})\times10^{11}$	$91.5^{+19.3}_{-14.6}$	$4.34^{+0.62}_{-0.31}$	–	$(4.93^{+2.67}_{-1.64})\times10^{7}$	$2.3^{+3.9}_{-1.3}$	$20^{+16}_{-7.3}$	$(1.07^{+0.25}_{-0.42})\times10^{-1}$	$0.95^{+0.18}_{-0.26}$	$1.44^{+0.50}_{-0.89}$	$0.38^{+0.13}_{-0.22}$
3.75	10.125	$(2.76^{+0.90}_{-0.60})\times10^{11}$	$84.3^{+8.5}_{-7.2}$	$4.61^{+0.39}_{-0.15}$	–	$(7.33^{+1.57}_{-1.52})\times10^{7}$	$1.8^{+4.2}_{-1.0}$	$42^{+12}_{-8.7}$	$(4.12^{+2.49}_{-3.26})\times10^{-2}$	$0.93^{+0.25}_{-0.25}$	$1.87^{+0.86}_{-1.35}$	$0.50^{+0.29}_{-0.34}$
3.75	10.375	$(1.31^{+0.11}_{-0.16})\times10^{12}$	$62.0^{+3.0}_{-2.6}$	$4.86^{+0.14}_{-0.08}$	$2.01^{+0.25}_{-0.23}$	$(8.79^{+1.58}_{-1.24})\times10^{7}$	$1.4^{+3.6}_{-1.0}$	194^{+21}_{-15}	$(7.10^{+5.86}_{-6.86})\times10^{-3}$	$0.90^{+0.24}_{-0.40}$	$2.8^{+1.6}_{-2.0}$	$0.85^{+0.49}_{-0.60}$
3.75	10.625	$(2.25^{+0.27}_{-0.13})\times10^{12}$	$61.9^{+2.6}_{-2.3}$	$4.79^{+0.18}_{-0.09}$	$2.17^{+0.11}_{-0.20}$	$(1.33^{+0.16}_{-0.19})\times10^{8}$	$1.1^{+4.1}_{-0.8}$	330^{+35}_{-21}	$(3.33^{+3.58}_{-3.27})\times10^{-3}$	$0.86^{+0.37}_{-0.39}$	$3.9^{+2.1}_{-2.5}$	$1.23^{+0.76}_{-0.57}$
3.75	10.875	$(2.61^{+0.24}_{-0.26})\times10^{12}$	$66.3^{+3.0}_{-3.5}$	$4.49^{+0.24}_{-0.25}$	$1.79^{+0.16}_{-0.17}$	$(2.74^{+0.47}_{-0.28})\times10^{8}$	$0.81^{+4.1}_{-0.62}$	383^{+31}_{-37}	$(2.10^{+2.97}_{-2.06})\times10^{-3}$	$0.78^{+0.46}_{-0.37}$	$4.7^{+1.9}_{-2.3}$	$1.49^{+0.48}_{-0.79}$
3.75	11.125	$(4.22^{+0.44}_{-0.47})\times10^{12}$	$65.9^{+3.5}_{-3.2}$	$4.31^{+0.22}_{-0.22}$	$1.90^{+0.13}_{-0.22}$	$(4.06^{+0.48}_{-0.55})\times10^{8}$	$0.73^{+5.7}_{-0.53}$	619^{+68}_{-56}	$(1.18^{+2.20}_{-1.14})\times10^{-3}$	$0.77^{+0.37}_{-0.36}$	$5.1^{+1.4}_{-2.0}$	$1.57^{+0.54}_{-0.65}$
3.75	11.375	$(7.91^{+0.74}_{-0.68})\times10^{12}$	$57.2^{+2.0}_{-2.6}$	$4.66^{+0.21}_{-0.21}$	–	$(3.81^{+0.39}_{-0.41})\times10^{8}$	$0.78^{+2.6}_{-0.43}$	1177^{+124}_{-88}	$(6.65^{+6.84}_{-5.60})\times10^{-4}$	$0.87^{+0.17}_{-0.44}$	$5.5^{+1.1}_{-1.9}$	$1.72^{+0.37}_{-0.83}$
4.25	9.625	$(5.75^{+8.29}_{-2.64})\times10^{10}$	$81.6^{+20.3}_{-21.2}$	–	–	$(1.49^{+0.94}_{-0.69})\times10^{7}$	$2.4^{+2.6}_{-1.3}$	$7.2^{+9.7}_{-3.2}$	$(2.51^{+0.00}_{-0.29})\times10^{-1}$	$1.13^{+0.22}_{-0.29}$	$1.02^{+0.48}_{-0.61}$	$0.29^{+0.12}_{-0.16}$
4.25	9.875	$(1.31^{+0.87}_{-0.52})\times10^{11}$	$89.3^{+17.4}_{-13.7}$	$4.23^{+0.65}_{-0.41}$	–	$(5.10^{+2.18}_{-1.75})\times10^{7}$	$2.6^{+3.6}_{-1.5}$	$20^{+12}_{-8.5}$	$(1.17^{+0.27}_{-0.38})\times10^{-1}$	$1.03^{+0.18}_{-0.27}$	$1.30^{+0.54}_{-0.78}$	$0.36^{+0.13}_{-0.22}$
4.25	10.125	$(4.37^{+1.41}_{-0.99})\times10^{11}$	$73.2^{+7.2}_{-7.3}$	$4.69^{+0.30}_{-0.19}$	–	$(6.69^{+1.34}_{-1.36})\times10^{7}$	$2.1^{+4.6}_{-1.2}$	64^{+22}_{-14}	$(3.19^{+2.15}_{-1.94})\times10^{-2}$	$0.97^{+0.21}_{-0.23}$	$1.64^{+0.76}_{-1.07}$	$0.45^{+0.22}_{-0.31}$
4.25	10.375	$(1.54^{+0.26}_{-0.20})\times10^{12}$	$60.9^{+3.9}_{-3.7}$	$4.77^{+0.23}_{-0.10}$	$1.94^{+0.23}_{-0.21}$	$(1.11^{+0.30}_{-0.14})\times10^{8}$	$1.7^{+5.4}_{-1.0}$	227^{+39}_{-27}	$(7.51^{+6.84}_{-6.56})\times10^{-3}$	$0.92^{+0.19}_{-0.35}$	$2.6^{+1.3}_{-1.6}$	$0.74^{+0.51}_{-0.43}$
4.25	10.625	$(2.65^{+0.38}_{-0.29})\times10^{12}$	$59.0^{+3.4}_{-3.1}$	$4.71^{+0.29}_{-0.13}$	$2.02^{+0.24}_{-0.20}$	$(1.60^{+0.38}_{-0.19})\times10^{8}$	$1.3^{+5.0}_{-0.9}$	389^{+62}_{-45}	$(3.25^{+3.64}_{-3.03})\times10^{-3}$	$0.86^{+0.33}_{-0.34}$	$3.8^{+2.8}_{-1.5}$	$1.22^{+0.52}_{-0.68}$
4.25	10.875	$(3.66^{+0.40}_{-0.49})\times10^{12}$	$60.0^{+4.2}_{-2.4}$	$4.69^{+0.28}_{-0.14}$	–	$(2.40^{+0.35}_{-0.27})\times10^{8}$	$0.59^{+4.5}_{-0.42}$	553^{+62}_{-60}	$(1.06^{+1.96}_{-1.02})\times10^{-3}$	$0.75^{+0.38}_{-0.27}$	$4.8^{+1.6}_{-2.5}$	$1.55^{+0.29}_{-0.94}$
4.25	11.125	$(6.59^{+0.69}_{-0.70})\times10^{12}$	$61.1^{+2.9}_{-2.5}$	$4.68^{+0.28}_{-0.14}$	–	$(4.61^{+0.63}_{-0.45})\times10^{8}$	$0.22^{+0.70}_{-0.20}$	969^{+98}_{-95}	$(2.29^{+2.21}_{-2.28})\times10^{-4}$	$0.74^{+0.15}_{-0.26}$	$5.6^{+2.7}_{-1.8}$	$1.63^{+0.98}_{-0.35}$

TABLE 3 — *Continued*

z	$\log M_*$ ($M_\odot$)	$L_{\rm IR}$ ($L_\odot$)	$\lambda_{\rm peak}$ (μm)	$\alpha_{\rm MIR}$	$\beta_{\rm IR}$	$M_{\rm dust}$ ($M_\odot$)	$\rm SFR_{UV}$ ($M_\odot\,\rm yr^{-1}$)	$\rm SFR_{IR}$ ($M_\odot\,\rm yr^{-1}$)	$f_{\rm unobs}$	B'	$A_{\rm UV}$ (mag)	A_V (mag)
4.25	11.375	$(9.11^{+1.56}_{-0.94})\times10^{12}$	$56.6^{+3.1}_{-3.1}$	$4.57^{+0.29}_{-0.24}$	–	$(4.70^{+0.64}_{-0.61})\times10^{8}$	$0.098^{+0.323}_{-0.071}$	1354^{+234}_{-132}	$(7.23^{+6.96}_{-6.90})\times10^{-5}$	$0.82^{+0.05}_{-0.39}$	$6.6^{+2.8}_{-1.2}$	$2.26^{+0.26}_{-0.78}$
4.75	9.625	$(3.12^{+5.32}_{-1.86})\times10^{10}$	$102.8^{+35.1}_{-31.1}$	–	–	$(2.87^{+3.49}_{-1.81})\times10^{7}$	$2.7^{+2.9}_{-1.3}$	$6.0^{+11}_{-2.8}$	$(3.06^{+0.00}_{-0.30})\times10^{-1}$	$1.15^{+0.27}_{-0.23}$	$0.99^{+0.38}_{-0.70}$	$0.29^{+0.12}_{-0.16}$
4.75	9.875	$(8.61^{+5.59}_{-4.19})\times10^{10}$	$97.9^{+18.9}_{-18.1}$	–	–	$(5.95^{+3.01}_{-2.55})\times10^{7}$	$3.2^{+3.0}_{-1.8}$	$12^{+6.7}_{-5.0}$	$(2.09^{+0.45}_{-0.42})\times10^{-1}$	$1.05^{+0.21}_{-0.27}$	$1.20^{+0.49}_{-0.78}$	$0.33^{+0.13}_{-0.20}$
4.75	10.125	$(2.36^{+1.15}_{-0.67})\times10^{11}$	$89.3^{+12.1}_{-10.1}$	$4.31^{+0.67}_{-0.25}$	–	$(1.03^{+0.35}_{-0.27})\times10^{8}$	$2.7^{+8.2}_{-1.4}$	$35^{+13}_{-8.6}$	$(7.19^{+4.75}_{-4.72})\times10^{-2}$	$0.98^{+0.19}_{-0.24}$	$1.53^{+0.89}_{-0.95}$	$0.42^{+0.18}_{-0.30}$
4.75	10.375	$(4.42^{+1.69}_{-1.05})\times10^{11}$	$92.2^{+9.7}_{-9.3}$	$4.42^{+0.58}_{-0.20}$	$1.95^{+0.30}_{-0.31}$	$(2.39^{+0.87}_{-0.56})\times10^{8}$	$1.3^{+7.5}_{-1.0}$	64^{+23}_{-14}	$(2.00^{+2.40}_{-1.95})\times10^{-2}$	$0.87^{+0.18}_{-0.24}$	$2.7^{+1.8}_{-1.7}$	$0.72^{+0.54}_{-0.47}$
4.75	10.625	$(1.45^{+0.28}_{-0.29})\times10^{12}$	$72.6^{+5.3}_{-5.8}$	$4.65^{+0.35}_{-0.15}$	$1.91^{+0.22}_{-0.23}$	$(2.54^{+0.60}_{-0.51})\times10^{8}$	$0.40^{+5.0}_{-0.31}$	215^{+45}_{-38}	$(1.85^{+4.47}_{-1.81})\times10^{-3}$	$0.79^{+0.13}_{-0.27}$	$5.1^{+1.9}_{-3.3}$	$1.44^{+0.54}_{-1.00}$
4.75	10.875	$(2.75^{+0.58}_{-0.42})\times10^{12}$	$67.2^{+5.9}_{-4.1}$	$4.53^{+0.31}_{-0.30}$	–	$(3.18^{+0.64}_{-0.42})\times10^{8}$	$0.16^{+0.37}_{-0.15}$	417^{+82}_{-58}	$(3.95^{+2.63}_{-3.94})\times10^{-4}$	$0.70^{+0.17}_{-0.16}$	$7.2^{+2.4}_{-1.3}$	$2.05^{+0.60}_{-0.48}$
4.75	11.125	$(5.28^{+0.82}_{-0.84})\times10^{12}$	$61.5^{+4.8}_{-3.6}$	$4.64^{+0.35}_{-0.13}$	$2.54^{+0.19}_{-0.28}$	$(2.69^{+0.75}_{-0.49})\times10^{8}$	$0.20^{+0.34}_{-0.18}$	813^{+142}_{-88}	$(2.44^{+1.30}_{-2.43})\times10^{-4}$	$0.71^{+0.11}_{-0.24}$	$8.0^{+1.7}_{-1.0}$	$2.22^{+0.53}_{-0.43}$
4.75	11.375	$(7.50^{+1.60}_{-0.93})\times10^{12}$	$54.5^{+3.1}_{-4.1}$	$4.64^{+0.33}_{-0.12}$	–	$(3.59^{+0.49}_{-0.56})\times10^{8}$	$0.19^{+0.13}_{-0.16}$	1061^{+192}_{-161}	$(1.81^{+0.35}_{-1.79})\times10^{-4}$	–	$0.00^{+0.00}_{-0.00}$	$0.00^{+0.00}_{-0.00}$
5.25	9.875	$(4.40^{+5.01}_{-2.40})\times10^{10}$	$110.3^{+34.5}_{-29.1}$	$3.83^{+0.91}_{-0.59}$	–	$(6.44^{+8.09}_{-3.97})\times10^{7}$	$3.6^{+6.2}_{-1.5}$	$6.5^{+9.9}_{-3.6}$	$(3.55^{+0.35}_{-0})\times10^{-1}$	$1.17^{+0.27}_{-0.26}$	$0.94^{+0.41}_{-0.69}$	$0.27^{+0.11}_{-0.18}$
5.25	10.125	$(2.60^{+1.53}_{-0.93})\times10^{11}$	$88.8^{+16.2}_{-13.0}$	$4.08^{+0.70}_{-0.47}$	–	$(1.16^{+0.49}_{-0.42})\times10^{8}$	$3.6^{+6.0}_{-2.7}$	35^{+16}_{-12}	$(9.45^{+3.65}_{-7.18})\times10^{-2}$	$1.07^{+0.21}_{-0.35}$	$1.31^{+0.49}_{-1.12}$	$0.37^{+0.14}_{-0.28}$
5.25	10.375	$(1.06^{+0.36}_{-0.19})\times10^{12}$	$70.6^{+6.7}_{-6.5}$	$4.57^{+0.43}_{-0.18}$	–	$(1.64^{+0.29}_{-0.31})\times10^{8}$	$0.93^{+6.2}_{-0.77}$	151^{+47}_{-33}	$(6.09^{+8.78}_{-6.01})\times10^{-3}$	$0.93^{+0.14}_{-0.35}$	$2.5^{+2.4}_{-1.8}$	$0.77^{+0.66}_{-0.53}$
5.25	10.625	$(2.07^{+0.57}_{-0.39})\times10^{12}$	$66.6^{+6.1}_{-5.7}$	$4.63^{+0.37}_{-0.14}$	–	$(2.48^{+0.41}_{-0.44})\times10^{8}$	$0.28^{+2.7}_{-0.19}$	314^{+75}_{-57}	$(9.06^{+17.86}_{-8.46})\times10^{-4}$	$0.83^{+0.21}_{-0.21}$	$5.9^{+2.0}_{-3.3}$	$1.67^{+0.97}_{-0.64}$
5.25	10.875	$(4.89^{+1.09}_{-0.59})\times10^{12}$	$54.9^{+2.8}_{-4.1}$	$4.67^{+0.31}_{-0.14}$	–	$(2.64^{+0.36}_{-0.33})\times10^{8}$	$0.17^{+0.70}_{-0.15}$	730^{+121}_{-105}	$(2.39^{+2.63}_{-2.38})\times10^{-4}$	$0.71^{+0.11}_{-0.16}$	$7.4^{+1.4}_{-1.5}$	$2.22^{+0.53}_{-0.43}$
5.25	11.125	$(6.88^{+1.13}_{-0.91})\times10^{12}$	$54.5^{+3.5}_{-3.1}$	$4.65^{+0.33}_{-0.16}$	–	$(3.64^{+0.43}_{-0.51})\times10^{8}$	$0.23^{+0.88}_{-0.15}$	1025^{+145}_{-138}	$(2.29^{+2.50}_{-2.08})\times10^{-4}$	$0.63^{+0.09}_{-0.19}$	$7.89^{+1.91}_{-0.89}$	$2.22^{+0.50}_{-0.43}$
5.25	11.375	$(1.22^{+0.26}_{-0.19})\times10^{13}$	$50.5^{+3.6}_{-3.8}$	$4.69^{+0.30}_{-0.14}$	–	$(4.69^{+0.76}_{-0.59})\times10^{8}$	$0.53^{+0.56}_{-0.20}$	1860^{+383}_{-232}	$(2.86^{+1.11}_{-1.27})\times10^{-4}$	$0.66^{+0.00}_{-0.26}$	$8.2^{+2.1}_{-2.0}$	$2.349^{+0.006}_{-0.743}$
5.75	9.875	$(1.23^{+1.32}_{-0.56})\times10^{11}$	$83.5^{+25.1}_{-17.1}$	$4.01^{+0.82}_{-0.47}$	–	$(4.47^{+3.47}_{-2.03})\times10^{7}$	$4.2^{+6.6}_{-2.4}$	$16^{+16}_{-7.3}$	$(2.10^{+0.41}_{-0.37})\times10^{-1}$	$1.28^{+0.25}_{-0.25}$	$0.80^{+0.39}_{-0.58}$	$0.24^{+0.13}_{-0.15}$
5.75	10.125	$(2.69^{+2.98}_{-1.23})\times10^{11}$	$77.4^{+21.5}_{-18.2}$	$4.13^{+0.77}_{-0.41}$	–	$(6.79^{+4.16}_{-3.17})\times10^{7}$	$3.9^{+6.1}_{-2.5}$	45^{+52}_{-18}	$(8.01^{+1.94}_{-2.27})\times10^{-2}$	$1.21^{+0.23}_{-0.30}$	$1.13^{+0.39}_{-0.94}$	$0.34^{+0.16}_{-0.24}$
5.75	10.375	$(8.26^{+3.80}_{-2.63})\times10^{11}$	$72.4^{+12.3}_{-9.1}$	$4.36^{+0.60}_{-0.28}$	–	$(1.53^{+0.51}_{-0.39})\times10^{8}$	$2.3^{+15}_{-1.3}$	100^{+56}_{-34}	$(2.26^{+2.69}_{-1.50})\times10^{-2}$	$1.16^{+0.30}_{-0.33}$	$1.82^{+0.89}_{-1.16}$	$0.54^{+0.23}_{-0.40}$
5.75	10.625	$(4.83^{+1.20}_{-0.83})\times10^{12}$	$47.6^{+3.6}_{-4.0}$	$4.63^{+0.36}_{-0.16}$	–	$(1.59^{+0.28}_{-0.23})\times10^{8}$	$1.2^{+1.3}_{-1.1}$	708^{+195}_{-116}	$(1.74^{+0.47}_{-1.72})\times10^{-3}$	$0.98^{+0.32}_{-0.35}$	$4.2^{+1.5}_{-3.7}$	$1.25^{+0.68}_{-0.99}$
5.75	10.875	$(7.18^{+1.56}_{-0.99})\times10^{12}$	$49.5^{+3.6}_{-3.3}$	$4.61^{+0.32}_{-0.20}$	–	$(2.76^{+0.46}_{-0.31})\times10^{8}$	$0.67^{+7.8}_{-0.37}$	1064^{+176}_{-152}	$(6.30^{+14.91}_{-5.29})\times10^{-4}$	$0.75^{+0.12}_{-0.25}$	$6.92^{+0.68}_{-2.80}$	$2.23^{+0.56}_{-0.32}$
5.75	11.125	$(9.38^{+1.52}_{-1.46})\times10^{12}$	$47.8^{+3.3}_{-2.8}$	$4.61^{+0.27}_{-0.26}$	–	$(3.12^{+0.46}_{-0.38})\times10^{8}$	$0.67^{+6.5}_{-0.10}$	1369^{+212}_{-228}	$(4.87^{+10.22}_{-0})\times10^{-4}$	$0.75^{+0.01}_{-0.23}$	$7.16^{+1.86}_{-0.39}$	$2.244^{+0.547}_{-0.073}$
6.25	9.625	$(2.99^{+8.49}_{-1.90})\times10^{10}$	$100.7^{+49.8}_{-40.7}$	–	–	$(3.39^{+17.30}_{-2.40})\times10^{7}$	$3.8^{+6.1}_{-1.7}$	–	$(1.00^{+0.00}_{-0})\times10^{0}$	$1.38^{+0.24}_{-0.14}$	$0.59^{+0.26}_{-0.41}$	$0.187^{+0.085}_{-0.114}$
6.25	9.875	$(3.81^{+4.04}_{-1.82})\times10^{11}$	$58.6^{+15.2}_{-14.9}$	$4.33^{+0.66}_{-0.30}$	–	$(3.13^{+1.64}_{-1.32})\times10^{7}$	$4.4^{+7.9}_{-2.3}$	55^{+59}_{-20}	$(7.46^{+2.21}_{-1.82})\times10^{-2}$	$1.32^{+0.25}_{-0.20}$	$0.79^{+0.36}_{-0.58}$	$0.24^{+0.13}_{-0.15}$
6.25	10.375	$(3.15^{+3.29}_{-1.42})\times10^{11}$	$94.2^{+27.1}_{-21.8}$	$3.88^{+0.81}_{-0.62}$	–	$(2.22^{+1.96}_{-1.22})\times10^{8}$	$3.5^{+4.7}_{-1.9}$	45^{+38}_{-23}	$(7.24^{+1.07}_{-0.94})\times10^{-2}$	$1.21^{+0.27}_{-0.39}$	$2.10^{+0.42}_{-1.70}$	$0.68^{+0.18}_{-0.52}$
6.25	10.625	$(4.60^{+1.50}_{-1.18})\times10^{12}$	$53.2^{+5.6}_{-6.6}$	$4.59^{+0.41}_{-0.19}$	–	$(2.55^{+0.59}_{-0.54})\times10^{8}$	$1.5^{+6.7}_{-0.2}$	663^{+255}_{-128}	$(2.19^{+2.27}_{-0})\times10^{-3}$	$1.10^{+0.22}_{-0.34}$	$2.5^{+1.2}_{-2.0}$	$0.84^{+0.41}_{-0.66}$
6.25	10.875	$(7.83^{+2.38}_{-1.76})\times10^{12}$	$48.9^{+5.2}_{-5.4}$	$4.47^{+0.53}_{-0.19}$	–	$(3.07^{+0.67}_{-0.58})\times10^{8}$	$0.87^{+0.99}_{-0.66}$	1162^{+330}_{-278}	$(7.44^{+2.80}_{-6.40})\times10^{-4}$	$1.02^{+0.29}_{-0.31}$	$6.58^{+0.34}_{-3.33}$	$1.96^{+0.35}_{-0.73}$
6.25	11.125	$(1.33^{+0.44}_{-0.26})\times10^{13}$	$39.6^{+4.0}_{-3.6}$	$4.58^{+0.42}_{-0.18}$	–	$(2.23^{+0.46}_{-0.31})\times10^{8}$	$1.8^{+5.3}_{-0.6}$	1961^{+670}_{-381}	$(9.30^{+6.86}_{-3.33})\times10^{-4}$	$0.93^{+0.09}_{-0.22}$	$6.77^{+0.15}_{-2.65}$	$2.216^{+0.084}_{-0.910}$
6.75	10.625	$(3.69^{+1.71}_{-1.11})\times10^{12}$	$57.4^{+9.4}_{-8.0}$	$4.60^{+0.39}_{-0.19}$	–	$(2.97^{+0.87}_{-0.77})\times10^{8}$	$1.5^{+3.1}_{-0.0}$	573^{+291}_{-140}	$(2.53^{+1.47}_{-0})\times10^{-3}$	$1.19^{+0.60}_{-0.21}$	$3.5^{+1.0}_{-1.4}$	$1.232^{+0.084}_{-0.835}$
6.75	10.875	$(7.26^{+2.84}_{-2.28})\times10^{12}$	$46.8^{+7.0}_{-6.3}$	$4.33^{+0.58}_{-0.30}$	–	$(2.54^{+0.74}_{-0.51})\times10^{8}$	$1.1^{+5.6}_{-0.2}$	1044^{+381}_{-307}	$(1.02^{+1.19}_{-0})\times10^{-3}$	–	$0.00^{+0.00}_{-0.00}$	$0.00^{+0.00}_{-0.00}$

NOTE. — Derived SED and physical properties per redshift and stellar-mass bin from this work. $L_{\rm IR}$ and $M_{\rm dust}$ are derived from modified-blackbody SED fits to stacked photometry. $\alpha_{\rm MIR}$ and $\beta_{\rm IR}$ are the mid-infrared power-law slope and Rayleigh–Jeans emissivity index; entries with $\beta_{\rm IR}$ fixed to 2 by the fit prior and $\alpha_{\rm MIR}$ with no meaningful posterior constraint are shown as –. $\rm SFR_{UV}$ is uncorrected for dust attenuation; $\rm SFR_{IR}$ is inferred from $L_{\rm IR}$. $f_{\rm unobs}$ is the fraction of star formation unobserved in the UV; a lower error of 0 indicates the posterior lower bound is consistent with zero. B' is the ratio of bolometric corrections between the 1600Å to total UV and 8–1000 μm to total IR. Both $\rm A_{UV}$ and $\rm A_V$ are inferred from rest-frame UV/optical SED fitting where the quoted statistic is representative of the median and 68% confidence intervals on the stackable sample in the corresponding bin (where the number of sources included are $N_{\rm F}$; these are not representative of errors on individual galaxy $\rm A_{UV}$ or $\rm A_V$ measurements). This table is available online in fits format at https://github.com/caitlinmcasey/duststacks.

REFERENCES

S. Salim and D. Narayanan, arXiv e-prints , arXiv:2001.03181 (2020).
R. Schneider and R. Maiolino, A&A Rev. **32**, 2 (2024).
C. Reina and M. Tarenghi, A&A **26**, 257 (1973).
P. Gorenstein, ApJ **198**, 95 (1975).
P. Predehl and J. H. M. M. Schmitt, A&A **293**, 889 (1995).
T. Güver and F. Özel, MNRAS **400**, 2050 (2009).
N. A. Reddy, M. Kriek, A. E. Shapley, W. R. Freeman, *et al.*, ApJ **806**, 259 (2015).
I. Shivaei, B. Darvish, Z. Sattari, N. Chartab, *et al.*, ApJ **903**, L28 (2020).
A. J. Battisti, M. B. Bagley, I. Baronchelli, Y. S. Dai, *et al.*, MNRAS **513**, 4431 (2022).
D. Calzetti, L. Armus, R. Bohlin, A. Kinney, *et al.*, ApJ **533**, 682 (2000).
I. Smail, R. Ivison, and A. Blain, ApJ **490**, L5+ (1997).
A. Blain, I. Smail, R. Ivison, J. Kneib, *et al.*, Phys. Rep. **369**, 111 (2002).
C. Casey, D. Narayanan, and A. Cooray, Phys. Rep. **541**, 45 (2014a).
J. McKinney, O. R. Cooper, C. M. Casey, J. B. Muñoz, *et al.*, ApJ **985**, L21 (2025).
B. Draine and A. Li, ApJ **657**, 810 (2007).
A. Rémy-Ruyer, S. Madden, F. Galliano, M. Galametz, *et al.*, A&A **563**, A31 (2014).
P. De Vis, A. Jones, S. Viaene, V. Casasola, *et al.*, A&A **623**, A5 (2019).
R. Maiolino, T. Nagao, A. Grazian, F. Cocchia, *et al.*, A&A **488**, 463 (2008).
F. Mannucci, G. Cresci, R. Maiolino, A. Marconi, *et al.*, MNRAS **408**, 2115 (2010).
H. J. Zahid, G. I. Dima, R.-P. Kudritzki, L. J. Kewley, *et al.*, ApJ **791**, 130 (2014).
S. Jain, R. L. Sanders, A. A. Khostovan, T. Jones, *et al.*, ApJ **1000**, 109 (2026).
N. Scoville, H. Aussel, M. Brusa, P. Capak, *et al.*, ApJS **172**, 1 (2007).
M. Shuntov, H. B. Akins, L. Paquereau, C. M. Casey, *et al.*, arXiv e-prints , arXiv:2506.03243 (2025).
R. C. Arango-Toro, O. Ilbert, L. Ciesla, M. Shuntov, *et al.*, A&A **696**, A159 (2025).
C. M. Casey, J. S. Kartaltepe, N. E. Drakos, M. Franco, *et al.*, ApJ **954**, 31 (2023).
P. Kroupa, MNRAS **322**, 231 (2001).
Planck Collaboration, N. Aghanim, Y. Akrami, M. Ashdown, *et al.*, A&A **641**, A6 (2020).
J. Weingartner and B. Draine, ApJ **548**, 296 (2001).
B. Draine, ARA&A **41**, 241 (2003).
J. Cardelli, G. Clayton, and J. Mathis, ApJ **345**, 245 (1989).
S. Charlot and S. Fall, ApJ **539**, 718 (2000).
M. Disney, J. Davies, and S. Phillipps, MNRAS **239**, 939 (1989).
Y. I. Byun, K. C. Freeman, and N. D. Kylafis, ApJ **432**, 114 (1994).
A. N. Witt and K. D. Gordon, ApJ **463**, 681 (1996).
A. N. Witt and K. D. Gordon, ApJ **528**, 799 (2000).
J. Chevallard, S. Charlot, B. Wandelt, and V. Wild, MNRAS **432**, 2061 (2013).
D. Narayanan, R. Davé, B. Johnson, R. Thompson, *et al.*, MNRAS **474**, 1718 (2018).
J. W. Trayford, C. d. P. Lagos, A. S. Robotham, and D. Obreschkow, MNRAS **491**, 3937 (2020).
A. Ferrara, L. Sommovigo, P. Dayal, A. Pallottini, *et al.*, MNRAS **512**, 58 (2022).
J. Qin, X. Z. Zheng, S. Wuyts, Z. Lyu, *et al.*, MNRAS **528**, 658 (2024).
L. Sommovigo, L. Lancaster, S. H. Menon, J. A. O'Leary, *et al.*, ApJ **1003**, 170 (2026).
A. Natta and N. Panagia, ApJ **287**, 228 (1984).
D. Calzetti, A. Kinney, and T. Storchi-Bergmann, ApJ **429**, 582 (1994).
J. Goldader, G. Meurer, T. Heckman, M. Seibert, *et al.*, ApJ **568**, 651 (2002).
J. Howell, L. Armus, J. Mazzarella, A. Evans, *et al.*, ApJ **715**, 572 (2010).
C. Casey *et al.*, ApJ **796**, 95 (2014b).
G. L. Granato, C. G. Lacey, L. Silva, A. Bressan, *et al.*, ApJ **542**, 710 (2000).
R. Bohlin, B. Savage, and J. Drake, ApJ **224**, 132 (1978).
A. Diplas and B. D. Savage, ApJS **93**, 211 (1994).
B. T. Draine, G. Aniano, O. Krause, B. Groves, *et al.*, ApJ **780**, 172 (2014).
R. Hildebrand, QJRAS **24**, 267 (1983).
C. J. R. Clark, P. De Vis, M. Baes, S. Bianchi, *et al.*, MNRAS **489**, 5256 (2019).
J. S. Mathis, W. Rumpl, and K. H. Nordsieck, ApJ **217**, 425 (1977).
B. Draine and H. Lee, ApJ **285**, 89 (1984).
V. Ossenkopf and T. Henning, A&A **291**, 943 (1994).
T. Henning and R. Stognienko, A&A **311**, 291 (1996).
A. Li and B. Draine, ApJ **554**, 778 (2001).
R. Siebenmorgen, N. V. Voshchinnikov, and S. Bagnulo, A&A **561**, A82 (2014).
L. Sommovigo and H. Algera, MNRAS **540**, 3693 (2025).
J. A. Hodge and E. da Cunha, Royal Society Open Science **7**, 200556 (2020).
C. Conselice, ARA&A **52**, 291 (2014).
A. V. Mosenkov, M. Baes, S. Bianchi, V. Casasola, *et al.*, A&A **622**, A132 (2019).
G. Popping, A. Pillepich, G. Calistro Rivera, S. Schulz, *et al.*, MNRAS **510**, 3321 (2022).
C. M. Casey, H. B. Akins, V. Kokorev, J. McKinney, *et al.*, ApJ **975**, L4 (2024).
G. Aniano, B. T. Draine, D. Calzetti, D. A. Dale, *et al.*, ApJ **756**, 138 (2012).
G. Meurer, T. Heckman, and D. Calzetti, ApJ **521**, 64 (1999).
V. Buat, J. Iglesias-Páramo, M. Seibert, D. Burgarella, *et al.*, ApJ **619**, L51 (2005).
C.-N. Hao, R. C. Kennicutt, B. D. Johnson, D. Calzetti, *et al.*, ApJ **741**, 124 (2011).
L. Cortese, A. Boselli, P. Franzetti, R. Decarli, *et al.*, MNRAS **386**, 1157 (2008).
N. Reddy, C. Steidel, D. Erb, A. Shapley, *et al.*, ApJ **653**, 1004 (2006).
A. Gil de Paz, S. Boissier, B. Madore, M. Seibert, *et al.*, ApJS **173**, 185 (2007).
T. Takeuchi, F.-T. Yuan, A. Ikeyama, K. Murata, *et al.*, ApJ **755**, 144 (2012).
R. J. McLure, J. S. Dunlop, F. Cullen, N. Bourne, *et al.*, MNRAS **476**, 3991 (2018).
R. Kennicutt and N. Evans, ARA&A **50**, 531 (2012).
C. Conroy, ARA&A **51**, 393 (2013).
M. Franco, C. M. Casey, H. B. Akins, O. Ilbert, *et al.*, arXiv e-prints , arXiv:2508.04791 (2025).
S. Harish, J. S. Kartaltepe, D. Liu, A. M. Koekemoer, *et al.*, ApJ **992**, 45 (2025).
K. Barbary, K. Boone, C. McCully, M. Craig, *et al.*, "kbarbary/sep: v1.0.0," (2016).
S. Arnouts, L. Moscardini, E. Vanzella, S. Colombi, *et al.*, MNRAS **329**, 355 (2002).
O. Ilbert, S. Arnouts, H. J. McCracken, M. Bolzonella, *et al.*, A&A **457**, 841 (2006).
D. Sanders, M. Salvato, H. Aussel, O. Ilbert, *et al.*, ApJS **172**, 86 (2007).
D. Lutz, A. Poglitsch, B. Altieri, P. Andreani, *et al.*, A&A **532**, A90 (2011).
S. Oliver, J. Bock, B. Altieri, A. Amblard, *et al.*, MNRAS **424**, 1614 (2012).
J. Simpson, I. Smail, A. Swinbank, S. Chapman, *et al.*, ApJ **880**, 43 (2019).
C. R. Carvajal-Bohorquez, G. Lagache, A. Beelen, R. Adam, *et al.*, arXiv e-prints , arXiv:2605.00659 (2026).
M. Béthermin, G. Lagache, C. Carvajal-Bohorquez, R. Adam, *et al.*, A&A **708**, A295 (2026).
A. S. Long, C. M. Casey, J. McKinney, J. A. Zavala, *et al.*, ApJ **999**, 47 (2026).
C. M. Casey, J. A. Zavala, S. M. Manning, M. Aravena, *et al.*, ApJ **923**, 215 (2021).
J. A. Zavala, C. M. Casey, S. M. Manning, M. Aravena, *et al.*, ApJ **909**, 165 (2021).
J. A. Zavala, A. L. Faisst, M. Aravena, C. M. Casey, *et al.*, ApJ **998**, L36 (2026).
C. T. Donnan, R. J. McLure, J. S. Dunlop, D. J. McLeod, *et al.*, MNRAS **533**, 3222 (2024).
D. Liu, P. Lang, B. Magnelli, E. Schinnerer, *et al.*, ApJS **244**, 40 (2019).
S. Adscheid, B. Magnelli, D. Liu, F. Bertoldi, *et al.*, A&A **685**, A1 (2024).
J. McKinney, C. M. Casey, A. S. Long, O. R. Cooper, *et al.*, arXiv e-prints , arXiv:2408.08346 (2024).
E. da Cunha, S. Charlot, and D. Elbaz, MNRAS **388**, 1595 (2008).
E. da Cunha, F. Walter, I. Smail, A. Swinbank, *et al.*, ApJ **806**, 110 (2015).
D. Burgarella, V. Buat, and J. Iglesias-Páramo, MNRAS **360**, 1413 (2005).
S. Noll, D. Burgarella, E. Giovannoli, V. Buat, *et al.*, A&A **507**, 1793 (2009).
M. Boquien, D. Burgarella, Y. Roehlly, V. Buat, *et al.*, A&A **622**, A103 (2019).

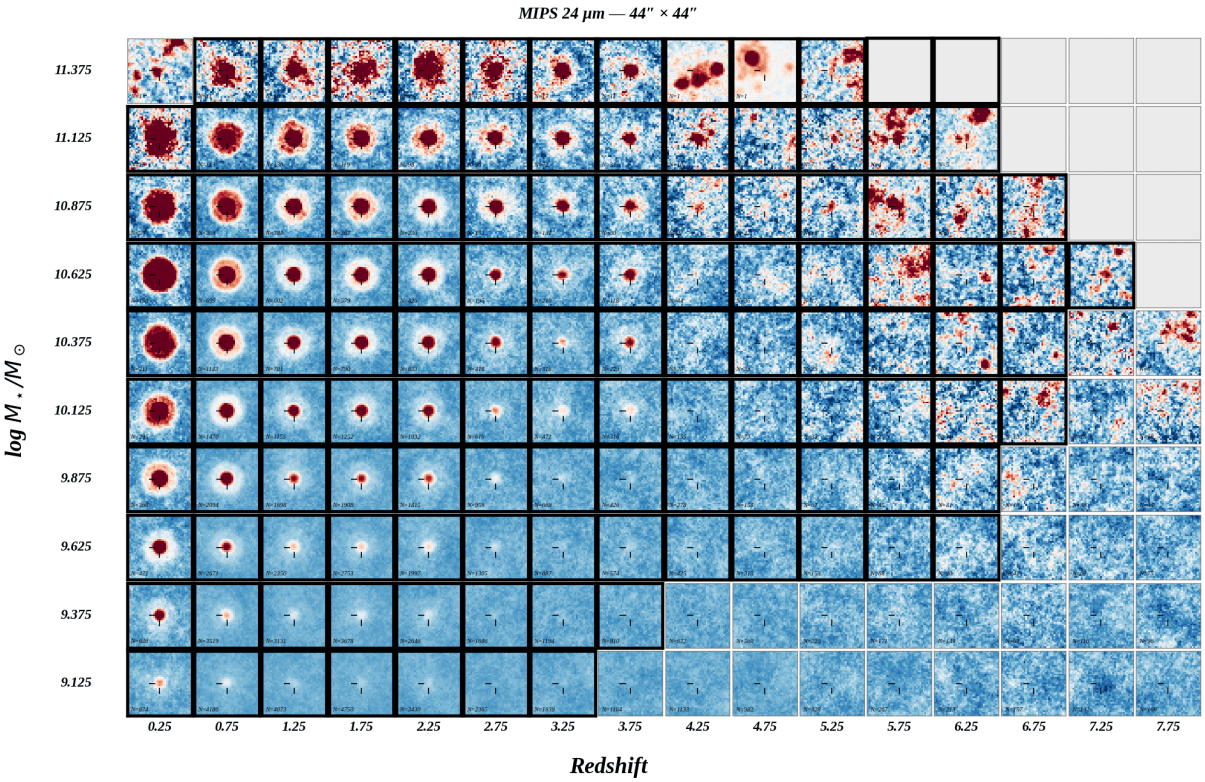

FIG. 31.— Two-dimensional stacked MIPS 24 μm cutouts.

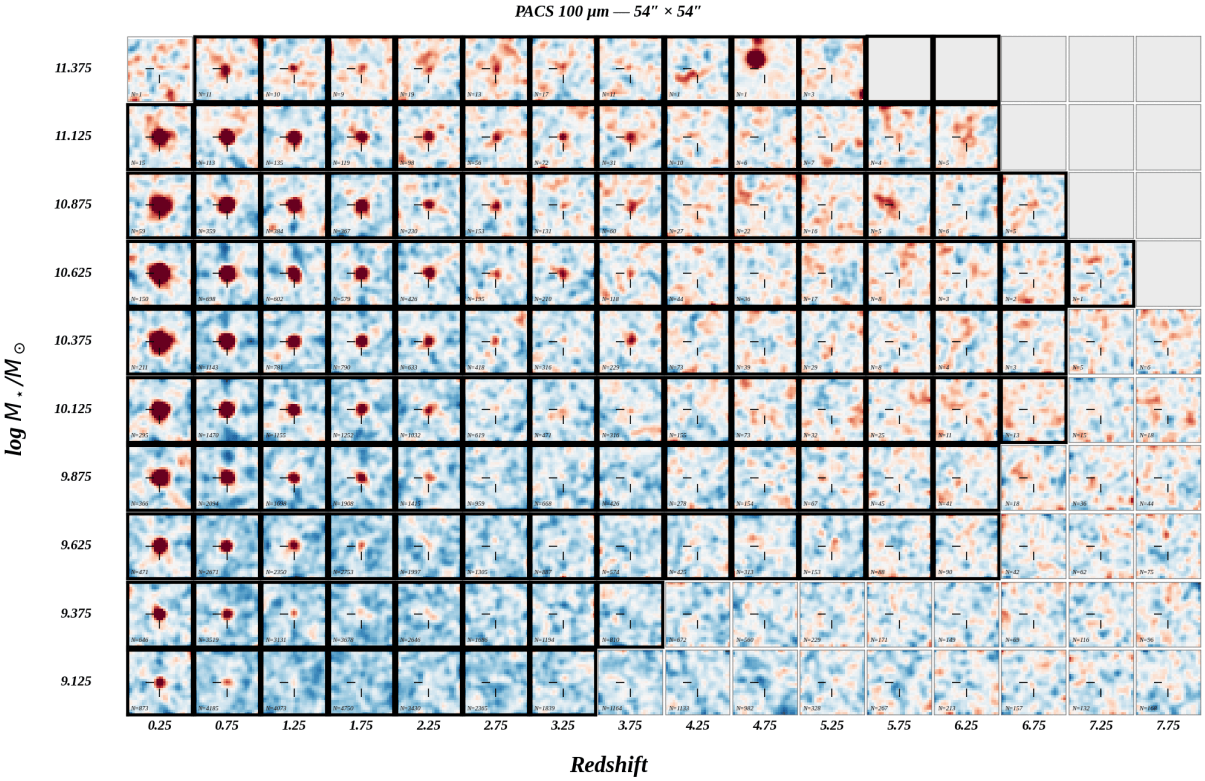

FIG. 32.— Two-dimensional stacked PACS 100 μm cutouts.

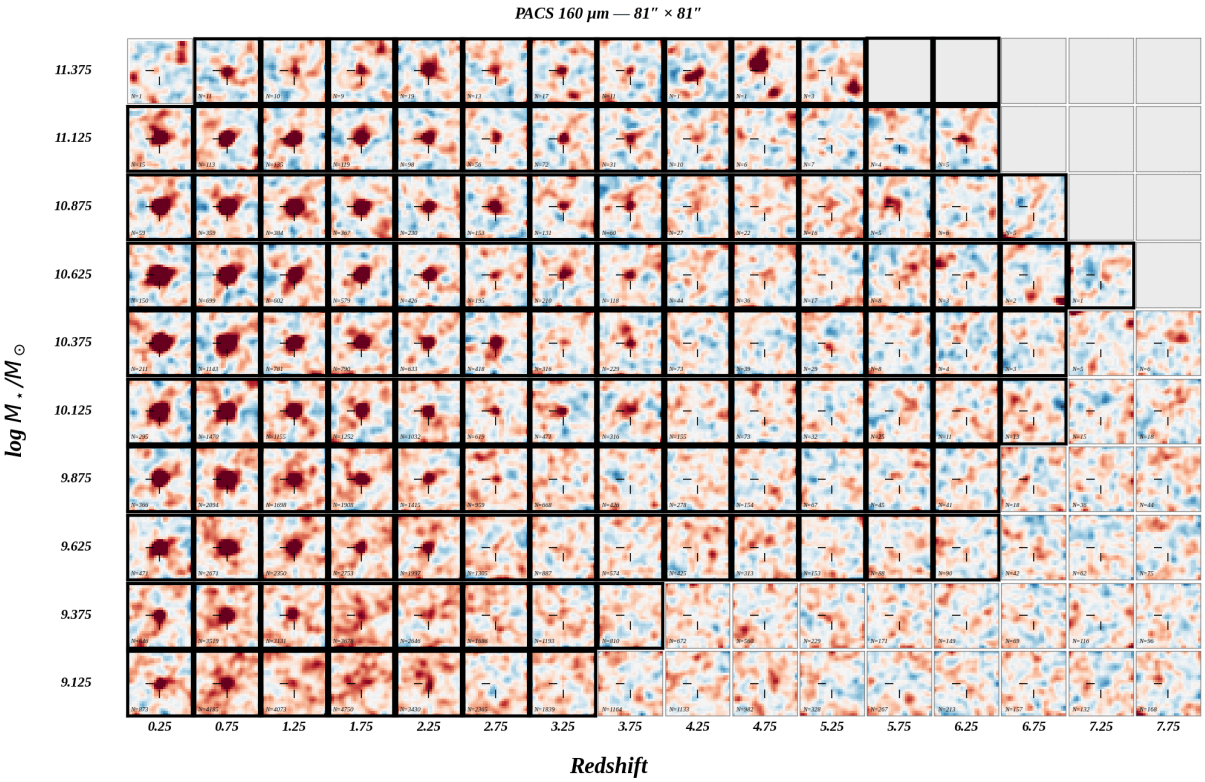

FIG. 33.— Two-dimensional stacked PACS 160 μm cutouts.

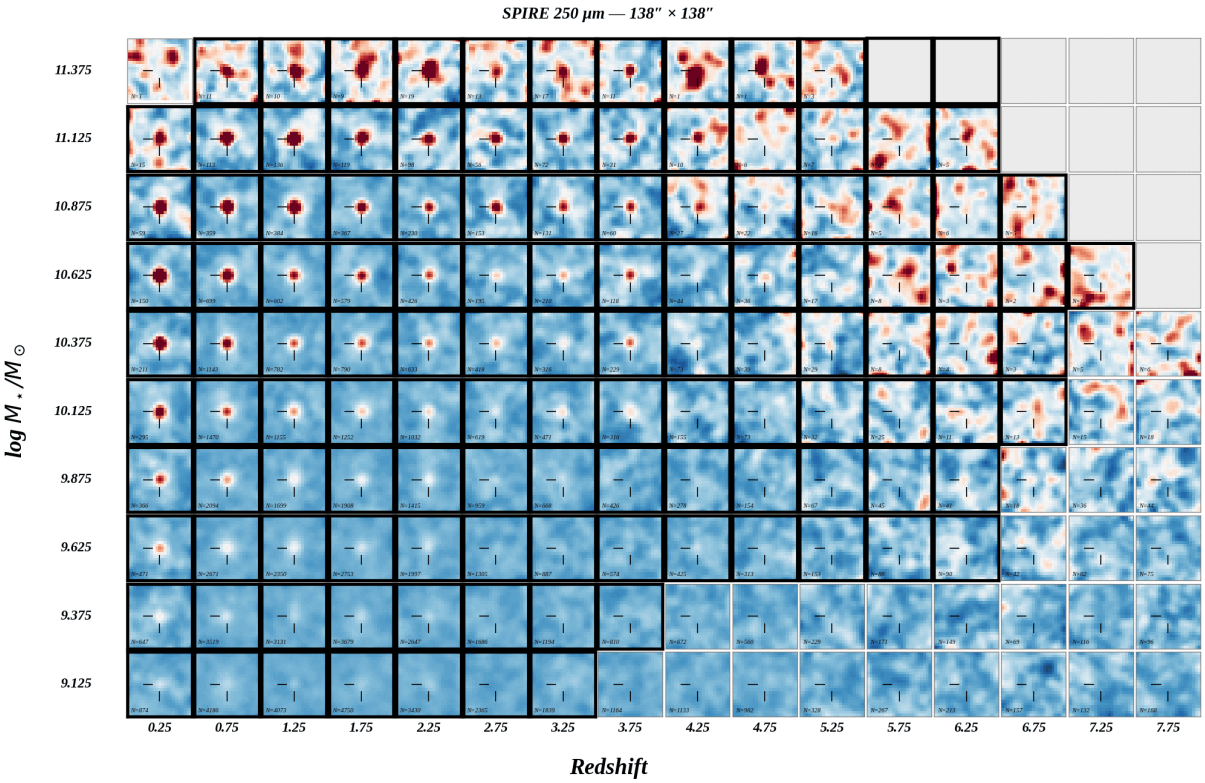

FIG. 34.— Two-dimensional stacked SPIRE 250 μm cutouts.

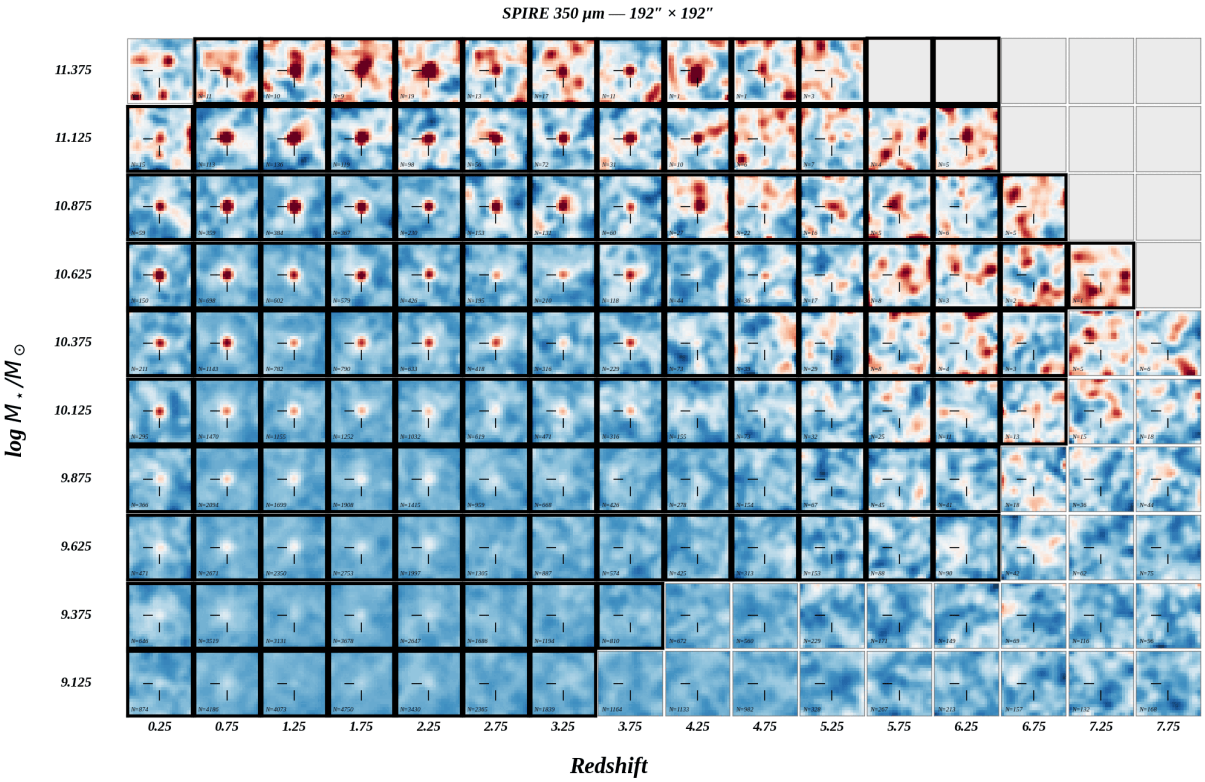

FIG. 35.— Two-dimensional stacked SPIRE 350 μm cutouts.

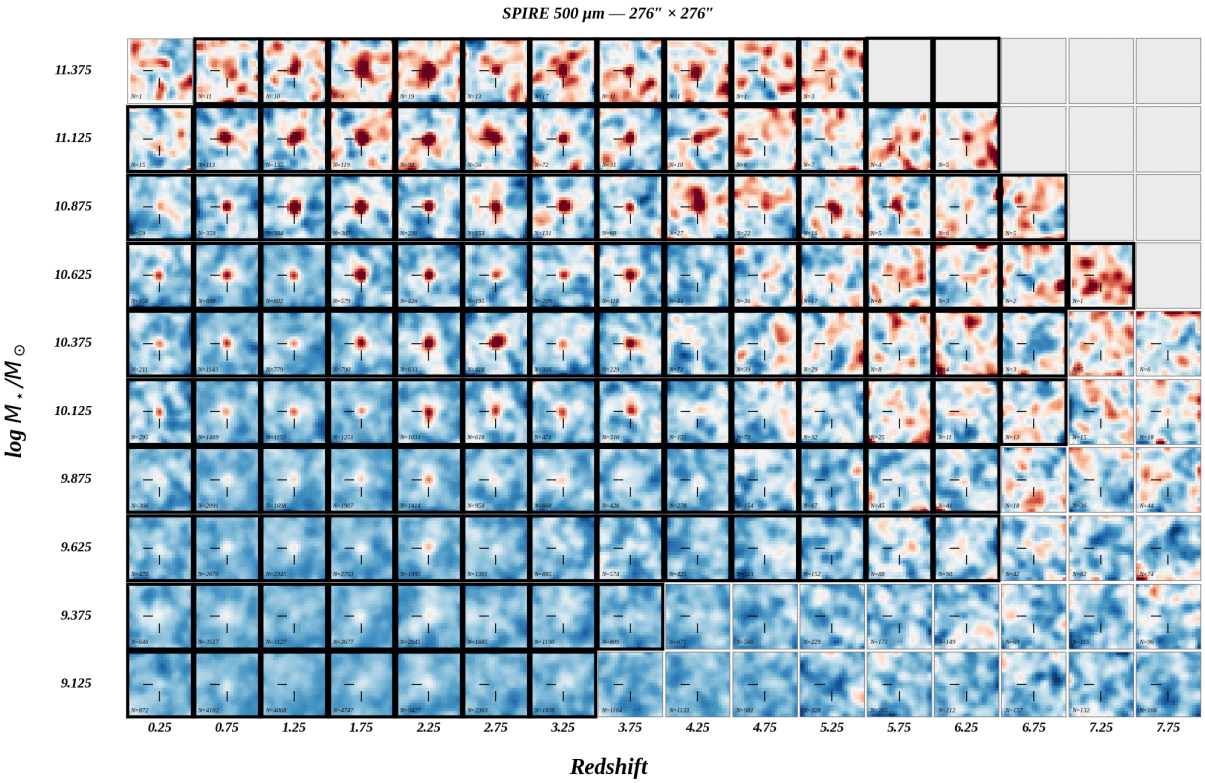

FIG. 36.— Two-dimensional stacked SPIRE 500 μm cutouts.

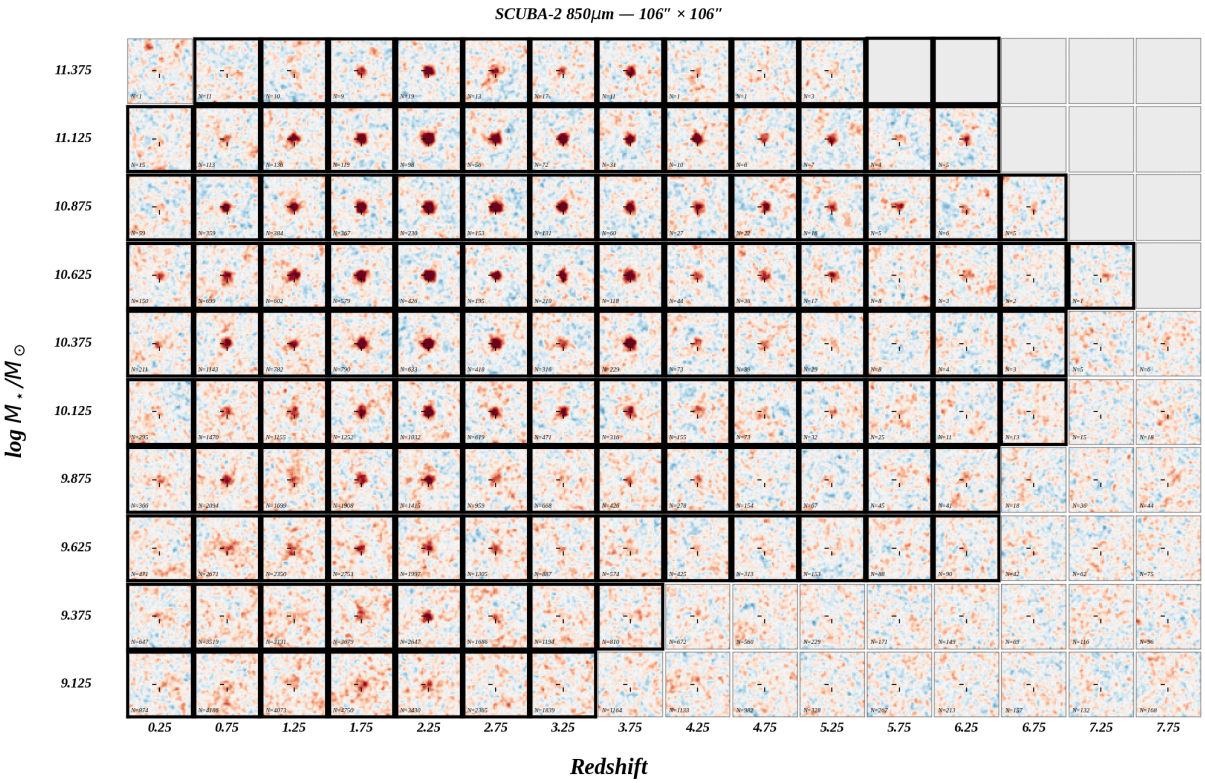

FIG. 37.— Two-dimensional stacked SCUBA-2 850 μm cutouts.

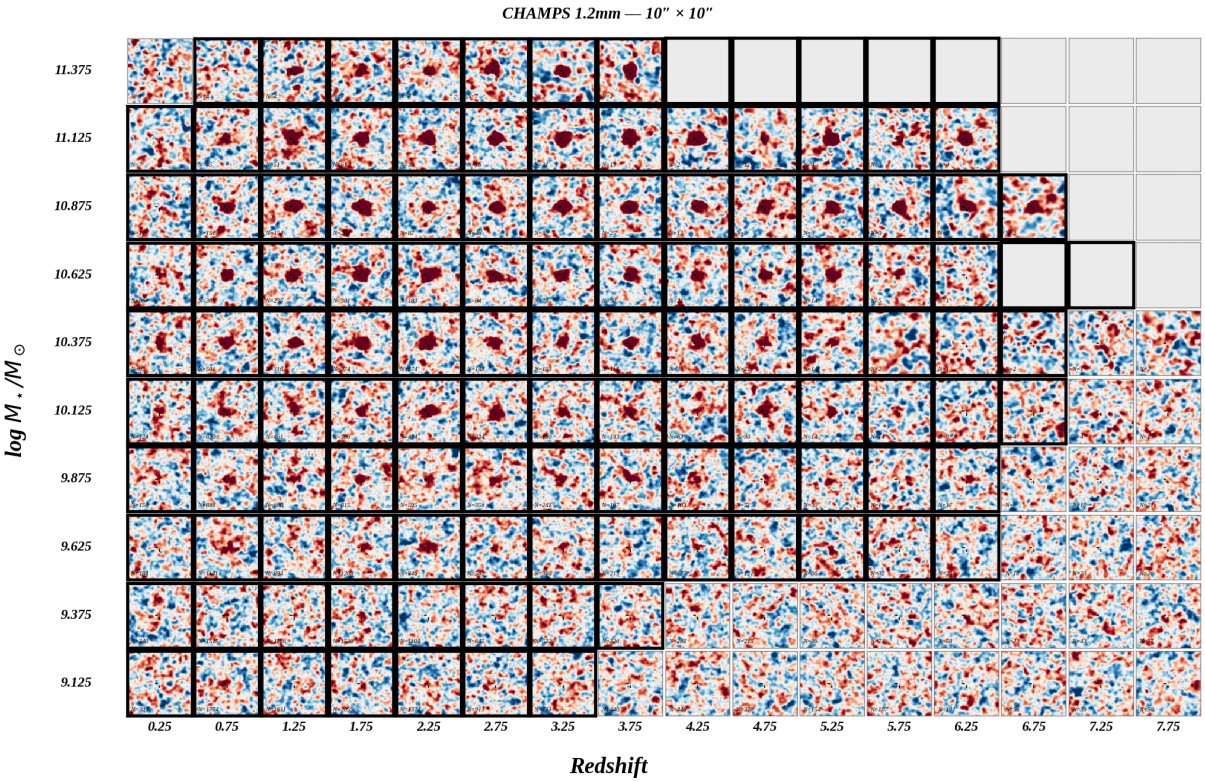

FIG. 38.— Two-dimensional stacked CHAMPS 1.2 mm cutouts.

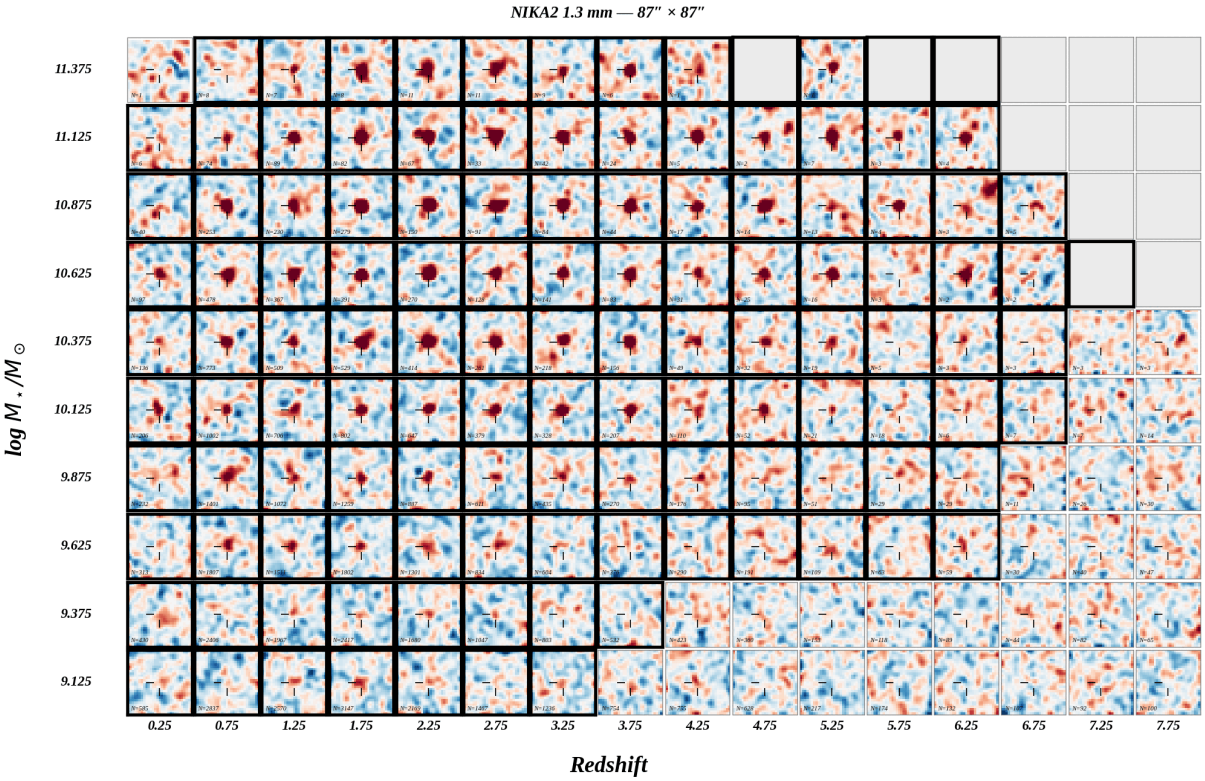

FIG. 39.— Two-dimensional stacked NIKA-2 1.2 mm cutouts.

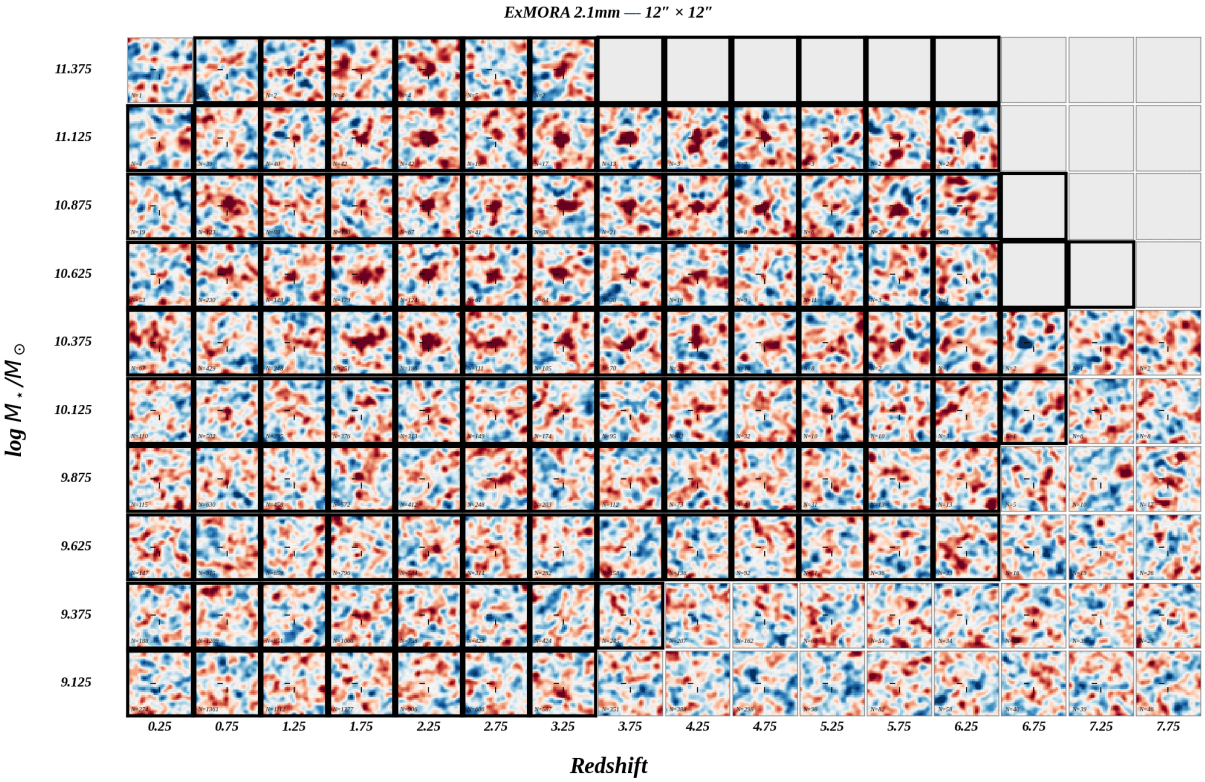

FIG. 40.— Two-dimensional stacked Ex-MORA 2.1 mm cutouts.

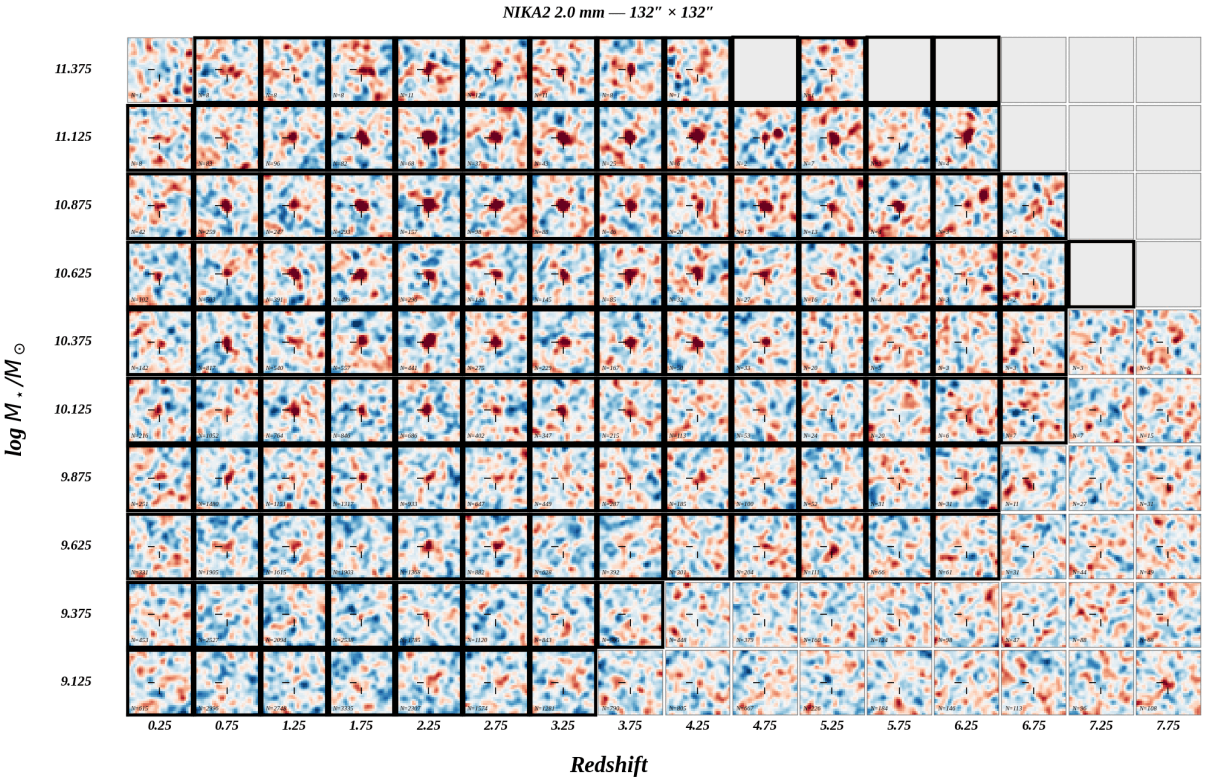

FIG. 41.— Two-dimensional stacked NIKA-2 2 mm cutouts.

L. Silva, G. Granato, A. Bressan, and L. Danese, ApJ **509**, 103 (1998).
E.-D. Paspaliaris, E. M. Xilouris, A. Nersesian, S. Bianchi, *et al.*, A&A **669**, A11 (2023).
W. Chang, G. Wilson, B. Forrest, I. McConachie, *et al.*, ApJ **1001**, 131 (2026).
H. Dole, G. Lagache, J.-L. Puget, K. I. Caputi, *et al.*, A&A **451**, 417 (2006).
E. Pascale, P. A. R. Ade, J. J. Bock, E. L. Chapin, *et al.*, ApJ **707**, 1740 (2009).
K. Penner, A. Pope, E. L. Chapin, T. R. Greve, *et al.*, MNRAS **410**, 2749 (2011).
M. Viero, L. Wang, M. Zemcov, G. Addison, *et al.*, ApJ **772**, 77 (2013).
M. Béthermin, E. Daddi, G. Magdis, C. Lagos, *et al.*, A&A **573**, A113 (2015a).
K. Coppin, J. Geach, O. Almaini, V. Arumugam, *et al.*, MNRAS **446**, 1293 (2015).
L. Tacconi, R. Genzel, A. Saintonge, F. Combes, *et al.*, ApJ **853**, 179 (2018).
H. Inami, R. Decarli, F. Walter, A. Weiss, *et al.*, ApJ **902**, 113 (2020).
B. Magnelli, L. Boogaard, R. Decarli, J. Gónzalez-López, *et al.*, ApJ **892**, 66 (2020).
Euclid Collaboration, R. Hill, A. Abghari, D. Scott, *et al.*, A&A **711**, A23 (2026).
R. K. Sheth and G. Tormen, MNRAS **308**, 119 (1999).
M. Boylan-Kolchin, Nature Astronomy **7**, 731 (2023).
N. Evans, II, M. Dunham, J. Jørgensen, M. Enoch, *et al.*, ApJS **181**, 321 (2009).
F. Bigiel, A. Leroy, F. Walter, L. Blitz, *et al.*, AJ **140**, 1194 (2010).
T. Thompson, E. Quataert, and N. Murray, ApJ **630**, 167 (2005).
E. C. Ostriker and R. Shetty, ApJ **731**, 41 (2011).
G. Toni, M. Maturi, G. Castignani, L. Moscardini, *et al.*, A&A **707**, A87 (2026).
J. Speagle, C. Steinhardt, P. Capak, and J. Silverman, ApJS **214**, 15 (2014).
P. Popesso, A. Concas, G. Cresci, S. Belli, *et al.*, MNRAS **519**, 1526 (2023), arXiv:2203.10487 [astro-ph.GA].
K. Iwasawa, D. B. Sanders, S. H. Teng, V. U, *et al.*, A&A **529**, A106 (2011).
L. Ciesla, V. Charmandaris, A. Georgakakis, E. Bernhard, *et al.*, A&A **576**, A10 (2015).
J. Florez, S. Jogee, S. Sherman, M. L. Stevans, *et al.*, MNRAS **497**, 3273 (2020).
J. Buchner, H. Starck, M. Salvato, H. Netzer, *et al.*, A&A **692**, A161 (2024).
A. Georgakakis, J. Aird, A. Schulze, T. Dwelly, *et al.*, MNRAS **471**, 1976 (2017).
J. Aird, A. L. Coil, and A. Georgakakis, MNRAS **474**, 1225 (2018).
G. Yang, W. N. Brandt, F. Vito, C.-T. J. Chen, *et al.*, MNRAS **475**, 1887 (2018).
F. Zou, Z. Yu, W. N. Brandt, H. Tak, *et al.*, ApJ **964**, 183 (2024).
I. Delvecchio, C. Gruppioni, F. Pozzi, S. Berta, *et al.*, MNRAS **439**, 2736 (2014).
P. Madau and M. Dickinson, ARA&A **52**, 415 (2014).
P. M. Drew and C. M. Casey, ApJ **930**, 142 (2022).
C. M. Casey, MNRAS **425**, 3094 (2012).
B. Draine, ApJ **636**, 1114 (2006).
A. Conley, A. Cooray, J. D. Vieira, E. A. González Solares, *et al.*, ApJ **732**, L35 (2011).
T. Greve, J. Vieira, A. Weiß, J. Aguirre, *et al.*, ApJ **756**, 101 (2012).
J. Simpson, I. Smail, A. Swinbank, R. Ivison, *et al.*, ApJ **839**, 58 (2017).
V. U, D. Sanders, J. Mazzarella, A. Evans, *et al.*, ApJS **203**, 9 (2012).
A. Kirkpatrick, A. Pope, D. Alexander, V. Charmandaris, *et al.*, ApJ **759**, 139 (2012).
L. Dunne and S. Eales, MNRAS **327**, 697 (2001).
O. R. Cooper, C. M. Casey, J. A. Zavala, J. B. Champagne, *et al.*, ApJ **930**, 32 (2022).
E. da Cunha, B. Groves, F. Walter, R. Decarli, *et al.*, ApJ **766**, 13 (2013).
G. Brammer, P. van Dokkum, and P. Coppi, ApJ **686**, 1503 (2008).
S. Arnouts, E. Le Floc'h, J. Chevallard, B. D. Johnson, *et al.*, A&A **558**, A67 (2013).
S. Salim, M. Boquien, and J. C. Lee, ApJ **859**, 11 (2018).
A. C. Carnall, R. J. McLure, J. S. Dunlop, and R. Davé, MNRAS **480**, 4379 (2018).
J. J. Eldridge and E. R. Stanway, MNRAS **400**, 1019 (2009).
T. Garn and P. N. Best, MNRAS **409**, 421 (2010).
S. Salim, J. C. Lee, S. Janowiecki, E. da Cunha, *et al.*, ApJS **227**, 2 (2016).
S. Heinis, V. Buat, M. Béthermin, J. Bock, *et al.*, MNRAS **437**, 1268 (2014).
M. Pannella, D. Elbaz, E. Daddi, M. Dickinson, *et al.*, ApJ **807**, 141 (2015).
A. E. Shapley, R. L. Sanders, S. Salim, N. A. Reddy, *et al.*, ApJ **926**, 145 (2022).
B. M. Devour and E. F. Bell, MNRAS **459**, 2054 (2016).
J. Bogdanoska and D. Burgarella, MNRAS **496**, 5341 (2020).
J. Miralda-Escudé and M. J. Rees, ApJ **497**, 21 (1998).
H. Katz, A. J. Cameron, A. Saxena, L. Barrufet, *et al.*, arXiv e-prints , arXiv:2408.03189 (2024).
C. Conroy, D. Schiminovich, and M. Blanton, ApJ **718**, 184 (2010).
V. Buat, S. Noll, D. Burgarella, E. Giovannoli, *et al.*, A&A **545**, A141 (2012).
M. Kriek and C. Conroy, ApJ **775**, L16 (2013).
N. Reddy, C. Steidel, M. Pettini, and M. Bogosavljevic, ArXiv e-prints (2016).
J. Leja, B. D. Johnson, C. Conroy, P. G. van Dokkum, *et al.*, ApJ **837**, 170 (2017).
A. J. Battisti, D. Calzetti, and R.-R. Chary, ApJ **818**, 13 (2016).
A. P. Vijayan, P. A. Thomas, C. C. Lovell, S. M. Wilkins, *et al.*, MNRAS **527**, 7337 (2024).
V. Markov, S. Gallerani, A. Ferrara, A. Pallottini, *et al.*, Nature Astronomy **9**, 458 (2025a).
V. Markov, S. Gallerani, A. Pallottini, M. Bradač, *et al.*, A&A **702**, A33 (2025b).
I. Shivaei, R. P. Naidu, F. Rodríguez Montero, K. Matsumoto, *et al.*, arXiv e-prints , arXiv:2509.01795 (2025).
E. Le Floc'h, C. Papovich, H. Dole, E. Bell, *et al.*, ApJ **632**, 169 (2005).
K. Caputi, G. Lagache, L. Yan, H. Dole, *et al.*, ApJ **660**, 97 (2007).
C. Casey, S. Berta, M. Béthermin, J. Bock, *et al.*, ApJ **761**, 140 (2012).
C. Gruppioni *et al.*, MNRAS **432**, 23 (2013).
M. P. Viero, G. Sun, D. T. Chung, L. Moncelsi, *et al.*, MNRAS **516**, L30 (2022).
G. T. Jones and E. R. Stanway, MNRAS **525**, 5720 (2023).
C. M. Casey, H. B. Akins, S. L. Finkelstein, M. Franco, *et al.*, ApJ **990**, L61 (2025).
D. J. Setton, J. E. Greene, J. S. Spilker, C. C. Williams, *et al.*, arXiv e-prints , arXiv:2503.02059 (2025).
M. Xiao, P. A. Oesch, L. Bing, D. Elbaz, *et al.*, arXiv e-prints , arXiv:2503.01945 (2025).
M. Béthermin, C. De Breuck, M. Sargent, and E. Daddi, A&A **576**, L9 (2015b).
C. Schreiber, D. Elbaz, M. Pannella, L. Ciesla, *et al.*, A&A **609**, A30 (2018).
R. Bouwens, J. González-López, M. Aravena, R. Decarli, *et al.*, ApJ **902**, 112 (2020).
A. D. Burnham, C. M. Casey, J. A. Zavala, S. M. Manning, *et al.*, ApJ **910**, 89 (2021).
U. Dudzevičiūtė, I. Smail, A. M. Swinbank, S. M. Stach, *et al.*, MNRAS **494**, 3828 (2020), arXiv:1910.07524 [astro-ph.GA].
K. E. Whitaker, A. Pope, R. Cybulski, C. M. Casey, *et al.*, ApJ **850**, 208 (2017).
D. T. Zimmerman, D. Narayanan, K. E. Whitaker, and R. Davé, ApJ **973**, 146 (2024).
K. Whitaker, M. Franx, J. Leja, P. van Dokkum, *et al.*, ApJ **795**, 104 (2014).
R. Skelton, K. Whitaker, I. Momcheva, G. Brammer, *et al.*, ApJS **214**, 24 (2014).
F. Galliano, M. Galametz, and A. P. Jones, ARA&A **56**, 673 (2018).
N. Scoville, K. Sheth, H. Aussel, P. Vanden Bout, *et al.*, ApJ **820**, 83 (2016).
E. da Cunha, V. Charmandaris, T. Díaz-Santos, L. Armus, *et al.*, A&A **523**, A78 (2010).
L. Dunne, H. L. Gomez, E. da Cunha, S. Charlot, *et al.*, MNRAS **417**, 1510 (2011).
P. Santini, R. Maiolino, B. Magnelli, D. Lutz, *et al.*, A&A **562**, A30 (2014).
L. Cortese, L. Ciesla, A. Boselli, S. Bianchi, *et al.*, A&A **540**, A52 (2012).
P. Andreani, A. Boselli, L. Ciesla, R. Vio, *et al.*, A&A **617**, A33 (2018).
F. Galliano, A. Nersesian, S. Bianchi, I. De Looze, *et al.*, A&A **649**, A18 (2021).
S. Eales, M. Smith, T. Bakx, J. D'Silva, *et al.*, arXiv e-prints , arXiv:2605.19661 (2026).
M. A. Strauss, D. H. Weinberg, R. H. Lupton, V. K. Narayanan, *et al.*, AJ **124**, 1810 (2002).
R. G. Kron, ApJS **43**, 305 (1980).
A. Swinbank, I. Smail, S. Chapman, A. Blain, *et al.*, ApJ **617**, 64 (2004).

S. Chapman, A. Blain, I. Smail, and R. Ivison, ApJ **622**, 772 (2005).
K. Adelberger and C. Steidel, ApJ **544**, 218 (2000).
I. Smail, S. Chapman, A. Blain, and R. Ivison, ApJ **616**, 71 (2004).
F. Cullen, R. J. McLure, S. Khochfar, J. S. Dunlop, *et al.*, MNRAS **470**, 3006 (2017).
M. Seibert, D. Martin, T. Heckman, V. Buat, *et al.*, ApJ **619**, L55 (2005).
R. Overzier, T. Heckman, J. Wang, L. Armus, *et al.*, ApJ **726**, L7 (2011).
L. Yang, J. S. Kartaltepe, M. Franco, X. Ding, *et al.*, ApJS **281**, 68 (2025).
P. F. Hopkins, N. Murray, E. Quataert, and T. A. Thompson, MNRAS **401**, L19 (2010).
Y. Cheng, M. Giavalisco, B. E. Backhaus, R. Bhatawdekar, *et al.*, ApJ **979**, 71 (2025).
L. Sommovigo, A. Ferrara, A. Pallottini, S. Carniani, *et al.*, MNRAS **497**, 956 (2020).
L. Liang, R. Feldmann, C. C. Hayward, D. Narayanan, *et al.*, MNRAS **502**, 3210 (2021).
M. Parente, C. Ragone-Figueroa, P. López, H. J. Martínez, *et al.*, ApJ **966**, 154 (2024).
C. W. Engelbracht, K. D. Gordon, G. H. Rieke, M. W. Werner, *et al.*, ApJ **628**, L29 (2005).
D. Calzetti, R. C. Kennicutt, C. W. Engelbracht, C. Leitherer, *et al.*, ApJ **666**, 870 (2007).
R. Maiolino and F. Mannucci, A&A Rev. **27**, 3 (2019).
R. Asano, T. Takeuchi, H. Hirashita, and A. Inoue, Earth, Planets, and Space **65**, 213 (2013a).
R. S. Asano, T. T. Takeuchi, H. Hirashita, and A. K. Inoue, Earth, Planets and Space **65**, 213 (2013b).
S. Zhukovska, C. Dobbs, E. B. Jenkins, and R. S. Klessen, ApJ **831**, 147 (2016).
H. Hirashita and K. Omukai, MNRAS **399**, 1795 (2009).
G. Jones, C. Willott, C. Carilli, A. Ferrara, *et al.*, ArXiv e-prints (2017).
A. Laor and B. T. Draine, ApJ **402**, 441 (1993).
R. Maiolino, A. Marconi, M. Salvati, G. Risaliti, *et al.*, A&A **365**, 28 (2001a).
R. Maiolino, A. Marconi, and E. Oliva, A&A **365**, 37 (2001b).
S. Aoyama, K.-C. Hou, I. Shimizu, H. Hirashita, *et al.*, MNRAS **466**, 105 (2017).
K.-C. Hou, S. Aoyama, H. Hirashita, K. Nagamine, *et al.*, MNRAS **485**, 1727 (2019).
D. Narayanan, P. Torrey, D. Stark, J. Chisholm, *et al.*, The Open Journal of Astrophysics **9**, 59986 (2026).
S. Chapman, A. Barger, L. Cowie, D. Scott, *et al.*, ApJ **585**, 57 (2003).
M. Symeonidis *et al.*, MNRAS **431**, 2317 (2013).
B. Magnelli, D. Lutz, A. Saintonge, S. Berta, *et al.*, A&A **561**, A86 (2014).
M. Lehnert and T. Heckman, ApJ **462**, 651 (1996).
P. Chanial, H. Flores, B. Guiderdoni, D. Elbaz, *et al.*, A&A **462**, 81 (2007).
D. Lutz, S. Berta, A. Contursi, N. Förster Schreiber, *et al.*, A&A **591**, A136 (2016).
T. Díaz-Santos, V. Charmandaris, L. Armus, A. Petric, *et al.*, ApJ **723**, 993 (2010).
M. Parente, C. Ragone-Figueroa, G. L. Granato, L. Silva, *et al.*, A&A **697**, A231 (2025).
U. Dudzevičiūtė, I. Smail, A. M. Swinbank, C.-F. Lim, *et al.*, MNRAS **500**, 942 (2021), arXiv:2010.06605 [astro-ph.GA].
G. Popping, R. Somerville, and M. Galametz, MNRAS **471**, 3152 (2017).
C. d. P. Lagos, A. S. Robotham, J. W. Trayford, R. Tobar, *et al.*, MNRAS **489**, 4196 (2019).
C. d. P. Lagos, M. Bravo, R. Tobar, D. Obreschkow, *et al.*, MNRAS **531**, 3551 (2024).
A. P. Vijayan, S. J. Clay, P. A. Thomas, R. M. Yates, *et al.*, MNRAS **489**, 4072 (2019).
O. Osman, G. De Lucia, F. Fontanot, L. Xie, *et al.*, arXiv e-prints , arXiv:2512.15902 (2025).
C. d. P. Lagos, R. J. Tobar, A. S. Robotham, D. Obreschkow, *et al.*, MNRAS **481**, 3573 (2018).
D. Donevski, A. Lapi, K. Małek, D. Liu, *et al.*, A&A **644**, A144 (2020).
J.-B. Jolly, K. Knudsen, N. Laporte, A. Guerrero, *et al.*, A&A **693**, A190 (2025).
O. Ilbert, H. McCracken, O. Le Fèvre, P. Capak, *et al.*, A&A **556**, A55 (2013).
A. Mortlock, C. J. Conselice, W. G. Hartley, K. Duncan, *et al.*, MNRAS **447**, 2 (2015).
H. J. Zahid, M. J. Geller, L. J. Kewley, H. S. Hwang, *et al.*, ApJ **771**, L19 (2013).
M. Curti, F. Mannucci, G. Cresci, and R. Maiolino, MNRAS **491**, 944 (2020).
R. L. Sanders, A. E. Shapley, T. Jones, N. A. Reddy, *et al.*, ApJ **914**, 19 (2021).
R. L. Sanders, A. E. Shapley, M. W. Topping, N. A. Reddy, *et al.*, ApJ **955**, 54 (2023).
C. Schreiber, M. Pannella, D. Elbaz, M. Béthermin, *et al.*, A&A **575**, A74 (2015).
P. Kurczynski and E. Gawiser, AJ **139**, 1592 (2010).
M. Béthermin, H.-Y. Wu, G. Lagache, I. Davidzon, *et al.*, A&A **607**, A89 (2017).
C. Casey, J. Zavala, J. Spilker, E. da Cunha, *et al.*, ApJ **862**, 77 (2018).
A. S. Long, C. M. Casey, C. del P. Lagos, E. L. Lambrides, *et al.*, ApJ **953**, 11 (2023).
A. Klypin, G. Yepes, S. Gottlöber, F. Prada, *et al.*, MNRAS **457**, 4340 (2016).
A. Rodríguez-Puebla, P. Behroozi, J. Primack, A. Klypin, *et al.*, MNRAS **462**, 893 (2016).
A. Vale and J. P. Ostriker, MNRAS **353**, 189 (2004).
M. Sargent, M. Béthermin, E. Daddi, and D. Elbaz, ApJ **747**, L31 (2012).
M. Béthermin, E. Le Floc'h, O. Ilbert, A. Conley, *et al.*, A&A **542**, A58 (2012).
M. Béthermin, L. Wang, O. Doré, G. Lagache, *et al.*, A&A **557**, A66 (2013)

Affiliations

1 Department of Physics, University of California, Santa Barbara, Santa Barbara, CA 93106, USA
2 Cosmic Dawn Center (DAWN), Denmark
3 Department of Astronomy, The University of Texas at Austin, 2515 Speedway Blvd Stop C1400, Austin, TX 78712, USA
4 International Centre for Radio Astronomy Research, University of Western Australia, 35 Stirling Hwy, Crawley, WA 6009, Australia
5 Research School of Astronomy and Astrophysics, Australian National University, Cotter Road, Weston Creek, ACT 2611, Australia
6 Instituto de Alta Investigación, Universidad de Tarapacá, Casilla 7D, Arica, Chile
7 University of Massachusetts Amherst, 710 North Pleasant Street, Amherst, MA 01003-9305, USA
8 Academia Sinica Institute of Astronomy and Astrophysics (ASIAA), No. 1, Sec. 4, Roosevelt Road, Taipei 10617, Taiwan
9 Instituto de Estudios Astrofícos, Facultad de Ingeniería y Ciencias, Universidad Diego Portales, Av. Ejército 441, Santiago, Chile
10 Millenium Nucleus for Galaxies (MINGAL)
11 Department of Astronomy, The University of Washington, Seattle, WA 98195, USA
12 Department of Physics and Astronomy, University of Hawaii, Hilo, 200 W Kawili St, Hilo, HI 96720, USA
13 Caltech/IPAC, MS 314-6, 1200 E. California Blvd., Pasadena, CA 91125, USA
14 Université Paris-Saclay, Université Paris Cité, CEA, CNRS, AIM, 91191 Gif-sur-Yvette, France
15 David A. Dunlap Department of Astronomy & Astrophysics, University of Toronto, 50 St. George Street, Toronto, ON M5S 3H4, Canada
16 Department of Computer Science, Aalto University, P.O. Box 15400, FI-00076 Espoo, Finland
17 Department of Physics, University of Helsinki, P.O. Box 64, FI-00014 Helsinki, Finland
18 Department of Physics and Astronomy, University of California, Riverside, 900 University Ave, Riverside, CA 92521, USA
19 Space Telescope Science Institute, 3700 San Martin Dr., Baltimore, MD 21218, USA
20 Institute of Physics, GalSpec, Ecole Polytechnique Federale de Lausanne, Observatoire de Sauverny, Chemin Pegasi 51, 1290 Versoix, Switzerland
21 INAF, Astronomical Observatory of Trieste, Via Tiepolo 11, 34131 Trieste, Italy
22 Aix Marseille Univ, CNRS, CNES, LAM, Marseille, France
23 Kavli Institute for Astronomy and Astrophysics, Peking University, Beijing 100871, China

24 Laboratory for Multiwavelength Astrophysics, School of Physics and Astronomy, Rochester Institute of Technology, 84 Lomb Memorial Drive, Rochester, NY 14623, USA

25 National Astronomical Observatory of Japan, 2-21-1 Osawa, Mitaka, Tokyo 181-8588, Japan

26 NASA-Goddard Space Flight Center, Code 662, Greenbelt, MD 20771, USA

27 Purple Mountain Observatory, Chinese Academy of Sciences, 10 Yuanhua Road, Nanjing 210023, China

28 DTU-Space, Technical University of Denmark, Elektrovej 327, 2800, Kgs. Lyngby, Denmark

29 Niels Bohr Institute, University of Copenhagen, Jagtvej 128, DK-2200, Copenhagen, Denmark

30 Department of Physics, Centre for Extragalactic Astronomy, Durham University, South Road, Durham DH1 3LE, UK

31 Department of Physics, Northeastern University, 360 Huntington Ave, Boston, MA

32 Institut d'Astrophysique de Paris, CNRS, Sorbonne Université, 98 bis Boulevard Arago, F-75014 Paris, France

33 University of Bologna – Department of Physics and Astronomy "Augusto Righi" (DIFA), Via Gobetti 93/2, I-40129 Bologna, Italy

34 INAF – Osservatorio di Astrofisica e Scienza dello Spazio, Via Gobetti 93/3, I-40129 Bologna, Italy

35 INFN – Sezione di Bologna, Viale Berti Pichat 6/2, I-40127 Bologna, Italy

36 Department of Astronomy, University of Florida, 211 Bryant Space Sciences Center, Gainesville, FL 32611, USA

37 Department of Space, Earth and Environment, Chalmers University of Technology, SE-412 96 Gothenburg, Sweden

38 Jet Propulsion Laboratory, California Institute of Technology, 4800 Oak Grove Drive, Pasadena, CA 91109, USA

39 Department of Astronomy and Astrophysics, University of California, Santa Cruz, 1156 High Street, Santa Cruz, CA 95064, USA

40 Department of Astronomy, National Research Institute of Astronomy and Geophysics (NRIAG), Cairo 11421, Egypt

41 Minnesota Institute for Astrophysics, School of Physics and Astronomy, University of Minnesota, 116 Church St. SE, Minneapolis, MN 55455, USA

42 University of Geneva, 24 rue du Général-Dufour, 1211 Genève 4, Switzerland

43 Center for Computational Astrophysics, Flatiron Institute, 162 Fifth Avenue, New York, NY 10010, USA

44 Astronomy Centre, University of Sussex, Falmer, Brighton BN1 9QH, UK

45 School of Astronomy and Space Science, Nanjing University, Nanjing, Jiangsu 210093, China

46 Key Laboratory of Modern Astronomy and Astrophysics, Nanjing University, Ministry of Education, Nanjing 210093, China

47 Kavli Institute for the Physics and Mathematics of the Universe (WPI), The University of Tokyo, Kashiwa, Chiba 277-8583, Japan

∗ NSF Graduate Research Fellow

† NASA Hubble Fellow

‡ NPP Fellow

This paper was built using the Open Journal of Astrophysics LaTeX template. The OJA is a journal which provides fast and easy peer review for new papers in the `astro-ph` section of the arXiv, making the reviewing process simpler for authors and referees alike. Learn more at http://astro.theoj.org.